Full-field vibrometry by high-speed digital holography for middle-ear mechanics

A Dissertation
submitted to the faculty of the

Worcester Polytechnic Institute

as a partial fulfillment of the requirements for the
Degree of Doctor of Philosophy
in
Mechanical Engineering

By

Ivo T. Dobrev

14 July 2014

Approved:

Prof. Cosme Furlong, Advisor

Prof. John J. Rosowski, Mass. Eye & Ear Infirmary, Harvard-MIT Div. of
Health Science and Technology, Member, Dissertation Committee

Prof. John M. Sullivan, Member, Dissertation Committee

Prof. Allen H. Hoffman, Member, Dissertation Committee

Prof. Pilar Arroyo, University of Zaragoza, Spain, Member, Dissertation Committee

Prof. Jamal S. Yagoobi, Graduate Committee Representative

By

NEST – NanoEngineering, Science and Technology

CHSLT – Center for Holographic Studies and Laser micro-mechaTronics

Mechanical Engineering Department

Worcester Polytechnic Institute

Worcester, MA 01609-2280

Abstract

Hearing loss affects approximately 1 in 10 people in the world and this percentage is increasing every year. Some of the most common causes of hearing loss are disorders of the middle-ear. Early detection and diagnosis of hearing loss as well as research to understand the hearing processes depend on medical and research tools for quantification of hearing capabilities and the function of the middle-ear in the complex acousto-mechanical transformation of environmental sounds into vibrations of the middle-ear, particular of the human tympanic membrane (TM or eardrum).

Current ear exams assess the state of a patient’s hearing capabilities mainly based on qualitative evaluation of the healthiness of the TM. Existing quantitative clinical methods for description of the motion of the TM are limited to either average acoustic estimates (admittance or reflectance) or single-point displacement measurements. Such methods could leave examiners and researchers blind to the complex spatio-temporal response of the nanometer scale displacements of the entire TM. Current state-of-the-art medical research tools provide full-field nanometer displacement measurements of the surface of the human TM excited by steady state (tonal) stimuli. However, to fully understand the mechanics of hearing, and the complex acousto-mechanical characteristics of TM in particular, new tools are needed for full-field high-speed characterization of the nanometer scale displacements of the human TM subjected to impulse (wideband) acoustic excitation.

This Dissertation reports the development of a new high-speed holographic system (HHS) for full-field nanometer transient (i.e., > 10 kHz) displacement measurement of the human middle-ear and the tympanic membrane, in particular. The HHS allows spatial (i.e., >500k data points) and temporal (i.e., > 40 kHz) resolutions that enable the study of the acoustical and mechanical characteristics of the middle-ear at a level of detail that have never been reached before.

The realization of the HHS includes the development and implementation of novel phase sampling and acquisition approaches that allow the use of state-of-the-art high-resolution (i.e., >5 MP) and high-speed (> 80,000 fps) cameras through modular and expandable control architectures. The development of novel acquisition approaches allows the use of conventional speed (i.e., <20 fps) cameras to realize high-temporal resolutions (i.e., <15 µs) at equivalent sampling rates of > 50,000 fps with minimum hardware cost and modifications. The design and implementation of novel spatio-temporal phase sampling methods utilize the high temporal resolution (i.e., < 5 µs exposure) and frame rate (i.e., >80,000 fps) of high-speed cameras without imposing constraints on their spatial resolution (i.e., >20 µm pixel size). Additionally, the research and *in-vivo* applications capabilities of the HHS are extended through the development and implementation of a holographic otoscope head (OH) and a mechatronic otoscope positioner (MOP).

The large (i.e., > 1 GB with > 8×10^9 parameters) spatio-temporal data sets of the HHS measurements are automatically processed by custom parallel data mining and interpretation (PDMI) methods, which allow automatic quantification of medically relevant motion parameters (MRMPs), such as modal frequencies, time constants, and acoustic delays. Such capabilities could allow inferring local material properties across the surface of the TM.

The HHS is a new medical tool that enables otologists to improve the quality of diagnosis and treatments as well as provides researchers with spatio-temporal information of the hearing process at a level of detail never reached before.

Acknowledgements

I would like to thank my advisor, Prof. Furlong, and Prof. Rosowski who provided me with the opportunity to work on cutting-edge technologies to address challenges in medical research and engineering. I would like to thank them and my committee for their assistance and support during my completion of this Dissertation research. In addition, I gratefully acknowledge the support of the Center for Holographic Studies and Laser micro-mechaTronics (CHSLT) in Mechanical Engineering Department of WPI for the use of their facilities and equipment in my studies. I would like to thank Mr. Peter Hefti and Mr. Ellery Harrington for their help and guidance in my work at CHSLT. I would also like to thank Dr. Geffrey T. Cheng and Mr. Mike Ravicz from Eaton Peabody Laboratories (EPL) at MEEI for their help and guidance in my experimental work at MEEI.

I would particularly like to thank my family, and especially my wife Larissa, for their assistance and unending support during my work over the last couple of years. Without them, I know I couldn’t be where I am today.

This Dissertation has been supported with the funding of the National Institute of Health (NIH), National Institute of Deafness and other Communication Disorders (NIDCD), Massachusetts Eye and Ear Infirmary (MEEI), the Mittal Fund. The Mechanical Engineering Department has provided the CHSLT with an award from the James Nichols Heald Research Fund.

Table of contents

List of Figures

List of Tables

Nomenclature

2+1 LCPS	1+2 frame local correlation phase sampling (method)
3DHDS	3 dimensional holographic data set
ACSTW	array of control signal time waveforms
AOI	area of interest
AOM	acousto-optic modulator
BSE	Bayes spectral entropy
CHHS	continuous high-speed holographic system
CPU	central processing unit
CS	control software
CTS	correlated timing signal
CW	continuous wave (laser)
DAQ	data acquisition system
DE	double exposure
DESPS	double exposure spatial phase sampling (method)
DHS	digital holographic system
DMF	dominant modal frequency
DOF	depth of focus
FEM	finite element methods
FILO	first in, last out
FLPT	first local peak time

FOV	field of view
GD	group delay
GPT	global peak time
GPU	graphics processing unit
HHS	high-speed holographic system
HMP	holographic measurement process
HS	high-speed (camera)
LD	laser delivery
LDH	lensless digital holography
LDV	Laser Doppler Vibrometer
MBTE	minimum time between exposures
MCA	modular control approach
MF	modal frequency
MOP	mechatronic otoscope positioner
MPDE	multi-pulsed double exposure (acquisition method)
OCT	optical coherence tomography
OH	otoscope head
OS	optical setup
PCC	Pearson product-moment Correlation Coefficient
PDMI	parallel data mining and interpretation
PFV	Photron Fastcam Viewer
PHHS	pulsed high-speed holographic system

PS	phase sampling
PZT	piezo-electric transducer
RT	response time
SD	standard deviation
SLDV	scanning Laser Doppler Vibrometer
SP	sound presentation
SPL	sound pressure level
SPS	spatial phase sampling (method)
SSP	steady state position
STDDC	spatio-temporal displacement data cube
TC	time constant
TM	tympanic membrane
TWF	time waveform
GUI	graphical user interface
WD	working distance
α	angle between reference beam and camera sensor normal
$\boldsymbol{B}$	magnetic field strength
β	light sensitivity of the recording medium (sensor)
c	speed of light
$\boldsymbol{d}$	displacement field vector
d	working distance between the object and camera sensor
$\Delta\xi$	camera sensor horizontal pixel size

$\Delta\eta$	camera sensor vertical pixel size
$\Delta\phi$	phase change of the object
d_{image}	image size in the reconstructed hologram plane
d_{min}	minimum working distance
d_o	object size
$d_{optimal}$	optimal working distance
d_s	sensor size
$\boldsymbol{E}$	electric field strength
ξ	horizontal axis in the holographic plane
η	vertical axis in the holographic plane
f_d	dominant modal frequency
f_{fringe}	spatial fringe density
f_m	modal frequency
f_{max}	maximum resolvable spatial frequency
h	complex field of a recorded hologram
J_1	First order Bessel function
$\boldsymbol{k}$	wave vector
$\boldsymbol{k_i}$	illumination vector
$\boldsymbol{k_o}$	observation vector
$\boldsymbol{k_s}$	sensitivity vector
λ	laser light wavelength

ω	angular frequency
r	distance between reference beam and camera center
ρ	cross-correlation function
τ	time constant of a decaying harmonic oscillation
τ_g	group delay
t_f	first local peak time
t_m	measurement time
t_{max}	maximum measurement time
t_p	global peak time
t_r	response time
θ_{max}	maximum resolvable angle between a reference and object beam

Objectives

The aim of this work is to *develop* and *implement* a full-field high-speed holographic system for measurement and analysis of the spatio-temporal complexity of the transient response of the human middle-ear and the tympanic membrane (TM) in particular. This includes developments of novel:

(i) single frame phase sampling methods,
(ii) control and synchronization procedures for high-speed image acquisition,
(iii) hardware to allow measurements in medical research and *in-vivo* environment,
(iv) numerical methods and software implementation,
(v) parallel data mining and interpretation of spatio-temporal displacement data.

This work is to *demonstrate* the capabilities of the measurement system for quantification of the transient displacements of the human middle-ear and extraction of medically relevant motion parameters.

1 Introduction

Problem statement

Ongoing hearing research efforts for the understanding of the mechanics of the human hearing process are mainly focused on the response of the ear to tonal acoustic stimulation [Decraemer et al., 1999; De Greef et al., 2014; Khaleghi et al. 2013; Puria and Allen, 1998; Rosowski et al., 2013a]. However, studying the transient (wideband) response of the human ear, and of the human middle ear in particular, could expand the understanding of the processes by which acoustical energy is transformed into mechanical energy and transmitted through the tympanic membrane (TM) and the ossicular chain [Rosowski et al., 2014].

However, current state-of-the-art methods to measure the acousto-mechanical response of the middle-ear rely on averaged acoustic [Rosowski et al., 2013b] information or local displacement response (at 1 to 50 points on the membrane) using single-point or scanning Laser Doppler Vibrometry [Decraemer et al., 1999; Puria, 2003] and/or capacitive probes [Wilson and Johnstone, 1975]. The average or sparsely sampled points are not sufficient for the full description of the complex patterns unfolding across the full surface of the TM and the ossicles. Therefore, there is a need for a full-field high-speed measurement method that can quantify the spatio-temporal complexity of the acoustically induced transient displacement of the TM.

Significance of the problem

Development and implementation of tools for the study of the full spatio-temporal complexity of the transient response of the human ear, and of the human tympanic membrane (TM) in particular, could expand the understanding of the acousto-mechanical energy transformation in the middle-ear [Rosowski et al, 2009]. Measurements of transient phenomena on the surface of the TM allow quantification of corresponding motion parameters such as traveling wave speeds [Puria and Allen, 1998], standing wave ratios [Rosowski et al, 2009; Puria and Allen, 1998], acoustic absorbance and immittance [Rosowski et al., 2013b], damping [Zhang and Gan, 2010], stiffness, and modal frequencies. Such measurements could explain better the differences between experimentally measured traveling wave speeds [Cheng et al., 2013] and those predicted by estimates of the middle ear delays [Puria and Allen, 1998]. Capabilities to measure the transient repose of the TM and the ossicles to acoustic impulses would also allow detection and quantification of impedance discontinuities in the cochlea that could lead to traveling waves and reflections back into the middle ear giving rise to secondary disturbance of the TM [Kemp, 1978]. Full field transient measurements of the middle-ear can be used for validation and improvement of physical models [Puria and Allen, 1998; Cheng et al., 2013], identification and diagnosis of pathologies, and improvement the design of hearing aids.

2 Dissertation outline

This Dissertation is organized in three parts each consisting of several Chapters, as follows:

Part 1 provides relevant background information regarding physiology and anatomy of the human ear, existing diagnosis techniques and corresponding measurements methods, state-of-the-art high-speed measurement methods in engineering, as well as mathematical background for digital interferometry. Part 1 consists of the following Chapters:

Chapter 3 presents relevant background information regarding hearing research and transient measurement of the human middle ear. The Chapter includes an overview of the physiology and anatomy of the human, types of hearing loss, as well as clinical and research techniques for quantification of conductive hearing loss and the function of the human ear in general.

Chapter 4 provides an overview of state-of-the-art measurement methods in engineering that provide high-speed full-field displacement measurement capabilities. Chapter 4 includes discussions, from the perspective of applications in hearing research, on various high-speed acquisition and single frame phase sampling methods.

Chapter 5 describes the physical principles and mathematics of interference and lensless digital holographic interferometry for study of deformation of objects. The

Chapter is also focused on the challenges that have to be overcome in order to apply digital holography methods for transient measurements applications.

Chapter 6 provides a summary of the design constraints, from the medical, technological and holographic standpoint, that has been overcome for the realization of a high-speed measurement system for transient measurements of the human middle ear and the tympanic membrane (TM) in particular. The Chapter outlines specific constraints related to physiology of the human TM, technological challenges of current state-of-the-art cameras, as well as holographic recording constraints.

Part 2 describes the development of innovative methodologies to perform full-field measurements of the transient nanometer scale displacements in the confined volumes defined by the human middle-ear. Developments include the design and implementation of a full-field high-speed holographic system (HHS), single frame phase sampling methods and corresponding acquisitions and control methods for measurement and analysis of the response of the human middle ear to transient stimuli. The developments also include hardware realization of holographic otoscope and mechatronic otoscope positioner systems, as well as design and implementation of numerical methods for parallel data mining and interpretation of spatio-temporal displacement data sets. Part 2 consists of the following Chapters:

Chapter 7 presents developments on two single frame phase sampling methods that have been enhanced and implemented to allow high acquisition speed (i.e., > 40 kHz) and high temporal resolution (i.e., <10 μs). A double exposure spatial phase sampling (DESPS) methods have been enhanced and implemented in order to take advantage of the high spatial resolution (i.e., >5 MP and <5 μm) and global shutter capabilities of modern charge-coupled device (CCD) sensors. A 2+1 frame local correlation phase sampling (2+1 LCPS) method has been developed and implemented in order to take advantage of the temporal resolution (i.e., < 5 μs exposure) of high-speed (i.e., >40 kfps) cameras without imposing constraints on their spatial resolution (i.e., >20 μm pixel size).

Chapter 8 describes the development and implementation of two sets of acquisition and control methods. A multi-pulsed double exposure (MPDE) acquisition method has been developed in order to allow the use of the DESPS method for transient measurements of the human middle-ear. The implementation of the MPDE acquisition method allows high-temporal resolution (i.e., <20 μs) and an equivalent sampling rate of > 50 kfps, by using a conventional speed (i.e., <20 fps) camera. A high-speed 2+N frame (HS 2+N) acquisition method based on the (2+1 LCPS) method have been developed and implemented for use with high-speed (i.e., >40 kfps) cameras.

Chapter 9 describes the hardware design and realization of a holographic otoscope head (OH) and a mechatronic otoscope positioner (MOP). Both systems are aimed at extending the capabilities of the HHS for both research and in-vivo applications. The Chapter also outlines the hardware realization the two versions of the HHS, pulsed (PHHS) and continuous (CHHS).

Chapter 10 explains the development of numerical methods, and corresponding software implementation, for the realization of a set of procedures as part of a holographic measurement process (HMP) that allows the acquisition, processing, and analysis of holographic data.

Chapter 11 outlines the development and implementation of parallel data mining and interpretation methods (PDMI), based on spatio-temporal displacement data cubes (STDDCs), aimed at quantification of medically relevant motion parameters (MRMP) for the characterization of the transient response of the human middle ear.

Part 3 presents experimental and numerical validation of the design criteria and transient measurement capabilities of the HHS. Part 3 also includes representative results on application of the HHS for steady state, transient and *in-vivo* measurements of the human middle-ear. Part 3 consists of the following Chapters:

Chapter 12 provides results on experimental and FEM validation of the design criteria of the HHS as well as its transient measurement capabilities. The main design parameters and assumptions of each HHS model, pulsed and continuous, have been tested against LDV measurements on both artificial and human samples. The temporal resolution design parameters of the HHS are validated with FEM.

Chapter 13 demonstrates the application of the high-speed holographic system (HHS) for time-averaged, stroboscopic, MPDE, and HS 2+1N acquisition modes for research and clinical applications. Included are results on the quantification of the transient response of the human TM excited by pulsed acoustic or mechanical stimuli as well as preliminary results on *in-vivo* applications in clinical conditions.

Conclusions and future work (Chapter 14) provides conclusions and recommendations for future work.

Part 1: Background

3 Hearing research and transient measurement of the human tympanic membrane

This Chapter provides an overview of the anatomy of the human ear and the tympanic membrane (TM) in particular. It also provides general descriptions of different types of hearing losses as well as corresponding medical diagnosis and research techniques for quantification of the transient response of the human TM.

3.1 Human ear anatomy

The primary purpose of the human ear is to transduce acoustically driven variations in air pressure, whether from music, speech, or other sources, into the neural activity necessary for our perception and interpretation of sound [Geisler, 1998]. The *auditory periphery* of the hearing organ can be broken into three functionally (physiologically) and anatomically distinct components: external, middle, and inner ear, as shown in Fig. 3.1.

The primary role of the external and middle ear is to pass the sound stimulus from the environment to the inner ear. The sound waves from the environment are diffracted and scattered by the body, head, and ear, and some fraction of the incident sound energy is gathered at the entrance to the ear canal. That sound is transformed as it travels down the roughly cylindrical ear canal to the Tympanic Membrane (TM), also known as eardrum. The TM forms the boundary between the external and middle ear, shown in Fig. 3.1a. A complex acousto-mechanical transformation occurs at the TM that couples the acoustical energy from the sound field at the surface of the eardrum into mechanical energy into the ossicular chain [Rosowski, 2010], shown in Fig. 3.1b. The mechanical motion of the ossicles (malleus, incus, and stapes) produces a sound pressure and volume velocity of the stapes at the oval window, the entrance to the lymph-filled inner ear. The sound pressure and volume velocity in the lymphs within the vestibule (or entrance) of the inner ear stimulates the cochlear partition, resulting in motion of the partition's basilar membrane and mechanical stimulation of the hair cells within the partition. Hair cells responding to lower frequencies are located further from the stapes, resulting in tonotopic mapping that allows for direct geometrically defined coding of sound frequency. The mechanical motion of the hair cells generate electric signals that are conducted by the cochlear nerve to the nervous system and specialized auditory parts of the brain for further interpretation [Rosowski, 2010; Geisler, 1998].

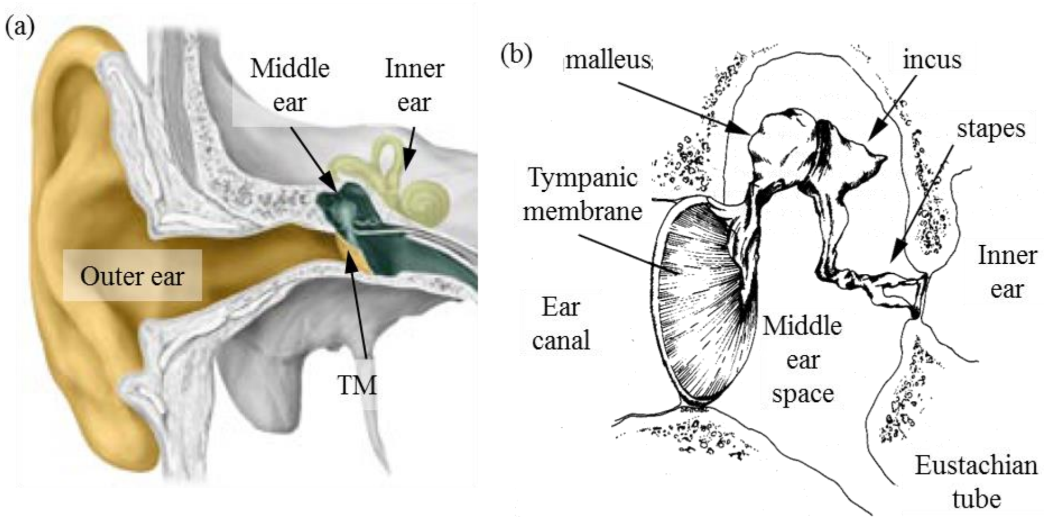

Fig. 3.1. Schematic of auditory system with its primary components [Chittka and Brockmann, 2005]: (a) the human ear consists of an external, middle-, and inner-ear with the tympanic membrane (TM) at the boundary of the external and middle-ears; and (b) the middle-ear ossicles (i.e., malleus, incus, and stapes) mechanically couple the TM with the inner-ear.

3.2 Tympanic membrane

The human tympanic membrane is a multi-layered, fiber reinforced structure situated at the boundary between the outer and middle ears, as shown in Fig. 3.2. The TM is composed of three main structural layers [Sanna et al., 2003]:

- Lateral (outside) – a skin-like epidermis layer.
- Middle – a lamina propria layer consisting of a network of fibers oriented tangentially and radially relative to the umbo and the tympanic ring.
- Medial (inside) – a mucosal lining layer similar to the lining of the mouth and nose.

The surface of the TM is separated into a *pars flaccida* and a *pars tensa*. The *flaccida* is about 10% of the area of the TM, and moves independently from the ossicular chain, while the *pars tensa* is tightly coupled to the ossicular chain [Sundberg, 2008]. The exterior edge of the TM (annulus or annular ring) consists of a fibrous and cartilaginous tissue that is both thicker and stiffer than the rest of the membrane [Sundberg, 2008; Van der Jeught et al., 2013]. The TM thickness varies spatially between 50-150 μm, as shown in Fig. 3.2d.

The TM has a cone shape with a diameter of 6-10 mm and depth of 1-3 mm [Khaleghi et al. 2013; Dirckx and Decraemer, 2000], as shown in Fig. 3.2e. The TM cone is situated at the end of the ear canal at ~20-30 mm from its entrance [Dirckx and Decraemer, 1997; Stinson and Lawton, 1989]. The plane formed by the tympanic ring is orientated at 30-60° relative central axis of the ear canal, with the superior part of the TM tilted laterally, as shown in Fig. 3.2f [Stinson and Lawton, 1989].

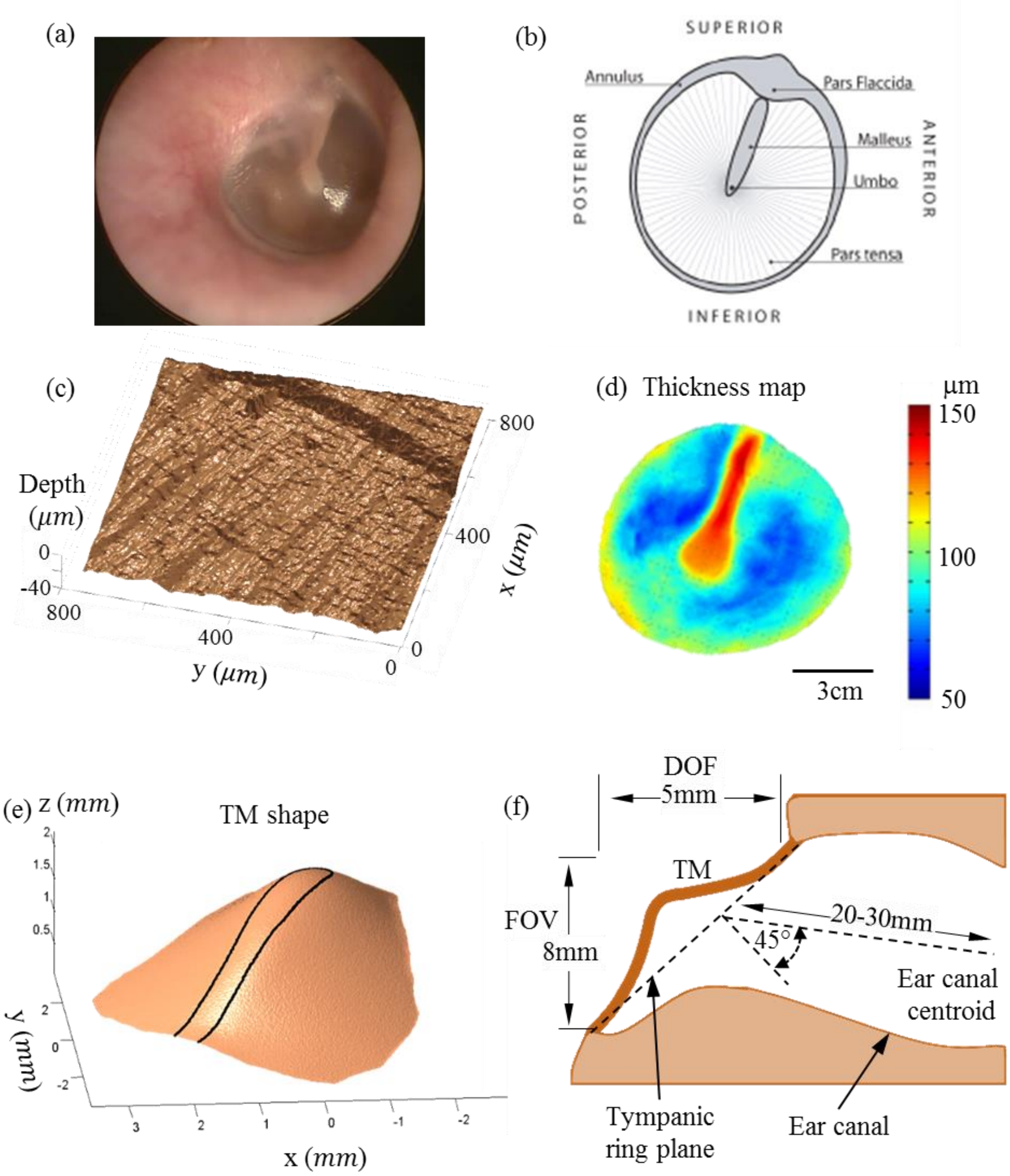

Fig. 3.2. Overview of the structure, shape and position of human tympanic membrane within the ear: (a) normal tympanic membrane as seen through an otoscope [ENT USA, 2014]; (b) schematic of the anatomy of the right tympanic membrane [Sundberg, 2008]; (c) depth map of the surface of the TM indicating the undelaying fibrous structures [Rutledge et al., 2013]; (d) representative thickness measurements across the surface of the TM [Van der Jeught et al., 2013]; (e) representative shape measurement [Khaleghi et al., 2013]; and (f) position and orientation of the TM in a human ear relative to the ear canal [Stinson and Lawton, 1989]. Indicated in (f) are the field-of-view (FOV) and depth of focus (DOF) required to observe the TM through the ear canal [Hernández-Montes et al., 2009].

3.3 Types of hearing loss

Any lessening of the hearing ability of the human ear is referred to as ‘hearing impairment’, or ‘hearing loss,’ and can range from barely appreciable disturbances to total deafness. There are two major types of hearing loss:

- Conductive hearing loss – refers to problems in sound conduction (acoustical or mechanical) pathways in the external and/or middle-ears.
- Sensorineural hearing loss – refers to sensory, neural and central hearing losses, which refer to conduction of sound to the inner-ear, the perception of sound by the sensory cells of the cochlea (sensory), the processing of sound in the cochlear nerves (sensory), the auditory pathway (neural), or the cortical auditory centers (central).

A functional classification of hearing impairment is schematically given in Fig. 3.3.

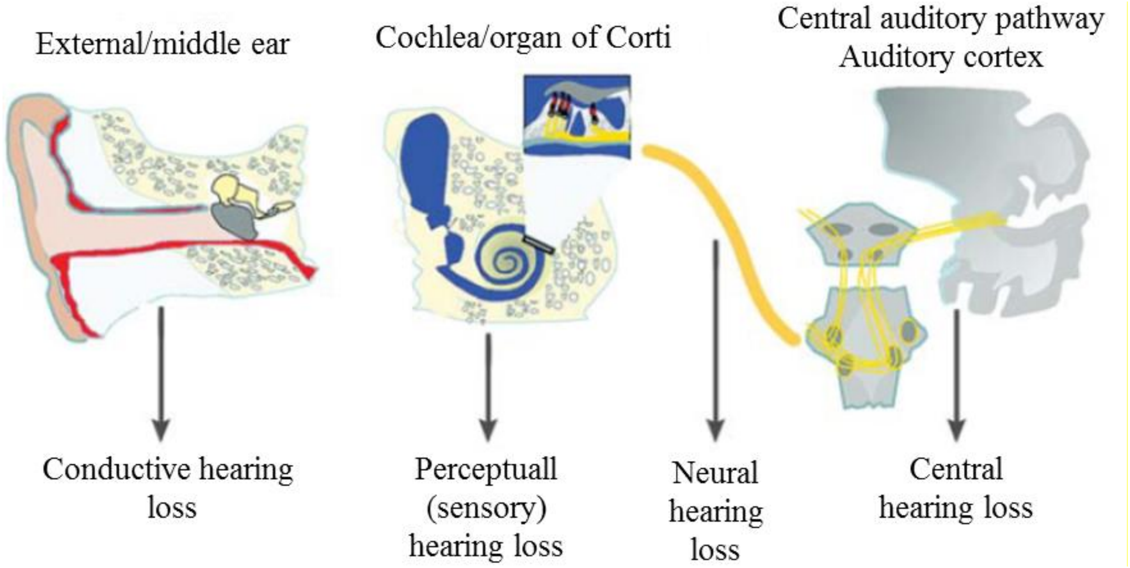

Fig. 3.3. Topographic functional classification of conductive, perceptual, neural, and central hearing impairment (loss) [Zahnert et al., 2011].

3.4 Clinical and research techniques for quantification of conductive hearing loss

Large extent of the conductive hearing loss diagnosis and research techniques rely on measurements of (or related to) the motion of the TM excited by a controlled stimuli. Most of the methods for quantification of the motion of the TM can be classified based on their spatial and temporal resolution, shown in Table 3.1. The spatial resolution range relative to the surface of the TM can be classified as: averaged (global) across the full surface; single point (local); and full-field/scanning that provides a grid of independent measurement points across the full surface of the TM.

Table 3.1. Overview of the most common methods for characterizing the acousto-mechanical response of the TM, including its diagnosis for conductive hearing loss.

Spatial resolution	Temporal resolution		
	Quasi-static	Steady state (tonal)	Transient (wideband)
Global (averaged)	• Tympanometry [Rosowski et al., 2013b); Mikoklai et al., 2008]	• Tympanometry • Ear canal reflectance [Nakajima et al., 2013; Nakajima et al., 2012]	• Tympanometry • Ear canal reflectance
Local (point)	• Indentation [Huang et al., 2008]	• Indentation [Aernouts and Dirckx, 2012] • LDV [Rosowski et al., 2008] • Capacitive probes [Wilson and Johnstone, 1975]	• LDV • Capacitive probes
Full-field or scanning (grid)	• Interferometry [von Unge et al., 1993] • OCT [Rutledge et al., 2013; Djalilian et al., 2008]	• Holography[Rosowski et al., 2013a], • OCT [Sudhash et al., 2012] • SLDV [Decraemer et al., 1999]	• SLDV • Still open for new developments as described in this Dissertation

Most medical diagnosis techniques, such as the ones in Row 1 of Table 3.1, are based on measurements of an averaged (global) displacement of the TM due to quasi-static, steady state (tonal) to transient (wideband) excitation [Rosowski et al., 2013b; Nakajima et al., 2013]. Such measurements, together with qualitative observation with an otoscope, provide the information necessary to make proper diagnoses of specific ear ailments [Katz, 1994]. However, such tests may provide insufficient (inconclusive) quantitative information.

Novel medical diagnosis and research techniques, such as the ones in Row 2 of Table 3.1, rely on local displacement measurements based on indentation [Huang et al., 2008; Aernouts and Dirckx, 2012], Laser Doppler Vibrometry (LDV) [Rosowski et al. 2008] or capacitive probes [Wilson and Johnstone, 1975]. Such measurement methods have been demonstrated to be sensitive to several middle-ear pathologies including TM perforations and ossicular fixations and interruptions. LDV's temporal resolution allows for both steady state (tonal) and transient (wideband) excitation, however, spatial resolution is limited to single point measurements.

Novel research techniques use full-field-of-view or scanning measurement methods, such as the ones in Row 3 of Table 3.1, including digital holography [Rosowski et al., 2013a], optical coherence tomography (OCT) [Sudhash et al., 2012], and Scanning Laser Doppler Vibrometry (SLDV) [Decraemer et al., 1999]. Full-field methods provide large amount (i.e., ~1-50 GB [Harrington et al., 2011]) of quantitative data for more than 100 k points across the surface of the TM, however their temporal resolution is limited to static and steady state (tonal) measurements.

Currently, only the SLDV could allow for sufficient temporal resolution (i.e., >50 kHz) for transient scanning measurements, however, the total measurement time (dictated by the scan rate) for a sufficient spatial resolution (i.e., >1000 points) would require several minutes per measurement [Decraemer et al., 1999]. Therefore, there is a need for a full-field high-speed measurement method that can rapidly quantify the full spatio-temporal complexity of the acoustically induced transient displacement of the TM.

This Dissertation adds to the existing knowledge by providing tools for full-field high-speed measurements of the nanometer displacements of the surface of the human TM excited by single tone as well as by transient stimuli [Dobrev et al, 2014a-d ; Dobrev et al, 2015].

4 Methods for transient displacement measurements in engineering

This Chapter provides an overview of state-of-the-art full-field high-speed displacement measurements methods in engineering. Since typical rapid (i.e., >20 kHz) measurement methods with nanometer displacement capabilities rely on holographic techniques, this Chapter provides an overview of existing state-of-the-art high-speed acquisition and single frame phase sampling methods [Dobrev et al. 2013a; Dobrev et al., 2014a-d] for holographic recording.

4.1 High-speed acquisition methods

Existing high-speed full-field optical acquisition methods can be classified based on the number frames that are provided by each method, as shown in Fig. 4.1.

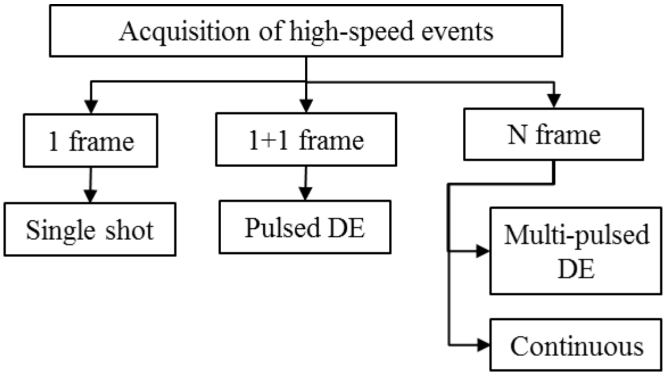

Fig. 4.1. Overview of existing high-speed optical acquisition methods, classified based on the number of frames (temporal data points) captured.

Single frame (shot) acquisition methods can be executed with conventional speed cameras (i.e., <100 Hz) and can be synchronized with the event; however it provides only

1 frame for the duration of the event. Pulsed double exposure (DE) acquisition can be executed with conventional speed cameras (i.e., <100 Hz) or specialized double exposure cameras (i.e., <1 μs inter-frame time) [Adrian, 2005]. It provides 2 frames that can be used to compare (i.e., DE) the state of the object at two time instances of the transient event.

In order to adequately quantify the temporal evolution of the transient events, typically multiple (i.e., *N*) frames are required. Several types of N-frame acquisition methods exist and can be classified in two groups: multi-pulsed double exposure (MPDE) and continuous [Wåhlin et al., 1994; Dancer et al., 1975; Dobrev et al., 2013a; Pedrini et al., 2006]. The MPDE, analogue to the pulsed DE methods, allow quantification of the transient event throughout its full duration by repeatedly executing the transient event and performing a new pulsed DE acquisition synchronized with each new execution. The MPDE allows for the use of conventional or specialized DE cameras [Adrian, 2005]; however, it assumes temporal and spatial repeatability of the transient event [Dobrev et al., 2013b]. Continuous high-speed acquisition allows for instantaneous measurement of the full duration of a transient without the need for repeatability. Continuous high-speed methods are typically based on high-speed (i.e., >1 kfps), ultra-high-speed (i.e., >1 Mfps) or framing (i.e., 0.1-1 Gfps) cameras [Reu and Miller, 2008; Dobrev et al. 2015]. Such cameras are commercially available at higher prices (10-1000 fold) than conventional cameras, while allowing 10^2-10^7 fold increase in acquisition speed.

4.2 Single frame phase sampling algorithms

Existing high-speed nanometer displacement measurement methods are typically based on holographic techniques that require single frame (shot) phase sampling methods, which can be classified by their phase modulation requirements and spatial extent of operation, shown in Table 4.1. The phase modulation requirements can refer to spatial (global, local and point-wise) and temporal (amplitude and frequency) optical techniques. The spatial extent of operation of the algorithms refers to the spatial size (full-field, kernel, or a pixel) of the data that is used as an input for each type of phase sampling algorithm.

Table 4.1. Comparison of various single frame phase sampling methods based on phase modulation requirements and spatial extent of operation [Arroyo and Loberta, 2008; Badulescu et al., 2013].

Phase modulation	Spatial extent of operation		
	Global (full-field)	Local (kernel)	Point (pixel)
Modulated	• Spatial carrier frequency [Takeda et al. 1982]	• Phase step [Awatsuji et al., 2004] • Polarization step [Millerd et al., 2004b]	• Heterodyning [Dandliker and Thalmann, 1985] • SLDV [Decraemer et al. 1999] • MLDV [Kilpatrick and Markov, 2008]
Random	• Multi-sensor [Smythe and Moore, 1984; Chen and Chen, 2011] • Multi-image [Millerd et al., 2004a]	• Spiral phase transform [Larkin, 2001] • Local phase retrieval [Liebling et al., 2002] • Local phase correlation [Schmitt and Hunt, 1997; Georgas and Schajer, 2012; Dobrev et al., 2014c]	• Subtraction [Dancer et al., 1975]

Several phase sampling algorithms, such as the ones in Row 1 of Table 4.1, rely on a particular spatial or temporal structure of the phase of the optical signal that typically requires complex optical setups and electronics [Saldner et al., 1996; Takeda et al. 1982]. The phase modulation can be achieved optically by a global spatial carrier frequency, local spatial phase mask (based on phase gradient, step or polarization), or point-wise temporal modulation (amplitude and/or frequency based). Typically point-wise temporal modulation approaches have high displacement (i.e., ~λ/1000) and temporal (i.e., >1 MHz) resolutions, but require time consuming spatial scanning across the sample to achieve full-field measurement capabilities. In the case of Scanning Laser Doppler Vibrometry (SLDV), a scan of 512x512 points in the 0.1-20 kHz range would require several hours [Decraemer et al. 1999], while with matrix Laser Doppler Vibrometer (MLDV) the measurement time could be reduced to seconds [Kilpatrick and Markov, 2008]. Local phase sampling algorithms with spatially modulated phase provide instantaneous phase sampling across the full-filed-of-view, however, typically require a costly spatial mask in order to create a pixel-wise phase step (polarization or optical path length based) [Millerd et al., 2004b; Novak et al., 2005]. Global phase sampling algorithms, based on a spatial carrier frequency, require relatively simple optical setup and no specialized electronics; however, at the expense of increased spatial resolution requirements (pixel size and number of pixels) for the camera sensor [Pedrini et al., 2006].

Several phase sampling algorithms such as the ones in Row 2 of Table 4.1 avoid the use of phase modulation (spatial or temporal) of the optical signal in the interferometric system. Global phase sampling algorithms based on unstructured (random) phase typically rely on several instantaneous global phase shifts that are captured by multiple camera sensors [Smythe and Moore, 1984; Chen and Chen, 2011] or several independent areas of a single camera sensor [Millerd et al., 2004a]. While these methods allows for high spatial resolution, it comes at the expense of greatly increased optical setup complexity. Point-wise phase sampling algorithms, based on unstructured (random) phase, typically rely on direct pixel-wise substation of the intensity between any two images, typically used in double-exposure algorithms. The method uses a simple optical setup; however, quantification of the data requires complex post-processing algorithms [Ramesh et al., 1991; Dancer et al., 1975]. Local (kernel based) phase sampling algorithms based on unstructured (random) phase rely on direct numerical solution for the value of the phase within a kernel (small neighborhood) of pixels. The method uses a simple optical setup and has reduced spatial resolution requirements for the camera sensor; however, the spatial resolution of the method is limited by the size of the spatial kernel [Schmitt and Hunt, 1997; Georgas and Schajer. 2012].

5 Principles of digital holographic interferometry

This Chapter describes the basics of interferometry and holography, and their use as non-contact metrology techniques. Discussions are provided on the wave theory of light as far as it is required to understand the recording and reconstruction of holograms as well as the use of holographic interferometry for metrology. The Chapter is mainly focused on the description of the use of holography for measurements of the object deformations.

5.1 Electromagnetic waves

The primary phenomena constituting holography are interference and diffraction, which take place because of the wave nature of light. The study of the interaction of light waves as they intersect one another in some medium comprises the foundation of optical interferometry [Hecht, 1989]. Light can be described as a transverse electromagnetic wave with time varying electric, $\boldsymbol{E}$, and magnetic, $\boldsymbol{B}$, field components. These two fields are perpendicular to each other and the composed wave of $\boldsymbol{E}$ and $\boldsymbol{B}$ travels in the direction of $\boldsymbol{E}\times\boldsymbol{B}$ as shown in Fig. 5.1.

Since the spatio-temporal variation of the electromagnetic waves can be described with the Maxwell equations, the propagation of light is described by the wave equation, which is derived from the Maxwell equations. The wave equation for propagation of light in vacuum is

$$\nabla^2 \boldsymbol{E} - \frac{1}{c^2}\frac{\partial^2 \boldsymbol{E}}{\partial t^2} = 0\,, \tag{5.1}$$

where $\boldsymbol{E}$ is the electrical field strength vector, ∇ is the Laplace operator

$$\nabla^2 = \frac{\partial^2}{\partial x^2} + \frac{\partial^2}{\partial y^2} + \frac{\partial^2}{\partial z^2}\,, \tag{5.2}$$

where (x, y, z) are the Cartesian spatial coordinates, t denotes the temporal coordinate, time, and c is the propagation speed of the wave which depends on the refractive index of the propagation medium and the speed of light, c_0, in vacuum (i.e. ~3×10^8 m/s).

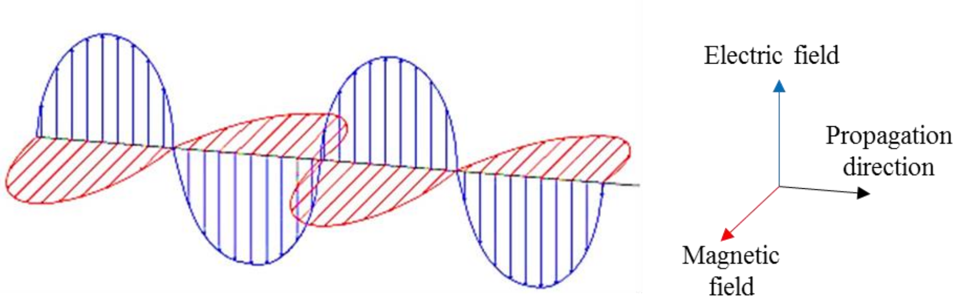

Fig. 5.1. Light described as an electro-magnetic wave propagating in a direction perpendicular to its electric and magnetic field components.

The direction of vibration of the light is described by its polarization and it is transverse to the direction of propagation. The polarization direction could be horizontal, vertical or in any combination of these. Light waves vibrating in a single plane is called plane polarized light. For a plane polarized light propagating in the z –direction, Eq. 5.1 could be converted to a scalar wave equation

$$\frac{\partial^2 E}{\partial z^2} - \frac{1}{c^2}\frac{\partial^2 E}{\partial t^2} = 0\,. \tag{5.3}$$

The wave field described by the scalar wave equation, Eq. 5.3, retains its form during propagation. The scalar wave equation is a linear differential equation, thus the superposition principle is valid for it. Most practical applications of holography rely on a solution of the wave equation called the harmonic wave

$$E(z,t) = E_0 \cos(kz - \omega t + \phi)\ , \tag{5.4}$$

where E_0 is the real amplitude of the wave, the $kz - \omega t + \phi$ term is the phase of the wave, ϕ is the initial phase offset, k is the wave number and ω is the angular frequency of the light wave

$$\omega = 2\pi f = \frac{2\pi c}{\lambda} \text{ and } k = \frac{2\pi}{\lambda}\ , \tag{5.5}$$

where f and λ are the frequency and corresponding wavelength of the light wave. The wave number, k, quantifies the fundamental relationship between phase of the harmonic wave and its spatial and temporal distribution. Using the Euler's formula, the trigonometric functions in Eq. 5.4 can be represented as complex exponentials

$$E(z,t) = \frac{1}{2} E_0 \mathrm{e}^{i(kz-\omega t+\phi)} + \frac{1}{2} E_0 \mathrm{e}^{-i(kz-\omega t+\phi)} = \frac{1}{2} E_0 \mathrm{e}^{i(kz-\omega t+\phi)}\ , \tag{5.6}$$

where the second term of Eq. 5.6 represents the complex conjugate of the first term and it can be omitted since only the real part of Eq. 5.6 represents the physical light wave. The spatial distribution of the harmonic wave forms surfaces of constant phase, called wavefronts, which are normal to the direction of propagation of the harmonic wave. A wavefront that has constant phase in all planes orthogonal to the propagation direction for a given time *t* is called a planar wave. Analogously, a spherical wavefront is called spherical wave.

In an arbitrary coordinate system, the position vector

$$\boldsymbol{r} = (x, y, z)\,, \tag{5.7}$$

and the wave (propagation) vector, $\boldsymbol{k}$

$$\boldsymbol{k} = \left(k_x, k_y\ k_z\right). \tag{5.8}$$

can be used to define the harmonic wave by substituting Eqs 5.7 and 5.8 into Eq. 5.6 to yield (within a constant)

$$E(\boldsymbol{r}, t) = E_0 \mathrm{e}^{i(\boldsymbol{k}\cdot\boldsymbol{r} - \omega t + \phi)}\,. \tag{5.9}$$

5.2 Holographic recording and reconstruction

5.2.1 Recording of light waves

In practice, existing sensors, such as photo diodes and cameras, measure directly only the intensity and (on a rougher scale) the wavelength of light. The intensity is defined by the energy flux through an area per unit of time. Based on the Maxwell equations, the intensity is

$$I = \varepsilon_0 c E^2, \tag{5.10}$$

where ε_0 is the vacuum permittivity. In practice, only the proportionality of the intensity, I, to the electric field strength, E^2, is used

$$I \sim E^2\,. \tag{5.11}$$

Measurement of the momentary (instantaneous) intensity is currently limited by the typical measurement times (i.e., 1ns - 1s) of commercially available sensors, which are much longer (i.e., 10^{14} fold) than the period of oscillation of the light waves. This means that typical intensity measurements are an average over multiple wave oscillations. The averaged intensity over the measurement time of a sensor is expressed as (omitting proportionality constants)

$$I = E_0 E_0^* = |E_0|^2, \tag{5.12}$$

where * denotes the complex conjugate. Based on Eqs 5.9 and 5.12, the short time intensity at a moment t measured by a sensor with finite measurement (integration) time T_m is [Kreis, 2005]

$$I(\boldsymbol{r}, t, t_m) = \frac{1}{t_m} \int_{t-t_m/2}^{t+t_m/2} E(\boldsymbol{r}, t') E^*(\boldsymbol{r}, t') \, dt'. \tag{5.13}$$

Equation 5.13 represents the measured intensity as a sliding average with a temporal window centered at t and with a width t_m.

5.2.2 Interference of light waves

The basis for holography and interferometry is the interference between two or more coherent light waves when they are superimposed. In order to mathematically describe the coherent superposition, we consider two linearly polarized waves of the same frequency, emitted by the same source, with wave vectors $\boldsymbol{k_1}$ and $\boldsymbol{k_2}$, phases ϕ_1 and ϕ_2, and amplitudes E_{01} and E_{02}

$$\begin{aligned} E_1(\boldsymbol{r}, t) &= E_{01} \mathrm{e}^{i(\boldsymbol{k_1} \cdot \boldsymbol{r} - \omega t + \phi_1)}, \\ E_2(\boldsymbol{r}, t) &= E_{02} \mathrm{e}^{i(\boldsymbol{k_2} \cdot \boldsymbol{r} - \omega t + \phi_2)}. \end{aligned} \tag{5.14}$$

Based on Eqs 5.12 and the superposition principle, the intensity of the interference between the two waves can be expresses as

$$I(\boldsymbol{r}, t) = (E_1 + E_2)(E_1 + E_2)^*. \tag{5.15}$$

Substituting Eq. 5.14 into 5.15 results in

$$\begin{aligned} I(\boldsymbol{r},t) &= \left[E_{01}\mathrm{e}^{i(\boldsymbol{k_1}\cdot\boldsymbol{r}-\omega t+\phi_1)} + E_{02}\mathrm{e}^{i(\boldsymbol{k_2}\cdot\boldsymbol{r}-\omega t+\phi_2)}\right]\cdot \\ &\quad \left[E_{01}\mathrm{e}^{-i(\boldsymbol{k_1}\cdot\boldsymbol{r}-\omega t+\phi_1)} + E_{02}\mathrm{e}^{-i(\boldsymbol{k_2}\cdot\boldsymbol{r}-\omega t+\phi_2)}\right] \\ &= E_{01}^2 + E_{02}^2 + E_{01}E_{02}\left[\mathrm{e}^{i(\boldsymbol{k_1}\cdot\boldsymbol{r}-\boldsymbol{k_2}\cdot\boldsymbol{r}+\phi_1-\phi_2)}\right. \\ &\qquad \left. + \mathrm{e}^{-i(\boldsymbol{k_1}\cdot\boldsymbol{r}-\boldsymbol{k_2}\cdot\boldsymbol{r}+\phi_1-\phi_2)}\right] \\ &= E_{01}^2 + E_{02}^2 + E_{01}E_{02}\cos(\boldsymbol{k}''\cdot\boldsymbol{r}+\phi)\,, \end{aligned} \tag{5.16}$$

where $\boldsymbol{k}'' = \boldsymbol{k_1} - \boldsymbol{k_2}$ and $\phi = \phi_1 - \phi_2$. Equation 5.16 can be written in terms of intensities of the two waves

$$I(\boldsymbol{r}) = I_1 + I_2 + 2\sqrt{I_1 I_2}\cos(\boldsymbol{k}''\cdot\boldsymbol{r}+\phi)\,. \tag{5.17}$$

It should be noted that the resulting interference pattern between two waves of equal frequency does not depend on the temporal variation of their electromagnetic field. The cosine term produces a spatial variation in intensity, called interference fringes, that depends on the phase difference and relative angle of propagation between the two waves.

5.2.3 Holographic process

The holographic process consists of two steps: recording and reconstruction. In the recording step, principles of interferometry can be used to record the wavefronts scattered off the surface of an object at a specified time. In this step, light with sufficient coherence length [Kreis, 2005] (typically a laser source) is split into two partial waves by a beamsplitter (BS), as shown in Fig. 5.2.

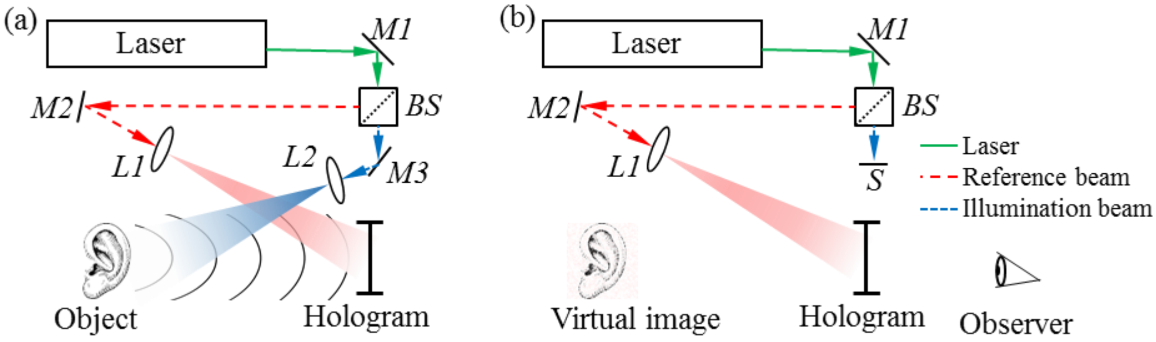

Fig. 5.2. Holographic recording and reconstruction: (a) during holographic recording, the object and hologram are illuminated with illumination and reference beams, respectively; and (b) the hologram is illuminated with only the reference beam during holographic reconstruction. In the figure, *M* is mirror; *L* is lens; *BS* is beam splitter; and *S* is shutter.

One wave, called the illumination wave, illuminates the object and is then scattered and reflected as an object wave to the recording medium, e.g., a photographic plate or a camera sensor, as shown in Fig. 5.2a. The second wave, called the reference wave, illuminates the sensor directly. In this case, the reference and object waves can be described with

$$O(x,y) = o(x,y)\mathrm{e}^{i[\phi_o(x,y)]}\,, \qquad R(x,y) = r(x,y)\mathrm{e}^{i[\phi_r(x,y)]}\,, \tag{5.18}$$

where o and ϕ_o are the amplitude and phase of the complex object wave and r and ϕ_r are the amplitude and phase of the complex reference wave. The interference between the two waves at the plane of the sensor (hologram plate) is recorded by the holographic plate. The intensity, $I(x,y)$, of the complex field of the hologram can be expressed, similar to Eq. 5.17 as

$$I(x,y) = |O(x,y) + R(x,y)|^2 \tag{5.19}$$

$$= [O(x,y) + R(x,y))] \cdot [O(x,y) + R(x,y)]^*$$

$$= r^2(x,y) + o^2(x,y) + O(x,y)R^*(x,y) + R(x,y)O^*(x,y)$$

$$= I_o(x,y) + I_r(x,y) + 2\sqrt{I_o(x,y)I_r}(x,y)\cos[\Delta\phi(x,y)] \,,$$

where $I_o(x,y)$ and $I_r(x,y)$ are the intensities of the two waves at the plane of the sensor, and $\Delta\phi$ is the phase difference between the two waves. The recorded holographic wavefront, $h(x,y)$, at the sensor is proportional to $I(x,y)$

$$h(x,y) = h_0(x,y) + \beta t_m\, I(x,y) \cong \beta t_m\, I(x,y) \,, \tag{5.20}$$

where β is a constant related to the light sensitivity of the sensor (holographic plate or camera sensor), t_m is the exposure time (measurement time), and h_0 represents the read-out noise (or amplitude transmission of the unexposed plate) of the sensor and it will be neglected in further descriptions of the holographic recording process.

During the reconstruction step, the object beam is typically off and only the reference beam illuminates the hologram, as shown in Fig. 5.2b. This produces a virtual image of the original object that can be observed by a viewer through the holographic plate. The reconstruction process can be mathematically described as a multiplication between the hologram and the reconstruction (reference) wave. Based on Eqs 5.18-20, the reconstructed hologram, U, at the recording plane can be expressed as

$$U = h * R = \beta t_m(r^2 + o^2 + OR^* + RO^*)R \tag{5.21}$$

$$= \beta t_m[(r^2 + o^2)R + r^2 O + R^2 O^*] \,,$$

where the spatial dependence, (x,y), of all variables has been omitted for brevity. The first term represents undiffracted wave, also called zero diffraction order, which does not have any information about the phase of the object wave. The second term is the reconstructed object wave that forms an image at the object plane that can be observed through the recording media, as shown in Fig. 5.2b, assuming a holographic plate was used. The third term produces a real image of the object at a different plane.

5.3 Digital holography

5.3.1 Digital holographic reconstruction

The reconstruction process, using a holographic plate as a recording media, is a time consuming for practical applications such as in the reconstruction of recordings of the transient response of the tympanic membrane [Dancer et al., 1975]. In order to overcome such limitations, state-of-the-art digital holographic measurement systems utilize digital cameras for rapid (i.e., >100 Hz) recording of holograms. However, since a camera sensor is only passively recording the intensity of the hologram, the reconstruction process cannot be done optically, as shown in Fig. 5.2b. In order to use the holographic information recorded by the digital sensor, the reconstruction process needs to be numerically simulated. In this case, the reconstruction is accomplished by multiplication of the digitized intensity distribution of the hologram with a digital model of the reference wave and subsequent numerical reconstruction of the object. In this Section, the numerical reconstruction of digitally recorded holograms is addressed.

There are two main types of reconstruction algorithms, Fresnel transform and Convolution with each one having specific requirements for the holographic setup. The main difference between the two types of algorithms is their optimal recording distance, defined as the distance between the sensor and the object. Table 5.1 shows an overview of the differences between the two reconstruction algorithms.

Table 5.1. Comparison between Fresnel transform and Convolution approach based numerical reconstruction algorithms based on working distance, depth of field and field of view [Yaroslavsky et al., 2012]. All values are based on a 532nm wavelength and a 3.45um pixel size.

Reconstruction algorithm	**Working distance**	**Depth of field (normalized to WD)**	**Field of view (FOV)**
Fresnel transformation	>5 cm	>2% [Kreis, 2005]	>size of camera sensor
Convolution approach	<2-3 cm	<0.5% [Kreis, 2005]	< size of camera sensor

The optimal recording distance range for each algorithm depends on the size of the object relative to the camera sensor, wavelength, and the number of pixels and pixel pitch of the camera sensor [Yaroslavsky et al., 2004]. Under equivalent recording conditions, the Fresnel transformation based reconstruction algorithm typically allows for larger DOF and larger object size, unconstrained by sensor size. The main advantage of the Fresnel transformation, in the context of human TM measurements, is that its suitable recording distance range is more than a few centimeter. The practical implication of this property is that the digital sensor can be away from the external ear canal, thus greatly reducing the spatial constraints for the holographic optical system. Based on this, further discussions within this Chapter are based on the Fresnel transform reconstruction.

5.3.2 Light diffraction modeled by the Fresnel-Kirchhoff integral

During the process of holographic reconstruction, the reconstruction (reference) wave (digital or optical) is diffracted by the aperture of the hologram and it produces a diffraction pattern at the image plane. We can establish a coordinate system such that

(x', y') are Cartesian coordinates in the object plane, (ξ, η) are Cartesian coordinates in the hologram plane, (x, y) are Cartesian coordinates in the image (observation) plane, z is the Cartesian coordinate along the surface normal of the hologram plane in the direction of the image plane, as shown in Fig. 5.3.

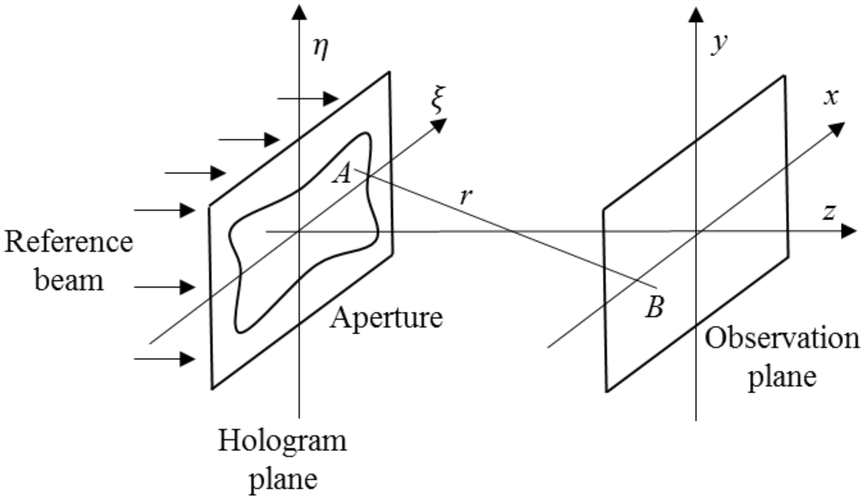

Fig. 5.3. Schematics of the coordinate system nomenclature for lensless digital numerical reconstruction [Kreis, 2005].

During numerical reconstruction, the propagating wavefronts can be modeled by the Fresnel-Kirchoff diffraction formula [Goodman, 1996]

$$\Gamma(x, y, z) = \frac{1}{i\lambda} \iint_{-\infty}^{\infty} U(\xi, \eta) \frac{e^{i\frac{2\pi}{\lambda}r}}{r} \cos\theta \, d\xi d\eta \,, \tag{5.22}$$

where $\cos\theta = z/r$ for assumed parallax conditions, $U(\xi, \eta)$ is the reconstructed hologram defined in Eq. 5.21, and r is the distance between any two points on the hologram and image planes, as shown in Fig. 5.3 and defined as

$$r = \sqrt{(\xi - x)^2 + (\eta - y)^2 + z^2} \,. \tag{5.23}$$

5.3.3 Numerical reconstruction by the Fresnel transformation

5.3.3.1 Fresnel approximation

For practical applications of the Fresnel transformation, several assumptions can be made in order to simplify Eq. 5.22 to a computationally efficient form. It can be assumed that the distance between the hologram and the image plane is large compared to the lateral size of the hologram and the image. This means that r in the denominator of the integral of Eq. 5.22 can be replaced by z. However, since r is typically in the centimeter to meter range and λ is in the sub-micron range, slight variations of r in the exponential term may lead to significant phase errors. Thus, an approximation of r is required in order to simplify the exponential term. This leads to the Fresnel approximation that relies on the binomial expansion of Eq. 5.23 to approximate r with only the linear terms of the binomial expansion series

$$\begin{aligned} r &= z\sqrt{\left(\frac{\xi - x}{z}\right)^2 + \left(\frac{\eta - y}{z}\right)^2 + 1} \\ &\cong z\left[\frac{1}{2}\left(\frac{\xi - x}{z}\right)^2 + \frac{1}{2}\left(\frac{\eta - y}{z}\right)^2 + 1\right]. \end{aligned} \tag{5.24}$$

The Fresnel approximation is valid as long as the quadratic term in the binomial expansion series of Eq. 5.23 leads to a phase changes $\ll 1$ radian

$$z\frac{2\pi}{\lambda}\frac{1}{8}\left[\left(\frac{\xi - x}{z}\right)^2 + \left(\frac{\eta - y}{z}\right)^2\right]^2 \ll 1\,, \tag{5.25}$$

leading to

$$\frac{\pi}{4\lambda}\left[(\xi - x)^2 + (\eta - y)^2\right]^2 \ll z^3\,. \tag{5.26}$$

Equation 5.26 defines the near field region, where the Fresnel approximation can be applied. Assuming that the requirements stated by Eq. 5.26 are met, the Fresnel approximation, Eq. 5.24, can be applied to the exponential term of Eq. 5.22 as follows

$$\begin{aligned}\Gamma(x,y,z) &= \frac{1}{i\lambda}\iint_{-\infty}^{\infty} U(\xi,\eta)\,\frac{1}{z}\,e^{i\frac{2\pi z}{\lambda}\left[\frac{1}{2}\left(\frac{\xi-x}{z}\right)^2+\frac{1}{2}\left(\frac{\eta-y}{z}\right)^2+1\right]}\,d\xi d\eta \\ &= \frac{e^{i\frac{2\pi z}{\lambda}}}{i\lambda z}\iint_{-\infty}^{\infty} U(\xi,\eta)e^{i\frac{\pi}{\lambda z}\left[(\xi-x)^2+(\eta-y)^2\right]}\,d\xi d\eta\,.\end{aligned} \tag{5.27}$$

By changing to variables $\nu = x/\lambda z$ and $\mu = y/\lambda z$, Eq. 5.27 can be modified to

$$\Gamma(\nu,\mu) = \frac{e^{i\frac{2\pi z}{\lambda}}}{i\lambda z}\,e^{i\pi z\lambda(\nu^2+\mu^2)}\iint_{-\infty}^{\infty} U(\xi,\eta)e^{i\frac{\pi}{\lambda z}[\xi^2+\eta^2]}\,e^{-i2\pi[\xi\nu+\eta\mu]}d\xi d\eta\,. \tag{5.28}$$

Aside from a constant intensity and phase factors preceding the integrals, Eq. 5.28 is the inverse Fourier transform of the product of $U(\xi,\eta)$ with a two-dimensional chirp function $\exp\left[i\frac{\pi}{\lambda z}(\xi^2+\eta^2)\right]$. In practical applications with recordings of diffuse (optically rough) objects, the constant intensity and phase factors preceding the double-integrals of Eq. 5.28 can be omitted since only the phase change and not the absolute phase of the object field is of importance, therefore Eq. 5.28 can be expressed as

$$\Gamma(\nu,\mu) = \Im\left[U(\xi,\eta)e^{i\frac{\pi}{\lambda z}[\xi^2+\eta^2]}\right], \tag{5.29}$$

where $\Im$ denotes the continuous Fourier transform.

5.3.3.2 Discrete Fresnel transformation

Using digital cameras, instead of holographic plates, provides a finite discrete representation of intensity of the hologram. Assuming a digital sensor array with $N \times M$

pixels and a pixel pitch of $\Delta\xi$ and $\Delta\eta$, the discrete spatial coordinates in the hologram plane are defined as

$$\begin{aligned} \xi &= n\Delta\xi\,, \qquad n = 1..N\,, \\ \eta &= m\Delta\eta\,, \qquad m = 1..M\,. \end{aligned} \tag{5.30}$$

The corresponding discrete spatial frequency coordinates, (k, l), and resolution, $(\Delta k, \Delta l)$, of the reconstructed hologram in the image plane becomes:

$$\begin{aligned} k &= n\Delta k\,, \qquad \Delta k = \frac{1}{N\Delta\nu} = \frac{z\lambda}{N\Delta\xi}\,, \\ l &= m\Delta l\,, \qquad \Delta l = \frac{1}{M\Delta\mu} = \frac{z\lambda}{M\Delta\eta}\,. \end{aligned} \tag{5.31}$$

Using Eqs 5.30 and 5.31, the discrete form of Eq. 5.29 can be expressed as the Fast Fourier Transformation (FFT)

$$\Gamma(k,l) = FFT[h(n,m)R(n,m)w(n,m,z)]\,, \tag{5.32}$$

where $h(m,n)$ is the discretized hologram recorded by the sensor, $R(m,n)$ is discrete numerical model of the reconstruction (reference) wave, and $w(m,n,z)$ is the discrete chirp function used for reconstruction at a position z away (behind the sensor) from the hologram plane

$$w(n,m,z) = e^{i\frac{\pi}{\lambda z}[n^2\Delta\xi^2 + m^2\Delta\eta^2]}\,. \tag{5.33}$$

Equation 5.32 allows for numerical reconstruction of a digitally recorded hologram. Adjustment of the reconstruction distance, z, during the numerical reconstruction process, allows focusing at a user defined imaging plane, thus allowing free-focusing capabilities after the recording of the hologram. Based on Eq. 5.32, the intensity $I(k,l)$

and phase $\phi(k,l)$ of the reconstructed hologram can be defined as the magnitude and phase of the FFT and computed with

$$I(k,l) = |\Gamma(k,l)|^2 ,$$

$$\phi(k,l) = tan^{-1}\left\{\frac{Im[\Gamma(k,l)]}{Re[\Gamma(k,l)]}\right\} . \tag{5.34}$$

In order to avoid the $(-\pi/2\,,\pi/2)$ ambiguity of the tan^{-1} function, the computationally efficient $atan2$ function is utilized, allowing for quantification of the phase within the full $(-\pi,\pi)$ range.

5.3.3.3 Sampling criteria for digital holograms

In order to apply the discrete Fresnel transformation, the hologram at the sensor plane has to be digitized with sufficient spatial frequency resolution and intensity (bit depth). Modern digital cameras have a bit depth in the rage of 10- to 16-bits (i.e., 2^{10}-2^{16} gray scale levels) and high (i.e., 70 – 120 dB) signal to noise ratio (SNR) allowing adequate intensity sampling of digital holograms [Schnars and Jüptner, 2005]. The maximum spatial frequency resolution, f_{cam}, of digital cameras is defined by the Nyquist criteria

$$f_{cam} < \frac{1}{2\Delta\xi} , \tag{5.35}$$

where $\Delta\xi$ is the pixel pitch of the sensor. For modern CCD sensors with 100% fill factor, the pixel pitch is approximately equivalent to the pixel size, which is in the order of less than 4μm, resulting in f_{cam} > 100 lines/mm. In comparison, typical holographic plates (i.e., silver halides based) allow more than 30 fold higher spatial frequency resolutions (i.e., 3000-7000 lines/mm). In order to quantify the spatial resolution requirements for an adequate digitization of a hologram with a sensor array, it is necessary to quantify the limits of the spatial frequency content of a hologram.

In order to determine these requirements, an off-axis lensless Fourier transform holography setup is considered, as shown in Fig. 5.4. The coordinate system at the object is designated as (x', y', z'). Without loss of generality, the object and the sensor are considered approximately flat within the scale of the optical setup size and centered relative to the *z*-axis.

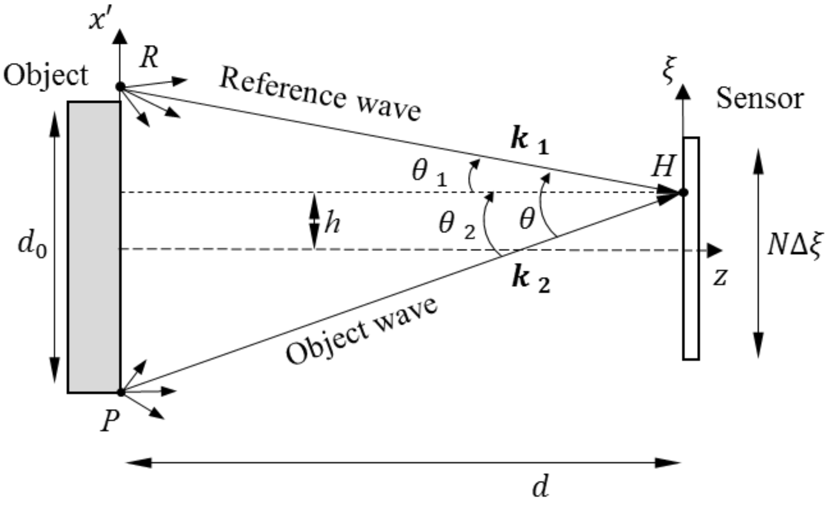

Fig. 5.4. Geometrical parameters of the optical setup for recording an off-axis digital lensless Fourier transform hologram.

The optical setup of a lensless Fourier transform holography consists of an object of interest, a reference wave, and the camera sensor array. By assuming a diffuse object with a uniform illumination, every point on the object's surface can be treated as an independent spherical wave source that contributes to the illumination of all pixels at the camera. We can assume a spherical reference wave with an origin *R* at the object plane at the boundary of the object, as shown in Fig. 5.4. The interference pattern at any point, *H*, on the sensor is a linear superposition of the interference patterns between the reference wave, emanating from point *R*, and all object waves, emanating from all points on the surface of the object. Equation 5.17 describes the reference wave and an object wave emanating from point *P* to create an interference pattern (fringes) at point *H* on the sensor plane with a spatial frequency content, f_{fringe}, which is defined by the relative angle, θ, between the directions of propagation, $\boldsymbol{k_1}$ and $\boldsymbol{k_2}$**,** of the two waves, so that

$$\begin{gathered} |\boldsymbol{k}''| = \frac{4\pi}{\lambda}\sin\left(\frac{\theta}{2}\right) \cong \frac{2\pi}{\lambda}\theta = 2\pi f_{fringe} \,, \\ f_{fringe} = \frac{\theta}{\lambda} \,. \end{gathered} \tag{5.36}$$

Based on Eqs 5.17 and 5.36, it can be seen that spatial frequency content at point *H* will be proportional to the angle between the directions of propagation of the two waves. Based on this, the maximum of the spatial frequency, f_{max}, content at a point *H* on the sensor, will be defined by the interference pattern of a reference and object waves with the largest relative angle, θ_{max} , between their directions of propagation. Assuming point *H* on the sensor surface is at distance *h* from the z-axis, as shown in Fig. 5.4. The maximum spatial frequency, f_{max}, will occur when point *P* is at a maximal distance from point *R*, at the opposite end of the object. In this condition, the relative angle θ_{max} can be expressed as

$$\begin{gathered} \theta_1 \cong \tan(\theta_1) = \frac{\frac{d_0}{2} + h}{d} \,, \\ \theta_2 \cong \tan(\theta_2) = \frac{\frac{d_0}{2} - h}{d} \,, \end{gathered} \tag{5.37}$$

$$\theta_{max} = \theta_1 + \theta_2 = \frac{d_0}{d},$$

where d_0 is the size of the object, and d is the distance between the object and the sensor. Based on the Nyquist criteria, $f_{fringe} < f_{max}/2$, as well as Eqs 5.36 and 5.37, the following condition for adequate spatial resolution of the sensor needs to be fulfilled

$$\frac{1}{2\Delta\xi} > \frac{1}{\lambda}\frac{d_0}{d}. \tag{5.38}$$

This results in a required minimum distance, d_{min}, between the sensor and the object for a given object size, d_0, and sensor pixel size, $\Delta\xi$

$$d_{min} = \frac{d_0 2\Delta\xi}{\lambda}. \tag{5.39}$$

For an 8mm circular object, 532nm wavelength, and a 3.45μm pixels size, the minimum standoff distance between the sensor and object is 104 mm. Equation 5.39 provides a conservative limit as it assumes that all points of the object have to be sampled by all pixels on the sensor. In practical applications even a fraction of the sensor's pixels are sufficient to reproduce the object with adequate quality. This means that shorter distances, d, can be achieved in measurement conditions where the size of the overall experimental setup is constrained.

5.4 Displacement measurements by digital holography

Utilizing digital holography for numerical reconstruction (focusing) of the object of interest and determination of the corresponding interference phase are key to calculations of quantities representative of the shape and deformation of the object. Digital holography allows the full-field quantification of the shape and displacement of the surface of an opaque object or the refractive index changes within the volume of a transparent object. These capabilities can be used for a variety of mechanical measurements ranging from shape, deformation and strain for opaque objects to temperatures, density and mass flow for transparent objects [Schnars and Jüptner, 2005]. This Section focuses on the use of digital holography for measurements of the displacement of the full surface of an opaque object of interest.

Digital holography allows for quantification of the deformation of an object, by comparing holograms of the object before and after deformation. The holograms are individually reconstructed using Eq. 5.32 and their double exposure phase difference, $\Delta\phi$, corresponding to the deformation of the object, can be expressed as [Schnars and Jüptner, 2005]

$$\Delta\phi = \begin{cases} \phi_{ref} - \phi_{def} & ,if\ \ \phi_{ref} \geq \phi_{def}\ , \\ \phi_{ref} - \phi_{def} + 2\pi & ,if\ \ \phi_{ref} < \phi_{def}\ , \end{cases} \tag{5.40}$$

where $\phi_{def}$and ϕ_{ref} are the phase angles of the reconstructed holograms taken before (reference state) and after (deformed state) the deformation of the object. The spatial distribution (k, l) is omitted for brevity. Equation 5.40 accounts for the discontinuous nature of the tangent function in Eq. 5.34.

Assuming a coordinate system as given in Fig. 5.5, the direction of observation and illumination is described by unit vectors $\boldsymbol{k_o}$ and $\boldsymbol{k_i}$. Based on this geometrical setup, the resulting sensitivity vector is defined as $\boldsymbol{k_s} = \boldsymbol{k_o} - \boldsymbol{k_i}$ [Sollid et al., 1969]. The sensitivity vector is defined only by the geometry of the holographic arrangement and it does not depend on the reference wave. The sensitivity vector, $\boldsymbol{k_s}$, indicates the direction of the component of the displacement field vector, $\boldsymbol{d}(x, y, z)$, of the object's surface, which the holographic system is sensitive to. In other words, at each object point the holographic system measures the projection of the displacement vector, $\boldsymbol{d}$, onto the sensitivity vector, $\boldsymbol{k_s}$.

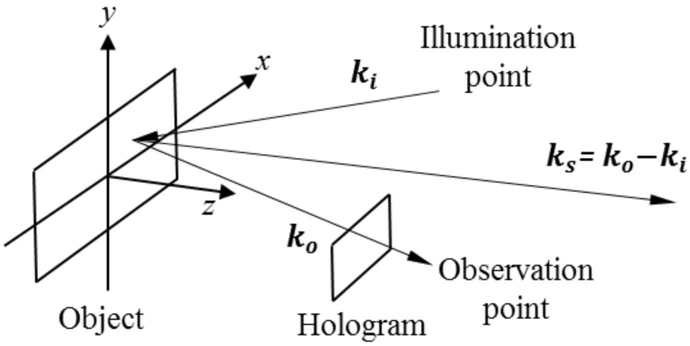

Fig. 5.5. Geometrical definition of the sensitivity vector [Pryputniewicz and Stetson, 1990].

The fringe locus function describes the relation between $\Delta\phi$ and the displacement vector field, $\boldsymbol{d}(x, y, z)$ of the object's surface [Sollid et.al., 1969]

$$\Delta\phi(x, y) = \frac{2\pi}{\lambda}\boldsymbol{d}(x, y, z)(\boldsymbol{k_o} - \boldsymbol{k_i}) = \frac{2\pi}{\lambda}\boldsymbol{d}(x, y, z)\boldsymbol{k_s} \,. \tag{5.41}$$

Equation 5.40 is the basis of all quantitative measurements of the displacement of the surface of opaque objects. The full three dimensional displacement vector field, $\boldsymbol{d}(x, y, z)$, contains three components at each point of the object. To fully quantify $\boldsymbol{d}(x, y, z)$, three holograms of the object are to be recorded, each with a different (linear independent) sensitivity vector. In typical practical applications, only the component of displacement normal to the object's surface is of interest. For objects that are approximately flat, the holographic setup can be simplified such that the illumination and observation direction are collinear (parallel), resulting in a sensitivity vector $\boldsymbol{k_s} =$

$(0,0,2)$. Based on that, the component d_z can be calculated from the phase difference, $\Delta\phi$, of a single set of double-exposure holograms

$$d_z(x,y) = \frac{\lambda}{4\pi}\Delta\phi(x,y)\ . \tag{5.42}$$

According to Eq. 5.42, a phase change of 2π (one fringe) would indicate a displacement of $\lambda/2$, or 266nm for a 532nm wavelength. The key to the nanometer sensitivity of digital holography and interferometry is the physical correlation between object displacement and intensity changes (fringes) that can be detected by a camera sensor with a fraction of a fringe accuracy. It should be noted that the temporal, Eq. 5.13, spatial, Eq. 5.31, and displacement, Eq. 5.42, resolutions of holographic measurements are mainly dependent on the camera sensor capabilities (i.e., bit depth and noise floor) as well as on the reconstruction and phase sampling methods [Dobrev et al., 2013b].

6 Summary of physiological, technological and holographic design constraints

In order to design a full-field measurement system for quantification of transient responses of the middle ear, we first need to establish criteria and corresponding design parameters defining the temporal, spatial and displacement resolution requirements of all components of the measurement system. The design criteria can be categorized in three domains:

- Human TM - physiological and anatomical constraints defining the displacement, temporal and spatial resolution of the measurement system
- Phase sampling - holographic recording principles that define the temporal and displacement resolution of the system.
- Camera – technological constraints that define the temporal and spatial resolution of the system.

The interaction of constraints from all domains is graphically represented in Fig. 6.1. This Chapter discusses the contribution of physiological, technological and holographic factors to the design criteria of the spatial, temporal and displacement resolution of the measurement system and its components.

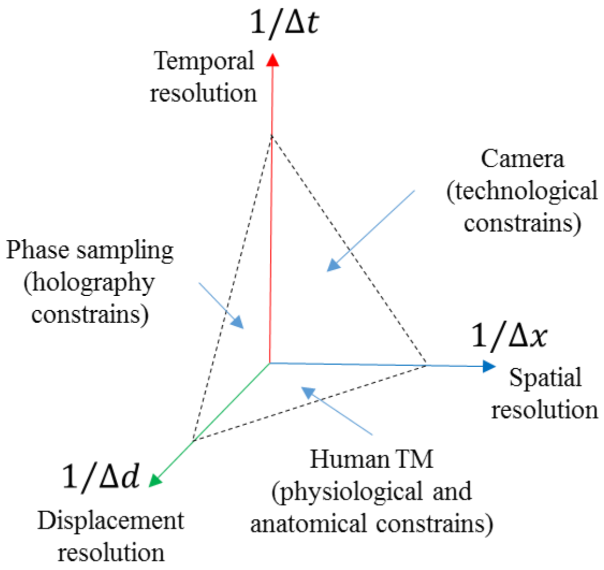

Fig. 6.1. Overview of phase sampling, camera, physiological and anatomical constraints of the human TM affecting the design criteria of the spatial, temporal and displacement resolution of the measurement system and its components.

6.1 Temporal and spatial resolution of state-of-the-art cameras

The temporal and spatial resolution of current state-of-the art cameras is dependent on their sensor, readout and memory technology. In terms of temporal resolution only, all camera technologies can be separated into three main types:

- Conventional – the most common type of cameras. Frame rate range ~1-500 fps.
- Double-exposure (DE) – specialized for rapid (inter-frame time < 1us) acquisition of two consecutive frames. Typically used for particle image velocimetry (PIV) which also gives the common market name “PIV cameras”.
- High-speed – specialized in acquiring a finite amount of frames (16-50000) at frame rates of >10K fps.

Based on a summary, shown in table 6.1, of all 3 main types of camera, it can be seen that the spatial and temporal resolutions are inversely proportional.

Table 6.1. Comparison of various camera types based on their temporal and spatial resolutions.

Camera type	**Frame rate[1]**	**Inter-frame time[2]**	**Resolution (MP)**	**# of frames[1]**	**Price ($K)**
Conventional [AVT, 2014; Mamiya Leaf, 2014]	1-500 fps	2-1000 ms	0.1-80	unlimited[3]	0.5-15
Double-exposure [LaVision, 2014]	10-100 fps	<1 μs	0.1-30	2	5-30
High-speed [Photron, 2014]	1-50k fps	20-1000 μs	0.01-5	5-50k	20-150
Ultra-high speed [Specialized Imaging, 2014]	1-5M fps	0.2-1 μs	0.3-1	50-200	~200
Framing [Specialized Imaging, 2013]	0.1-1G fps	1ns	0.3-1.3	16-64	>500

[1] At maximum resolution; [2] at maximum frame rate; [3] dependent on frame grabber memory.

In typical high-speed metrology applications, as described in Chapter 4, high-speed camera types are the primary choice. There are three main types of high-speed cameras (last 3 rows of Table 6.1), which can be differentiated by their spatial and temporal resolution as well as the maximum number of fames per recording (sampling length). Conventional high-speed cameras have relatively large memory (5-50K frames) however at the expense of limited data transfer bandwidth between the sensor and the memory. This causes inversely proportional dependence between the spatial and temporal resolution. In other words, higher temporal resolution is achieved at the expense of lower spatial resolution. Ultra-high speed cameras alleviate this problem by embedding the memory within the circuitry of the imaging sensor, thus reducing the data transfer bandwidth limitations. In other words, the temporal resolution becomes independent of spatial resolution. However, the size of the embedded memory is typically limited to <200 frames [Specialized Imaging, 2014], resulting in <20 μs of maximum sampling duration (at 5 Mfps). The temporal resolutions (exposure time) of both high and ultra-high-speed cameras are limited by the optical sensor readout speed. Framing cameras avoid the readout speed constrain through the use of multiple (i.e., 16-64) high-speed sensors allowing for frame rates of >1 Gfps. However, framing cameras typically require higher illumination power, and maintenance cost.

6.2 Holographic recording of transient events

During an examination procedure, the motion of the TM, although driven by controlled sound stimuli, could be also affected by external disturbances such as the patient's heartbeat, breathing, tremor as well as random environmental disturbances. The natural human tremor and breathing are of relatively low frequency (i.e., <15 Hz) and high amplitude (i.e., >100 µm) [Stiles and Randall, 1967; Hömberg et al., 1987] while typical sound induced vibration of the TM are with high frequency (i.e., >200 Hz) [Rosowski et al., 2009] and low amplitudes (i.e., <200 nm). Both of the these motion components result in a change of the speckle pattern (microscopic fringe pattern) of the interferogram during the recording process, which could result in speckle decorrelation, reduced fringe visibility and deterioration of the quality of measured data [Jones and Wykes., 1983].

6.2.1 Speckle decorrelation due to relative motion during holographic recording

The effect of speckle decorrelation and its relationship to the amount and type of relative motion during the recording process can be described by evaluation of the effects of the phase variation within the speckles and changes in the spatial distribution of the speckle pattern due to the individual components of motion (i.e., rotational and translational) along all 3 Cartesian axes, as shown in Fig. 6.2:

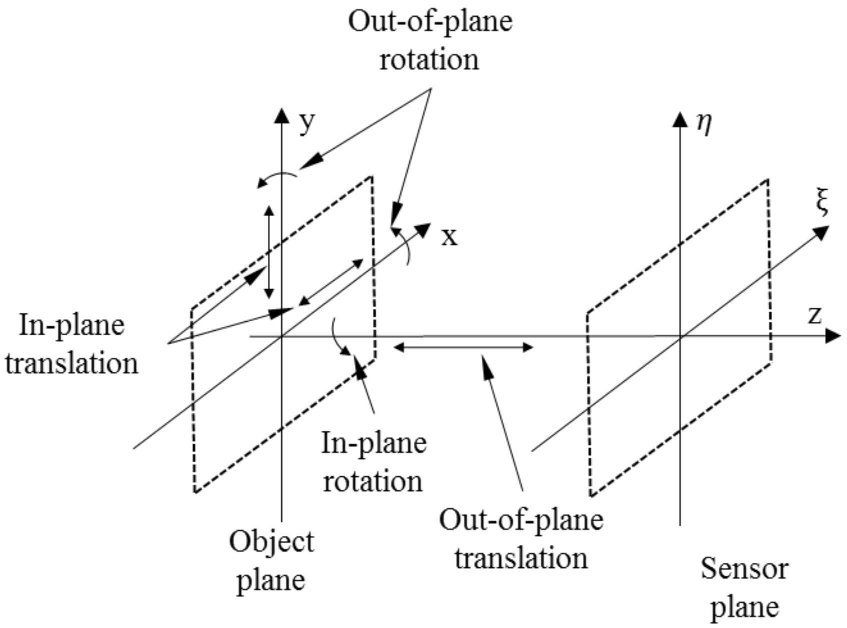

Fig. 6.2. Components of the relative displacement between the object plane and the measurement system (sensor plane). Translations and rotations along all Cartesian axis can be categorized as in-plane and out-of-plane relative to the object plane.

6.2.1.1 Out-of –plane translation

Out-of-plane translation, or translation along the z axis as defined in Fig. 6.2, can be categorized as in-plane and out-of-plane relative to the object plane. Out-of-plane translation causes changes in the phase within the speckle [Jones and Wykes, 1983]. Analogously, out-of-plane rotation around the x or y axis can be viewed as an out-of-plane translation gradient along the z axis. In both cases, the speckle decorrelation [Owner-Petersen,1991] causes degradation of the corresponding fringe contrast, Z, and consequently the data quality as follows

$$Z = sinc\left(\frac{\pi}{N}\right) = sinc\left(\frac{4\pi}{\lambda}z\right), \tag{6.1}$$

where $1/N$ is the fringe order of the phase change that occurred within the speckle pattern, λ is the laser wavelength and z is the out-of-plane translation magnitude. For an in-line out-of-plane sensitive interferometric system with laser wavelength of 532 nm, a full decorrelation (i.e, Z < 0.5) will occur within <266 nm of out-of-plane displacement during the recording process. In typical interferometric applications, the phase change is kept within 1rad [Jones and Wykes, 1983] or 27 nm based on the previous example.

6.2.1.2 In-plane translation

In-plane translation, or translation along the x and y axis as defined in Fig. 6.2, causes changes in the speckle pattern spatial distribution. Analogously, in-plane rotation around the z axis can be viewed as an in-plane translation gradient along the x and y axis. In both cases, the speckle decorrelation [Owner-Petersen,1991] causes degradation of the corresponding fringe contrast as follows

$$Z = 2\frac{J_1\left(\frac{q}{x}\right)}{\frac{q}{x}}, \tag{6.2}$$

where q is the speckle size, x is the in-plane motion component, and J_1 is the Bessel function of first order. Based on Eq. 6.2, it can be seen that full decorrelation occurs at an in-plane shift x within the average size of the speckles, q. In lensless digital holography, the speckle size is governed by the subjective speckle size that can be described as [Kreiss, 2005]

$$q = \frac{\lambda d\pi}{d_o}, \tag{6.3}$$

where d_o is the size of the object of interest. For a 532 nm laser wavelength, 8 mm object at 100 mm away Eqs 6.1 and 6.2 estimate that a full decorrelation (i.e, Z <0.5) will occur after approximately <20 μm of in-plane motion. As the limit imposed by Eq.6.2 is 2 orders of magnitude larger (less constraining) than the one imposed by Eq. 6.1, further discussion in the sections are focused on overcoming the acquisition constraints imposed by Eq.6.1.

6.2.2 Holographic recording implications on acquisition speed

In order to assess the maximum allowable measurement time, t_{max}, before full decorrelation occurs, we can assume that the relative out-of-plane motion between the OH and the TM can be approximated with a simple sinusoidal motion with an instantaneous velocity

$$V = A\omega\cos(\omega t)\,, \tag{6.4}$$

where A and ω are the amplitude and angular velocity of the relative motion, and t is the time variable. The maximum allowable measurement time, t_{max}, is related to the corresponding travelled distance, Δz, based on the relative velocity, V

$$\Delta z = \int_{-t_{max}/2}^{t_{max}/2} A\omega\cos(\omega t)\,dt = 2Asin\left(\frac{t_{max}\;\omega}{2}\right). \tag{6.5}$$

Based on this, t_{max} can be expressed as

$$t_{max} = sin^{-1}\left(\frac{\Delta z}{2A}\right)\frac{2}{\omega} = \frac{1}{f\pi}sin^{-1}\left(\frac{\Delta z}{2A}\right), \tag{6.6}$$

where f is the frequency corresponding to ω. Assuming a human tremor with 5 Hz frequency and 100 µm p-p amplitude [Hömberg et al., 1987], Eq. 6.6 predicts a full decorrelation to occur within 85 µs of measurement time. Analogous speckle decorrelation effects will occur due to the motion (vibration) of the object during the measurement time of the holographic system. Based on a typical acoustically induced displacement of the TM (i.e., 200 nm p-p @ 5 kHz), a full decorrelation will occur within measurement times (i.e., camera exposures) >50 µs. In order to maintain a speckle phase change of less than 1rad, as recommended by [Jones and Wykes, 1983], the measurement time should be less than 7 µs.

6.3 Spatial, temporal and displacement resolution constraints based on the physiology of the human TM

The spatio-temporal complexity of the acoustically excited nanometer displacement of the human TM, imposes constraints on the spatial, displacement and temporal resolution of the HHS. Previous research [Furlong et al., 2009; Cheng et al., 2010] indicates sufficient spatial (>7 lines/mm) and displacement (<15 nm) resolution and accuracy of previous [Flores-Moreno et al., 2011] digital holographic systems for the quantification of displacement of the human TM excited by tonal stimuli. Throughout the rest of this section, the main focus will be on the temporal sampling parameters of the holographic system that are dictated by the human hearing parameters, as shown in Table 6.2.

Table 6.2. Identification of measurement parameters to investigate transient behavior of the human TM.

Human hearing parameters	Value	Acquisition design constraints	Value
Frequency range	0.2-8 kHz [Suzuki and Takeshima, 2004]	Sampling rate	1-40 kHz[a]
		Exposure time	<6-12 μs[a] [Cheng et al., 2010]
TM's acoustical delay	40 μs- 1.3 ms [Cheng et al., 2013; O'Connor and Puria, 2008]	Minimum sampling rate	>30 kHz [Pedrini et al., 1998]
Click response duration	<5 ms settling time [Kemp, 1978]	Number of samples	~150 frames @ 30 kHz
		Frequency resolution	200 Hz

[a] With 5 samples per cycle and 5-10% duty cycle.

The human ear is most sensitive to sounds of frequencies between 0.2-8 kHz [Suzuki and Takeshima; Crochiere et al., 1976]. To allow sufficient temporal resolution for the measurement of the instantaneous magnitude and phase [Rosowski et al. 2012] of the acoustically induced motion of the TM as well as its total harmonic distortion [Cheng et al., 2010], the acquisition system needs to capture at least 5-10 samples per cycle [Cheng et al., 2013]. Thus, a sampling rate of 40 kHz is required to capture the motion produced by sounds with frequencies at the high end of this sensitive range.

If acoustic energy is propagated across the surface of the TM, such propagation depends on wave speed and direction. Existing methods, based on steady state measurements, estimate surface wave speed in the 5-70 m/s range resulting in acoustic delays across the 8 mm diameter membrane of 110-1600 μs [Cheng et al., 2013;

O’Connor and Puria, 2008]. In order to reliably quantify the speed and direction of acoustic energy propagation across the surface of the TM, an acquisition method should allow the capture of at least 3 instances [Pedrini et al., 1998] of the spatio-temporal evolution of the surface waves within the duration of the acoustical delay. Considering a more conservative estimate for acoustic delay (i.e., ~100 μs), capturing 3 instances of the propagation of the surface waves would require <33 μs inter-frame time resulting in minimal sampling rate of 30 kHz.

Typical duration on an acoustical click response of the human TM is <5 ms [Kemp, 1978]. At a minimal sampling rate of 30 kHz, the full duration of the transient will be represented within ~150 frames. The duration of the click response defines a minimal frequency resolution of > 200 Hz for a single measurement. The frequency resolution of the acquisition method could be further improved by longer sampling or capturing several consecutive click responses of the TM.

In order to establish suitable exposure time to capture the transient response of the human TM, we use an analogy with previous stroboscopic holographic acquisition methods where the illumination duty cycle relative to a steady state excitation frequency defines the effective exposure time per cycle [Cheng et al., 2010; Khaleghi et al. 2013]. Using this analogy, for frequencies within the range of highest sensitivity of the human hearing [Suzuki and Takeshima, 2004] (i.e. up to 8 kHz), a typical stroboscopic duty cycle [Cheng et al., 2010] of 5-10% would correspond to an equivalent single frame exposure time of ~6-12 μs, consistent with estimates based on Eq. 6.6.

Identification of measurement parameters to investigate transient behavior of the human TM summarizes the human hearing characteristics and the corresponding sampling parameters implemented in the HHS to achieve temporal resolutions better than 7 μs at sampling rates greater than 40 kHz, and measurement duration of 5 ms to provide a frequency resolution of 200 Hz.

Part 2: Developments

7 Single frame phase sampling methods

As it has been demonstrated in Chapter 6, measurements of transient acoustic events in the middle-ear, and the human TM in particular, require high acquisition speed (>40 kHz) and high temporal resolution (<10 μs). Such short recording window limits the use of conventional temporal phase sampling algorithms [Cheng et al., 2010]. These constraints make the development of single frame phase sampling algorithms crucial for the realization of a high-speed measurement system for the middle-ear. While there is a large variety of existing single frame phase sampling algorithms, as described in Chapter 4, their applicability greatly depends on the spatial resolution of the camera sensor and the complexity and cost of the optical system. In order to minimize optical setup complexity and accounting for current state-of-the-art cameras, two types of single frame phase sampling algorithms have been developed and implemented within this Dissertation.

A double exposure spatial phase sampling (DESPS) method has been enhanced and implemented in order to take advantage of the high spatial resolution (i.e., >5 MP and <5 μm), global shutter capabilities, and simultaneous readout and capture of modern charge-coupled device (CCD) sensors. A 2+1 frame local correlation phase sampling (2+1 LCPS) method has been developed and implemented in order to take advantage of the temporal resolution (i.e., <5 μs exposure) of high-speed (i.e., >40 kfps) cameras without imposing constraints on their spatial resolution (i.e., >20 μm pixel size)

7.1 Double exposure spatial phase sampling (DESPS)

A double exposure spatial phase sampling (DESPS) methods has been optimized and implemented for the rapid (1 frame) quantification of optical phase changes corresponding to deformations of the human middle-ear between a reference and a deformed state. The method utilizes lensless digital holographic reconstruction [Dobrev et al., 2012] and spatial phase sampling (SPS) methods [Khaleghi et al., 2014b] to extract the phase information of the object based on a single frame recording at each loading state.

7.1.1 Spatial phase sampling (SPS)

A spatial phase sampling (SPS) method is enhanced and implemented in order to allow quantification of the optical phase of the object through a single hologram. During the holographic recording process, a spatial carrier frequency is introduced into the spatial frequency content of the recorded hologram. This is achieved by development of means to control the relative angle between the object and reference waves impinging onto the camera sensor, Section 9.2.

Based on Eq. 5.20 and 5.36, the spatial intensity distribution of a hologram, $h(\xi,\eta)$, can be expressed as

$$h(\xi,\eta) = r^2(\xi,\eta) + o^2(\xi,\eta) + 2r(\xi,\eta)o(\xi,\eta)\cos[\boldsymbol{k}''\cdot\boldsymbol{r} + \phi(\xi,\eta)]\,, \qquad (7.1)$$

where $\boldsymbol{r}$ is the position vector, ϕ is a random phase difference between the object and reference waves, and $\boldsymbol{k}''$ is difference between the vectors describing the direction of propagation of the two waves at each spatial location. Based on Eq. 5.36, the spatial frequency content, $f_{fringe} = \boldsymbol{k}'' \cdot \boldsymbol{r}$, within the hologram, containing a spatial carrier frequency, can be expressed as

$$f_{fringe}(\xi,\eta) = \frac{\theta(\xi,\eta)}{\lambda} = \frac{\theta_{varying}(\xi,\eta) + \theta_0}{\lambda}\,, \qquad (7.2)$$

where $\theta(\xi,\eta)$ is the angle of any two rays of the object and reference waves impinging at a location (ξ,η) of the hologram plane (camera plane). The angle $\theta(\xi,\eta)$ can be separated into a spatially varying component, $\theta_{varying}(\xi,\eta)$, and a constant offset, θ_0, related to relative angle between the object and reference waves.

After sampling of Eq. 7.1 by the camera sensor and application of the numerical reconstruction based on Eq. 5.32, the complex amplitude, Γ, in the frequency domain of the reconstructed hologram can be expressed as

$$\Gamma(k,l) = A(k,l) + C(k - f_{k0}, l - f_{l0}) + C^{*}(k + f_{k0}, l + f_{l0})\,, \qquad (7.3)$$

where A is the DC term, C and C^{*} corresponds to the twin images components that are complex conjugates of one another, $f_{k0}$and f_{l0} denote the components of the spatial carrier frequency f_{fringe}. Figure 7.1 illustrates a 1D representation of the size and position, in the frequency domain, of all components of a hologram with a spatial carrier frequency, f_0. In practical applications, only the real image, C, of the object is of interest, while the presence of the DC and the twin image components deteriorate quality of the real image and need to be removed.

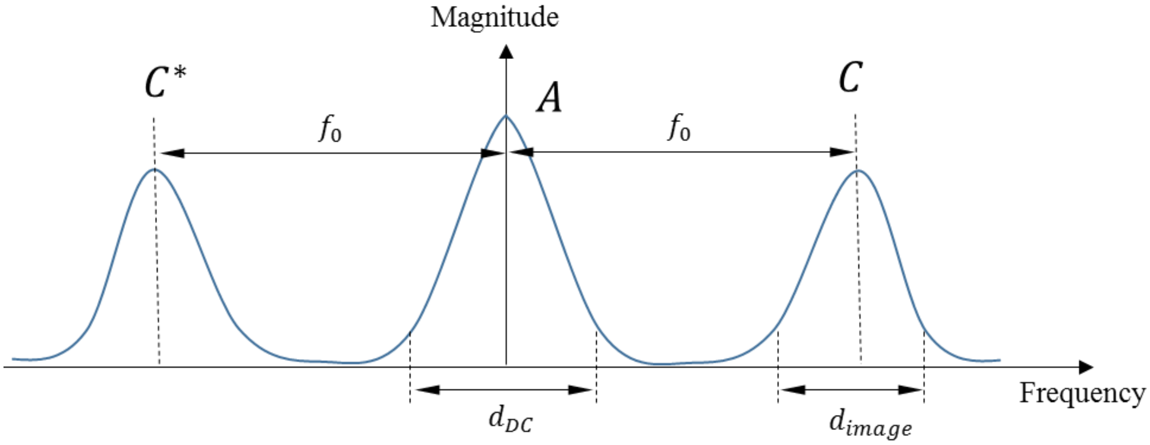

Fig. 7.1. Illustration of the spatial phase sampling (SPS) method to separate the object information from the hologram components by adding a spatial carrier frequency, f_0. Indicated are major parameters for the practical application of the SPS method.

7.1.1.1 DC component filtration

The DC component represents the spatial frequency content of background illumination, $r^2 + o^2$, and its size (bandwidth), d_{DC}, in the imaging plane in units of camera pixels can be approximated as [Schnars and Jüptner, 2002]

$$d_{DC} = \left(\frac{(N\,\Delta\xi)^2}{d\,\lambda}, \frac{(M\,\Delta\eta)^2}{d\,\lambda} \right), \tag{7.4}$$

where d is the recording distance (working distance), N and M are the number of pixels along the (k, l) coordiantes, $\Delta\xi$ and $\Delta\eta$ pixel sizes, and λ is the light wavelength. Assuming that the carrier frequency is sufficiently large, the DC can be approximated as a low spatial frequency component of the hologram, which can be estimated with low-pass spatial filter such as mean or Gaussian. The DC can then be separated from the other components by high-pass filtration of the hologram.

7.1.1.2 Twin image masking

The twin images carry the same information about the object, but they appear in focus at different reconstruction distances. For extraction of the complex field of the object, only one of the images is sufficient, however its twin will appear as out-of-focus and it will deteriorate the quality of the focused image. The twin images have equal size, d_{image}, and can be expressed in units of pixels in the imaging plane as [Khaleghi et al., 2014b]

$$d_{image} = \left(\frac{d_{ox}\, N\, \Delta\xi}{d\, \lambda}, \frac{d_{oy}\, M\, \Delta\eta}{d\, \lambda}\right), \tag{7.5}$$

where d_{ox} and d_{oy} are the horizontal and vertical size of the illuminated area of the object. By introducing a sufficiently large spatial frequency and improving the optical setup, the size and location of the twin images, as shown in Fig. 7.1, can be adjusted so they are spatially separated. Based on this, a spatial mask can be used to extract the complex field containing only the object wavefront. Realization of an optical setup that utilizes the SPS method is described in Chapter 9 and its measurement capabilities are validated in Chapter 12.

7.1.2 Double exposure phase difference

After applying the SPS method to extract the phase of the object at a reference and a deformed state, the double exposure phase difference, corresponding to the object deformation, can be quantified. Equation 5.40, allows for calculation of the phase difference, however it would require the computation of two arctangent functions. In practical applications, it is more computationally efficient to extract the phase difference,

$\Delta\phi$, information directly from the complex data of the reconstructed holograms[Dobrev et al., 2010] as

$$\Delta\phi = \tan^{-1}\left[\frac{Re(\Gamma_{ref})Im(\Gamma_{def}) - Im(\Gamma_{ref})Re(\Gamma_{def})}{Im(\Gamma_{ref})Im(\Gamma_{def}) + Re(\Gamma_{ref})Re(\Gamma_{def})}\right], \tag{7.6}$$

where $Re(\Gamma)$ and $Im(\Gamma)$ specify the real and imaginary parts of the complex field of a reconstructed holograms, and Γ_{ref} and Γ_{def} are the reconstructed holograms taken before (reference state) and after (deformed stated) the deformation of the object. The spatial distribution (k, l) is omitted for brevity. Equation 7.6 requires the computation of only one arctangent function.

7.2 2+1 frame local correlation phase sampling (2+1 LCPS)

The 2+1 frame local correlation phase sampling (2+1 LCPS) method [Dobrev et al., 2014c] is based on family of hybrid spatio-temporal phase sampling methods [Schmitt and Hunt, 1997; Georgas and Schajer, 2012]. This Section describes the development and implementation of a novel 2+1 LCPS method for high-speed applications. The 2+1 LCPS method uses a combination of temporal and spatial phase sampling to provide single frame quantification of the deformed state of the object based on multiple temporally phase shifted reference images.

In the 2+1 LCPS method relies on two data sets acquired at different temporal resolutions. The first set consists of two temporally phase shifted reference frames before object deformation and the second set consists of series of rapidly acquired frames during object deformation. The method quantifies the double-exposure phase change at each time instance by correlating deformed with reference states. The correlation of individual frames relies on the assumption that the object is sufficiently stable during the acquisition of the two phase shifted reference frames, which is the case for the high-speed events of interest.

Considering two individually recorded camera frames at a reference, I_{ref}, and at a deformed, I_{def}, state with intensities

$$I_{ref} = I_r + I_o + 2\sqrt{I_r I_o}\cos(\theta)\,, \tag{7.7}$$

$$I_{def} = I_r + I_o + 2\sqrt{I_r I_o}\cos(\theta + \phi)\,, \tag{7.8}$$

where I_r and I_o are the intensities of the reference and object beams, respectively, θ is the initial random phase difference between the two interfering beams, and ϕ is the phase change corresponding to the object deformation. By assuming that only ϕ varies, the cross-correlation function, $\rho\left(I_{ref}, I_{def}\right)$, can be expressed as [Jones and Wykes, et al., 1983]

$$\rho\left(I_{ref}, I_{def}\right) = \frac{1 + r^2 + 2r\cos\phi}{(1 + r)^2}\,, \tag{7.9}$$

where $r = I_r/I_o$. The $I_r + I_o$ terms, estimated by temporally averaging each measurement point and corresponding to a constant background illumination (DC), can be subtracted from Eqs 7.7 and 7.8 to yield an expression equivalent to Eq. 7.9

$$\rho\left(I_{ref}, I_{def}\right) \cong \cos\phi\,, \tag{7.10}$$

which contains information about the deformation of the object. Furthermore, by acquiring a second reference state with a $\pi/2$ phase shift

$$I_{ref+\pi/2} = I_r + I_o + 2\sqrt{I_r I_o}\cos\left(\theta + \frac{\pi}{2}\right), \tag{7.11}$$

and correlating it with a deformed state represented by Eq. 7.8 leads to

$$\rho\left(I_{ref+\pi/2}, I_{def}\right) \cong \cos(\phi + \frac{\pi}{2}) = \sin(\phi) \,. \tag{7.12}$$

By assuming a constant beam ratio, r, the phase change of interest, ϕ, in space, (m, n), corresponding to the deformation of the object at a specific time instance, t, can be computed with the combination of Eqs 7.10 and 7.12 as

$$\phi(m,n,t) = tan^{-1}\left[\frac{\rho\left(I_{ref+\pi/2},\ I_{def}\right)}{\rho\left(I_{ref},\ \ I_{def}\right)}\right]. \tag{7.13}$$

The computational process to recover $\phi(m,n,t)$, as schematically illustrated in Figure 7.2, utilizes data sets from two phase shifted reference images, I_{ref} and $I_{ref+\pi/2}$, recorded at times t_{ref} and $t_{ref+\pi/2}$ before object excitation and from deformed images, I_{def}, at time instances, t_{def}, during and after object excitation. A temporally estimated DC is subtracted from the intensity values of I_{ref}, $I_{ref+\pi/2}$, and I_{def}, as described in Chapter 10. The DC compensated frames I_{ref} and I_{def} are then used for the evaluation of the correlation coefficient, $\rho\left(I_{ref},\ I_{def}\right)$, at every measurement point on the frame. Assuming that ϕ is constant within a small spatial kernel, the numerical calculation of $\rho\left(I_{ref},\ I_{def}\right)$ is implemented based on a computationally efficient Pearson product-moment Correlation Coefficient (PCC) method [Dobrev et al., 2014c; Dobrev et al., 2013a] that uses sets of intensity values from spatial kernels (e.g., 3×3 pixels) around each measurement point of frames I_{ref} and I_{def}. Analogous procedure is applied to the evaluation of the PCC for $\rho\left(I_{ref+\pi/2},\ I_{def}\right)$. By pointwise substituting $\rho\left(I_{ref},\ I_{def}\right)$ and $\rho\left(I_{ref+\pi/2},\ I_{def}\right)$ into Eq. 7.13, $\phi(m,n,t)$ is computed modulus 2π, requiring further processing to obtain a continuous phase distribution by application of spatial or temporal phase unwrapping algorithms, Section 10.5.

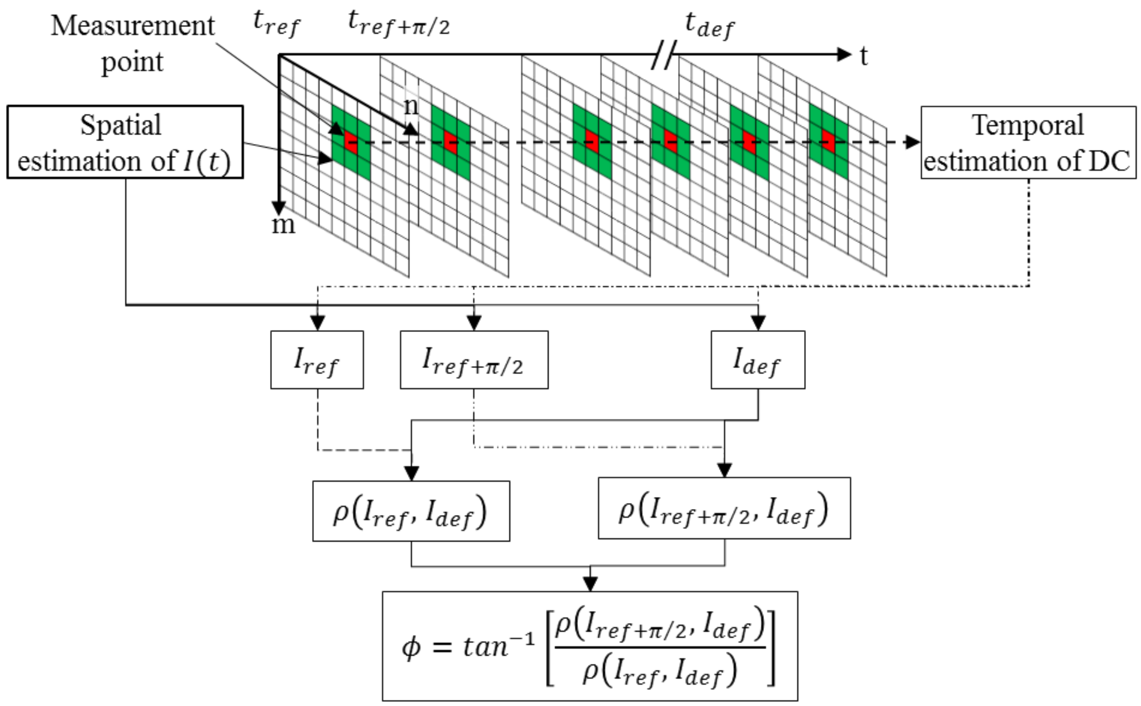

Fig. 7.2. Flowchart illustrating the pointwise implementation of the 2+1 frame local correlation phase sampling (method to recover the phase change, $\phi(m,n,t)$, corresponding to transient deformations of an object. The correlation coefficient, ρ, at a measurement point between any two consecutive frames is based on the evaluation of intensities defined by a kernel within the proximity of the measurement point.

The pointwise evaluation of the correlation coefficients assume that ϕ is spatially varying slower than all of the other parameters in Eqs 7.7 and 7.8 and it is sufficiently constant within a small kernel [Schmitt and Hunt, 1997; Georgas and Schajer, 2012]. This assumption is adequate for the acoustically induced response of the human TM under typical loading conditions since the resulting fringe density, corresponding to the TM's deformation, is small (< 4 fringes/mm) [Furlong et al., 2009] compared to the spatial resolution (>25 lines/mm) of a typical high-speed camera [Dobrev et al., 2013a]. Kernel sizes as small as 2×2 pixels have been reported; however, based on experimental observations, kernel sizes of 5×5 to 9×9 are typically used [Dobrev et al., 2013a].

Experimental validation of the accuracy of Eq. 7.13 versus conventional 4-frame temporal phase sampling methods [Rosowski et al., 2012] is presented in Chapter 12.

8 Control and synchronization of high-speed image acquisition

Implementation of the single frame phase sampling methods, described in Chapter 7, for quantification of the acoustically induced transient events in the human middle-ear, relies on the precise control and synchronization between the excitation, illumination and image acquisition. This requires the development and implementation of automatic control and synchronization of high-speed image acquisition methods.

This Chapter describes the development and implementation of two sets of acquisition and control methods. A multi-pulsed double exposure (MPDE) acquisition method have been developed in order to allow for the use of the DESPS method, Section 7.1, for transient measurements of the human middle-ear. The implementation of the MPDE acquisition method allows for high-temporal resolution (i.e., <20 μs) and an equivalent sampling rate of > 50 kfps, by using a conventional speed (i.e., <20 fps) camera. A high-speed 2+N frame (HS 2+N) acquisition method based on the 2+1 LCPS method, Section 7.2, have been developed and implemented for use with high-speed (i.e., >40 kfps) cameras.

While the two acquisition methods utilize different camera types and phase sampling algorithms, both share common control and synchronization procedures as well as equivalent hardware modules, making them modular and customizable. The combination of both acquisition methods expands the range of applications of the HHS to all major camera types.

8.1 Multi-pulsed double exposure acquisition and control methods

This Section describes the development and implementation a multi-pulsed double exposure (MPDE) acquisition method, based on the double exposure spatial phase sampling (DESPS) method described in Section 7.1. The MPDE allows the full-field quantification of the transient (i.e., >10 kHz) acoustically induced response of the human TM using a conventional camera (i.e., <20 fps).

8.1.1 Design goals and assumptions

A major design goal is incorporation of transient measuring capabilities to an existing DHS [Rosowski et al. 2012], while making minimum hardware modifications [Pedrini et al., 2006; Pedrini et al., 1997; Wåhlin et al., 1994]. To fulfill this goal, it is assumed that the acoustically induced transient displacement response of the TM is sufficiently repetitive. This means that the response of the human TM can be represented by several individual pulsed displacement measurements at different time instances by applying the same transient acoustic excitation. It is also assumed that the particular transient acoustic excitation can be reproduced with sufficient repeatability.

The assumption for repetitive transient response of the TM is supported by previous measurements of nanometer scale displacements induced by steady state acoustic excitation [Rosowski et al. 2012; De Greef et al., 2014; Tonndorf and Khanna, 1972]. Such measurements indicate that, even at high (i.e., >100 dB) sound pressure levels (SPL), the displacements of the surface of the TM are more than 3 orders of magnitude smaller than typical TM characteristic dimensions [Van der Jeught et al., 2013]. This suggests that the strains within the TM are in the linear regime and have negligible hysteresis [Aernouts and Dirckx, 2012]. Previous experimental work on transient measurements of guinea pig TM by pulsed holographic acquisition [Dancer et al., 1975] suggests sufficient sample repeatability. Experimental validations of these hypotheses, based on both artificial membranes and human TM, are presented in Chapter 12.

8.1.2 Principle of operation

Based on the specified design assumptions and constraints, I propose a multi-pulsed double exposure (MPDE) acquisition method for the acquisition of the full-field acoustically induced transient displacement response of the human TM [Dobrev et al., 2013a].

The MPDE operates by repeatedly applying a pulsed acoustic excitation while sequentially capturing holograms at consecutive time increments throughout the duration of the transient response of the TM. The MPDE was implemented with minimal modifications to the existing hardware of the HHS including a conventional (<20 fps) camera capable of global shutter, instantaneous readout and capture, as well as sufficient light sensitivity with low readout noise.

The principle of the MPDE, shown in Fig. 8.1, is based on the synchronization of the camera exposure, illumination time, and acoustic excitation in a double exposure mode of acquisition. For the acquisition of a single pair of double exposure holograms, a reference hologram (P_{REF}) is captured at an initial state of deformation, an acoustic excitation is applied, and a deformed hologram (P_{DEF}) is captured after a controlled time delay, as shown in Fig. 8.1a. The temporal resolution of the double exposure pair is constrained by the minimum time between exposures (MTBE) allowed by the camera.

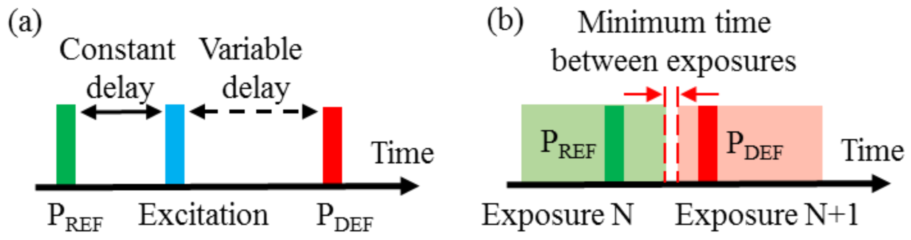

Fig. 8.1. Timing diagrams of the acquisition of a set of double exposure holograms with the MPDE method: (a) synchronization between the reference hologram, acoustic excitation, and deformed hologram; and (b) the minimum time between exposures is achieved by setting the exposure time of the camera to the minimum inter-frame time. Pulsed illumination for the reference state, $P_{REF,}$ is applied at the end of the first camera exposure while a pulsed illumination for the deformed state, P_{DEF}, is applied at the beginning of the second exposure.

By utilizing the simultaneous readout and capture capability of the camera, the MTBE is minimized by setting the exposure time to the minimum inter-frame time, as shown in Fig. 8.1b [AVT, 2013]. Under these conditions the laser illumination is strobed (P_{REF}) once before the end of the first exposure and once (P_{DEF}) at the beginning of the next exposure. The minimum gap between P_{REF} and P_{DEF} achievable with commercially available cameras is in the range of 20 – 200 µs, without any hardware or firmware modifications [AVT, 2013]. The temporal resolution of the method is defined by the strobe length of the illumination pulse of each hologram. For cadaveric human TM samples tested with the HHS, the typical strobe length is less than 15 µs.

Assuming sufficient repeatability of the acoustical response of the TM, we execute the double exposure acquisition multiple times by reapplying the same excitation while recording a new deformed state with a controlled time delay that allows for the capture of slightly different (i.e., < 20 µs) instance of the transient response of the TM in every successive acquisition. A timing diagram of all controlled events of the acquisition and control algorithm of the MPDE is shown in Fig. 8.2.

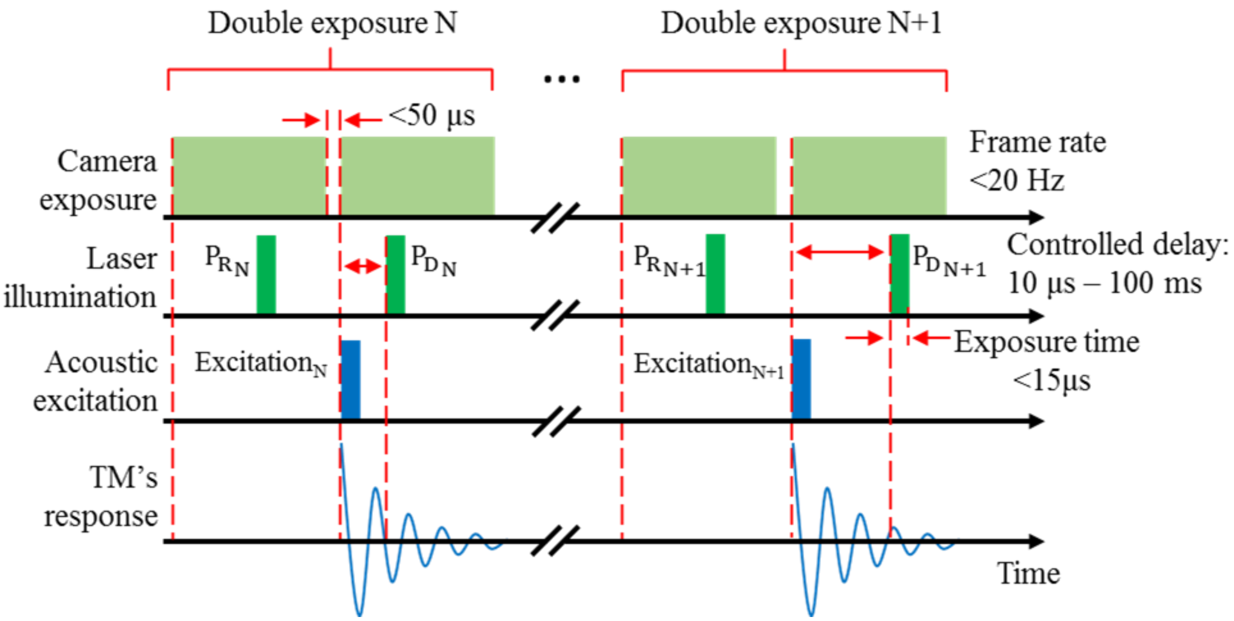

Fig. 8.2. Timing diagram of the control signals of the pulsed double-exposure acquisition method. Representative values of major parameters are indicated. P_R and P_D are the illumination periods

The acquisition method allows for reconstruction of the transient response of the TM by temporal "scanning" through multiple sequential transient pulses and combining the individual full-field-of-view temporal data points into a 3D structure of data representing the time-waveform of every recorded point on the surface of the TM. The maximum practical sampling rate of the MPDE is dependent only on the geometrical repeatability of the transient displacement of the TM and the acoustic excitation. It should be noted that the temporal resolution of the proposed method is independent of the MTBE of the camera, making it independent of type of camera used.

8.1.3 Control architecture

The hardware implementation of the MPDE acquisition, shown in Fig. 8.3, allows synchronization of procedures for acoustic excitation of the sample, pulsed illumination, and frame acquisition. The existing control architecture of the DHS has been improved to allow for the MPDE acquisition with minimal hardware modifications. The improvement relies on the use of the I/O module's digital output component to trigger the execution of all procedures of the MPDE acquisition. The corresponding hardware modification required rewiring only three of the control signal lines and no modification or customization of any components or modules of the control architecture.

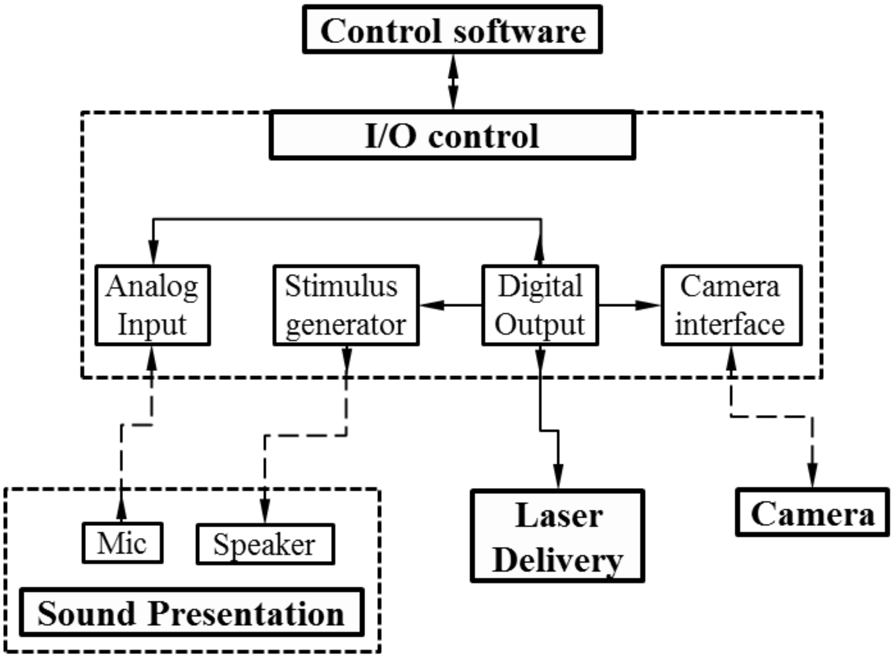

Fig. 8.3. Schematic showing the major modules of the MPDE acquisition hardware and software. The components within the I/O control module communicate with the sound presentation, laser delivery and, and camera modules that are synchronized by the digital output component serving as the master clock.

The software implementation of the MPDE acquisition and control algorithms is presented in Chapter 10. Experimental validation of the repeatability and accuracy of the MPDE acquisition algorithm on human TM samples is presented in Chapter 12.

8.2 High-speed 2+N frame high-speed acquisition method

In order to allow the application of the 2+1 LCPS method (Chapter 7.2) for transient measurements of the human ME, a high-speed 2+N frame (HS 2+N) acquisition method has been developed and implemented.

8.2.1 Principle of operation

In the HS 2+N method, two reference frames, $I_{ref}, I_{ref+\pi/2}$, and N consecutive frames, $(I_{def})_{i,\ \ i\in 1,2..N}$, are recorded before and throughout the evolution of an event. Figure 8.4 shows timing diagrams of the events that occur during the high-speed 2+N acquisition, including camera exposure, acoustic excitation, phase shifting, and TM's response. According to this diagram, the two reference frames, I_{ref} and $I_{ref+\pi/2}$, are recorded with a suitable temporal separation to bypass the PZT settling time after the introduction of the initial $\pi/2$ phase shift [Physik Instrumente, 2014].

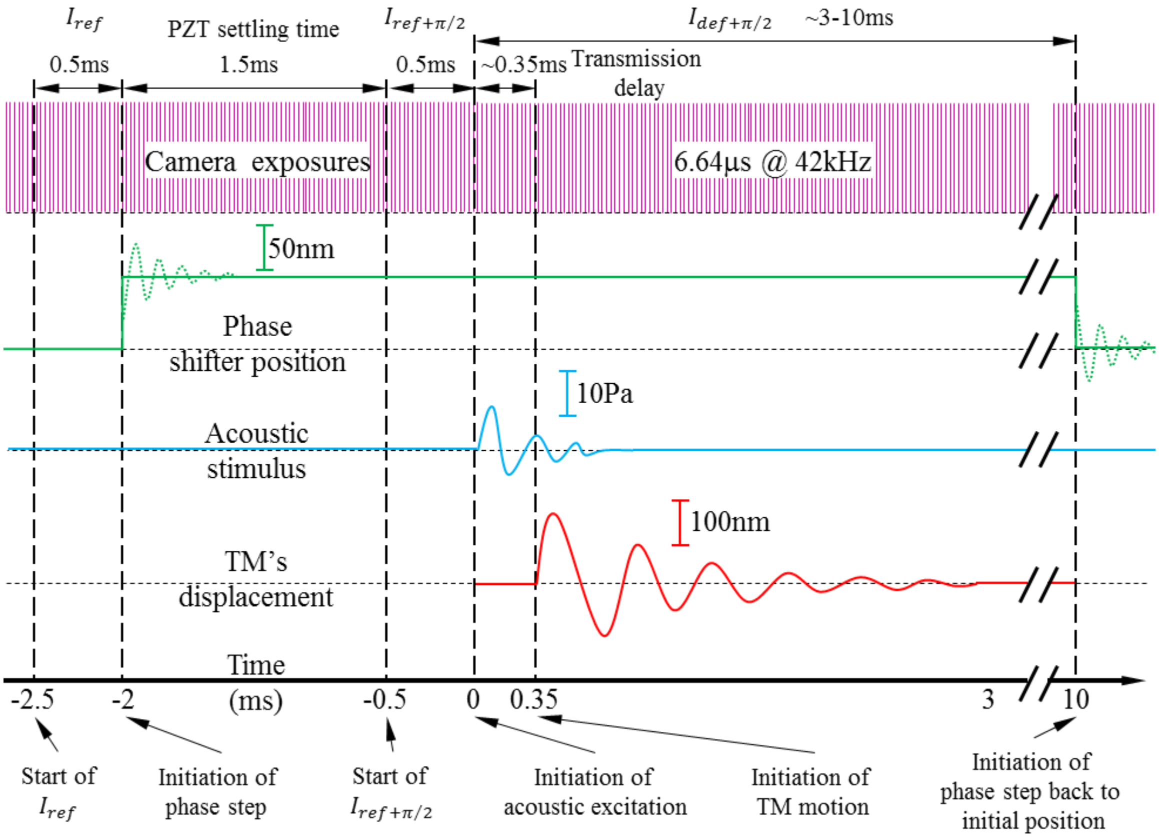

Fig. 8.4. Timing diagrams of the events occurring during the high-speed 2+N frame acquisition (HS 2+N) method. *N* deformed frames are acquired at the maximum frame rate of the camera and referenced relative to two frames captured before acoustic excitation. Acquisition takes into account the settling time of the PZT phase shifter, while minimizing the overall acquisition time. The PZT is returned to its original position at the end of the acquisition. Due to the distance between the sound source and the sample, there is an acoustic transmission delay. Representative values of major parameters are indicated.

For efficient acquisition of an $(I_{def})_i$ frames, the PZT is kept at its final position after phase shifting, which leads to the $(I_{def})_i$ frames containing a constant $\pi/2$ phase offset and expressed as $(I_{def+\pi/2})_i$. Therefore, the optical phase, ϕ, within any $(I_{def+\pi/2})_i$ frame, and corresponding to the deformation of the TM at a specific instance, can be determined from Eq. 7.13 with

$$\phi = tan^{-1}\left[\frac{\rho\left(I_{ref},\ I_{def+\pi/2}\right)}{\rho\left(I_{ref+\pi/2},\ I_{def+\pi/2}\right)}\right]. \tag{8.1}$$

All deformed frames, $(I_{def+\pi/2})_{i,\ i\in 1,2..N}$, before and throughout the evolution of the transient response of the TM, are relative to the same reference frames, I_{ref} and$I_{ref+\pi/2}$, before acoustic excitation.

The camera continuously records frames during the full duration of the measurement, including during the settling time of the PZT, with the maximum sampling rate of acquisition constrained by the frame rate of the camera. During a typical acquisition, multiple frames (i.e., >20 frames @ 42 kfps) at each reference position are captured and temporally averaged in order to compensate for potential external disturbances. In addition, and by confirmation with LDV measurements, 1.5 ms are allocated for settling time of the PZT while discarding the frames recorded over this time.

8.2.2 Control architecture

The hardware implementation of the HS 2+N acquisition method involves the synchronization of the procedures for acoustic excitation of the sample, temporal phase shifting, and frame acquisition. This is achieved by the development and implementation of a control architecture that consists of four major hardware modules that include electronic I/O control (I/O), sound presentation (SP), phase shifter (PS), and HS camera (HSC), as shown in Fig. 8.5 [Dobrev et al., 2014c; Harrington et al., 2010]. Hardware modules are managed by a unified control software with a graphical user interface (GUI) for setting and customizing acquisition and synchronization parameters, as described in Chapter 10.

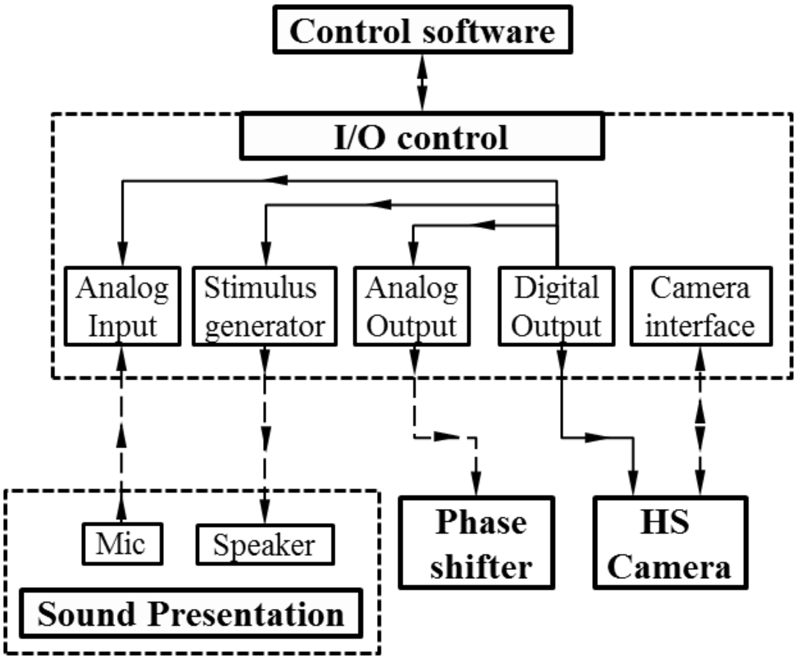

Fig. 8.5. Schematic showing the major modules of the high-speed acquisition hardware and software. The components within the I/O control module communicate with the sound presentation, phase shifter, and HS camera modules that are synchronized by the digital output component serving as the master clock.

By comparing Fig. 8.3 and 8.5, it can be seen that the I/O control modules of both acquisition algorithms, presented in this Chapter are very similar and use identical hardware components as previous DHS [Rosowski et al., 2012]. This allows for rapid reconfiguration between all acquisitions methods, including time-averaged and stroboscopic acquisition of previous DHS, without any major hardware modifications.

The software implementation of the HS 2+N acquisition and control algorithms is presented in Chapter 10 and experimental validation of the repeatability and accuracy of the HS 2+N acquisition algorithm on human TM samples is presented in Chapter 12.

9 Hardware realization

This Chapter describes the design and realization of the hardware for the high-speed holographic system (HHS); specifically of the holographic otoscope head (OH) and the mechatronic otoscope positioner (MOP), which are aimed at extending the capabilities of the HHS for research and *in-vivo* applications.

9.1 Overview of the high-speed holographic system

The hardware realization of the high-speed holographic system (HHS), schematically shown in Fig. 9.1, consists of 6 major modules:

- *Control software (CS)* – provides user control over the parameters of all acquisition modes of the system: time-averaged [Rosowski et. al, 2009], stroboscopic [Cheng et al., 2013], MPDE, Section 8.1, and HS 2+N, Section 8.2.
- *I/O control (I/O)* – controls the synchronization of illumination, excitation, acquisition, and phase stepping, based on the acquisition mode and parameters defined by the control software [Harrington et al., 2010].
- *Laser delivery (LD)* – provides temporal phase stepping, stroboscopic and pulsed illumination, and fiber coupled output capabilities [Flores-Moreno et al., 2011].
- *Sound presentation (SP)* – provides calibrated acoustical excitation and sound pressure level (SPL) measurements for both steady state and transient measurements [Bapat, 2011].

- *Optical setup (OS)* – incorporates an off-axis lensless holographic optical setup and a digital camera allowing for rapid holographic recording. Laser illumination to the optical setup is provided by the LD module.
- *Otoscope head (OH)* – a compact and ergonomic package for the OS and SP [Dobrev et al. 2012].
- *Mechatronic otoscope positioner (MOP)* – assists the examiner during positioning of the OH and provides autonomous support of the OH during measurements [Dobrev et al., 2013b].

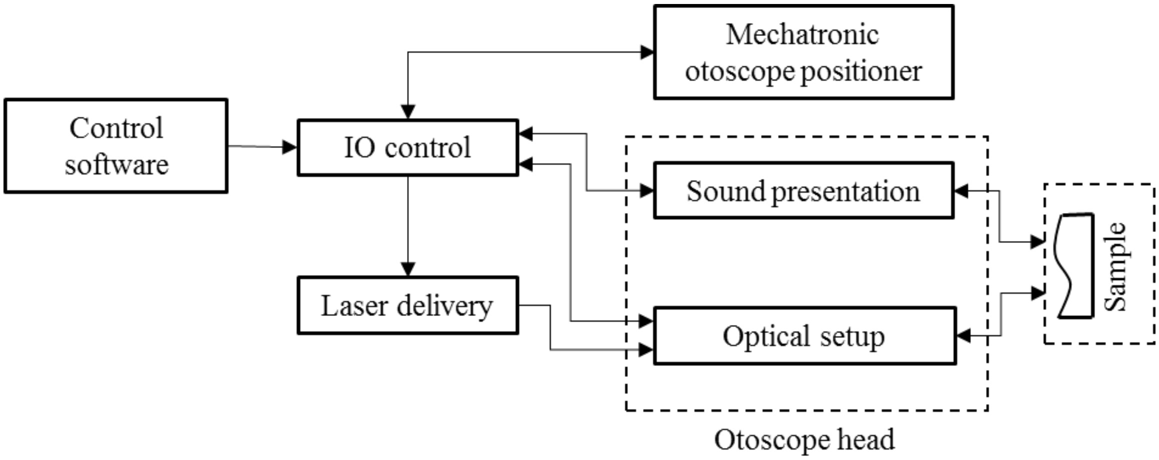

Fig. 9.1. Block diagram of the hardware components of the high-speed holographic system (HHS) consisting of six major modules: control software (CS), I/O control (I/O), laser delivery (LD), sound presentation (SP), optical setup (OS), and a mechatronic otoscope positioner (MOP).

A high-speed holographic system (HHS) has been designed and implemented, such that it minimizes hardware modifications and cost, by utilizing components and modules from previously developed digital holographic system (DHS) [Rosowski et al., 2013a], such as the SP [Bapat, 2011] and LD [Flores-Moreno et al., 2011] modules. Improvement of the I/O [Furlong et al., 2009] and CS [Harrington et al., 2011] modules, based on previous DHS designs and enhanced in the HHS, are discussed in Chapters 8 and 10 respectively.

This Chapter focuses on the design and hardware realization of the MOP and OH modules and their implementation within the full HHS. The Chapter also provides an overview of the full system realization of the HHS for MPDE and HS 2+N acquisition modes.

9.2 Otoscope head (OH)

This Section describes the improvement of a lensless digital holography optical setup (OS) and its realization within a compact otoscope head (OH), to allow *in-vivo* applications with the HHS. The OH design is an improvement of previous optical designs implemented for *in-vitro* measurements [Flores-Moreno et al., 2011]. The design and realization of the new OH includes the implementation of double-exposure spatial phase sampling (DESPS) methods, Chapter 7, while accounting for design constraints imposed by the Fresnel transform reconstruction methods, Chapter 5, as well as anthropometrics of the human ear, Chapter 3.

9.2.1 Optical setup improvement

In order to realize an OH that can be used for *in-vivo* applications, the footprint of the optical setup (OS) needs to be minimized while maintaining the field-of-view (FOV), minimum working distance (WD), and minimum depth of focus (DOF), as specified in Chapter 3. Figure 9.2 shows a schematic of the OS, indicating the major parameters that define its footprint. By utilizing a lensless Fourier transform holographic OS, Chapter 7, the OH design avoids the use of magnifying optics or complex focusing mechanisms, which help define a compact OS with sufficient depth of focus (DOF).

In Fig. 9.2, points A' and B' are the outermost points on the object, while points A and B are the outermost points on the camera sensor relative to the optical axis OO'. Point P is the point source of the reference beam located at a distance r and angle α from OO'.

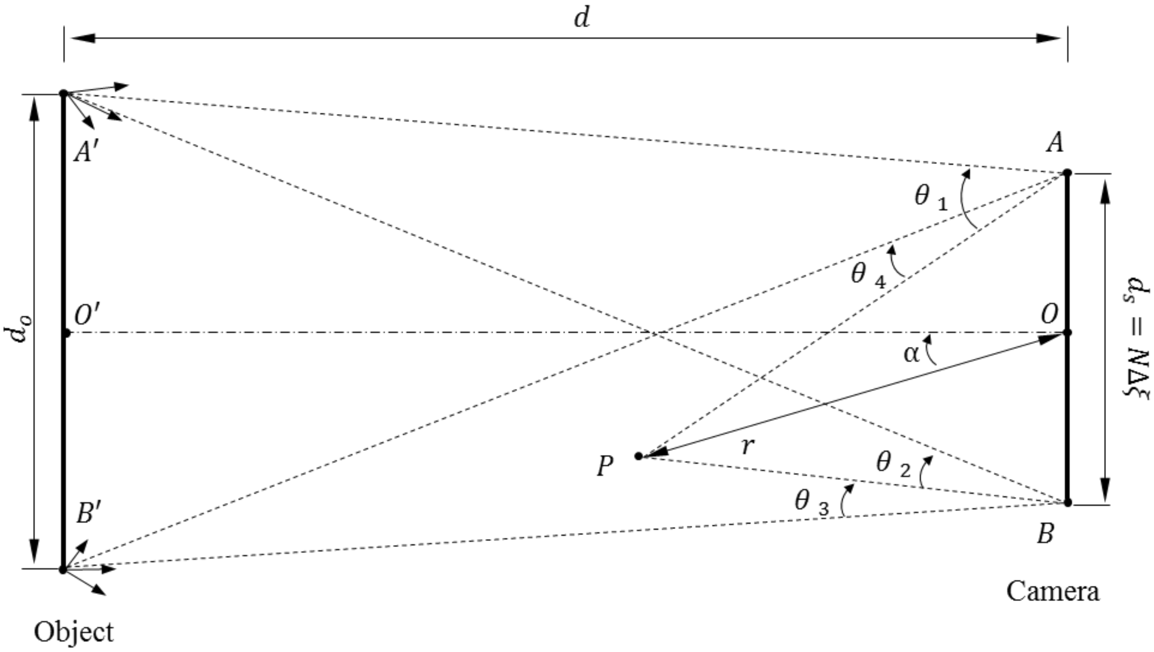

Fig. 9.2. Schematic of the off-axis lensless Fourier transform holographic geometry showing the major optical parameters used in the improvement of the OH to minimize its footprint. Indicated are object size, d_o, the sensor size, d_s, working distance (WD), d, and the position of the point source, P, of the reference beam.

The improvement of the optical setup was done in two stages. In the first stage, the reference beam angle and the working distance were determined to allow for sufficient FOV and minimum WD for the DESPS method, Chapter 7. In the second stage, the distance of the reference beam to the camera was minimized while maintaining the spatial frequency content (Chapter 6) of the recorded hologram within the maximum resolvable spatial frequency of the camera.

9.2.1.1 Working distance and reference beam angle

In the first stage of the improvement, the reference beam angle and the working distance were determined based on the technological constraints imposed by the spatial resolution of the camera and by the minimum working distance of the holographic reconstruction algorithm, respectively.

Reference beam angle

The DESPS method, Chapter 7, requires the introduction of a spatial carrier frequency in the hologram, which is done by introduction of a relative angle, α, between the reference and reflected object wavefront. The technological constraints related to the spatial resolution of the camera define the maximum resolvable spatial resolution, f_{max}, corresponding to a maximum resolvable angle, θ_{max}, with

$$\theta_{max} < f_{max}\lambda = \frac{\lambda}{2\Delta\xi}. \tag{9.1}$$

For a digital camera (AVT Pike F-505B) with 3.45μm pixel size illuminated by 532nm wavelength light, the maximum sampling frequency is in the order of 150 lines/mm, resulting a maximum resolvable angle of 4.4°. However, the spatial frequency content of the object beam is symmetrically centered on a carrier frequency, which means that the maximum of its frequency range is higher than the carrier frequency, as shown in Fig. 7.2. In order to maintain the spatial frequency content of the object within the capabilities of the camera, the optimum carrier frequency is achieved at approximately half of f_{max} [Saldner et al., 1996]. This means the optimal value for the angle α, between the reference and object beams is approximately 2.2° for a 3.45μm pixel size sensor. In order to allow for larger range of applications, and corresponding FOV and WD, the optical setup of OH allows for adjustment of α in the range of 0° to 5°.

Working distance

The minimum working is defined based on constraints imposed by the Fresnel transform and the Fresnel approximation, Chapter 5, as well as by the FOV requirements of the DESPS method, as described in Chapter 7. According to Eq. 5.26, the minimum working distance, for the application of the Fresnel approximation in the Fresnel transform, can be defined through the geometrical parameters of the optical system of the OH with

$$d_{min} = \sqrt[3]{\frac{\pi}{64\lambda}[d_o + d_s]^4}\,. \tag{9.2}$$

By assuming object size, d_o = 8 mm, sensor size d_s = 7 mm, and wavelength, λ = 532 nm, the minimum working distance for application of the Fresnel approximation is d_{min} = 75 mm, while the minimum working distance for application of the Fresnel transform without the Fresnel approximation is given by [Yaroslavsky et al., 2004]

$$d_{min} = \frac{d_o \Delta\xi}{\lambda}\,. \tag{9.3}$$

In this case, by assuming object size, d_o = 8 mm, and wavelength, λ = 532 nm, and pixel size $\Delta\xi$ = 3.45μm, the minimum working distance for application for the Fresnel transform is d_{min} = 52 mm.

The FOV of the DESPS method is defined by the size of reconstructed object, d_{image}, in the image plane, which can be estimated with Eq. 7.5. The required working distance, d, for a particular image size d_{image} is therefore

$$d = \frac{d_o d_s \Delta\xi}{d_{image}\lambda}. \tag{9.4}$$

By assuming that the object image should occupy only ¼ of the area (1/2 of the size) of the sensor to avoid overlap [Saldner et al., 1996] with the twin image, an optimal image size $d_{image} = d_s/2$ corresponds to an optimal working distance of

$$d_{optimal} = \frac{2d_o \Delta\xi}{\lambda}. \tag{9.5}$$

By assuming d_o = 8 mm, wavelength, λ = 532 nm, and pixel size $\Delta\xi$ = 3.45μm, an optimal working distance, $d_{optimal}$, is 104mm. Based on Eqs 9.2-9.5, the working distance, d, between the object and camera sensor was chosen to be 104mm.

9.2.1.2 Reference beam distance

In the second stage of the improvement, distance between the reference beam and the sensor was determined based on constraints related to the spatial frequency content in the hologram. In a conventional lensless Fourier transform holographic setup, Section 5.3.3, the point source, *P*, of the reference beam is close to the object plane, which results in an optical configuration that, because of the resultant dimensions, may have limited applications for *in-vivo* measurements. Therefore, an analysis is performed to quantify the optimal range for distance r, based on the schematic shown in Fig. 9.2 with details presented in Appendix A and with the following assumptions:

- Object size d_o is larger than sensor size d_s.
- Working distance is much larger than d_o or d_s.
- Reference to sensor distance, r, is much larger than d_o or d_s.
- Distance r is smaller than d.
- Angle α is small, thus the distance from P to OO' is considered smaller than BO.
- For a diffuse object, every surface point can be considered an individual point source with a spherical wavefront.

The last assumption implies that every point on the object contributes to the interference pattern of every point on the imaging plane (camera plane). Based on this assumption, the spatial frequency representation of object point A' on the sensor position A is defined by the angle θ_1, formed by the object wave ray $A'A$ and reference wave ray PA. This means that the contribution of A' to the spatial frequency content on any point on the sensor is defined by the range of angles (θ_1, θ_2). Based on Fig. 9.2, it can be observed that (θ_1, θ_2) is a function of all optical parameters including the reference beam distance, r. For example, as r decreases, the range of angles (θ_1, θ_2) increases, resulting in higher spatial frequency content across the sensor.

In order to minimize r, while keeping the range of spatial frequencies within the spatial resolution of the camera, the spatial frequency contribution of all points on the object is quantified. This is achieved by only considering the spatial frequency contribution of object points A' and B' on sensor points A and B, as they define a range of angles, $(\theta_1, \theta_2, \theta_3, \theta_4)$, that correspond to the maximum and minimum spatial frequency of any point on the sensor. Therefore, the range of possible values for r is determined by relating each of the angles, $(\theta_1, \theta_2, \theta_3, \theta_4)$, to the maximum resolvable angle, θ_{max}, defined by Eq. 9.1.

Based on Fig. 9.2., it can be seen that angle θ_1 is the maximum of the range (θ_1, θ_2), and it can be calculated with

$$\theta_1 \cong \frac{d_o - d_s}{2d} + \frac{d_s}{2r} + \alpha \, . \tag{9.6}$$

In addition, assuming that angle $\theta_1 < \theta_{max}$, the spatial frequency contribution of point *A'* can be adequately sampled by any sensor point. Based on this assumption and using Eqs 9.1 and 9.6, it is obtained that

$$\frac{d_s}{2\left(\theta_{max} - \alpha - \frac{d_o - d_s}{2d}\right)} < r \, , \tag{9.7}$$

which defines a lower bound for the selection of r. According to Eq. 9.7 and assuming $d_o = 8$ mm, $d_s = 7$ mm, $\alpha = 2.2°$ and $d = 104$ mm, results in $r > 95$ mm, which sets the location of P near the object plane. Similar to Eq. 9.7, while assuming that $\theta_2 < \theta_{max}$, it is obtained that

$$\frac{d_s}{2\left(\frac{d_o + d_s}{2d} + \alpha - \theta_{max}\right)} > r \, , \tag{9.8}$$

which defines a upper bound for the selection of r. Using the same optical parameters as before, Eq. 9.8 results in $r < 106$ mm. This constrain holds as long as r is long enough to cross BA', or approximately $r > 20$ mm. Since θ_2 represents the minimum of the range (θ_1, θ_2), Eq. 9.8 defines a condition where *A'* is adequately sampled by only one sensor point. In practical applications, adequate sampling of the frequency content of each object point with only parts of the sensor is sufficient. This means that *r* can be smaller than the lower bound defined by Eq. 9.7.

To further explore the range of values for *r*, constraints based on angles θ_3 and θ_4 can be formulated analytically by analogy with Eqs 9.7 and 9.8. A range for *r* based on angle θ_3 can be expressed as

$$\frac{d_s}{2\left(\theta_{max} + \alpha - \frac{d_o - d_s}{2d}\right)} < r\,. \tag{9.9}$$

Based on the same optical parameter values as with the above example, Eq. 9.9 results in *r* > 33 mm. Analogously, a range for *r* based on angle θ_4 can be expressed as:

$$\frac{d_s}{2\left(\theta_{max} - \alpha + \frac{d_o + d_s}{2d}\right)} < r\,. \tag{9.10}$$

Based on the same optical parameter values as with the above example, Eq. 9.10 results in *r* > 30 mm. Based on Eqs 9.8 - 9.10, the range of possible values for *r* is defined as:

$$\frac{d_s}{2\left(\frac{d_o + d_s}{2d} + \alpha - \theta_{max}\right)} > r > \frac{d_s}{2\left(\theta_{max} + \alpha - \frac{d_o - d_s}{2d}\right)}\,. \tag{9.11}$$

9.2.2 Miniaturization of the OH assembly

Accounting for all optical constraints defined by Eqs 9.1 - 9.11, an improved lensless Fourier transform holographic setup has been implemented, as shown in Fig. 9.3. The setup consists of a camera sensor, object and reference beams delivered through two fiber optic cables from a laser illumination system, situated externally to the OH [Flores-Moreno et al., 2011]. The reference beam is redirected by a beam splitter cube in order to limit the footprint of the OH in the area in close proximity (i.e., <5 cm) to the human external ear

[Alexander and Laubach, 1968] and shoulders [Burkhard and Sachs, 1975] defining the OH's workspace.

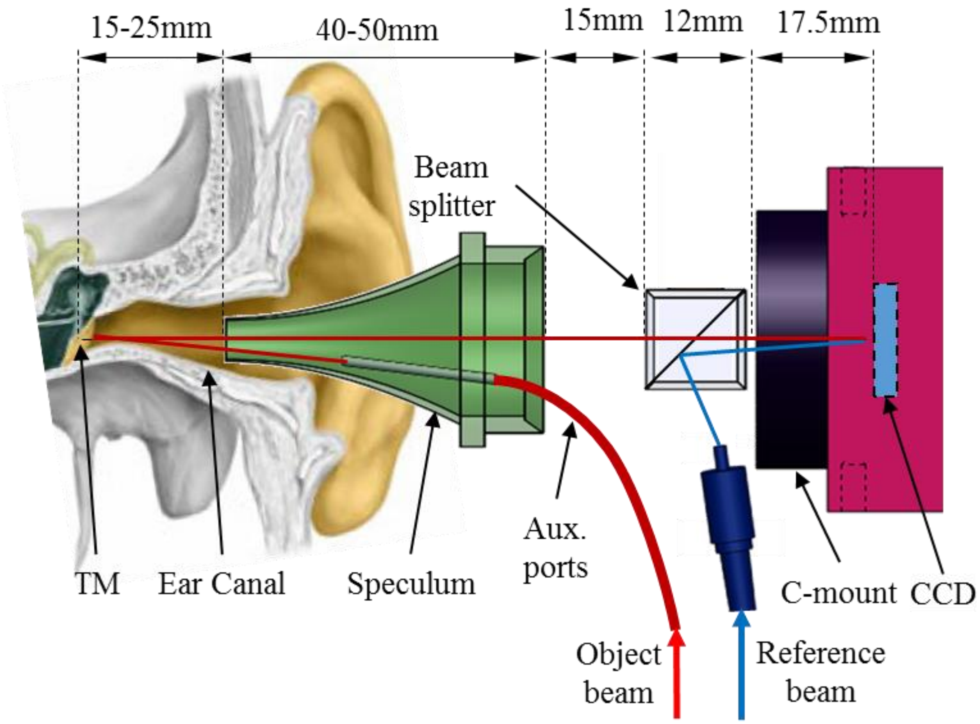

Fig. 9.3. Schematic of the realization of the optical design of the OH and overview of the components that contribute to the overall size and working distance (WD).

In order to minimize the cost of the realization of the OH, several of the components within the OH are based on commercially available parts, such as otoscope speculum, beam splitter and a CCD camera. The fixed size of these components imposes constraints on the packaging and the corresponding minimum WD of the OH. Figure 9.3 shows an overview of the individual components of the OH, with corresponding sizes, that contributes to its overall size.

Based on the anatomical [Stinson and Lawton, 1989] constraints of the ear canal (described in Chapter 3) and corresponding geometry of standard otoscope speculums

[Medscope, 2011], there is a minimal stand-off distance of 55-75 mm between the frontal section of the OH and the TM. Additionally, the OH design has to accommodate for auxiliary access ports to the inside of the speculum, which account for approximately 15mm of the WD. These include ports for optical fibers from the laser delivery (LD) system and acoustical guides for the speaker and microphone from the sound presentation (SP) system [Bapat, 2011]. In order to introduce the reference beam, a beam splitter cube is used with a size of 12.5 mm (0.5 inch). Due to the specific geometry of the standard C-mount attachment at the front of the camera, the sensor is constrained at minimum distance of 17.5 mm away from the back face of the beam splitter. The combination of all these constraints defines the minimum WD, d, within the range of 100-120 mm.

Based on additional constraints related to packaging and manufacturability, the parameters of the optical system within the OH are defined as follows: $d_o = 8$ mm, $d_s = 7$ mm, $\alpha = 2.2°$ and $d = 104$ mm, $r = 50$ mm. The sensor size is based on the AVT Pike F-505B camera allowing for 2048x2048 pixels with 3.45 μm pixel size.

9.2.3 Realization and system integration

Compactness of all subsystems and integration in a modular OH package, as shown in Fig. 9.4, allows for the OH's mobility and usability in clinical and research environment.

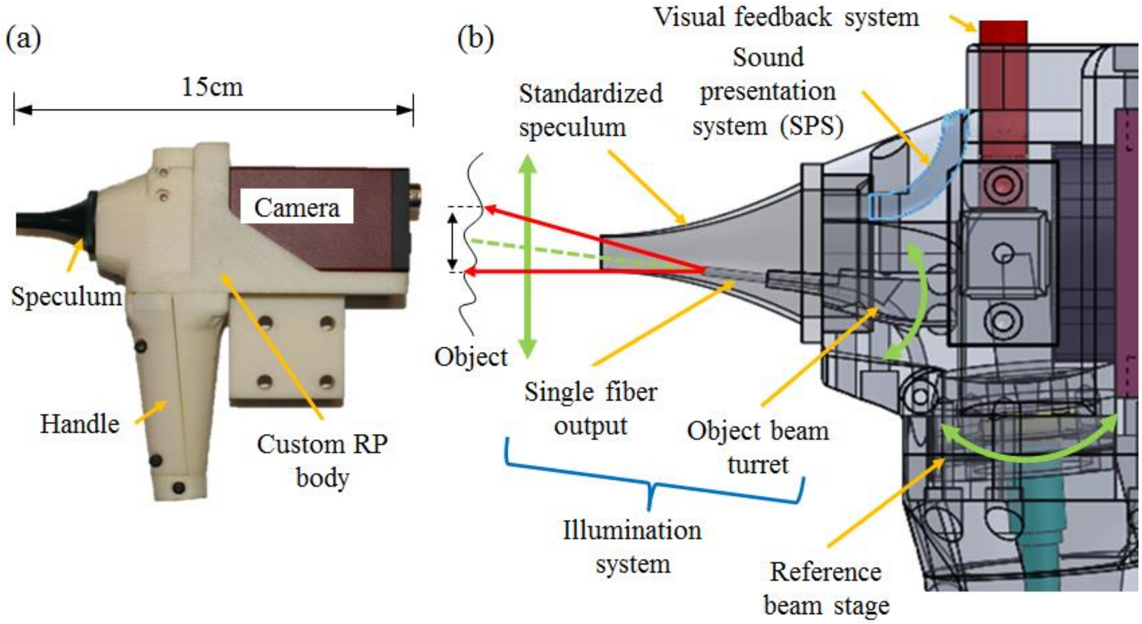

Fig. 9.4. Realization of the OH design enhanced for *in-vivo* measurements: (a) picture of the OH with major components indicated; and (b) CAD model of the internal features and sub-systems of the OH.

Aside from the optical setup module, the OH design integrates several other modules and features enhanced for in-vivo measurements:

- *Sound presentation* (SP) [Bapat, 2011] allows for acoustic measurements [Rosowski et al., 2013b] of the averaged impedance of the ear, via integrated capabilities for controlled sound stimuli and sound pressure measurements.
- *Live color video feedback* allows for standard qualitative ear examinations via build-in miniature (<7 mm diameter) camera (lipstick camera). This system also aids in the navigation of the OH in the ear canal during insertion for *in-vivo* measurements.
- *Reference beam stage* allows for precise control (<0.5° accuracy) of the angle α between the reference beam and the reflected object beam. The stage is based on a

custom semi-spherical joint with a remote center of rotation positioned at the center on the camera censor, accounting for the reflection at the beam splitter. This allows for control over α while preserving optimal illumination distribution of the reference beam across the sensor. The realization of the reference beam stage is crucial for improvement of the DESPS image quality and FOV as well as compensation for possible misalignments related to manufacturing and assembly.

- *Object beam turret* allows for precise control (<0.5 mm accuracy) of the position of the reference beam on the TM in order to reduce reflections from the ear canal walls that could decrease the image quality.

The DH lensless setup reduces constraints on the manufacturing tolerances of the system, allowing for use of customizable rapid prototyping techniques and overall reduction of size compared to previous designs [Flores-Moreno et al., 2011]. This also improves the OH's ergonomics and usability in *in-vivo* conditions by expanding the useful kinematic workspace of the OH around the patient's ears as well as simplifying the examination procedure. The OH design accounts for anthropometrics of the human ear. The range of typical orientations of the auditory canal relative to the head [Todd, 2009] defines the overall workspace of the full OH assembly around the pinna, head and shoulders. The size of the pinna [Alexander and Laubach, 1968] defines the area of the OH assembly in close proximity (i.e., <5 cm) to the ear and the speculum. The position of the external ear relative to the shoulders [Burkhard and Sachs et al., 1975] defines the OH's maximum workspace.

9.3 Mechatronic otoscope positioner (MOP)

The stability of the otoscope head (OH) during measurement is paramount for the quality of the measured data. The Section provides an overview of the design and implementation of the mechatronic otoscope positioner (MOP) module that allows for ease of positioning of the OH to the patient's ear or sample of interest and autonomously maintaining its relative position and orientation during the examination [Dobrev et al., 2010; Dobrev et al., 2013b].

In order to ensure an intrinsically safe positioning system, a novelty control approach [Culmer et. al, 2005] was taken by using only adjustable friction elements [Rondeau, 2010] together with custom haptic feedback control system [Seraji et al., 1994] resulting in a passively-actuated admittance control system [Dobrev et al., 2010]. This design approach renders a positioning system that is as safe as conventional static positioner systems [Dobrev et al., 2013b]. This allows the positioner to be operated in clinical settings without the need for expensive and time consuming testing and certification that is required with similar actively actuated mechanisms.

Two kinematic configurations have been synthesized and implemented based on quantification of the required degrees-of-freedom and the workspace constraints of clinical examination conditions. The first mechatronic otoscope positioner (MOP-1) was developed as a test platform for testing the kinematics and a novel control scheme. The second mechatronic otoscope positioner (MOP-2) was developed to satisfy kinematic and stability requirements for use of the OH in clinical conditions.

9.3.1 Design requirements

The proposed MOP module has several design objectives and functional requirements. A foremost objective is to provide a passively actuated system to facilitate an operator in positioning and holding the OH during measurements in research or clinical settings. The device must augment the operator's hand in creating smooth, natural, and intuitive motions and subsequently maintain a specified position indefinitely until the user repositions the device. Additionally, the control system should not actively position the MOP, rather only constrain and limit the operator's present input. This requirement makes the device inherently safer than a traditional actively actuated manipulator.

9.3.2 MOP-1

A first iteration of the mechatronic otoscope positioner (MOP-1), utilizing a novel control scheme, was developed as a proof-of-concept test platform for the enhancement of the kinematics and control systems [Dobrev et al., 2010]. MOP-1 kinematics allows for full 6 degrees of freedom, orientation and position, of the OH with respect to a patient's ear, as shown in Fig. 9.5. In order to achieve this, the kinematics configuration was chosen based on existent industrial manipulator [Fanuc Robotics, 2007] to ensure sufficient and even dexterity distribution throughout the required workspace. The kinematic configuration is simplified to a three pin joints in series with a spherical (ball) joint at the tip, as shown in Fig. 9.5a.

A custom controller was developed and implemented to allow for tip position and/or velocity control and haptic feedback [Dobrev et al., 2010]. Custom position and force feedback electronics has been developed and implemented within structure of the MOP-1, as shown in Fig. 9.5b.

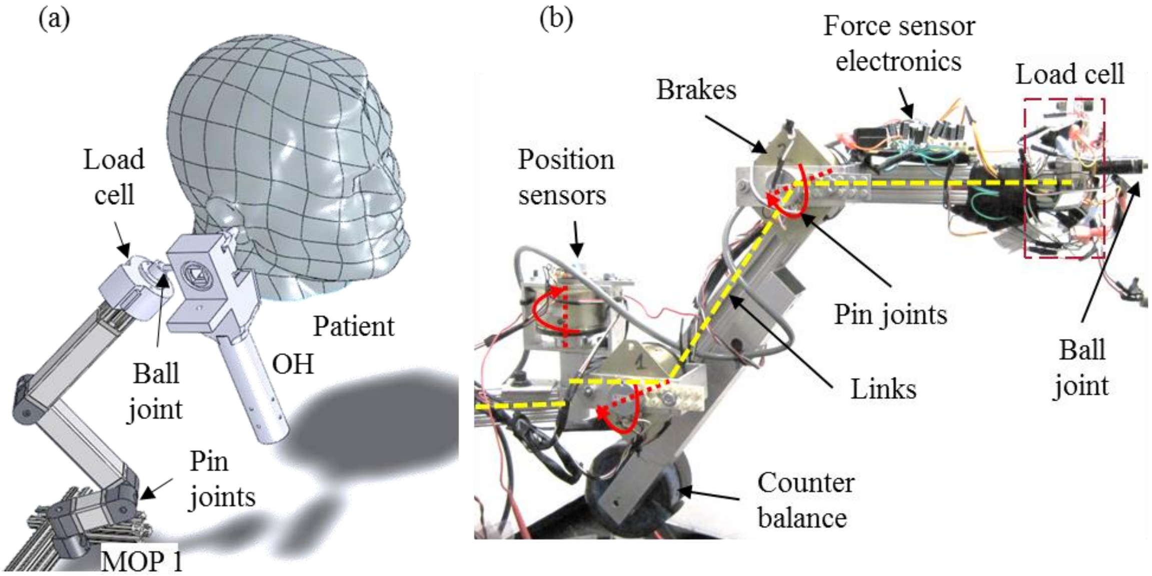

Fig. 9.5. Kinematic configuration and realization of MOP-1: (a) CAD model of the kinematic configuration and the examination setup for *in-vivo* measurements with the OH; and (b) hardware realization including brakes and position sensors at each joint; and force sensor (load cell) composed of 3 full strain gage bridges configured to provide direct measurement of the individual Cartesian components of the tip force.

9.3.3 MOP-2

The second mechatronic otoscope positioner (MOP-2) was developed to satisfy kinematic and stability requirements for use of the OH in clinical conditions [Dobrev et al., 2013b]. The MOP 2 allows examiner to position the OH in the patient’s ear by intuitively applying a force to the positioner’s control handle. Figure 9.6 shows the workspace, kinematic configuration, and the realization of the MOP-2.

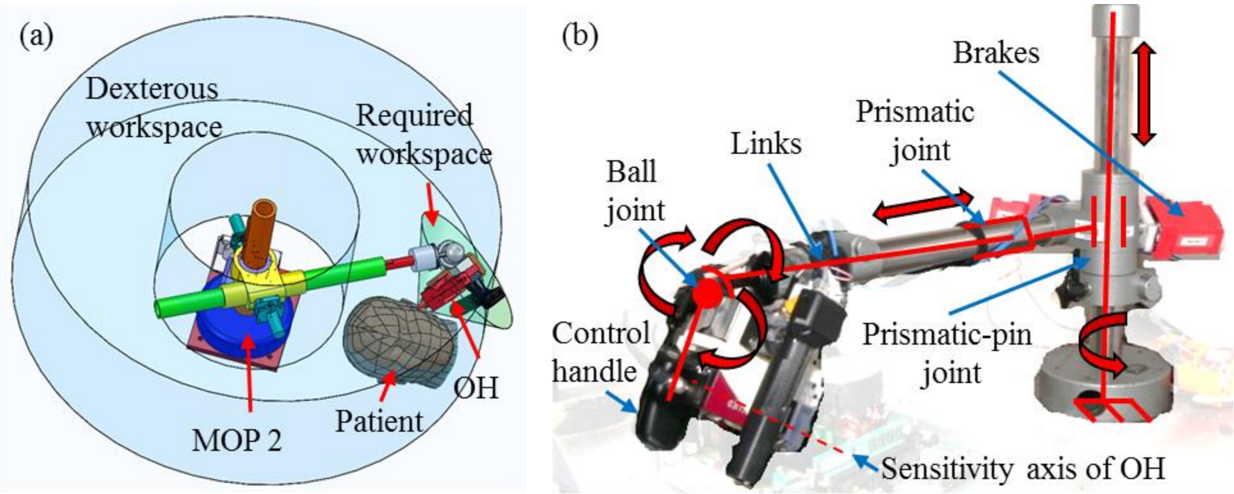

Fig. 9.6. Kinematic configuration and realization of MOP-2: (a) CAD model of the required workspace for one ear and the full workspace of the positioned – generic model of patients head is included for scale; and (b) MOP-2 hardware realization. Kinematic links are highlighted with solid lines.

The required degrees of freedom and workspace to position the otoscope near the patients' ear, as shown in Fig. 9.6a, was synthesized based on measurements and observations of the trajectories of typical otology clinical exams. The MOP-2 hardware realization, as shown in Fig. 9.6b, is based on a commercially available bench-top microscope stand that was enhanced with an adjustable braking system and improved kinematics consisting of 4 links in parallel with a total of 6 degrees of freedom. The 1st and 2nd links are connected by a compound prismatic-pin joint that allows for individual control over the rotation and extension of the 2nd joint, while minimizing the footprint of the MOP-2. The 2nd and 3rd links are connected through a prismatic joint capable for >0.5 m of extension, which allow for reach to both left and right ears without repositioning of the patient. The 3rd and 4th links are connected through a ball joint allowing for ±30° control over the relative angle between the centroid axis of the ear canal, Chapter 3, and the sensitivity axis of the OH, as shown in Fig. 9.6a.

Similar to MOP-1, MOP-2 passively positions the OH, such that it only constrains and guides the user input without applying active actuation, resulting in an inherently safe system. The braking system in the MOP-2 consists of modular base elements connected in a parallel control system that is expandable without significant changes to the existing hardware of the MOP-2. This allows for the application of the control system to a variety of existing passive medical positioners, thus expanding the possibilities for implementation of the HHS in various clinical settings.

9.4 Realization of the full HHS system

Two models of the high-speed holographic system (HHS) have been designed and implemented. A pulsed HHS (PHHS) has been implemented for research and clinical applications, including *in-vivo*, focused on the steady state and transient response of the middle ear (ME). The PHHS has been realized as an upgrade to an existing digital holographic system (DHS) with the addition of the OH and MOP. A continuous HSS (CHHS), based on the HS 2+N method and a high-speed camera, has been implemented with a focus on research applications related to the transient response of the middle ear.

9.4.1 Pulsed high-speed holographic system (PHHS)

The pulsed high-speed holographic system (PHHS), shown in Fig. 9.7, incorporates the OH and the MOP-2 and is capable of time-averaged, stroboscopic and MPDE measurements for study of the motion of the middle-ear under steady state and transient excitation. The PHHS has already been deployed in medical research conditions, where it has been used in steady state [Rosowski et al., 2013a], transient [Dobrev et al. 2014c] and *in-vivo* [Dobrev et al. 2014a] applications.

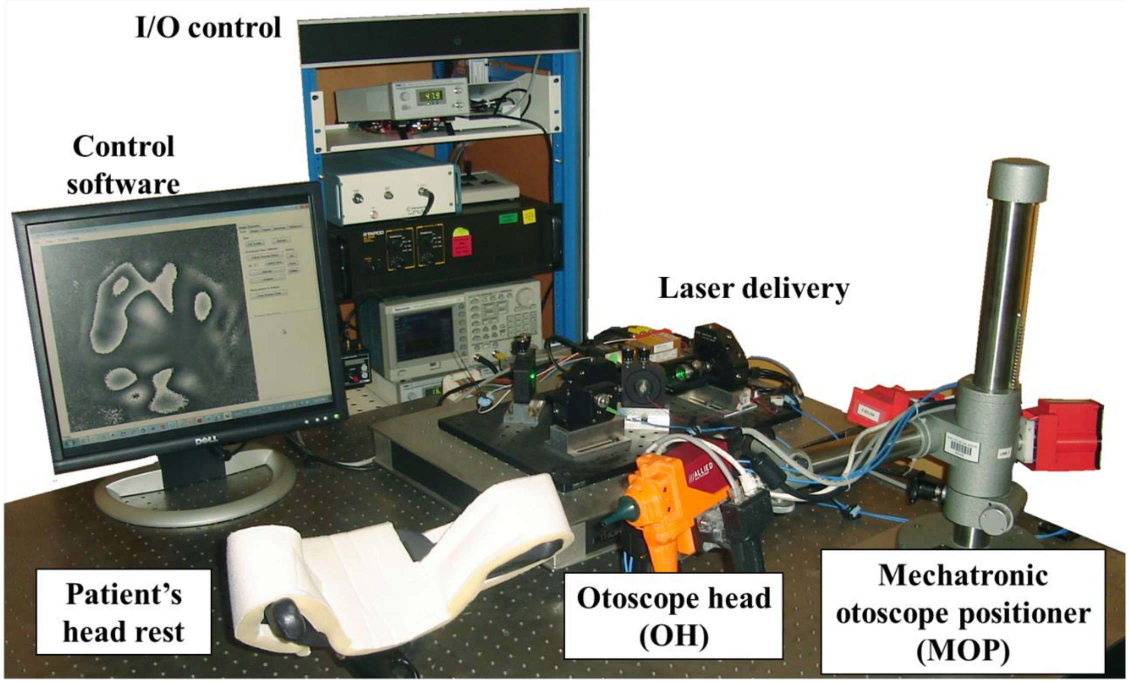

Fig. 9.7. Hardware realization of the pulsed high-speed holographic system (PHHS).

In order to minimize hardware costs and complexity, the PHHS has been realized as an upgrade to a previously developed digital holographic system (DHS) [Flores-Moreno et al. 2011]. The implementation of the PHHS utilized and upgraded [Dobrev et al. 2014b] the existing laser delivery, I/O and control software modules, and added the OH [Dobrev et al. 2012] and MOP 2 [Dobrev et al., 2010] modules to enable MPDE based transient measurement capabilities as well as for clinical use.

9.4.2 Continuous high-speed holographic system (CHHS)

The continuous high-speed holographic system (CHHS) has been implemented with a focus on research applications related to the transient response of the middle-ear, and it has already been applied in medical research conditions for measurements of the transient response of human TM samples [Dobrev et al., 2015]. The CHHS setup, as shown in Fig. 9.8, incorporates a custom laser delivery system, an compact optical setup with a high-speed (HS) camera (Photron SA5 1000k), and I/O and software control modules modified for transient HS 2+N acquisition. Improvements of the I/O module are described in Chapters 8, with corresponding software upgrades, Chapter 10. This Section focuses on the hardware development of the laser delivery (LD), sound presentation (SP), and optical setup (OS) of the CHHS, as shown in Fig. 9.8.

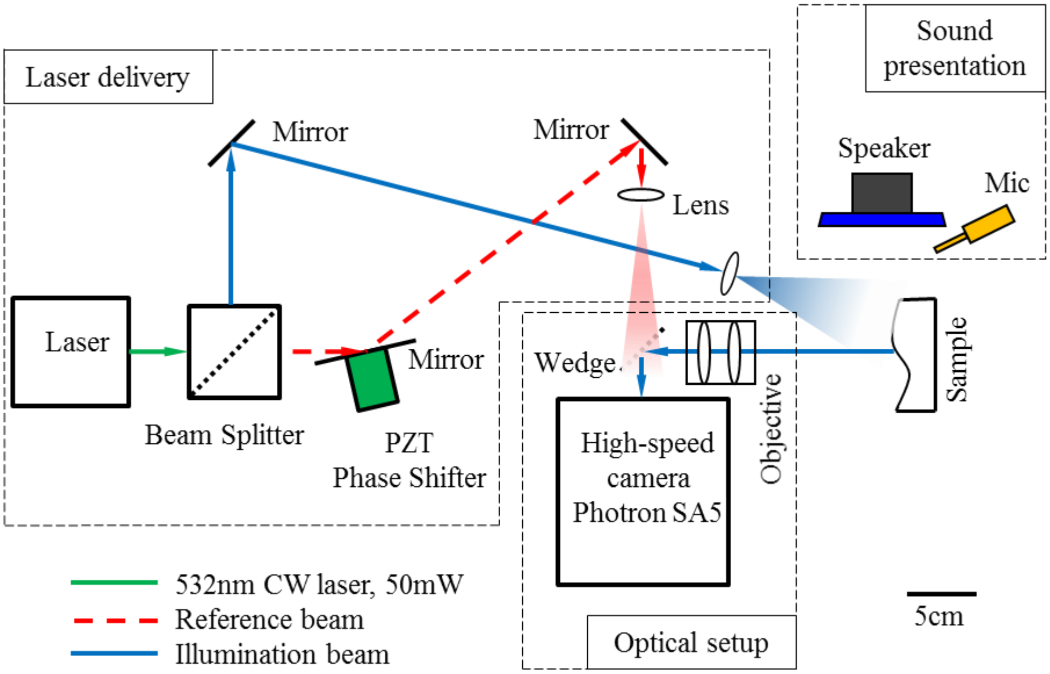

Fig. 9.8. Schematics of the hardware realization of the continuous high-speed holographic system (CHHS). The CHHS consists of sound presentation, laser delivery (LD), and optical setup (OS). The optical setup includes an interferometer, focusing optics (objective), and a high-speed camera (Photron SA5 1000k).

The optical system consist of an objective, beam splitter (wedge) and HS camera. The objective (relay lens JML Optical 41 mm 1016) has 80 mm WD, 1.5 mm DOF, 15 mm maximum FOV and f/4 aperture. The effective (i.e., >60% contrast) spatial resolution of the optical system is >25 lines/mm. In order minimize object light losses, the wedge was specified such that it redirects >95% of the object light at the sensor. The HS camera is based on the Phtoron SA5, which is capable of frame rates in the range of 25-140 kfps at reduced resolutions (i.e., 192^2 - 512^2 pixels) and up to a maximum of 1 Mfps at minimum resolution (i.e., 64×16 pixels), with minimum exposure time of 369 ns. Operation at such frame rates and exposure times requires sufficiently high illumination power in order to allow sufficient amount of light energy per camera exposure. However, a fiber coupled LD module, such as the one in PHHS and DHS, couples <40% of the laser power into the object illumination. This is mainly due to the diffraction efficiency [McCarron et al., 2007] (i.e., 70-90%) of the AOM and the coupling efficiency (i.e., 50-70%) of the fiber couplers [Laferriere et al., 2011]. In order to improve the power efficiency of the object illumination, the PHHS incorporates a custom LD module, as shown in Fig. 9.8, which couples laser light directly into the optical system and the sample without any fiber couplers and fiber optics. The LD does not include an AOM, as the control of the timing of each exposure is handled by the HS camera with an accuracy <100 ns, based on the internal sync clock of the camera. The LD includes a continuous wave (CW) laser (Oxxius SLIM-532, 50mW), variable ratio (1:20-1:4) beam splitter, and a PZT phase shifter. The LD allows for nearly 85% coupling efficiency resulting in >42 mW illumination power at the sample based on a 50 mW laser. This allows for > 2 fold increase in output power compared to the LD module in the PHHS.

10 Numerical methods and software implementation

This Chapter describes the development of numerical methods and corresponding software implementation of a set of procedures, as part of a holographic measurement process (HMP), which allow for manual and/or automated control of the acquisition, processing, and analysis of holographic data.

10.1 Overview of numerical methods for a holographic measurement process (HMP)

The acquisition, processing, and analysis of holographic data require the development and implementation of numerical methods for the realization of a set of procedures that are combined with the holographic measurement process (HMP). The workflow of the HMP can be separated in four major stages with corresponding set of procedures for:

- *Hardware setup and software controls*–adjustment of all hardware and software settings in preparation for a measurement.
- *Acquisition* –control and synchronization of camera frame capture, illumination, excitation and phase-shifting.
- *Processing* – sampling and reconstruction of the double-exposure phase data corresponding to the deformation of the object.
- *Analysis*– conversion from wrapped phase to displacement.

A set of numerical methods, implemented as software procedures, has been developed for every stage of the holographic measurement process (HMP), as shown in Fig. 10.1.

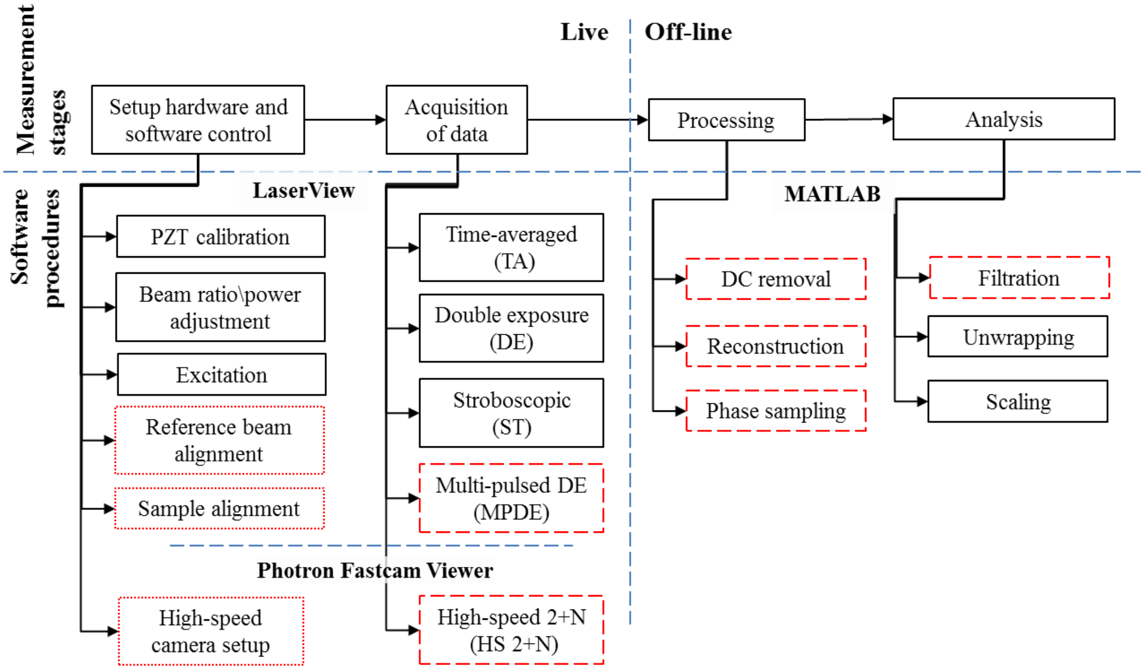

Fig. 10.1. Overview of the numerical methods that have been developed and implemented as software procedures to control and execute the main stages of a holographic measurement processes (HMP). The procedures that have been newly developed and implemented within this Dissertation are highlighted in dashed lines. Procedures that have been developed within this Dissertation, but are based on existing implementations [Harrington et al., 2011], are highlighted in dotted lines. Existing procedures [Furlong et al., 2009] are highlighted in solid lines.

The individual procedures are separated in two major categories, live and off-line, based on the time span of the particular procedure relative to the time span of the measured events. A procedure is considered live if it can be executed with >1 Hz rate and/or within less than 10s of the start of the measurement and can be handled automatically. This categorization also dictates the software implementation strategy for each HMP stage. Execution of live HMP stages is handled within the real-time LaserView software, designed and compiled within the visual C environment [Harrington, et. al, 2011]. Execution of off-line HMP stages is implemented within the

MATLAB scripting language that provides a set of technical computing libraries upon which a library of custom software procedures have been developed. Every numerical method, and corresponding software procedure, that has been newly developed and implemented as part of this Dissertation is highlighted in dashed lines in Fig. 10.1.

10.2 Hardware and software setup procedures

The hardware and software setup stage of the HMP is aimed at adjustment of all system modules and corresponding components for a particular measurement or a routine calibration/adjustment of the system. This hardware and software setup stage consists of procedures for:

- *PZT calibration* – automatic quantification of the PZT phase shift amount (in Volts) based on 5-frame temporal phase stepping algorithm [Dobrev, et al., 2009].
- *Beam ratio adjustment* - automatic measurement of the object-reference beam ratio in the interferometer and illumination modules [Harrington et al. 2010].
- *Excitation* – provides control over the excitation signal level, frequency, type (i.e., sine, pulse, chirp, etc.) and phase (delay), Chapter 8.
- *Reference beam alignment* - provides live visual feedback (2D FFT) and software adjustment capabilities to assist during the alignment of the reference beam (RB) for the improvement of the spatial phase sampling (SPS) method incorporated within the OH of the PHHS, Chapter 9.

- *Sample alignment* – provides rapid visual feedback for improved dexterity during sample manipulation and alignment. The procedure is available for the lensless digital holography reconstruction algorithms within the PHHS, Chapter 7.
- *High-speed camera setup* – allows for establishing connection with the high-speed camera as well as adjustment of major acquisition and synchronization parameters such as readout noise calibration, focus, I/O, triggers, etc., Chapter 8.

Appendix B illustrates the use of the Graphical User Interface (GUI) of the hardware and software setup procedures of the HMP stage implemented within LaserView and PFV.

10.3 Data acquisition procedures

The software implementation of the data acquisition stage of the HMP allows for time-averaged [Rosowski et al., 2009], double-exposure [Rosowski et al., 2013a], stroboscopic [Furlong et al., 2009], MPDE, Section 8.1, and HS 2+N, Section 8.2, acquisition modes. All acquisition modes share a similar control architecture, as shown in Fig. 10.2, where a unified control software governs the execution and synchronization of camera acquisition, laser illumination and phase shifting, excitation, and feedback recording procedures. The camera acquisition procedure adjusts the acquisition settings of the camera before a measurement and saves incoming data from the camera to the computer memory during a measurement. The illumination procedures allow for control over the temporal location and accuracy of the measured data. The phase shifting procedures allow for temporal phase stepping required by 4-frame and 2+1 LCPS phase sampling methods. The excitation procedures allow for control over an acoustical or mechanical source in order to induce controlled deformation of the sample. The feedback recording procedure collects data from acoustical (i.e., microphone), mechanical (i.e., load cell, accelerometer, gyroscope, etc.) or optical (i.e., LDV) sensors for quantification of the excitation or response (i.e., averaged or local) of the sample. In the case of the HHS, the excitation and feedback procedures control the SP hardware module, and the illumination and phase shifting procedures control the LD hardware module.

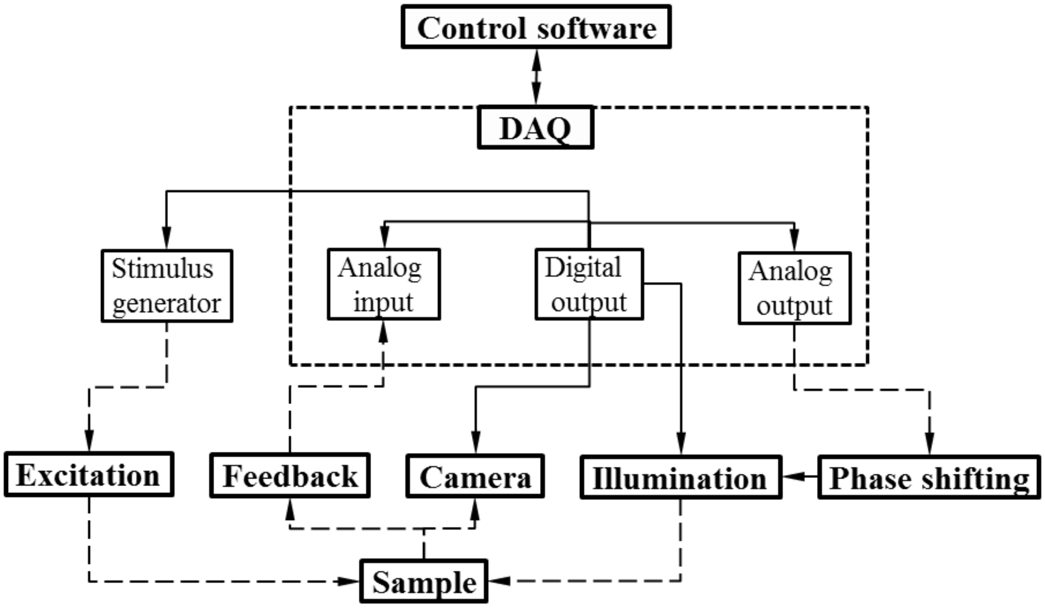

Fig. 10.2. Block diagram of the software and control architecture of the time-averaged, double-exposure, stroboscopic, MPDE, and HS 2+N acquisition modes of the HHS. Each acquisition mode allows for the execution and synchronization of camera acquisition, laser illumination and phase shifting, excitation, and feedback recording procedures for full-filed quantification of the static, steady state or transient response of a sample. The control timing signals are highlighted with solid lines and synchronization between all other modules are highlighted with dashed lines.

The time-averaged, double exposure and stroboscopic acquisition modes and their implementation in LaserView have been explained elsewhere [Harrington et al., 2011]. This Section is focused on the software implementation of the multi-pulsed double exposure (MPDE) and high-speed 2+N frame (HS 2+N) acquisition modes through a unified modular control approach (MCA).

10.3.1 Modular control approach (MCA) for transient acquisition methods

All acquisition modes, for quantification of a steady state or transient events, rely on a master clock that controls the synchronization of all real-time procedures during a measurement procedure. In a time-averaged or stroboscopic [Harrington et al., 2011] mode, the control software utilizes the signal generator component of the I/O module to provide synchronization between the excitation and illumination. However, transient acquisition algorithms, such as the MPDE or HS 2+N, could require the synchronization of multiple events, which imposes constraints on the number of channels of the existing signal generator within the HHS. In order to avoid costly hardware upgrades or development of custom timing electronics, a modular control approach (MCA) has been developed to allow for the control and synchronization of a wide variety of acquisition methods, while minimizing hardware and software modifications. The approach utilizes the capability of current state-of-the-art data acquisition systems (DAQ) for simultaneous output of correlated timing signals (CTSs) across multiple (i.e., >32) digital outputs. This allows for an array of synchronization signals that can control simultaneously multiple devices and processes during a transient acquisition procedure, as shown in Fig. 10.3.

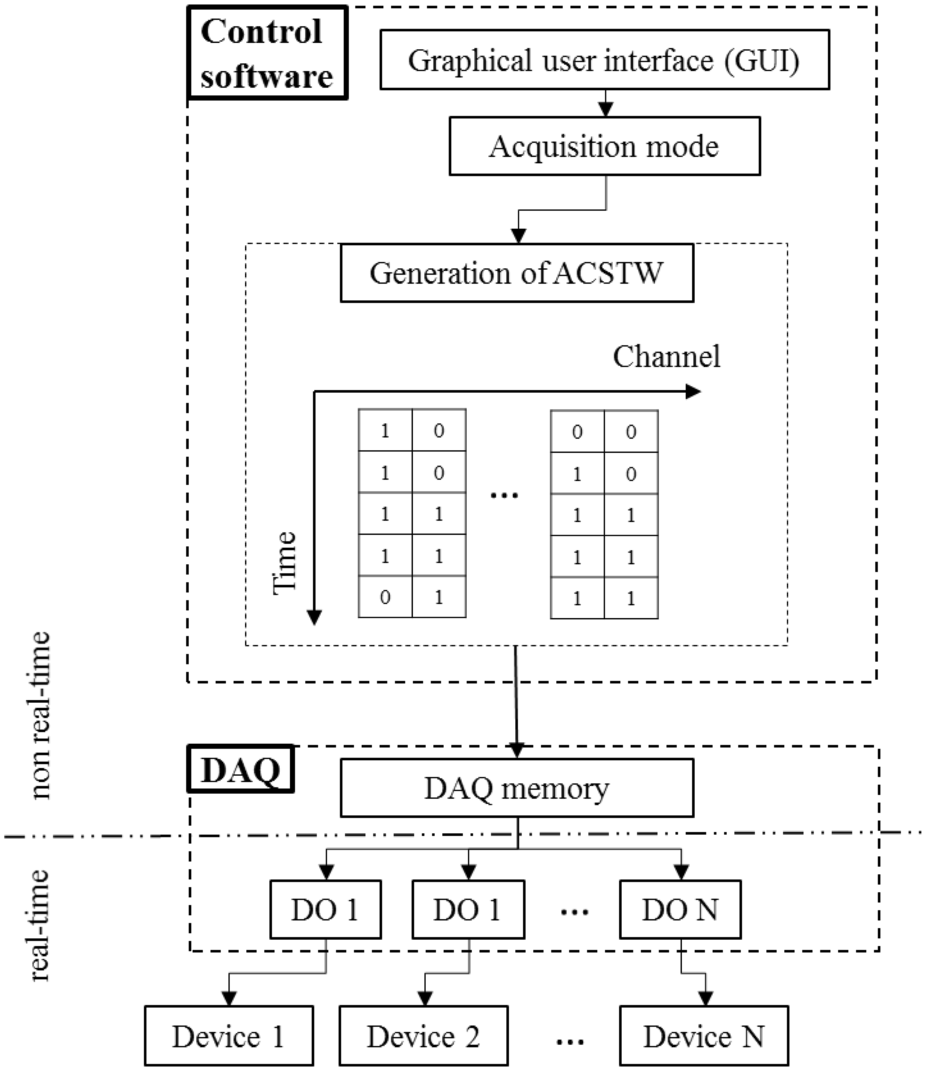

Fig. 10.3. Flow chart of the modular control approach (MCA) for automatic generation and real-time output of arrays of control signal time-waveforms (ACSTW) for the control and synchronization of multiple devices during an acquisition procedure. DO stands for digital output.

The MCA approach works in two stages: a non-real-time stage before and a real-time stage during a measurement. Before a measurement, based on user-defined settings of the acquisition mode, the control software generates an array of control signal time-waveforms (ACSTW), each one corresponding to a particular control signal for a specific device in the measurement system. Each time-waveform is based on a fully customizable binary time code based on a TTL signal. The ACSTW are then loaded into the memory of the DAQ. All operations during this stage are executed in non-real-time under the main control of the general-purpose PC operational system (i.e., Microsoft Windows 7). In the second stage, upon the beginning of the measurement, the full ACSTW is output in parallel through an array of digital outputs as correlated timing signals in real-time under the control of the DAQ's real-time firmware. The temporal accuracy of the ACSTW depends on the internal clock of the DAQ and is typically better than 1 μs. The maximum total temporal duration of the ACSTW depends on the user controllable sampling rate (i.e., 0.1, 10 or 20 MHz) and the size of the DAQ's memory. The DAQ (NI PCI-6259), implemented within the HHS, allows for more than 100 ms of data at sampling rate of 100 kHz across 32 channels simultaneously.

10.3.2 Multi-pulsed double exposure (MPDE) acquisition mode

The multi-pulsed double exposure (MPDE) acquisition mode is based on the MPDE acquisition algorithm, described in Chapter 8. The implementation of the acquisition mode within LaserView allows for user control over the camera acquisition, laser illumination and acoustic excitation through a custom GUI, described in Appendix B.

For implementation of the MPDE acquisition mode, the MCA approach was used to provide user control over 3 CTS that govern the beginning of every pair of camera exposures, the duration and temporal location of each light pulse and the temporal location of the beginning of the excitation.

A CTS controls the camera trigger for the capture of each DE frames pair. Additionally, a minimum time between the exposures (MTBA) is achieved, Chapter 8, by setting the camera exposure time close (varies with camera model) to the inter-frame time, as shown in Fig. 10.4. Since a typical exposure time of the conventional speed camera is much longer (i.e., >50 ms) than the duration of a transient response of the human ME (i.e., <5 ms), the beginning of the camera trigger is adjusted to compensate for the exposure time of the camera.

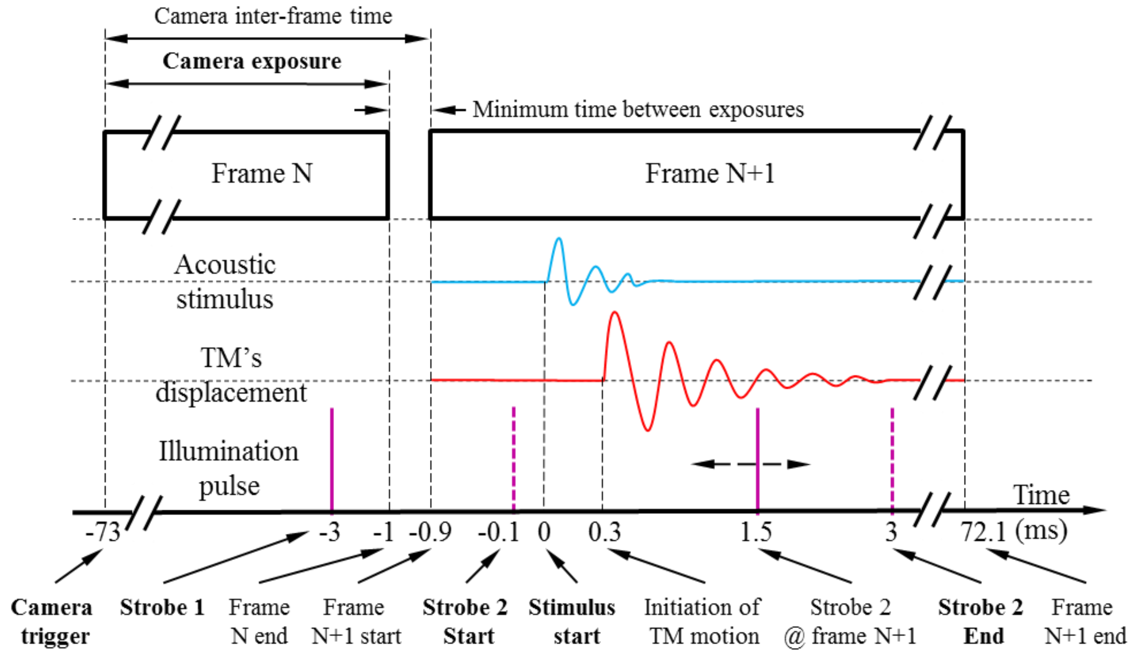

Fig. 10.4. Overview of the timing diagram and corresponding acquisition parameters (highlighted in bold) of the MPDE acquisition mode. The software implementation, based on the MCA approach, provides user control over 3 CTS that govern the beginning of every pair of camera exposures, the duration and temporal location of each light pulse and the temporal location of the beginning of the excitation.

A CTS governs each light pulse (*Strobe* in GUI) based on user-controlled parameters for duration and temporal location. During measurement, each light pulse is controlled by one of the ACSTW outputted from a DO to the AOM driver that, in turn, controls the light output in the LD module by the AOM.

A CTS governs the time of the beginning of the excitation (*Stimulus* in GUI) by sending a trigger input into the signal generator. Based on the MPDE procedure described in Chapter 8, the beginning of the excitation is adjusted to occur between the two light pulses (*Strobe1* and *Strobe2* in GUI); however, other configurations are also available. The type, level and duration of the excitation are adjusted manually through the front panel of the signal generator.

The software implementation of the MPDE acquisition mode allows for the user control of several major acquisition parameters, including:

- The effective *measurement time* for every frame is defined by the pulse duration (*Strobe length* in the GUI), which in turn defines the temporal accuracy.
- The equivalent *frame rate* is defined by the strobe interval (*Interval* in the GUI) which governs the incremental time step for each new deformed frame recording relative to the beginning of each new DE measurement.
- The effective *measurement duration* and number of samples are defined by the beginning and end (*Start* and *End* in UI) of the range of time instances for the deformed frames.
- The *number of samples* is defined by the combination of the *measurement duration* and *frame rate.*

10.3.3 High-speed 2+N (HS 2+N) acquisition mode

The high-speed 2+N (HS 2+N) acquisition mode is based on the HS 2+N acquisition method, described in Chapter 8, consisting of three major events: camera acquisition, temporal phase shifting, and excitation. To perform high-speed transient measurements of a TM sample in HS 2+N acquisition mode, the user is required to specify camera acquisition, temporal phase shifting, and excitation parameters.

User control over the camera acquisition parameters of the high-speed (HS) camera (Photron SA5 1000k) is provided by the Photron Fastcam Viewer (PFV v.3.3.8), which allows for selection of AOI (spatial resolution), exposure, sampling speed (frames per second), trigger mode, number of frames (number of samples), and camera I/O [Photron, 2013]. Adjustment of AOI, exposure, and camera I/O is analogue to a conventional speed camera (similar to LaserView), while the sampling speed, trigger mode, and number of frames are specific to the Photron SA5 camera and will be discussed in this section.

User control over the excitation and the temporal phase shifting is provided by the MPDE acquisition mode UI in LaserView (described in Appendix B) with no software modifications and only minor adjustment of the settings, which will be discussed in this section. A detailed description of the operation of the Laser View GUI is presented in Appendix B. A detailed description of the operation of the PFV GUI can be found in the Photron SA5 camera manual [Photron, 2013]. This Section presents an overview of the software procedures and corresponding parameters specific to the Photron SA5 high-speed camera used in the CHHS in HS 2+N acquisition mode.

10.3.3.1 Camera spatial and temporal resolution

The maximum frame rate (sampling speed) of the Photron SA5 is inversely proportional to the selected resolution (and corresponding AOI), as shown in Fig. 10.5, and is governed by the data transfer rate between the camera sensor and memory, typically measured in gigapixels per second (Gpix/s). This is due to the principle of operation of this type of high-speed cameras, Section 6.1. After every camera exposure, data from the individual pixels at the sensor are transferred to the camera memory at a data transfer rate that depends on the memory bus speed and the duration of the memory allocation operations. While the memory bus speed is constant, the duration of the memory allocation operations is nearly independent of data size, resulting in decreasing data transfer rate with increasing frame rate, as shown in Fig. 10.5. In the case of the SA5, the data transfer rate drops ~25% from 7k to 100k fps. Based on the sampling rate requirements listed in Chapter 6, the Photron SA5 is typically set for frame rates in the range of 40-140K fps, which allows for spatial resolution in the range of 200^2 to 400^2pixels.

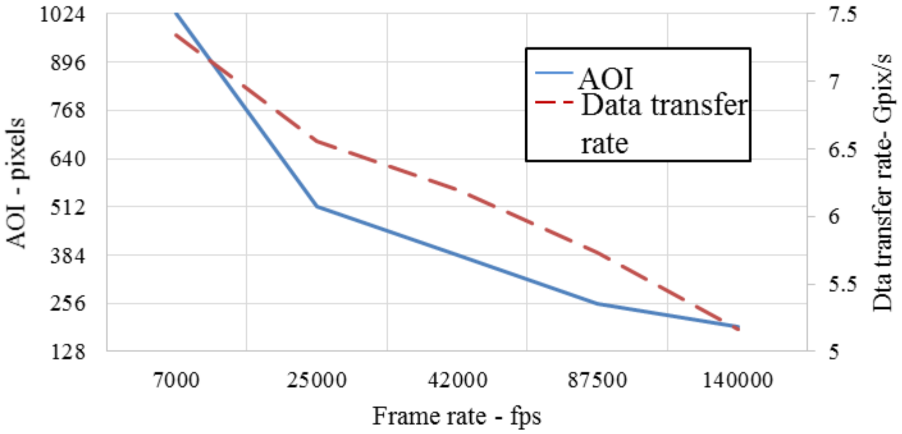

Fig. 10.5. Graph of the relationship between the size (in pixels) of the area of interest (AOI), data transfer rate (Gpix/s) and frame rate (fps) for the Photron SA5 high-speed camera. The graph suggests that the data transfer rate is not constant, but decreases with increasing frame rate.

10.3.3.2 Camera triggering modes

The PFV software (v3.3.9) and the Photron SA5 1000k camera allow for several trigger modes for synchronization with external events. The different trigger types are defined by the principle of data acquisition and storage of the camera. The Photron SA5 is always recording once it is armed, and a trigger event (independent of the source type) defines only what is stored in memory, and available for the user for download through the PFV software. This is achieved by a continuous cyclic recording utilizing a “first in, last out” (FILO) memory allocation principle. The cyclic FILO memory allocation principle means that once the memory is full, newly acquired frames are stored by overwriting the oldest frames. In practice, the continuous recording means that once a trigger event is received, any number of frames (within the memory capacity of the camera) before and/or after the trigger event can be accessed from the memory. The camera also allows multiple trigger events to be captured. The operation of the camera relative to the trigger event is defined by the trigger mode types, which are summarized in Table 10.1(nomenclature is based on the PFV software) and categorized based on the duration of the recording and the location of the recorded temporal window relative to the trigger event.

The typical duration of the transient response of the human TM exited by an acoustic click is <5 ms, Chapter 6, which results in <250 frames (384^2pix @ 42 kfps) or < 1% of the available camera memory (i.e., 8GB). Based on these criteria, a trigger mode should allow for recording of user specified number of frames after receiving a trigger event. This matches the capabilities of both “Random” and “Random Reset” trigger modes. However, only one of the trigger modes provides suitable accuracy in synchronization between the camera and the trigger event, as demonstrated in Fig. 10.6. In the case of the “Random” trigger mode, the beginning of only the next available camera exposure is synchronized with the trigger event, as shown in Fig. 10.6a. This can cause a random delay of up to one inter-frame period between the trigger event and the beginning of the first recorded frame.

Table 10.1. Trigger modes available within the PFV v3.3.9 software for the Photron SA5 1000k [Photron, 2013]. Organization is based on the duration of the recorded even and the position of the event relative to the trigger event. HS 2+N acquisition mode utilizes the "Random Reset" trigger mode, highlighted in bold. Nomenclature is based on the PFV software.

Temporal location of recording with respect to trigger input	**Duration**	
	Full memory	***N frames***
Before	"End"	N/A
During	"Center"	"Random Center"
After	"Start", "Two-stages"	"Random", "**Random Reset**"
Custom	"Manual"	"Random manual"

In the case of the "Random reset" mode (sync reset trigger) the exposure of the first recorded frame starts in <0.35 μs, governed by the internal clock of the Photron SA5, after the trigger event to ensure consistent synchronization. To achieve that, the camera resets the vertical synchronization of the sensor upon detection of a trigger even, independent of the inter-frame time, as illustrated in Fig. 10.6b. The HS 2+N acquisition mode utilizes the "Random Reset" trigger mode of the Photron SA5 to ensure consistent timing of the start of the recording relative to the trigger event.

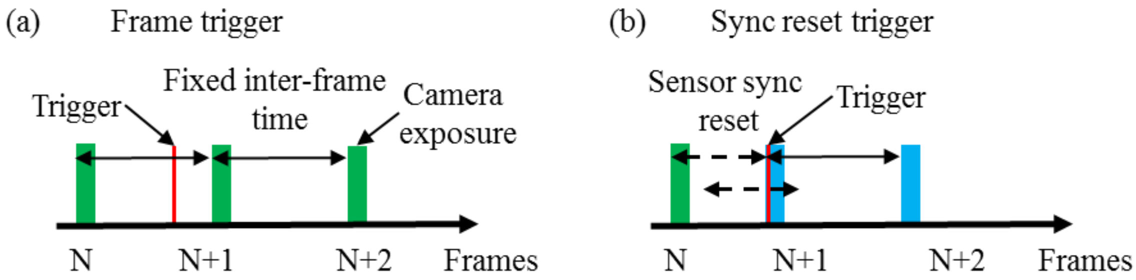

Fig. 10.6. Trigger mode types with different temporal accuracy of synchronization between the camera exposure and the trigger event: (a) frame trigger mode synchronizes the start of the exposure of the next available frame with the trigger event, resulting in a random delay (within one inter-frame period); and (b) sync reset trigger mode resets the sensor sync, thus evoking a new exposure upon the exact time (i.e., <0.35 μs delay) of the trigger even.

10.3.3.3 Control and synchronization

For control and synchronization of the HS 2+N acquisition mode, the modular control approach (MCA) was used to provide user control over 3 CTS that govern the temporal locations of the trigger of the HS camera, temporal phase shifting, and the beginning of the sample excitation. The user controls the parameters of each CTS by the same LaserView GUI, as with the MPDE acquisition mode, with no software modifications and only minor adjustments of the acquisition settings. While the camera trigger and the beginning of the excitation are analogues to the MPDE acquisition mode, the HS 2+N acquisition mode requires no illumination control. Instead, this CTS is adjusted to produce only one pulse (instead of 2 in the MPDE mode) that is used to control the beginning of the phase step.

10.4 Processing

At the end of the acquisition stage of the HMP, the HHS provides a 3D holographic data set (3DHDS) representative of the spatio-temporal intensity variation of the complex field (hologram) of the object undergoing transient deformations due to the excitation procedure. However, in order to characterize the deformation of the object, the corresponding phase information within each hologram is to be extracted (sampled). Two single frame phase sampling algorithms (i.e., DESPS and 2+1 LCPS, Chapter 7) have been implemented as a set of procedures comprising the processing stage of the HMP, which allows the conversion of each frame of the 3DHDS from intensity into wrapped phase map corresponding to the object's deformation, as shown in Fig. 10.7.

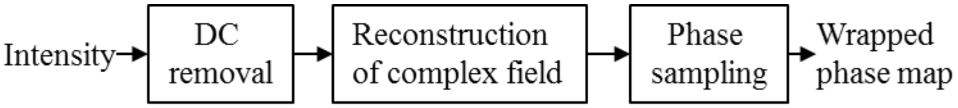

Fig. 10.7. A workflow of the procedures, comprising the processing stage of the HMP, to convert intensity of every recorded hologram into wrapped phase maps corresponding to the full-field transient displacement of the object.

The processing stage of the holographic measurement process (HMP) consists of the following procedures:

- *DC removal* – quantification and removal of the background illumination component of each recorded hologram, as described in Section 7.1.
- *Reconstruction* – application of numerical reconstruction algorithms, as described in Chapters 5 and 7, for the quantification of the complex field of the object at every camera frame.

- *Phase sampling* – application of single frame phase sampling algorithms, as described in Chapter 7, for quantification of the phase change corresponding to the full-field deformation of the object in time.

This section describes the details of the implementation of the procedures within the processing stage of the HMP.

10.4.1 DC removal

The constant background illumination (DC) component of each hologram, as described in Chapters 5 and 7, needs to be removed before further processing. Depending on the acquisition mode, MPDE or HS 2+N, used for recording of the 3DHDS, either a spatial or temporal DC removal procedures are applied to the full data set.

The temporal based DC removal procedure is based on the assumption that the background illumination varies slowly in time, as described in Chapter 7. Based on that, the DC component at each pixel is defined as its temporal average within the 3DHDS. The temporal DC estimation at each spatial pixel of the full 3DHDS is implemented in two ways, each minimizing either hard disk seek time or memory usage. In the first approach, the full 3DHDS is read simultaneously, thus minimizing hard disk seek time. The DC estimation is then performed on the full 3DHDS by using a computationally efficient low-pass filter applied along the temporal axis of the 3DHDS in parallel across all pixels. However, since typical transient recording of the human TM consists of ~250-1000 frames, Chapter 8, loading all data simultaneously could require large memory size (i.e., > 1 GB for a double precision data array of 384x384x1000). To alleviate this problem, a memory efficient temporal DC estimation is implemented based on a running average, which can be applied to the full data set at the memory expense of only 1 frame at a time. However, this approach would increase the total readout time by imposing longer hard disk seek times. By implementing both types of temporal DC estimation methods, the processing stage can be executed on various PC hardware. The temporal DC estimation is primarily used for measurements with short total duration (i.e., <10 ms), as is the case with the HS 2+N acquisition mode, in order to avoid environmental disturbances.

The spatial DC removal procedure is based on the assumption that the background illumination varies slowly in space, as described in Chapter 7, which allows for estimation of the DC component at each pixel based on the average of the pixel intensities within a small spatial kernel (i.e., 3×3 pixels or 5×5). The spatial DC estimation for the full hologram is implemented by a computationally efficient spatial low-pass filter (i.e., mean). The resulting DC component map is then subtracted from the intensity map (frame). The spatial DC removal procedure is typically applied to data sets obtained in MPDE acquisition mode, as described in Chapter 8, where the total measurement time (i.e., >1 min) could result in random temporal variation of DC level between individual frames, thus limiting the use of a temporal estimation techniques.

10.4.2 Reconstruction

Data obtained with the lensless digital holographic setup of the OH, typically based on MPDE acquisition mode, requires numerical reconstruction (focusing/refocusing) in order to obtain the object information.

10.4.2.1 Reconstruction algorithms

Reconstruction procedure, developed and integrated within the processing stage of the HMP, allows for holographic reconstruction algorithms based on either Fresnel transformation, Chapter 5, or the Convolution approach [Kreiss, 2005; Schnars and Jüptner, 2002]. The workflow of the software implementation of both reconstruction algorithms, as shown in Fig. 10.8, utilizes common subroutines such as forward and inverse Fast Fourier Transforms (FFT and IFFT) as well as spatial masking in the spatial or frequency domains.

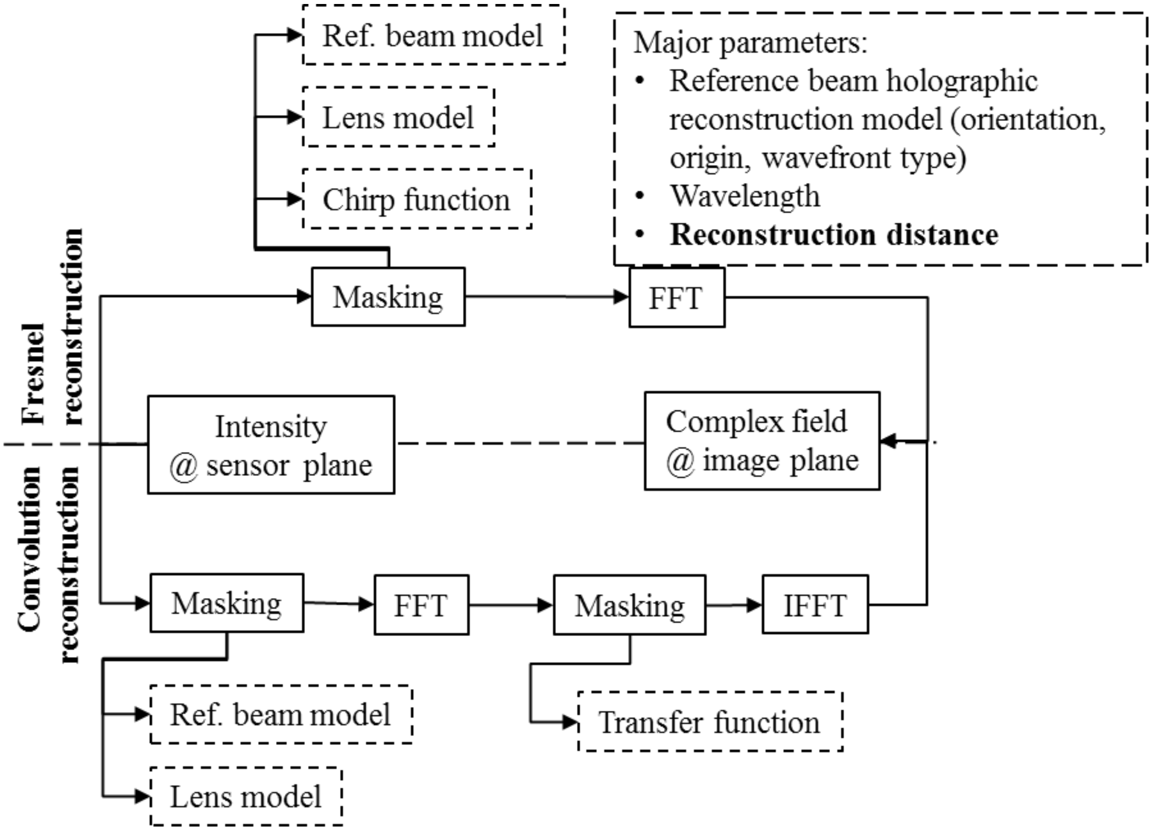

Fig. 10.8. Workflow of the software implementation based on the Convolution and Fresnel reconstruction procedures. The two approaches share common subroutines such as forward and inverse Fast Fourier Transforms (FFT and IFFT) as well as masking (spatial or frequency domain). Major user input parameters of the reconstruction procedure are outlined.

Each masking subroutine consists of several elements that can be computed based on either default values from the metadata information of the RTI or LVVID [Harrington et al., 2011] files, or user specified parameters. Each mask is a spatial map of complex values that are multiplied with the spatial or frequency domain of the holographic data during the computational procedures of the digital reconstruction. The various masks represent discrete mathematical models including:

- *Reference beam model* –the complex field of the reference beam at the sensor plane. Available options within the software implementation are of a parallel (default option) or spherical reference beam [Schnars and Jüptner, 2002] model.
- *Lens model* - the imaging properties of the lens (if present in the optical system) in order to be accounted for in the reconstruction process [Schnars and Jüptner, 2002].
- *Chirp function* - the complex field of a chirp function that is part of the Fresnel transformation, Eq. 5.33, typically used in the reconstruction of the digital lensless holograms captured by the MPDE acquisition methods.
- *Transfer function* - the complex field of an impulse function that is part of the Convolution reconstruction [Kreiss, 2005]. This is internally expressed as either a 2D FFT of an impulse response function in the spatial domain or a closed form solution of the corresponding transfer function in the frequency domain [Kreiss, 2005].

10.4.2.2 Automatic focusing

Most parameters (i.e., reference beam holographic reconstruction model, wavelength) needed for the reconstruction procedure are defined by the holographic optical and illumination setup and can be calibrated before a measurement. However, the working distance (WD) of the object, and the corresponding reconstruction distance, varies with the particular experimental setup. In order to provide a sufficiently accurate reconstruction distance, the reconstruction procedure allows for options:

- *Default* –automatically reads the reconstruction distance from the header (metadata) of the RTI and LVVID files [Harrington et al., 2011]. These parameters have been determined experimentally by the user during the hardware and software setup stage of the HMP.
- *Manual* – the user specifies a reconstruction distance manually based on/or independent of the *Default* settings.
- *Automatic* –allows for an automated iterative search for an optimal reconstruction distance based on several focus estimation algorithms.

The automatic reconstruction distance search uses simultaneously 3 focus (sharpness) estimation algorithms, shown in Fig. 10.9, that are executed iteratively through a predefined search range of possible reconstruction distances. The search range is either user-defined or is automatically set as a ±5% (user selectable) around the *Default* reconstruction distance.

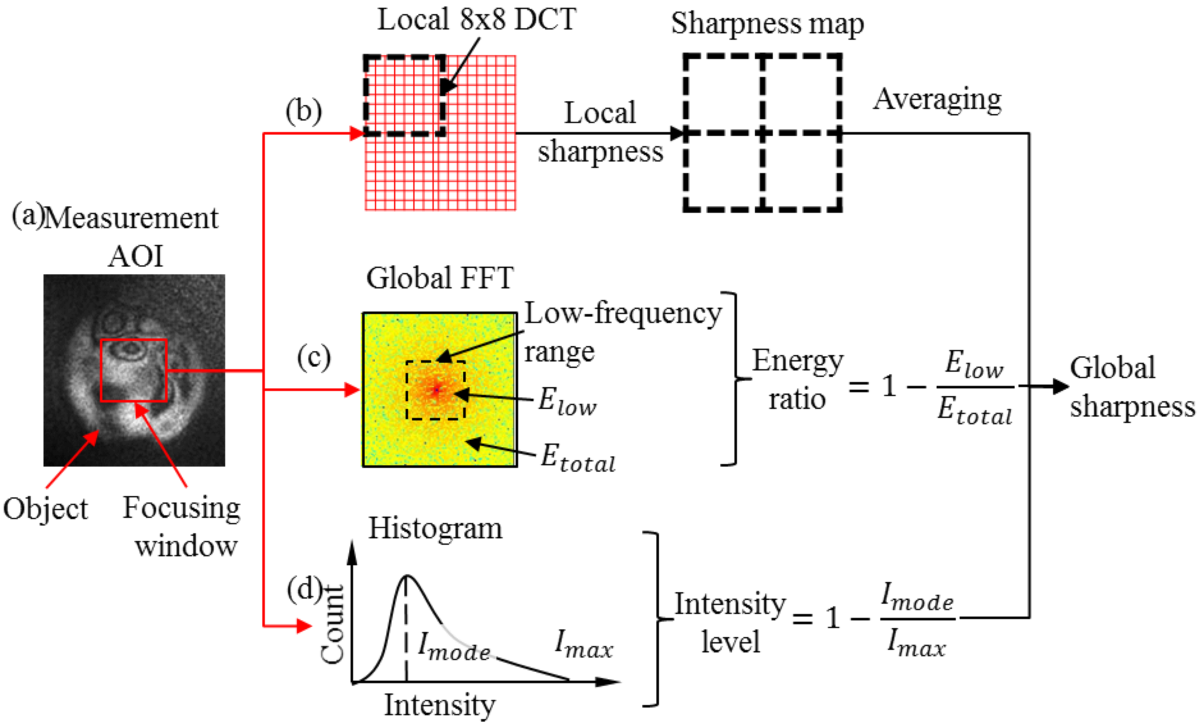

Fig. 10.9. Diagram of the principle of operation of 3 sharpness estimation algorithms: (a) original image with a selected focusing window; (b) Bayes spectral entropy (BSE) based algorithm estimates the local and global entropy through a discrete cosine transform (DCT); (c) FFT power spectrum based algorithm estimates the energy ratio between the low-frequency (central) part and the full spectrum; and (d) histogram based algorithm estimates the intensity level as the ratio of the most frequently occurring (mode) intensity relative the maximum value.

All sharpness estimation algorithms are used simultaneously to find the optimal reconstruction distance for the object, based on the data within the focusing window, shown in Fig. 10.9a.

The first focus estimation algorithm is based on a Bayes spectral entropy (BSE) of an image spectrum [Kristan et al., 2006]. The BSE is quantified locally by a discrete cosine transform (DCT) for each non-overlapping 8x8 kernel within the focusing window, as shown in Fig. 10.9b. The output of the BSE based focusing algorithm is defined by the average of the focus measures of all kernels within the focusing window. In this case, improved (higher) sharpness is indicated by a higher entropy value.

The second focus estimation algorithm is based on the distribution of the total energy across the 2D FFT power spectrum [Chikkerur et al., 2011] of the spatial frequencies within the focusing window. The output of the 2D FFT based focusing algorithm is defined by the energy ratio between the low-frequency (i.e., <10% of full range) part and the full spatial frequency spectrum, as shown in Fig. 10.9c. In this case, improved (higher) sharpness is indicated by a lower energy ratio corresponding to higher energy in the high-frequency region, indicating sharper spatial features within the focusing window.

The third focus estimation algorithm is based on the histogram (intensity data) of the reconstructed hologram and is specific to coherent light (speckled) imaging, as opposed to the first two algorithms that are originally designed for white light imaging. The output of the histogram based focusing algorithm is defined by the ratio between the most frequently occurring (mode) and the maximum intensities. In this case, improved (higher) sharpness is indicated by a lower illumination ratio corresponding to lower intensity of the mode of the histogram.

Figure 10.10 shows a practical example of the performance of the 3 algorithms applied at one instance of a stroboscopic recording of a TM. Typically the automatic focusing procedure is applied with 15-20 iterations, each requiring a new reconstruction at the computational time expense of ~1.2sec/DE frames (each at 2048^2 pixels). In order to speed up the overall procedure, only 15-25% of the resolution of the original hologram is used for reconstruction of each iteration of the focusing procedure, making the process 4-5 times faster without significant compromise in focusing accuracy.

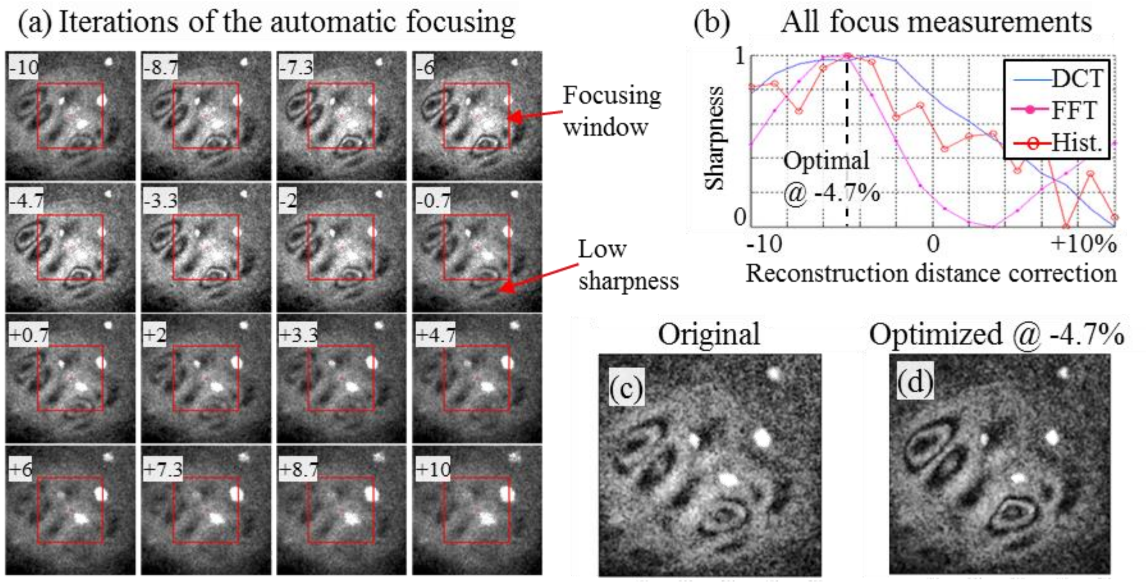

Fig. 10.10. Representative results of the automatic reconstruction processes utilizing the algorithms shown in Fig. 10.9 for one instance (double-exposure, DE frames) of a MPDE based transient measurement of a human TM: (a) iterations of the automatic focusing in the ±10% range relative to the *Default* reconstruction distance; (b) graph of normalized focus sharpness versus reconstruction distance for all 3 focusing algorithms; (c) DE modulation map of the human TM with the *Default* reconstruction distance; and (d) same as (c) but with a -4.7% correction of the reconstruction distance.

10.4.3 Phase sampling

10.4.3.1 1 frame spatial phase sampling (SPS)

The 1-frame SPS method, as described in Chapter 7, allows for quantification of the object’s complex field by separating the components of the reconstructed hologram in the frequency domain, as shown in Fig. 10.11. The software implementation of the SPS, allows the user to define the center of the object as well as the required AOI, Fig. 10.11a. This information is then automatically applied to all images within the 3DHDS to obtain the modulation and phase of the complex field of the object, Figs 10.11b and 10.11c.

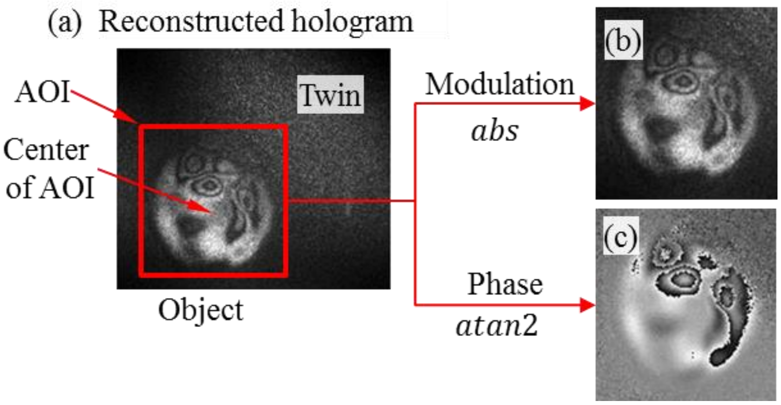

Fig. 10.11. Workflow of the software implementation of the spatial phase sampling method: (a) selection of AOI for spatial masking of the reconstructed hologram containing only the object information; (b) and (c) modulation and phase of the object's complex field computed with the abs and $atan2$ functions in MATLAB.

10.4.3.2 2+1 frame local correlation phase sampling (2+1 LCPS)

The software implementation of the computational process of the 2+1 LCPS method, as described in Chapter 7, utilizes data restructuring procedures, shown in Fig. 10.12, to minimize computational time by utilizing multi-core CPU and massive parallel GPU computing [Dobrev et al., 2013a]. Data restructuring procedures include:

Data reduction

Based on Eq. 7.17, the 2+1 LCPS method requires two evaluations of the Pearson product-moment Correlation Coefficient (PCC) at each spatio-temporal data point of the 3DHDS. Based on Fig. 7.2, each PCC calculation will require input from the intensity values within the spatial kernels at one deformed and two reference states. For a 384×384×1000 data size with a 3×3 spatial kernel, there will be ~3×10^8 PCC calculations with a total of ~ 8×10^9 input parameters. In order to reduce the computational load, a data reduction approach has been utilized for software implementation of the 2+1 LCPS method. Since each computation is based on data from small (i.e., 3×3 or 5×5) spatial kernels, evaluation of the PCC at each spatial point might be redundant, in the case of slowly varying spatial distribution of the object's phase change. Based on this, a spatial data reduction procedure has been implemented to allow restructuring of the data of each camera frame with size $k \times l$, based on sampling grid of smaller size $m \times n$, as shown in Fig. 10.12a. This means that the spatial kernels are sampled based on a grid with the same size as the original camera frames but with reduced spatial resolution, controlled independently of kernel size. This allows for independent control over the spatial sampling rate and sampling resolution of the resultant correlation maps (output of the PCC), used for quantification of the object's phase change.

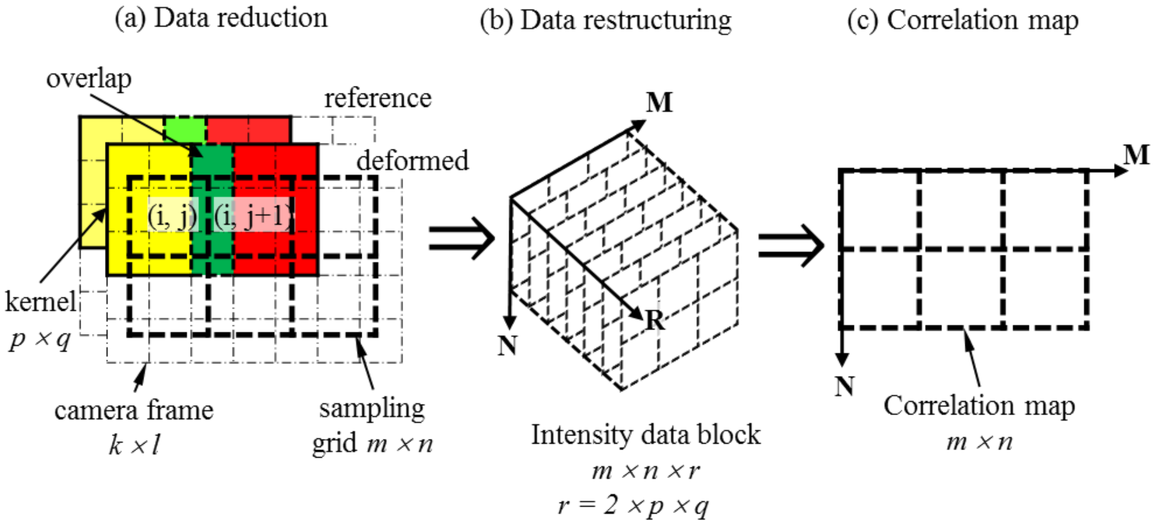

Fig. 10.12. Schematic of the data restructuring approaches for minimization of the computational time of the 2+1 LCPS method: (a) data reduction with separate control over kernel size and sampling resolution for improved CPU computing; (b) data restructuring designed for massive parallel GPU computing; and (c) correlation map output.

Data restructuring to enable parallel computing

Based on the sampling grid, the intensity data from each pair of reference and deformed frames are restructured in an intensity block with size $m \times n \times r$, as shown in Fig. 10.12b. The block is organized such that the intensity values, at each kernel (size $p \times q$) for each frame (reference and deformed), are organized along the 3rd dimension (R-axis) of the block. This allows access to all input parameters required for the execution of each PCC calculation at all data points in the correlation map (size $m \times n$), as shown in Fig. 10.12c, independently and simultaneously. This property allows execution of all PCC calculations in parallel without any data access delays. Based on this computational parallelism, the software implementation of the 2+1 LCPS method has been multi-threaded for execution with multi-core CPUs and massive parallel GPUs. The data restructuring approach to the software implementation of the 2+1 LCPS method allows for user control of the spatial resolution, kernel size and corresponding computational speed, as described in Appendix C.

10.5 Analysis

At the end of the processing stage of the HMP, the HHS provides a 3DHDS containing the spatio-temporal variation of the complex field of the object undergoing transient deformations. The complex field within each frame of the 3DHDS contains a DE modulation and wrapped phase map. However, in order to characterize the deformation of the object at each frame, the corresponding double-exposure wrapped phase map needs to be filtered, unwrapped and scaled, as illustrated in Fig. 10.13. This Section outlines the development and implementation of a set of procedures comprising the analysis stage of the HMP, which allow the conversion of each frame of the 3DHDS from a wrapped phase map into deformation.

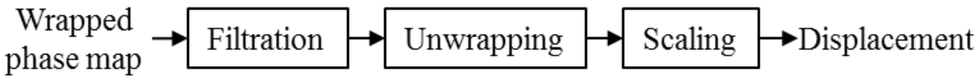

Fig. 10.13. A workflow of the procedures, comprising the analysis stage of the HMP, to convert the whapped phase maps, extracted from every camera frame, into full-field transient displacement maps of the object.

10.5.1 Filtration

Due to the nature of the holographic data, the low spatial frequency data related to the object’s deformation is typically convoluted with the high spatial frequency related to speckle noise. Additionally, in practical applications noise sources from the environment, object and experimental equipment [Furlong et al., 2002] contribute to the content of the holographic data and could degrade the retrieved object information.

In order reduce the noise in the phase information of the object, a set of spatio-temporal filtration procedures has been developed. However, direct filtration of the wrapped phase data would deteriorate the information about the spatial location of the wrapped phase discontinuities, which could hinder further analysis. Therefore, the software implementation of the filtration procedures applies noise reduction methods on the real and imaginary components of the complex data individually, as shown in Fig. 10.14.

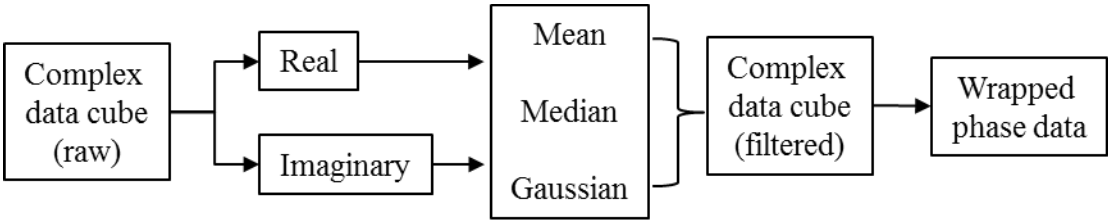

Fig. 10.14. A workflow of the filtration procedure individually applied to the real and imaginary parts of the complex data of the 3DHDS. The software implantation allows control over the spatial and temporal sizes of the kernels of several types of filters.

The filtration procedure is applied simultaneously on the full 3DHDS, thus allowing for both spatial and temporal filtration of the complex data. User control is provided over the types of filters (i.e., mean, median, Gaussian, MATLAB v8.1.0.604), as well as the spatial and temporal size of the kernel.

It should be noted that due to the numerical implementation of the phase sampling algorithms within the HHS, the complex data used in the analysis stage of the HMP is already spatially filtered relative to the initially recorded holograms. For example, the software implementation 2+1 LCPS procedure allows for user control over the weighing of the individual intensity values within the spatial kernel in order to obtain the frequency response of specific spatial filters, such as mean or Gaussian [Dobrev et al., 2015].

10.5.2 Unwrapping and scaling

Quantification of the phase, from the complex data obtained in the processing stage of the HMP, is typically done by using an arctangent function, such as Eq. 7.6., at each data point within the 3DHDS, resulting in spatial discontinuities, as shown in Fig. 10.15.

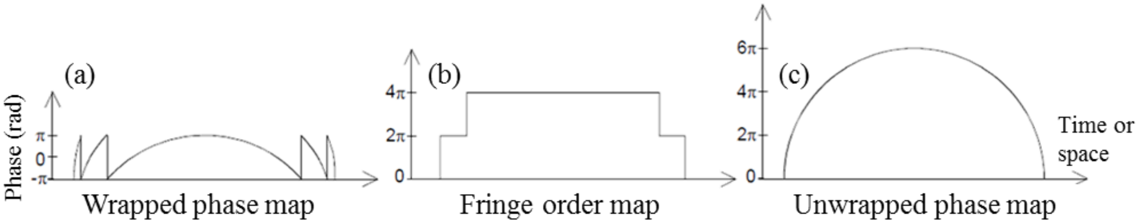

Fig. 10.15. A workflow of the unwrapping procedure to obtain continuous phase data.

The software implementation of the unwrapping procedures allows for a spatial and temporal approach to unwrapping. In the spatial approach, previously developed HoloStudio [Harrington et al., 2011] and 2D-SRNCP [Herráez et al., 2002] unwrapping functions have been incorporated within the unwrapping procedure of the HMP. Both spatial unwrapping algorithms start with quantification of the reliability of every spatial data point within a wrapped phase map, shown in Fig. 10.15a, based on user-defined criteria related to the interferometric modulation, noise floor and spatial connectivity. Data with insufficient reliability is ignored in further analysis. In the second stage of the spatial unwrapping process, a fringe order map is generated, as shown in Fig. 10.15b, indicating the locations of the 2π discontinuity within the reliable data of the wrapped phase map. In the final stage of the spatial unwrapping process, the fringe order map is used together with the wrapped phase map to reconstruct the continuous (unwrapped) phase map, as shown in Fig. 10.15c.

Assuming a sufficiently high temporal sampling rate relative to the deformation rate of the object, the temporal variation of the wrapped phase at each spatial location between any two consecutive frames can be reduced to within $[-\pi;\ \pi]$. Under this sampling criteria, a simple 1D phase unwrapping approach (*unwrap* in MATLAB v8.1.0.604) has been implemented such that it allows unwrapping for the phase waveform along the temporal axis of each spatial location within the 3DHDS in parallel, independent of other points in the spatial neighborhood [Khaleghi et al., 2014b]. This makes the temporal unwrapping approach robust to problems, associated with spatial discontinuities or high-spatial fringe densities, associated with spatial unwrapping methods. It should be noted that for transient measurements of the human ME, application of a temporal phase unwrapping approach would require significantly higher sampling rates than a spatial unwrapping approach. Therefore, in most transient measurement applications of the HHS, a spatial unwrapping approach is used.

Once the phase data of the 3DHDS is unwrapped, the displacement of the object can be obtained by a scalar multiplication of the continuous phase with a scaling constant based on Eq. 5.41. The scaling constant accounts for the recording wavelength and the sensitivity vector of the optical system, Chapter 5.

11 Parallel data mining and interpretation of spatio-temporal displacement data

The numerical methods, and their software implementation, discussed in Chapter 10 allow quantification of the displacement of the human middle-ear at every camera frame. However, further data interpretation is needed for the quantification of medically relevant parameters that could describe the transient mechanics of hearing. This Chapter outlines the development and implementation of parallel data mining and interpretation (PDMI) methods, based on spatio-temporal displacement data cubes (STDDCs), aimed at quantification of medically relevant motion parameters (MRMP) for the characterization of the transient response of the human middle-ear.

11.1 Conversion from 3DHDS to STDDC

This Section focuses on the development and implementation of procedures for conversion from individual displacement maps within a 3DHDS into a spatio-temporal displacement data cube (STDDC) in order to apply parallel data mining and interpretation (PDMI) methods.

The procedures, shown in Fig. 11.1, to convert from 3DHDS to STDDC are separated in 3 stages, which include:

- *Seed point temporal correction* – correction for the temporal variation of the seed point displacement resulting from the spatial unwrapping procedures in the analysis stage of the wrapped phase data of the 3DHDS, Section 10.5.

- *Rigid body motion compensation* – compensation for rigid body motions of the object.
- *Data reduction* – spatial resolution data reduction for increase of computational speed.

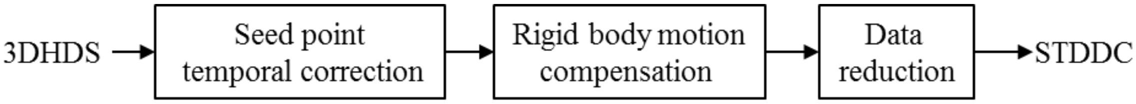

Fig. 11.1. Workflow for the conversion from individual displacement maps within a 3DHDS to spatio-temporal displacement data cube (STDDC). Included are procedures for correction of the temporal drift of the seed point, compensation for rigid body motions, as well as spatial resolution data reduction for improved computational speed.

11.1.1 Seed point temporal correction

Typically with transient displacement measurements with the HHS, a spatial phase unwrapping approach is used [Dobrev et al., 2013a]. At the end of the phase unwrapping of each frame, the corresponding continuous phase map is shifted based on a seed point that designates the zero position. The seed point is defined differently in the two phase unwrapping algorithms (unwrapper) used with the HHS, Chapter 10. The 2D-SRNCP unwrapper [Herráez et al., 2002] uses the global minima of the unwrapped phase maps as a seed point, which could result in spatial and temporal variations of the displacement at the seed point. The HoloStudio unwrapper [Harrington et al., 2011] utilizes a user-defined point that is used as a seed point for all unwrapped phase maps of the 3DHDS. While alleviating spatial variations, this approach could still result in temporal variations if the seed point is located at a point of significant motion, as demonstrated in Fig. 11.2.

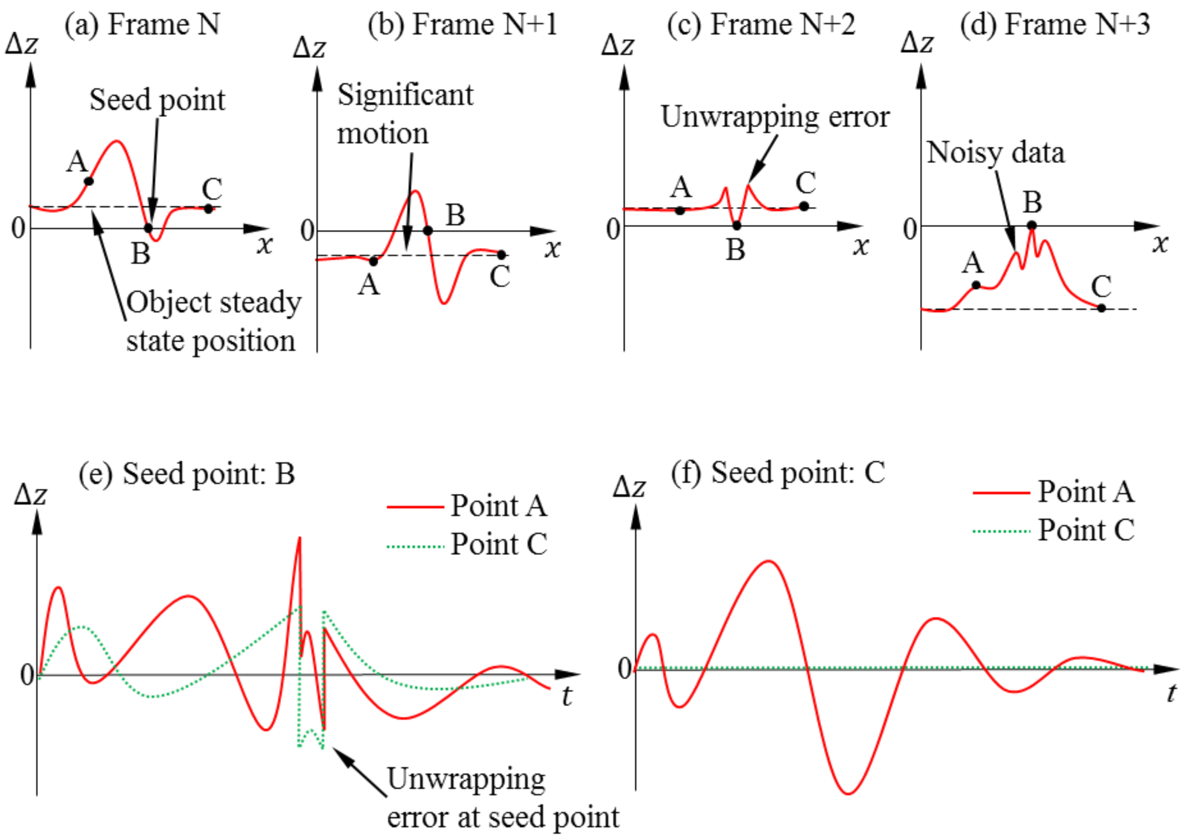

Fig. 11.2. Overview of the effects of seed point selection in the spatial phase unwrapping approaches that result in artificial temporal fluctuations in 3DHDSs: (a)-(d) examples showing the results of significant displacements, unwrapping errors, or significant noise at the seed point; (e) displacement time waveform at points A and C are superimposed with the temporal fluctuations at seed point B; and (f) corrected displacement time-waveform of point A based on seed point C. Selection of the seed point is critical for the accurate recovery of the time waveform at each point.

Possible seed point selection problems are associated with significant displacements, unwrapping errors, or significant noise at the seed point, as illustrated in Fig. 11.2a-d. Any of these phenomena will cause temporal fluctuations between consecutive displacement maps in the 3DHDS relative to true steady state position (SSP) of the object, as indicated in Fig. 11.2a-d. This will cause the superposition of the time waveform of the seed point (Point C) and all other point, as shown in Fig. 11.2e. In order to alleviate this problem, a software implementation for semi-automatic estimation of the object's SSP allows for correction of the seed point temporal fluctuation, as shown in Fig. 11.2f. The SSP estimation procedure is based on a user defined mask or seed kernel, as shown in Fig. 11.3. In the case of a masked based SSP, the motion of the object at the mask boundaries is assumed insignificant, thus its average is subtracted from each displacement map in the 3DHDS. In the case of kernel based SSP, the displacement of the object within a small kernel centered at a user-defined point is assumed insignificant, thus its average is subtracted from each displacement map in the 3DHDS.

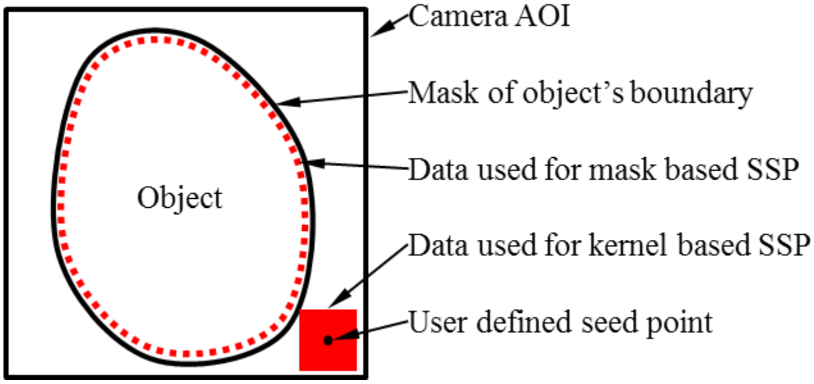

Fig. 11.3. Overview of parameters for software implementation of the semi-automatic estimation of the object's steady state position (SSP) accurate seed point temporal correction.

Removal of the temporal variation of the3DHDS, allows for organization of all displacement maps into a spatio-temporal displacement data cube (STDDC) that is representative of the time-waveform of every point across the surface of the object.

11.1.2 Rigid body motion compensation

Due to the broadband frequency content of the transient stimuli, which affects both the surface of the human TM as well as the temporal bone and the mechanical fixtures used to hold the sample, significant rigid body motion could occur. This could result in a detectable rigid body motion component as part of the measured transient displacement response of the sample. Typically, the rigid body motion component has frequency content below the typical low frequency (i.e., 200-1000Hz) response of the surface of the human TM [Hömberg et al., 1987]. However, due to the short (i.e., <5 ms) measurement time of the HHS acquisition governed by the duration of the transient response of the TM, motion components with frequencies <200 Hz are sampled with less than one cycle. This could result in the erroneous quantification of the rigid body motion components, as they would appear quasi-static within the temporal scale of the HHS measurements. Because of this, the quasi-static motion components are numerically estimated and compensated for within the contents of the STDDC by applying custom temporal high-pass filters. Three types of quasi-static motion component compensation approaches, illustrated in Fig. 11.4, have been implemented within the HHS, including:

- *Temporal average* – used for removal of static deformation component from each time-waveforms of STDDC. The software implementation is based on a temporal average of the time-waveform at each point, as shown in Fig. 11.4a.
- *Spatio-temporal running average* – used for removal of quasi-static motion components from the time-waveforms of STDDC. The software implementation is based on a running average along the temporal axis of the STDDC with a user controlled spatio-temporal kernel, also shown in Fig. 11.4a.
- *Polynomial fit* – analogue to the *Spatio-temporal running average.* The software implementation is based on a custom polynomial fitting algorithm that is run

along the temporal axis of all points of the STDDC in parallel, as shown in Fig. 11.4b.

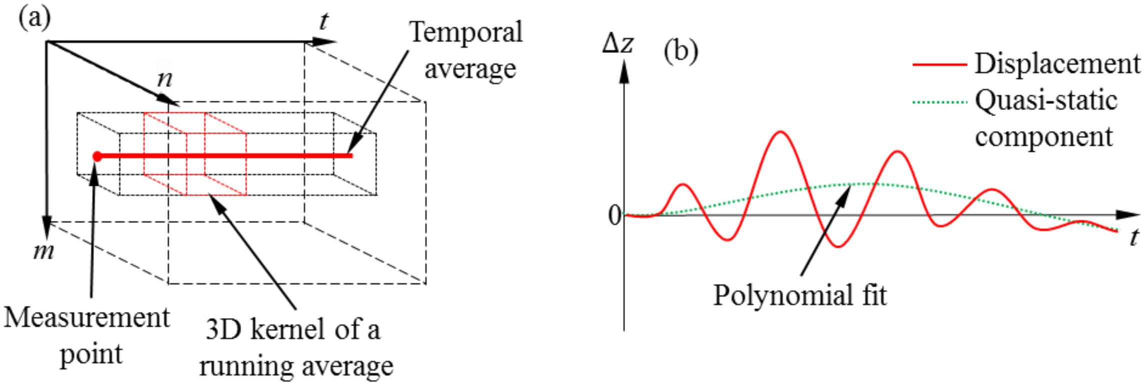

Fig. 11.4. Overview of the spatio-temporal approaches for estimation of the quasi-static rigid body displacement component in a measurement: (a) 3D representation of the STDDC with a highlighted subset of data that are utilized for both temporal average and spatio-temporal running average at each measurement point; and (b) displacement time waveform with polynomial fit estimation at a single measurement point.

11.1.3 Data reduction for improvement of computational speed

Since the STDDC contains only displacement maps as opposed to fringe patterns, the range of spatial frequencies of the data is lower than the corresponding 3DHDS. This allows data reduction of the spatial content of the STDDC in order to reduce the computational load for parallel data mining operations. The software implementation of the data restructuring is analogue to the one used with the 2+1 LCPS method, as described in Chapter 10. Each $k \times l$ displacement map from the STDDC is undersampled based on a sampling grid having a smaller spatial (more coarse) resolution $m \times n$, as shown in Fig. 11.5.

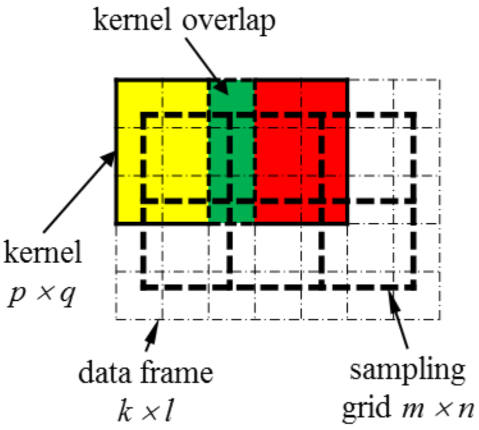

Fig. 11.5. Schematic of the data reduction approach for minimization of the computational load in STDDC. The software implementation of the approach allows independent control over the spatial filter kernel size and spatial grid resolution for improved computational speed. Two neighboring spatial kernels of dimensions $p \times q$ and their overlap are highlighted.

Each spatial data point in the coarse grid is based on the averaged data from the original grid within a small spatial kernel $p \times q$, which allows for additional spatial filtration. The software implementation allows for user control of the kernel size and the coarse grid resolution, independently. This allows for independent control over the spatial sampling rate and sampling resolution of the resultant STDDC.

Once the STDDC is formed from the 3DHDS, quasi-static motion components are removed and spatial data size is reduced, the STDDC can be used with parallel data mining and interpretation (PDMI) procedures for the quantification of medically relevant motion parameters (MRMP).

11.2 Parallel data mining and interpretation (PDMI) of medically relevant motion parameters (MRMP)

As a final output of each transient measurement, the HHS provides a STDDC that contains the time waveform of the nanometer scale displacement response at each point on the surface of the object of interest, as shown in Fig. 11.6.

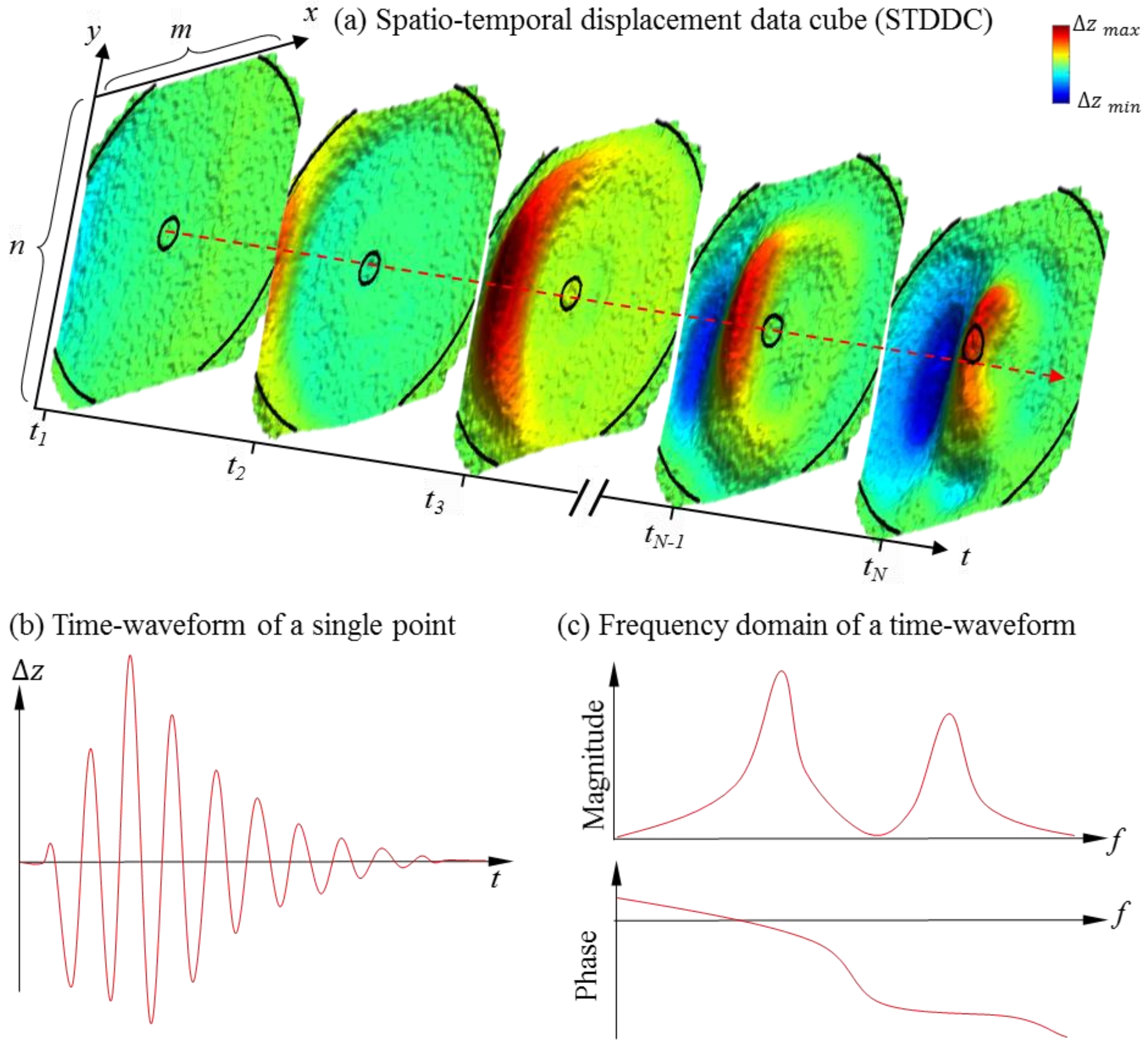

Fig. 11.6. Diagram of the of the spatial, temporal, and frequency measurement capabilities of the HHS for quantification of the transient nanometer scale displacement response of the human middle-ear: (a) full spatio-temporal displacement data cube containing the transient response at all measurement points; (b) representative plot of the displacement versus time waveform of an individual point of the STDDC; and (c) magnitude and phase of the frequency domain of the time waveform in (b).

Every spatial-temporal instance contains the displacement map $m \times n$ of the object at a specific time $(t_{def})_{i,\ i \in 1,2..N}$ of its transient deformation state, as shown in Fig. 11.6a. Typical spatial resolutions of the STDDC are ~100k points for CHHS and >500k points for PHHS, while typical temporal resolution for PHHS is >50 kHz independent of the spatial resolution, and 40-140 kHz for the CHHS depending on the spatial resolution. Converting raw holographic data into STDDCs provides spatially independent access to the time waveform, and corresponding frequency response, at every measurement point allowing execution of any PDMI, as shown in Figs 11.6b and 11.6c respectively.

This Section focuses on the development and software implementation of parallel data mining and interpretation (PDMI) methods, based on STDDC, for quantification of medically relevant motion parameters (MRMPs) for the characterization of the transient response of the human ME. Specifics on the software implementation of the all PDMI and MRMP are discussed in Appendix C.

11.2.1 MRMP in the temporal domain

This Section provides an overview of the software implementation of several MRMPs extracted from the time waveform of each spatial measurement point, as shown in Fig. 11.7. MRMPs, related to the initial stages of the transient response of the object, are based on the software procedures for estimation of the global peak time t_p (GPT), the first local peak time t_f (FLPT), and the response time, t_r (RT), as shown in Fig. 11.7a. The GPT is defined as the global extrema (min or max) based on the full time waveform. The FLPT is based on the temporal location of the first local extrema (min or max). The RT is defined as the time when the absolute of the time-waveform reaches a displacement threshold, defined as a percentage of the amplitude at GPT. For computational efficiency, the search for the FLPT and RT is only within the initial part of the time waveform, before GPT.

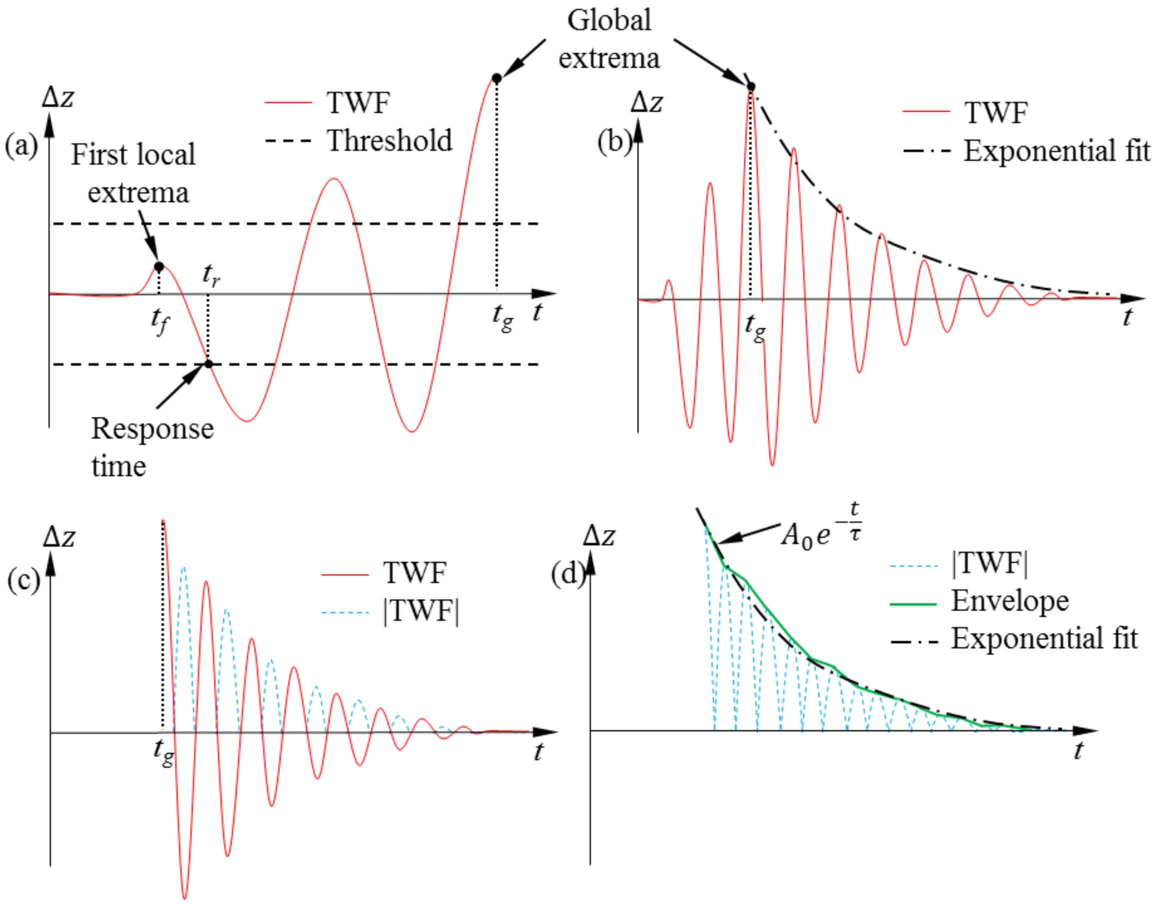

Fig. 11.7. Illustration of methods for quantification of time domain MRMPs: (a) and (b) graphical definition of the global peak time t_p (GPT), first local peak time t_f (FLPT), response time t_r (RT), and decay time constant τ (TC) as defined within the software implementation; (c) absolute of the TWF after the GPT; and (d) TC is determined based on an exponential fit of the envelope of the TWF.

A MRMP, describing the decay rate of the transient response of the object, is the time constant τ (TC), as shown in Fig. 11.7d. The software implementation to estimate TC is done in 3 stages. In the first stage, the absolute of the TWF for a temporal period greater or equal to t_p (GPT) is extracted, as shown in Fig. 11.7c, which corresponds to the decay part of the signal. In the second stage, an envelope estimation procedure is performed on the absolute value of the isolated section of the TWF. Several envelope estimation algorithms have been implemented based on Hilbert Transform [Khaleghi et al., 2014b] and local peak detection (Appendix C). This provides an initial estimate of the decay envelope of the TWF of the transient response, as shown in Fig. 11.7d. In the final stage of the TC estimation, the time constant of the TWF is quantified based on an exponential fit applied to the decay envelope.

11.2.2 MRMP in the frequency domain

This Section provides an overview of the software implementation of several MRMPs extracted from the frequency domain of the TWF of each spatial measurement point, as shown in Fig. 11.8. MRMPs, related to the frequency domain of the TWF are based on software procedures for estimation of the modal frequencies f_m (MF), dominant modal frequency f_d (DMF), and group delay τ_g (GD).

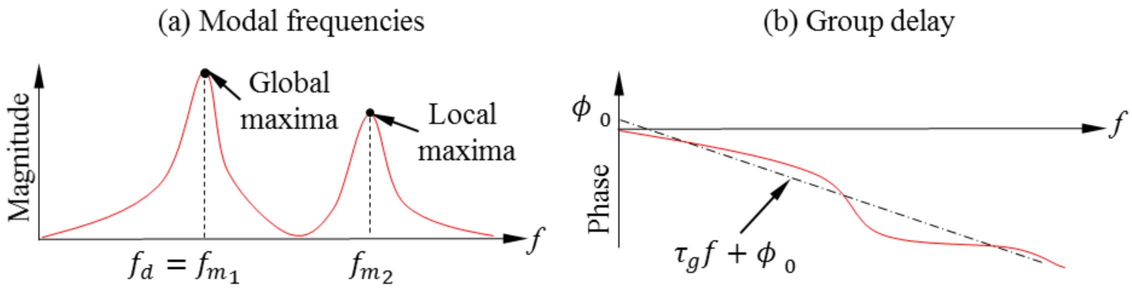

Fig. 11.8. Illustration of methods for quantification of frequency domain MRMPs: (a) graphical definition of the modal frequencies f_{m_i} (MF) and the dominant modal frequency f_d (DMF); and (b) graphical definition of the group delay τ_g (GD) defined as the slope of a linear fit to the phase in the frequency domain.

The software implementation to estimate modal frequencies is based on identification of the frequency locations, f_{m_i}, of all local maxima in the frequency domain power spectra, as shown in Fig. 11.8a. Similarly, dominant modal frequency, f_d, is the frequency location of the global maxima. The software implementation of the group delay estimation is based on the slope, τ_g, of a linear fit to the phase in the frequency domain. It should be noted that since the frequency domain of the TWF is estimated with a 1D FFT, the phase information has to be unwrapped before the linear fit.

Part 3: Validation and applications

12 Validation of the high-speed holographic systems (HHS)

In this Chapter validation of the design criteria of the HHS is presented. Validation is done through experimental and numerical methods to test the main design parameters and assumptions of each HHS model (i.e., PHHS and CHHS) based on measurements of both artificial and human samples.

12.1 Validation of the PHHS

The principle of operation of the MPDE acquisition mode of the PHHS is based on the assumption that the acoustically induced transient response of the samples is repetitive. This assumption was experimentally validated for both the samples and the PHHS, by:

- *Transient response repeatability of samples* – comparison between multiple LDV measurements of the acoustically induced transient response of each sample.
- *Validation of the DESPS* –double-exposure spatial phase sampling (DESPS) of the PHHS was compared against a conventional temporal 4-frame phase sampling algorithms based on stroboscopic recordings under steady state excitation conditions.
- *Validation of the PHHS transient measurements*
    - *Temporal repeatability* – comparison between multiple PHHS measurements of the response of each sample.

- *Temporal accuracy* – comparison of PHHS and LDV measurements of the transient displacement and velocity time-waveforms of both samples.

12.1.1 Experimental setup and sample preparation

The experimental setup of the PHHS, as shown in Fig. 12.1, includes an otoscope head (OH), described in Chapter 9, and a sound presentation module (SP) [Bapat, 2011]. The SP module consists of a calibrated microphone (Etymotic Research ER-7C) and a speaker (SB Acoustics SB29RDC-C000-4). The OH, shown in Fig. 12.1a, includes a camera (AVT Pike F505B) and an object illumination system providing 532nm laser light with 19mW/cm^2 intensity at the object plane. For validation of the transient measurement capabilities of the PHHS, a LDV is incorporated within the experimental setup.

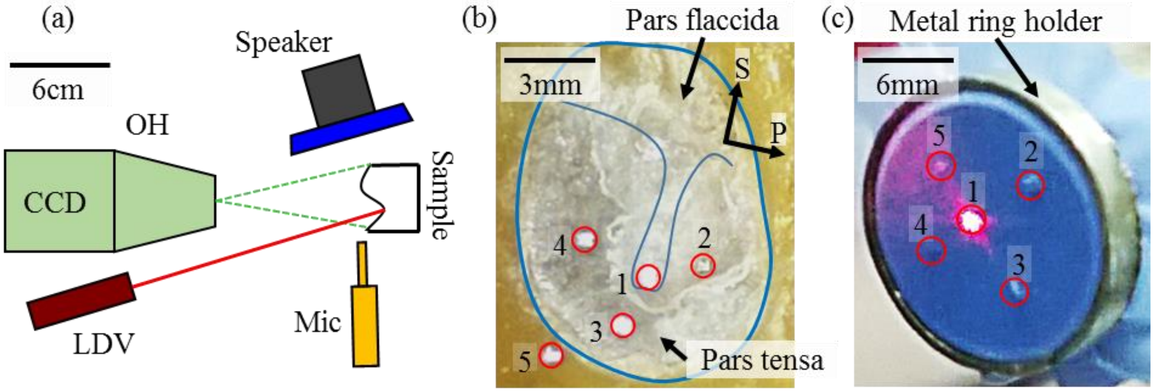

Fig. 12.1. Experimental setup and samples for validation of the PHHS: (a) schematic of the PHHS setup that includes otoscope head (OH) and sound presentation (SP) module; (b) cadaveric human TM sample; (c) circular latex membrane. The manubrium of the TM is outlined with solid line to also indicate the separation between Pars tensa and Pars flaccida in (b).

The samples used for the PHHS measurements presented in this Section include an 8mm diameter human cadaveric TM sample, shown in Fig. 12.1b, and a 10mm diameter latex circular membrane, shown in Fig. 12.1c. The human TM sample is part of a temporal bone from a 90-year-old female donor. The sample was prepared in accordance with previously established procedures [Cheng et. al, 2013]. The surface of the TM was coated with a solution of ZnO to improve the surface reflectivity and reduce required camera exposure times resulting in better temporal resolutions.

Complementary to each PHHS measurement, LDV measurements were conducted at several predefined points on the surface of each sample. In order to improve the signal quality of the LDV measurements, retro-reflective markers were applied at the predefined points of both samples. In the case of the human TM sample, as shown in Fig. 12.1b, markers were placed at the approximate centers of the umbo (Point 1) as well as the interior, inferior and posterior halves (Points 2-4) of the surface of the TM. Additionally, in order to monitor the rigid body motion of the temporal bone, a LDV marker was placed on the temporal bone close to the edge of the TM (Point 5). The markers on the latex membrane were distributed equidistantly (Points 1-5) to allow for even coverage of the surface, as shown in Fig. 12.1c.

12.1.2 Validation of the repeatability of the samples

In order to investigate the validity of the assumption behind the principle of operation of the MPDE acquisition mode, the transient response of all marked points on both samples was measured multiple times with an LDV at a sampling rate of 125 kHz and 16-bit digitization resolution. Representative results of the time waveforms and frequency domain transfer functions (TF) of the maximum and minimum response among all measurement points, at each sample, are shown in Fig. 12.2. The TF is calculated based on calibrated microphone readings of the sound pressure level near the surface of the samples [Cheng et. al, 2013]. The two LDV measurements, shown in Fig. 12.2, are temporally separated by ~1min, which is representative of the full recording time for one set of measurements with the MPDE method.

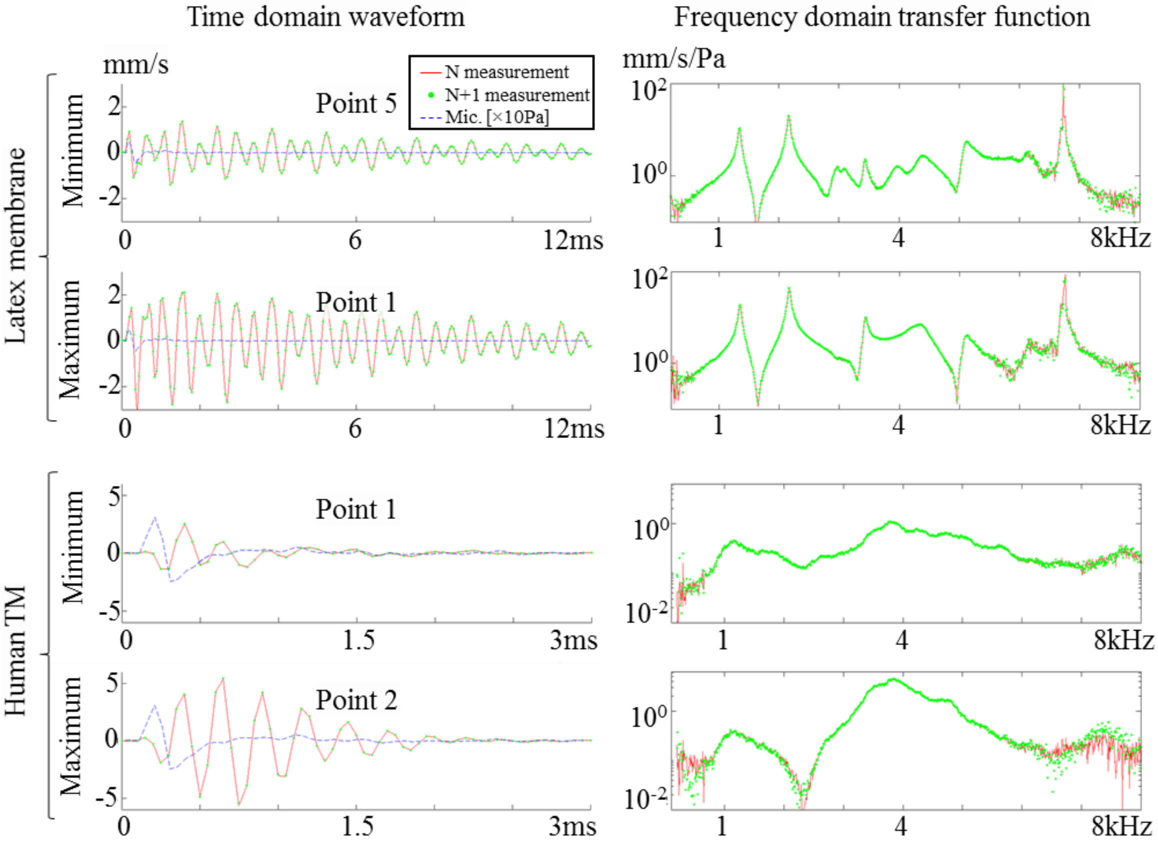

Fig. 12.2. Representative LDV measurements, in the time and frequency domains, demonstrating the repeatability of the acoustically induced transient response of the latex membrane and the human TM samples. The graphs correspond to the maximum and minimum amplitudes of time waveforms and frequency domain transfer functions across the surface of each sample of two consecutive measurements (solid and dotted lines). Measured time waveforms show >99% correlation, and frequency domain transfer functions show <3 dB variation. Maximum instantaneous sound pressure was 124 dB SPL for the human TM and 108 dB SPL for latex sample. The microphone response (Mic.) is marked with a dashed line.

The repeatability of the time waveforms of the response of all points on the surfaces of both samples is >99% based on cross-correlation between the time wavefront vectors. The deviation of the values of the local maxima and minima of the time waveforms of individual measurements is <5% of the global maximum. There is no significant temporal deviation in the locations of the local maxima and minima of the time waveforms of individual measurements within the temporal resolution of the LDV sampling (i.e., <10 μs). The frequency domain transfer function varies within <3 dB between all measurements. Response of the bony structure (Point 5 as indicated at Fig. 12.1b) of the human TM is <0.5% relative to displacement of the surface of the TM, indicating insignificant rigid-body motion.

12.1.3 Validation of the DESPS

The phase sampling (PS) method of the PHHS is based on the DESPS, which enables deformation measurements with a single frame acquisition (Chapter 7). In order demonstrate the displacement accuracy and repeatability of the DESPS, the 1-frame PS was compared against temporal 4-frame PS method, based on stroboscopic acquisition of the motion of a human TM under steady-state acoustic excitation [Rosowski et al., 2013]. Data from the 4-frame PS method were also used to extract 1-frame data for the DESPS method. Representative results of the PHHS stroboscopic measurements along with comparisons between the 1 and 4-frame methods are presented in Fig. 12.3. The difference in the displacement measurements between the 1 and 4-frame methods is shown in Fig. 12.3d. The repeatability of both 1 and 4-frame phase sampling methods was established based on the averaged repeatability at all phase positions of the stroboscopic displacement measurements, as shown in Fig. 12.3e.

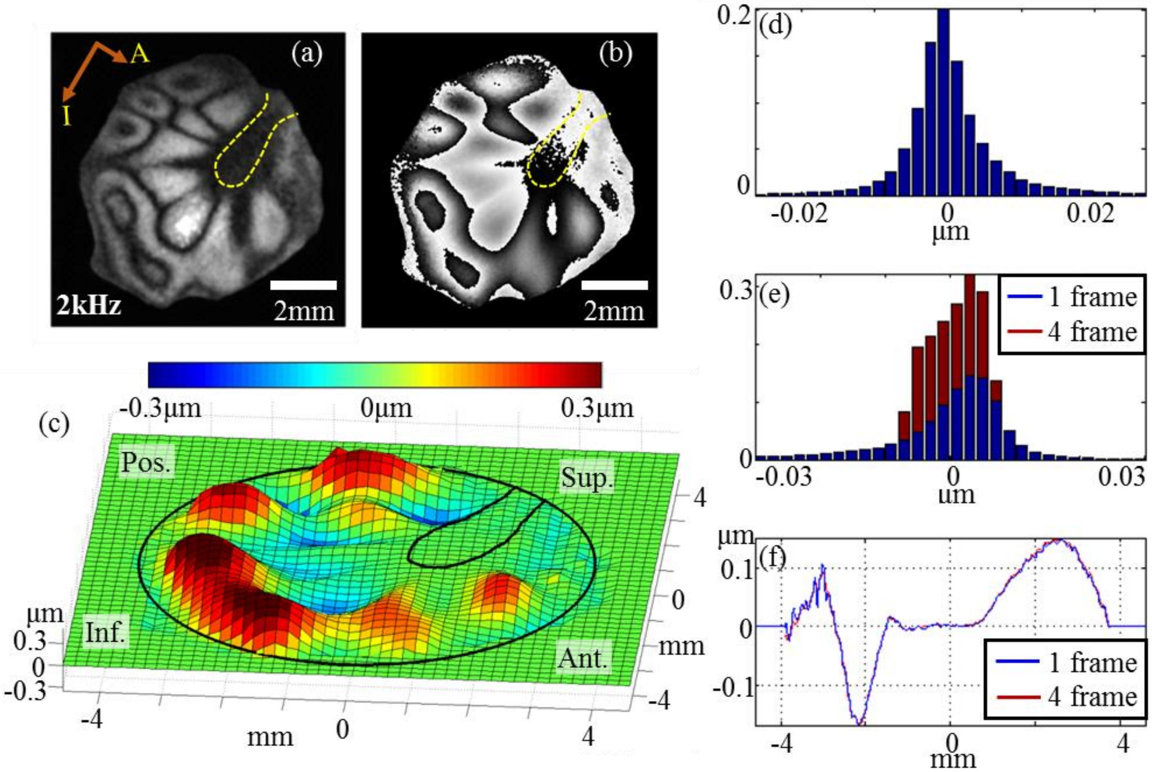

Fig. 12.3. Performance of the DESPS for stroboscopic measurements of acoustically induced vibrations of a human TM excited by 2 kHz at 92 dB SPL: (a) and (b) modulation and phase maps; (c) displacement map indicating 590 nm p-p amplitude; (d) histogram of the differences between measurements with 1 and 4 frame acquisition methods; (e) comparison of the histograms of the repeatability of measurements with 1 and 4 frame acquisition methods; and (f) anterior-posterior cross-section of the displacement maps measured with 1 and 4 frame acquisition methods. The handle, or manubrium, of the malleus is outlined in (a)-(c).

A summary of all results is presented in Table 12.1. The lower repeatability of the 1 frame algorithm is mainly attributed to the smaller amount of data (i.e., 1 versus 4 frames) and corresponding lower redundancy making the method more susceptible to measurement noise, e.g., digitization noise in the camera, non-homogeneous surface reflectivity of the TM, etc. [Furlong et al., 2002]. However, comparison between the displacement measurements of 1 and 4 frame algorithms, as shown in Fig. 12.3f, indicates no significant difference in the quantification of the spatial and temporal complexity of the displacement of the TM.

Table 12.1. Accuracy and repeatability of the 1 frame versus 4 frame phase sampling methods.

Parameter	**Value (±1σ)**	
	nm	λ normalized
Repeatability of 1 fame algorithm	9	λ /30
Repeatability of 4 fame algorithm	4	λ /65
Difference between 1 and 4 frame algorithm	9	λ /30

12.1.4 Validation of the PHHS transient measurements

To assess the repeatability of the MPDE acquisition mode of the PHHS, multiple sets of PHHS measurements for both a latex membrane and a human TM have been compared. The accuracy of the transient displacement measurement of the PHHS is quantified through comparisons with LDV.

To ensure adequate sampling of the full-field transient response of the both samples, the MPDE acquisition method's sampling rate, exposure time, and recording duration have been adjusted following acquisition design constraints indicated in Section 6.3, as well as through the analysis of the LDV measurements, shown in Fig. 12.2. The LDV measurements indicate a total duration of the transient event of <3 ms and significant frequency content of up to 8 kHz. The LDV was sampled as described in Section 12.1.2. The acoustic excitation were 100 μs clicks at 124 and 108 dB maximum SPL for the human TM and the latex membrane, respectively. Due to the relative distance between the speaker and the sample (i.e., ~5 cm), the time delay between the beginning of the acoustical excitation and the response of the sample was ~150 μs.

Based on preliminary measurements of a human TM and corresponding design parameters, the PHHS was set to 15μs exposure time (corresponding to a shutter speed of 67 kHz) and 20μs inter-frame time, equivalent to 50 kHz sampling rate. Furthermore, the exposure time was defined by the available laser light power at the object and by the light sensitivity of the camera. Although the exposure time was longer than the recommended in Section 6.3, the quality of the data was deemed sufficient for further processing.

Every transient PHHS measurements of the TM consisted of a set of 260 frames representing a time period from -0.1 ms to 5ms relative to the beginning of the acoustic excitation. Every deformed frame, corresponding to the transient response of the human TM, was related to a new reference frame recaptured at the same instance (i.e., 0.5ms) before the application of every acoustic excitation, as described in Chapter 8.

The latex membrane was measured using identical acquisition parameters as that of the human TM with the exception of the inter-frame time, which was increased to 50 μs (i.e., 20 kHz sampling rate). This accounts for the reduced range of the frequency response (i.e., <7 kHz) and the longer time waveform duration (i.e., >10 ms), as indicated in Fig. 12.2.

12.1.4.1 Temporal repeatability of the PHHS

To validate the repeatability of the PHHS measurements, three measurements of the transient time waveforms and corresponding frequency domain transfer functions (TFs) were compared. Figure 12.4 shows representative results of the maximum and minimum acoustically induced response of both samples. The repeatability at each spatial point is estimated based on the correlation of the time waveforms of every individual measurement relative to their average.

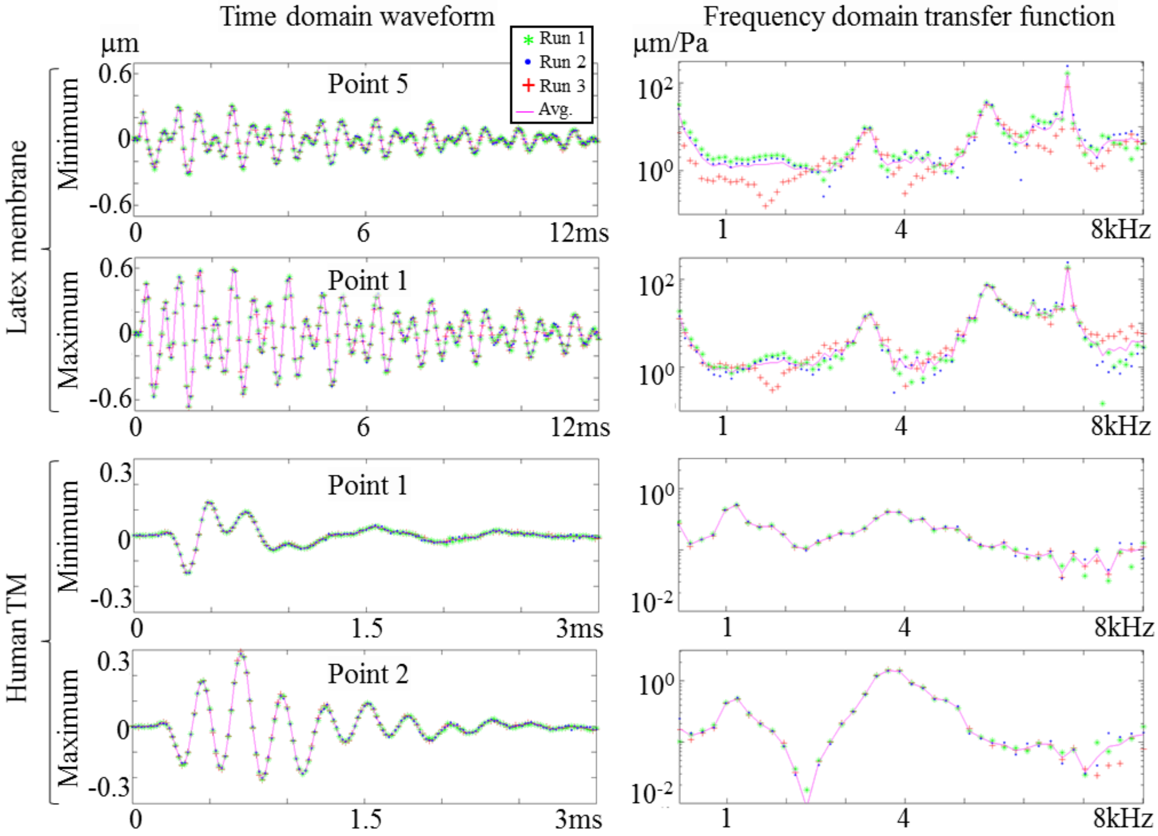

Fig. 12.4. Representative transient measurements demonstrating the repeatability of the MPDE acquisition in the PHHS. The graphs indicate the maximum and minimum time waveform and corresponding frequency domain transfer functions (TFs) across the surface of each sample at three consecutive measurements (dotted lines) and their average (solid line). Measured time waveforms show >99% correlation, and frequency domain transfer functions show <5 dB variation. Maximum instantaneous sound pressure was 124 dB SPL for the human TM and 108 dB SPL for latex sample

The temporal variation of the location of the maximum displacement positions of the time waveforms is <20 μs for both samples. The variation of the magnitudes of the maximum displacements of the time waveforms is <15 nm. Measured time waveforms show >99% correlation, and frequency domain transfer functions show <5 dB amplitude variations. The total measurement time for all three consecutive measurements is ~5min. This indicates that there are no significant variations (intrinsic or extrinsic to the system) that could degrade the repeatability of the PHHS measurements within the typical duration of the experiments (i.e., <2min).

12.1.4.2 Spatial repeatability of the PHHS

Another important parameter of the full-field-of-view PHHS is its spatial repeatability. In this case, the repeatability is defined as the correlation of the displacement map between multiple measurements at any instant of the transient motion of the sample. Figures 12.5a and 12.5c illustrate the spatial correlation of the displacement maps at three temporal instances (A, B, and C – approximately at the beginning, middle, and end of the recording) of the motion of the latex sample and the human TM of three individual measurements. Each of the three displacement maps is correlated with their temporal average. The average of the three correlation coefficients is used as a metrics for the spatial repeatability of the displacement measurements at each particular measurement instance. Figures 12.5a and 12.5c also indicate the spatial correlation metrics and the corresponding peak-to-peak amplitude of each set of repeated displacement measurements. The p-p displacements in Fig. 12.5b and 12.5d are based on the averaged displacement map of the three measurements at each time instance.

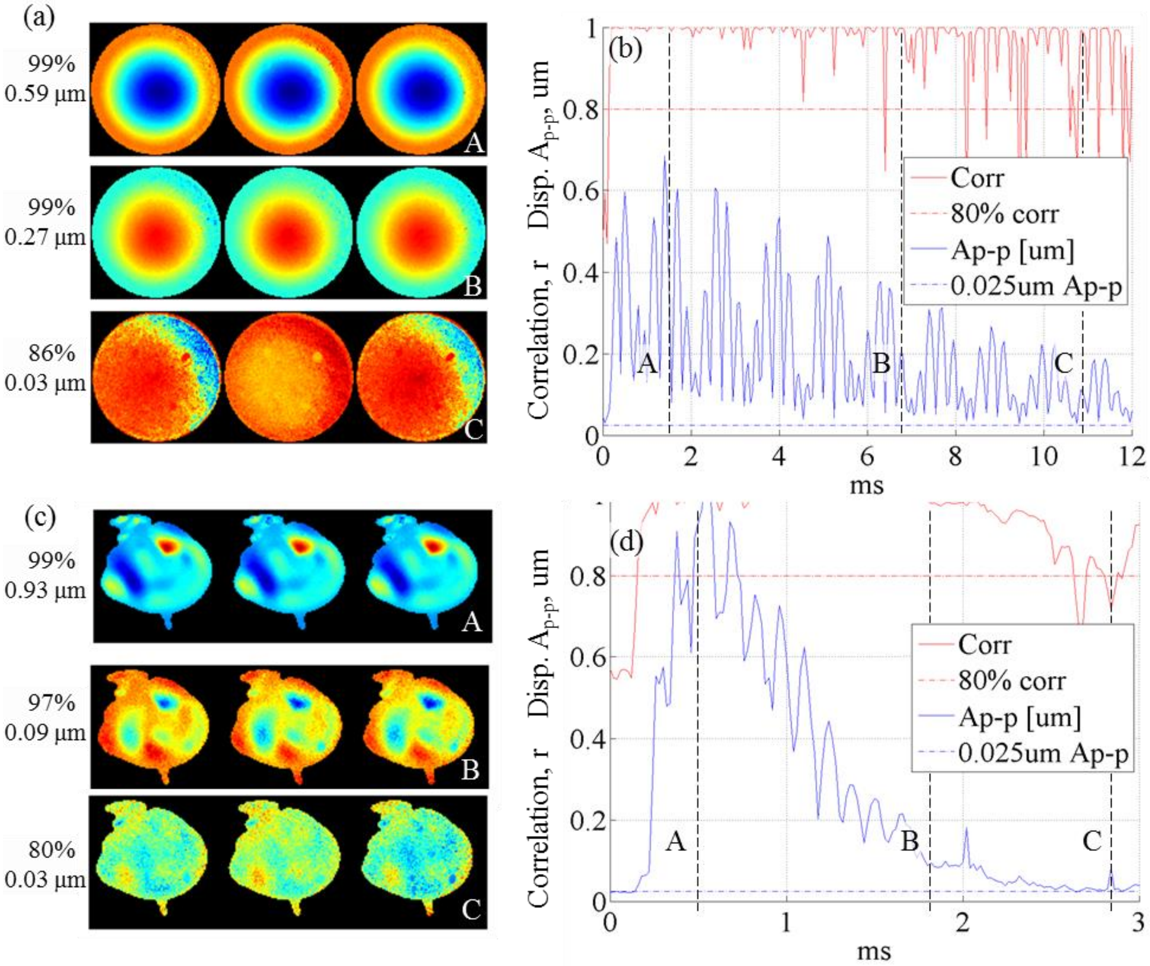

Fig. 12.5. Spatial repeatability of transient displacement measurements of latex membrane and human TM: (a) spatial repeatability of latex sample measurements at 3 time instances (A-C); (b) spatial correlation and displacement of (a) versus time relative to the displacement noise floor of the PHHS; (c) and (d) equivalent to (a) and (b) for human TM. Reference thresholds for the p-p displacement noise floor of the PHHS and 80% correlation level are indicated in vertical dotted lines in (b) and (d).

According to Fig. 12.5, the spatial repeatability is correlated with the p-p displacement, such that the repeatability decreases as the response of the sample approaches the displacement noise floor of the PHHS (i.e., <25 nm peak-to-peak). This observation is clearly noticeable in Fig. 12.5b and 12.5d, where the spatial correlations and the corresponding p-p displacements are plotted versus the duration of the measurements.

In the case of the latex membrane, the predominant mode shape of vibration, as shown in Fig. 12.5a, is similar to a (0, 1) mode shape of a circular plate. This means that most of the surface is moving in phase, resulting in near-zero instantaneous displacement at every motion cycle. This leads to cyclic variations of the corresponding spatial correlation, as shown in Fig. 12.5b. On the other hand, the human TM sample exhibits complex spatio-temporal displacement patterns, as shown in Fig. 12.5c, resulting in smaller areas of the TM passing simultaneously through a near-zero displacement. In both cases the spatial correlation is affected by the decay in the p-p displacement magnitude, as shown in Figs 12.5b and 12.5d.

12.1.4.3 Displacement accuracy of PHHS versus LDV

In order to validate the accuracy of the PHHS, its measurements were compared to LDV, as shown in Fig. 12.6. The time waveforms of both velocity and displacement were compared by integrating or differentiating the LDV and PHHS, correspondingly. Correlation between the time waveforms of the two methods is >96%. The differences in the temporal locations of the local maxima and minima of the time waveforms, measured by the PHHS and LDV, are <20 μs, which is below the temporal resolution of the PHHS that is constrained, in this case, by the available laser power. The velocity and displacement amplitude differences between the PHHS and LDV measurements are <5%, which are normalized to the maximum response of each sample.

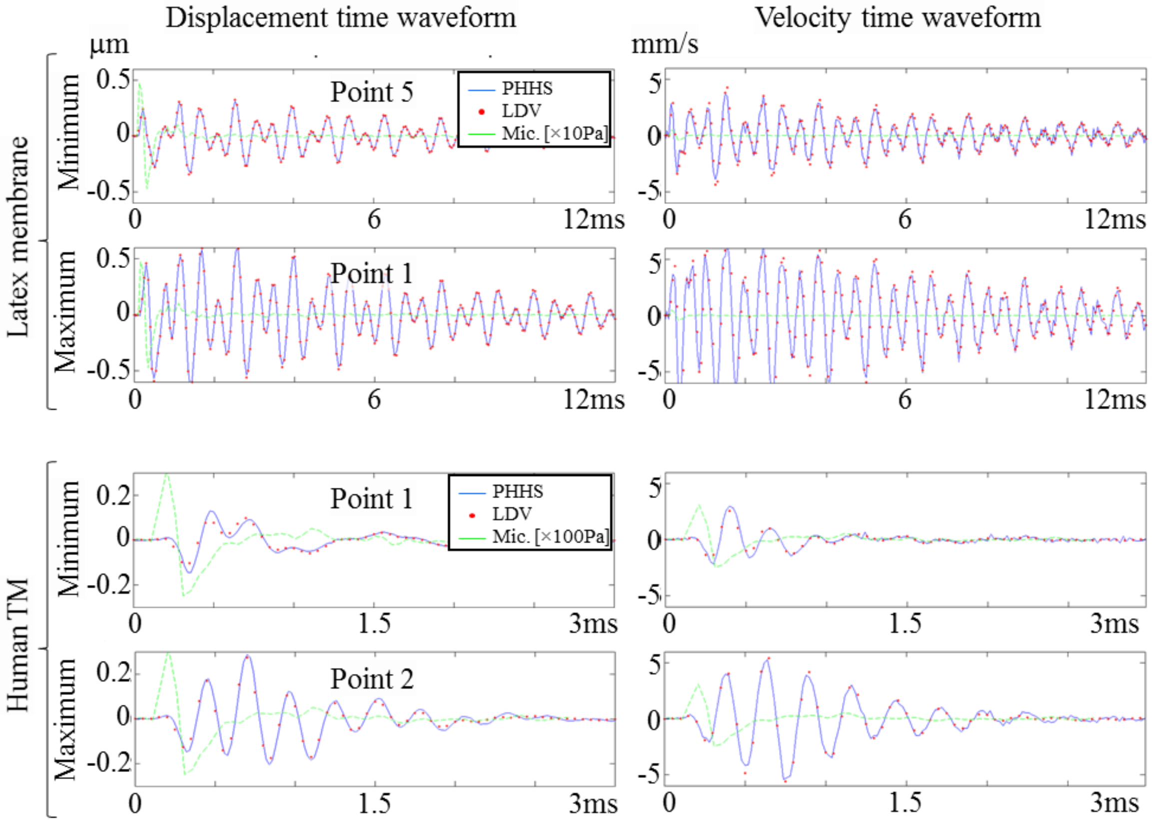

Fig. 12.6. Representative transient measurements demonstrating the accuracy of MPDE acquisition in the PHHS versus LDV. Correlation of the velocity and displacement time waveforms between PHHS (solid line) and LDV (dotted line) is >96%. Peak SPL was 124dB for the human TM and 108dB for latex sample. The microphone response (Mic.) is marked with a dashed line.

12.2 Validation of the CHHS

The measurement capabilities of the CHHS are validated with respect to accepted methodologies that include single point LDV and full-field DHS based on temporal phase sampling. In particular, validation is performed on the critical characteristics of the developed 2+1 LCPS phase sampling and HS 2+N acquisition methods by:

- 2+1 LCPS
  - *Noise floor* – quantification of the displacement of a static object with no external excitation.
  - *Displacement Accuracy* – comparison with 4-frame temporal phase sampling measurements of the steady state displacement of a statically loaded membrane.
- HS 2+N
  - *Phase stepping at high-speed* – quantification of the time constant and settling time of the response of the PZT shifter during the phase stepping procedure as described in Chapter 8.
  - *Temporal Accuracy* – comparison of CHHS and LDV measurements of displacement and velocity time-waveforms in a latex membrane sample excited by an acoustic click.

12.2.1 Experimental setup

The experimental setup for validation of the CHHS, as shown in Fig, 12.7, includes the CHHS, LDV and sound presentation (SP) modules. A detailed description of the CHHS is presented in Chapter 9. The LDV is incorporated only to provide validation of the transient measurement capabilities of the CHHS.

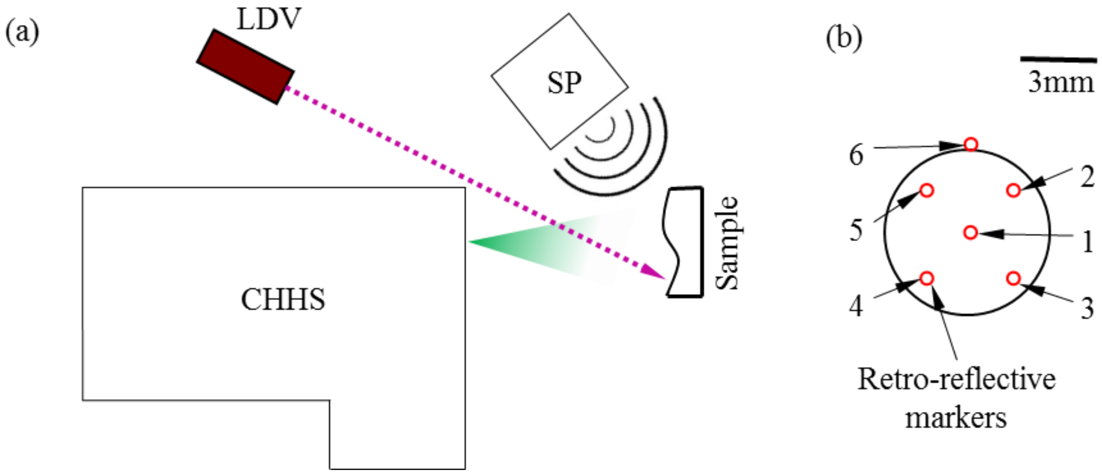

Fig. 12.7. Experimental setup and artificial sample used for validation of the CHHS: (a) schematic of the CHHS setup with sound presentation (SP) and LDV modules; and (b) latex membrane with six retro-reflective markers for LDV measurements. A LDV is incorporated as a mean to characterize the measuring capabilities of the CHHS

A schematic of a 10 mm diameter circular latex membrane used for transient measurements is shown in Fig. 12.7b. Retro-reflective markers were applied at several predefined points on the surface of the sample in order to improve the signal quality for LDV measurements. Five markers were distributed equidistantly to allow for even coverage of the latex surface (Points 1-5). A sixth marker was placed at the top of the rigid boundary of the latex membrane (Point 6), in order to monitor any rigid body motions.

12.2.2 Validation of the 2+1 LCPS method

The noise floor and accuracy of the 2+1 LCPS method were quantified relative to temporal phase sampling methods, independently of the HS 2+N acquisition method (Chapter 8), through a set of experiments performed in static conditions.

12.2.2.1 Noise floor

In order to quantify the noise floor of the 2+1 LCPS method, we measured the displacement of a solid object (i.e., 12.7 mm thick aluminum plate) under static conditions and no external excitation. We assumed that the changes of the sample during the measurements are insignificant and any detected deformations were associated with the noise floor of the phase sampling method.

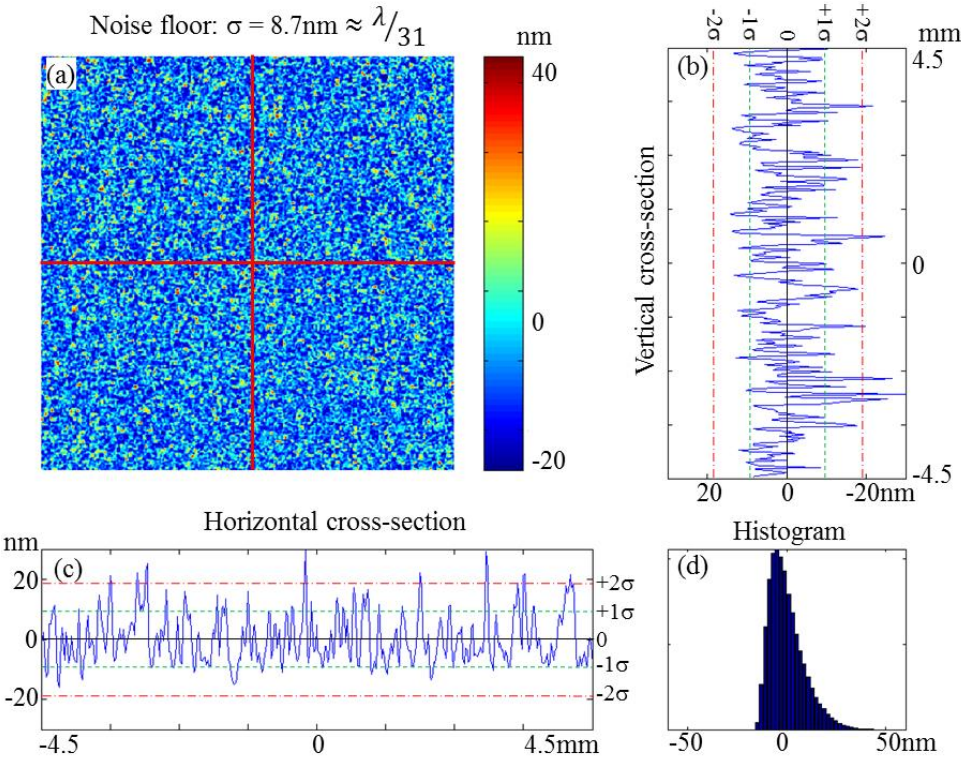

Fig. 12.8. Representative results of the spatial distribution of the noise floor of the 2+1 LCPS method under static conditions and no external excitation of the object: (a) map of the spatial distribution of the noise signal; (b) horizontal and (c) vertical cross-sections of (a); and (d) histogram of (a). The ±1σ (dashed line) and the ±2σ (dash dot line) of the noise measurement map cross-sections are highlighted.

During the noise floor measurements, all optical and sampling conditions were kept identical to the ones used during a typical measurement with the HS 2+N method

(Chapter 13). The spatial distribution of the noise floor, as shown in Fig. 12.8, indicates a standard deviation (SD) of 8.7 nm or $\lambda/31$.

12.2.2.2 Displacement accuracy

To assess the measurement accuracy, displacement measurements obtained with the 2+1 LCPS method with a 4-frame temporal phase sampling method of a statically deformed sample were compared [Rosowski et al., 2012; Khaleghi et al., 2013]. The sample was a 12 mm diameter aluminum membrane under static loading with a constant force applied normal to the back surface.

Because of the relatively long (i.e., >100ms) measurement time of the 4-frame acquisition method under static loading conditions, the camera's sampling rate was reduced to 60Hz (the minimum for Photron SA5). Aside from the sampling rate, the optical setup and illumination conditions were kept identical as those used in a typical HS 2+N acquisition (Chapter 13). Under these conditions, double-exposure displacement data sets were recorded with a 4-frame acquisition method and were used for both phase sampling methods. To compute the optical phase with a 4-frame phase sampling method, a conventional algorithm was used [Rosowski et al., 2012], whereas to compute the optical phase with the 2+1 LCPS method, only 2 of the reference and one of the deformed frames were used. The comparison of the double exposure modulation and phase maps of the 4-frame and the 2+1 LCPS methods are shown in Fig. 12.9. Based on the phase maps, the corresponding object displacements are calculated and their differences are shown in Figs 12.9e-f. The displacement differences between the two phase sampling methods are within one standard deviation (SD) of 11 nm or $\lambda/25$.

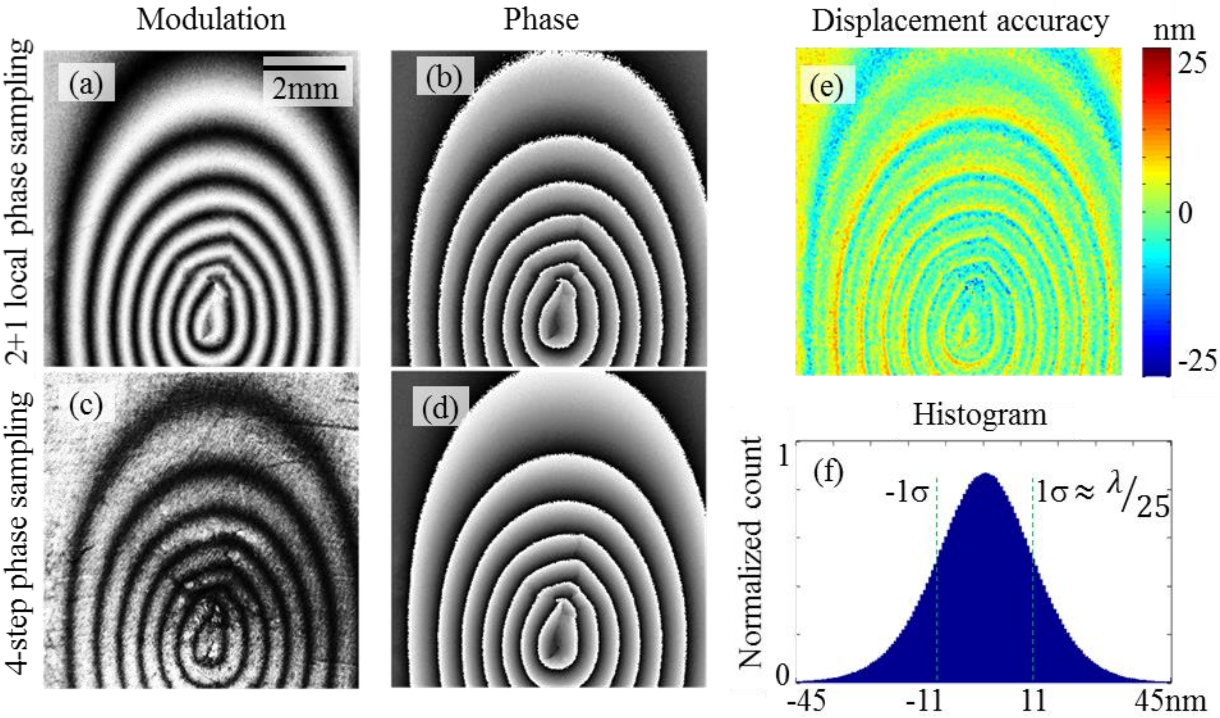

Fig. 12.9. Characterization of accuracy of the 2+1 LCPS relative to a conventional 4-frame phase sampling method: (a) modulation and (b) phase of the 2+1 LCPS method; (c) modulation and (d) phase of the 4-frame phase sampling method; (e) displacement differences between the two methods; and (f) histogram of (e). The displacement differences have a mean of 0 with a SD of 11 nm or $\lambda/25$.

12.2.3 Validation of HS 2+N acquisition method

12.2.3.1 Phase stepping at high-speed

The HS 2+N acquisition method requires one temporal phase step, which has to be properly applied in both magnitude and time as it governs the accuracy of the phase sampling. The temporal accuracy of the phase step is dependent on the dynamic characteristics of the phase shifter [Physik Instrumente, 2014], which has to have a settling time in the order of few milliseconds in order to be applied in the HS 2+N method. The dynamics of the phase shifter used in the CHHS was characterized by LDV, as shown in Fig. 12.10. Analysis of the data indicate a 0.5 ms time constant, <1.5 ms settling time based on 6% residual fluctuations, and a noise floor of <4% of the maximum response.

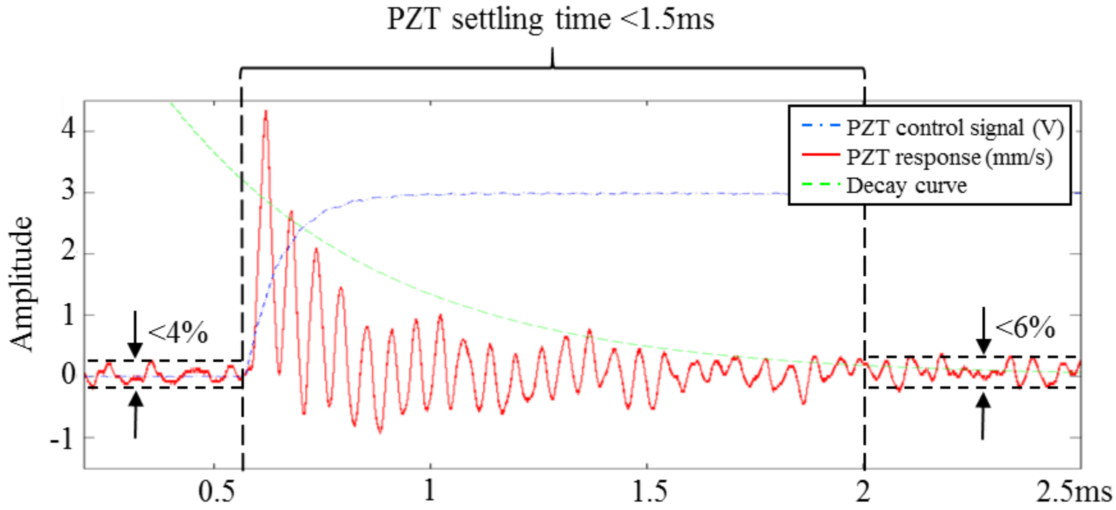

Fig. 12.10. Representative results of the velocity time-waveform of the response of the PZT phase shifter (PS) indicating 0.5 ms time constant, <1.5 ms settling time with <6% residual vibrations relative to the maximum response. The PZT control input (dash dot line), PZT velocity response (solid line), and fitted decay curve (dashed line) are shown.

12.2.3.2 Temporal accuracy

The temporal accuracy of the HS 2+N acquisition method was characterized relative to a LDV by correlating LDV and CHHS measurements under controlled transient acoustic stimulation of a latex sample. The LDV sampled the motion at the 6 Points indicated in Fig. 12.7. In order to characterize the accuracy in position and velocity, and due to the CHHS and LDV measuring domains, time waveforms were either differentiated or integrated.

The CHHS was set at a sampling rate of 42 kHz (corresponding to 23.8μs inter-frame time) with 6.62 μs exposure time (corresponding to a shutter speed of 151 kHz), in order to be consistent with the sampling parameters specified in Table 6.3. With these settings, the high-speed camera has a spatial resolution of 384×384 pixels corresponding to a lateral resolution on the order of 25 lines/mm at the imaging plane. The LDV was sampled at 84 kHz through a 16-bit analog input at the I/O module. Figure 12.11 show representative CHHS and LDV displacement and velocity results, corresponding to two discrete locations on the sample, as identified in Fig. 12.7. The locations were identified as points having the minimum (Point 5) and the maximum (Point 1) responses. The acoustical excitation was a 50 μs click with a peak SPL of 104 dB.

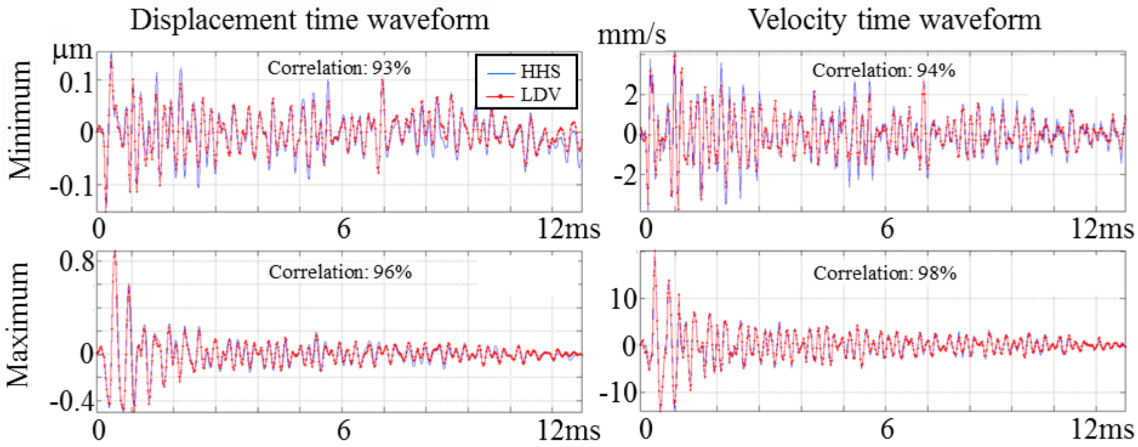

Fig. 12.11. Representative results of the temporal accuracy of the HS 2+N acquisition relative to LDV based on the minimum (Point 5) and maximum (Point 1) responses of the latex membrane. Acoustic excitation was a 50 μs click with a peak SPL of 104 dB. The time axis is relative to the beginning of the transient acoustic stimuli. Correlation between the time waveforms of each method is on average >95% for both displacement and velocity.

Correlation between the time waveforms is on average >95% for both displacements and velocities of all Points (1-5) identified in Fig. 12.7. The average amplitude differences between the time waveforms are <5% relative to the p-p response of the sample. Differences between temporal locations of the local maxima and minima in the time waveforms of the CHHS and LDV are within 10 μs.

12.3 Numerical simulation of an acoustic impulse

The transient propagation of acoustic waves in air is the first stage of the complex acousto-mechanical response of a human TM excited by pulsed acoustic stimuli. In order to better understand how this stage affects the temporal and spatial resolution requirements on the acquisition methods, as described in Chapter 6, the transient propagation of sound waves in air was modeled and studied by Finite Element Methods (FEM) based on the solution of the Helmholtz equation [Khaleghi et al., 2014b].

12.3.1 FEM simulation of transient response of an enclosed air volume

The domain analyzed by FEM consists of a disk of air with a 20mm diameter and 0.1 mm (100 μm) thickness, as shown in Fig 12.12. The acoustic excitation was provided by three point sources in order to mimic the larger size of a real acoustic source [Bapat, 2011]. The sources were arranged at the right boundary of the membrane, spanning a total of 4mm width, which is representative of the diameter of the sound guide tubes for the SP module in the OH, as described in Chapter 9. The temporal profile of the acoustic loading function was defined as a Gaussian impulse with a peak time of 8 μs and volumetric velocity amplitude of 4 m^3/s per unit of depth. The peak time of the impulse results in a frequency bandwidth of 114 kHz. In order to allow for adequate discretization of the spatio-temporal evolution of the model, a mesh size of <0.5 mm and a time step of 0.437 μs where chosen, resulting in >6 spatial and >20 temporal points per wavelength at the maximum frequency bandwidth. The mesh was composed of a planar-type 2D triangular elements and the FEM was based on solution of the Helmholtz equation. The sizes of elements of the mesh were in the range of 6-100μm. Several iterations of the simulation were executed with various maximum mesh element size and time step to find a stable solution. A hard boundary condition at the periphery of the domain ensures lossless reflection of the wavefronts relative to the local surface formal at the boundary.

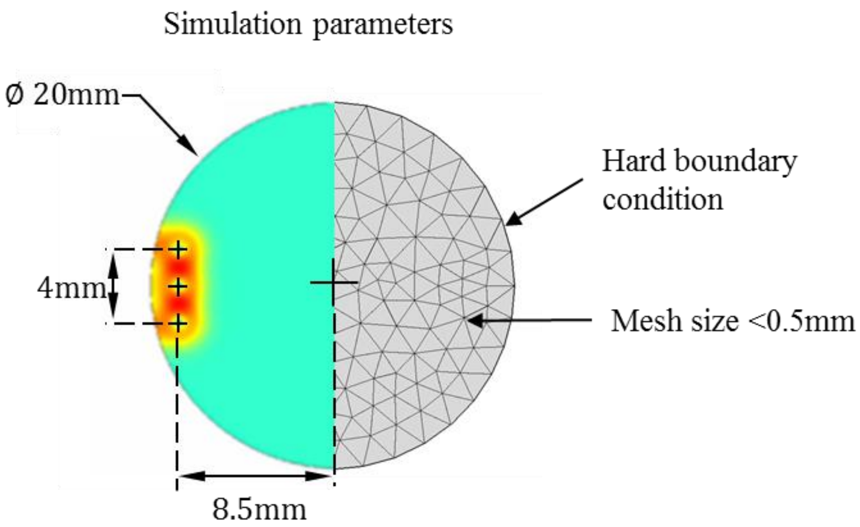

Fig. 12.12. Illustration of the geometrical parameters and boundary conditions used for FEM simulation of transient response of an enclosed air volume in 2D. The temporal profile of the acoustic loading was defined as a Gaussian impulse with 8 μs peak time and a volumetric velocity amplitude of 4 m^3/s per unit of depth.

12.3.2 Spatio-temporal evolution of an acoustic impulse in air

Figure 12.13 shows the first 100 μs of simulated spatio-temporal evolution of impulse-generated sound pressure wave within the FEM domain. The simulated spatio-temporal evolution of the acoustic pulse indicates four main stages:

- *Initiation* – the first 15-20μs of the evolution corresponding to the energy transfer between source and the surrounding air.
- *Propagation* – corresponds to the propagation of the acoustic energy from the source, through the air, to the work volume boundaries approximately 25-55μs after the application of the acoustic impulse.
- *Reflection* – interaction between the pressure wavefront and the boundary of the work volume occurring approximately 55-75μs after the application of the acoustic impulse. Due to the hard boundary condition at the periphery of the domain, the impinging pressure wavefront undergoes lossless reflected in a direction relative to the local surface formal at the boundary.
- *Interference* – wavefronts reflected from different sections of the boundary region interfere with each other after ~80μs, thus creating a spatio-temporal pressure distribution with constantly growing complexity.

Due to the constantly growing complexity of the spatio-temporal pressure distribution during the interference stage, as shown in Fig. 12.13, successful measurements and analysis should be focused on the preceding stages. It should be noted that it takes approximately 25-35 μs for the pressure waves to cover an area similar to the size (i.e., 8-10mm) of the surface of the human TM, which confirms the corresponding design requirements for the HHS, as described in Chapter 6. This means that quantification of the initial energy transfer, between source, the surrounding air, and the TM surface, would require inter-frame time corresponding to a fraction of the duration of the initiation stage in the FEM model, resulting in required sampling rates on the order of 80 -100 kHz.

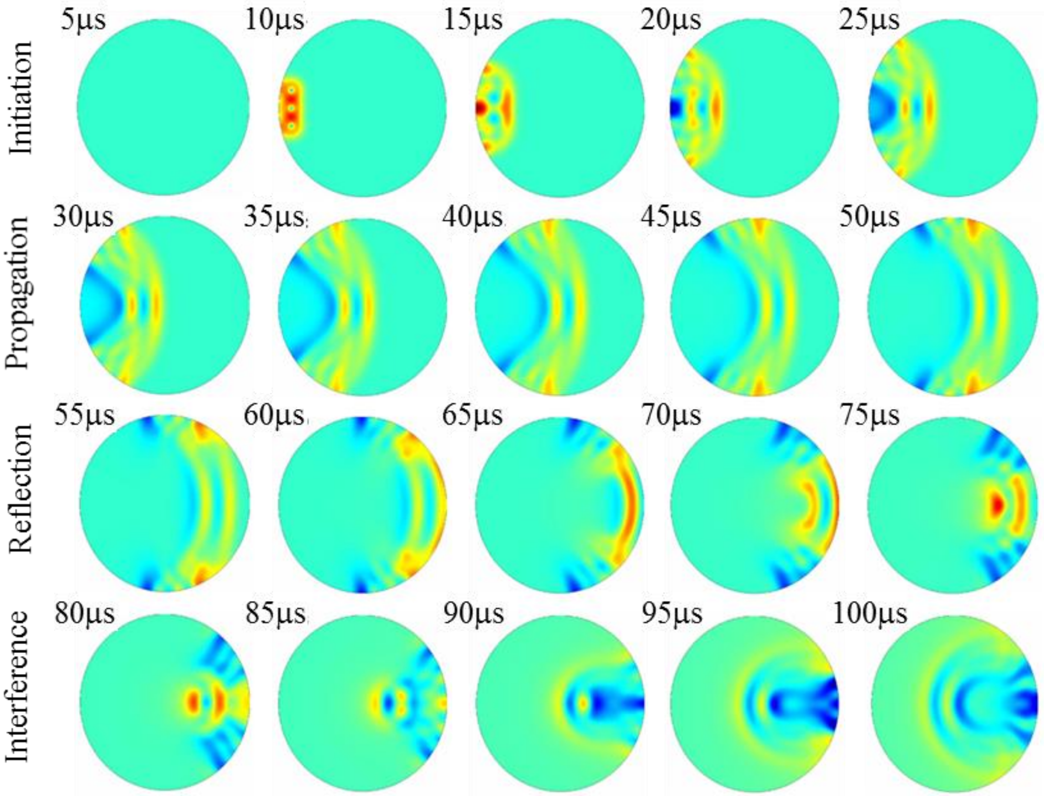

Fig. 12.13. Representative results from a FEM simulation of the spatio-temporal evolution of a pressure variation within a circular shell of air subjected to a local impulse pressure stimulus. The simulations indicate four main stages: initiation, propagation, refection, and interference. Computed pressure wavefront propagation speed is 338m/s, which is within 1% of the theoretical speed of sound in air under standard temperature and pressure.

13 Applications

This Chapter describes the application of the high-speed holographic system (HHS) for the quantification of the transient response of the human TM excited by pulsed acoustic or mechanical stimuli. Included are also preliminary results on *in-vivo* applications in clinical conditions.

The HHS systems allow for quantification of the response of the TMs of humans and other mammals under several types of excitation and environmental conditions. This Chapter includes applications of the HHS for:

- Behavior of a chinchilla TM under single tone excitation – time-averaged and stroboscopic measurements of a chinchilla TM under single tone excitation using the Pulsed-HHS (PHHS) and the OH. Representative results on the modal frequency and mode shapes of vibration under single tone excitations in range of 1-10 kHz.

- Behavior of a human TM under transient excitation – high-speed full-field transient measurements of a human TM under impulse excitation with acoustic and mechanical sources. Representative results of the Continuous-HHS (CHHS), in the form of spatio-temporal displacement data cubes (STDDC), are presented and used for data mining and interpretation of medically relevant motion parameters (MRMP).

- *In-vivo* measurements of a human TM.

13.1 Data mining of medically relevant motion parameters from experimental data

This Section discusses challenges related to the application of the parallel data mining and interpretation (PDMI) methods, as discussed in Chapter 11, for quantification of medically relevant motion parameters (MRMP) from experimental data of the transient response of the TM and middle-ear structures.

13.1.1 Time domain MRMP

Figure 13.1 shows an example of one time waveform (TWF) based on the average of 3 consecutive measurements, indicating measurements noise and corresponding challenges with the data mining of time domain MRMPs such as the global peak time t_g (GPT), first local peak time t_f (FLPT), response time, t_r (RT), and the time constant τ (TC).

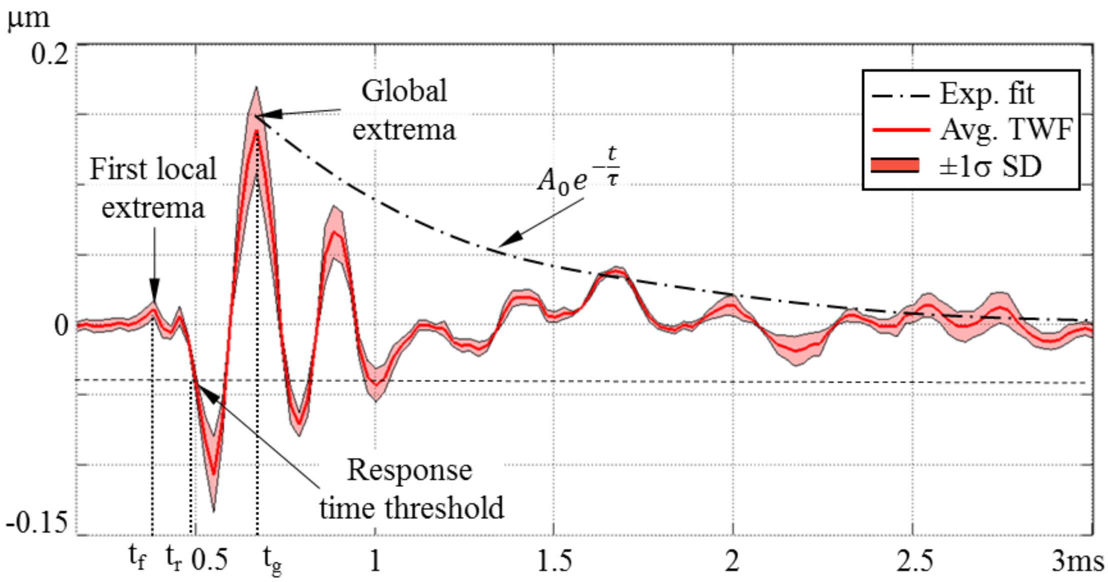

Fig. 13.1. An example of the data mining of time domain MRMPs based experimental data of the TWF of one spatial point on the surface of a human TM excited by an acoustic click. The TFW indicates the average and standard deviation (SD) of 3 consecutive measurements.

Since the GPT is based on the global extrema, the data mining process finds the global maxima and minima and compares their absolute values. However, the presence of noise and combined with the approximately similar absolute values of the global minima and maxima could result in inaccurate identification of the global extrema. In the example given in Fig. 13.1, the global maxima is 0.139±0.03 μm and the global minima is -0.107±0.027 μm, which means that identification of the global extrema can be ambiguous (within half a cycle) if only one of them is used for estimation.

The first local peak of the TWF is often with very low (i.e., <30 nm) absolute value, thus it can be mixed with significant noise where the signal to noise ratio (SNR), defined as the ratio of the local peak to the noise floor, is <3. Under such conditions, an ambiguous identification of the FLPT could occur. In the case of the TWF in Fig. 13.1, a possible unwrapping error in the temporal range of 0.3-0.5 μs results in two possible values (i.e., 0.35 μs and 0.45 μs)for the FLPT with a displacement difference of <5nm. Based on user defined thresholds, the significance (i.e., SNR>3) of the value of the first local peak is automatically checked before estimation of the FLPT.

The RT is defined based on the magnitude of the GPT, as described in Chapter 11, and its quantification in the presence of noise poses challenges analogues to the GPT. Additionally, typical user controlled threshold level is 20-30% of the global extrema, which requires validation of the significance (i.e., SNR >3) of the data.

Estimation of the TC is based on a single tonal decay model; however, the TWF of the response of each point of the human TM could be superposition of several harmonics. The multi-harmonic repose of the TM, as seen in the 1-2 ms range of the TWF in Fig.

13.1, could result in lower (i.e., $R^2 < 0.8$) confidence of the single tone decay fit. Additionally, any residual quasi-static deformation of the sample at the end of the TWF could also result in abnormally long TC. This can be partially avoided by removing the quasi-static (i.e., <200 Hz) motion component at each TWF, as described in Chapter 11.

13.1.2 Frequency domain MRMP

Figure 13.2 shows an example of a transfer function (TF) based on the average of 3 consecutive measurements, indicating measurement noise and corresponding challenges with the data mining of frequency domain MRMPs such as modal frequencies f_m (MF) and dominant modal frequency f_d (DMF).

Since the evaluation of the MF is based on estimation of frequencies of the local maxima (local peak detection) of the TF, the software allows user control over the minimum inter-peak frequency and amplitude difference, minimum absolute amplitude (amplitude limit), as well as maximum frequency (frequency limit). The minimum inter-peak frequency difference parameter controls the minimum distance, along the frequency axis, between two neighboring possible local peak locations in order to avoid selecting too many (i.e., >10) MF in the presence of noise. The minimum inter-peak amplitude difference parameter controls the minimum distance, along the amplitude axis, between two neighboring possible local peak locations in order reduce the effects of noise. The maximum frequency and minimum amplitude parameters define the search range for MF based on the displacement noise floor and the maximum sampling rate of the HHS.

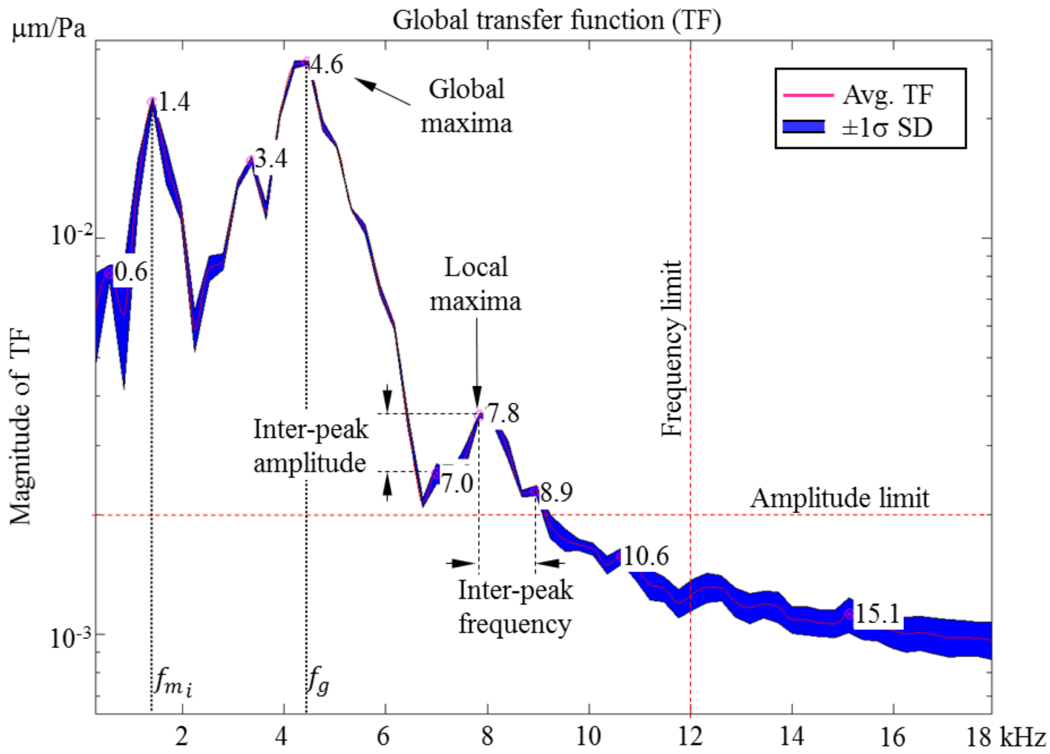

Fig. 13.2. An example of the data mining of frequency domain MRMPs based on experimental data of the TWF of one spatial point on the surface of a human TM excited by an acoustic click. The TFW indicates the average and standard deviation (SD) of 3 consecutive measurements. The values of the modal frequencies (MF) at the local maxima are indicated in kHz.

The DMF is based on the MF corresponding to the global maxima of the TF. However, the presence of noise combined with the approximately similar amplitudes of neighboring MF could result in inaccurate identification of the DMF. In the example given in Fig. 13.2, the DMF, located at 4.6 kHz, has an amplitude within less that 2 dB of the MF located at 1.4 kHz.

13.2 Behavior of chinchilla TMs under single tone excitation

In this Section, representative results of the use of HHS to quantifying the full-field nanometer scale displacements of chinchilla TMs under steady state (tonal) excitation are described. The experimental setup was similar to the one described in Section 12.1. Measurements are performed in both time-averaged and stroboscopic modes. In the measurements chinchilla TM samples, approximately 6mm in diameter, were prepared following previously established procedures [Cheng et al., 2013]. The surfaces of the TMs were coated with a solution of ZnO to improve the surface reflectivity and to reduce the required camera exposure times in order to obtain suitable temporal resolutions. .

13.2.1 Time-averaged measurements

In the first step of the steady state measurements, modal frequencies of the samples are identified by the use of time averaged holography [Rosowski et al., 2009]. Figure 13.3 shows modulation images of HHS time-averaged recordings in the frequency range of 1-10 kHz, indicating simple, complex and ordered modal patterns corresponding to the mode shapes of vibration of a chinchilla TM.

Acquisition was done with 10ms exposure time, ensuring >5cycles of TM motion during each camera exposure time, allowing for optimal fringe contrast [Rosowski et al., 2009].

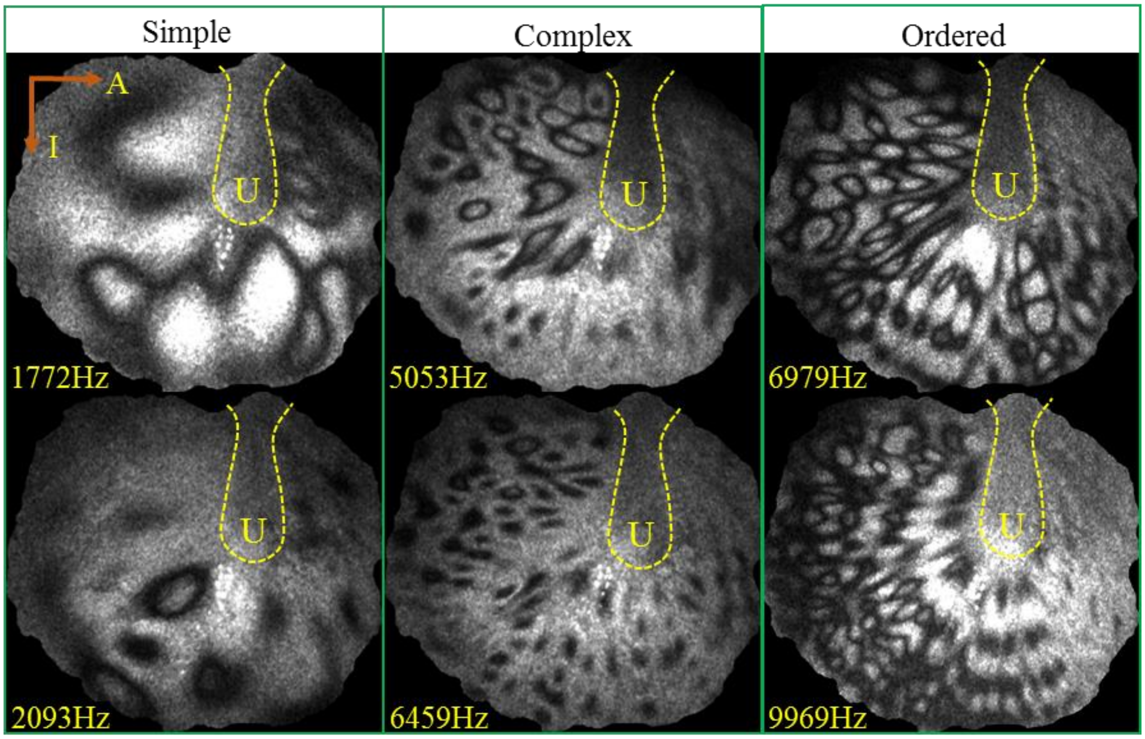

Fig. 13.3. Simple, complex and ordered modal patterns of an acoustically excited postmortem chinchilla TM recorded in time-averaged mode. The handle, or manubrium, of the malleus is outlined with dashed line. The umbo at the end of the handle near the center of the TM is labeled with a "U."

13.2.2 Stroboscopic measurements

To quantify the displacements for each identified modal pattern, the stroboscopic acquisition mode of HHS was utilized in double exposure (DE) mode [Socorro et al., 2009; Cheng et al., 2013]. Figure 13.4 shows the modulation, phase and displacement map at one phase of the harmonic motion of the TM excited by 6979 Hz at 91dB SPL acoustic stimuli. The interferometric DE wrapped phase for each stroboscopic position, as shown in Fig 13.4b, are analyzed to quantify the corresponding displacements, shown in Fig. 13.4c. Acquisition was done with <5% duty cycle relative to the excitation frequency, allowing for optimal fringe contrast [Cheng et al., 2013].

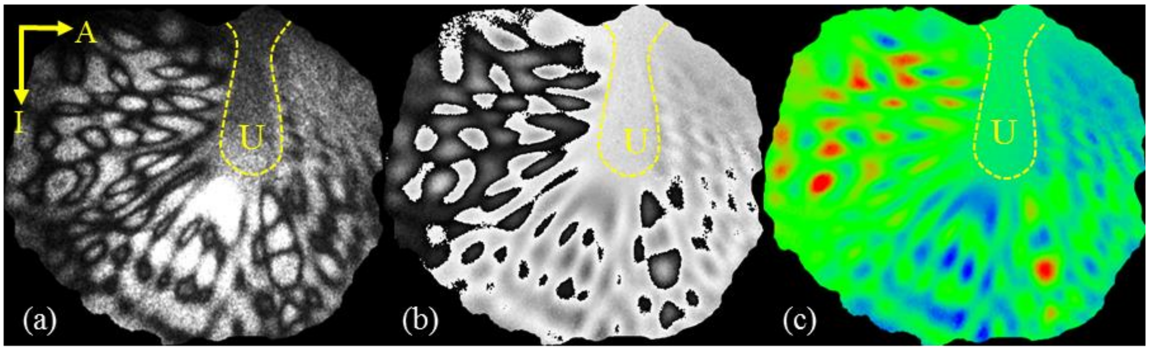

Fig. 13.4. Measurement of an amplitude distribution of the chinchilla TM at a sound excitation frequency of 6979 Hz and 91 dB SPL: (a) modulation map; (b) a full-field-of-view wrapped phase map; and (c) a displacement map across the TM corresponding to 389 nm p-p maximum amplitude. Data were recorded in stroboscopic acquisition mode with the HHS. The handle, or manubrium, of the malleus is outlined with dashed line. The umbo at the end of the handle near the center of the TM is labeled with a "U."

By recording and analyzing every phase position throughout one full cycle of the stroboscopic recording, the full-field displacement of the chinchilla TM is quantified. Figure 13.5 shows quantified displacements corresponding to different stroboscopic phase instances in the range of 0-270°.

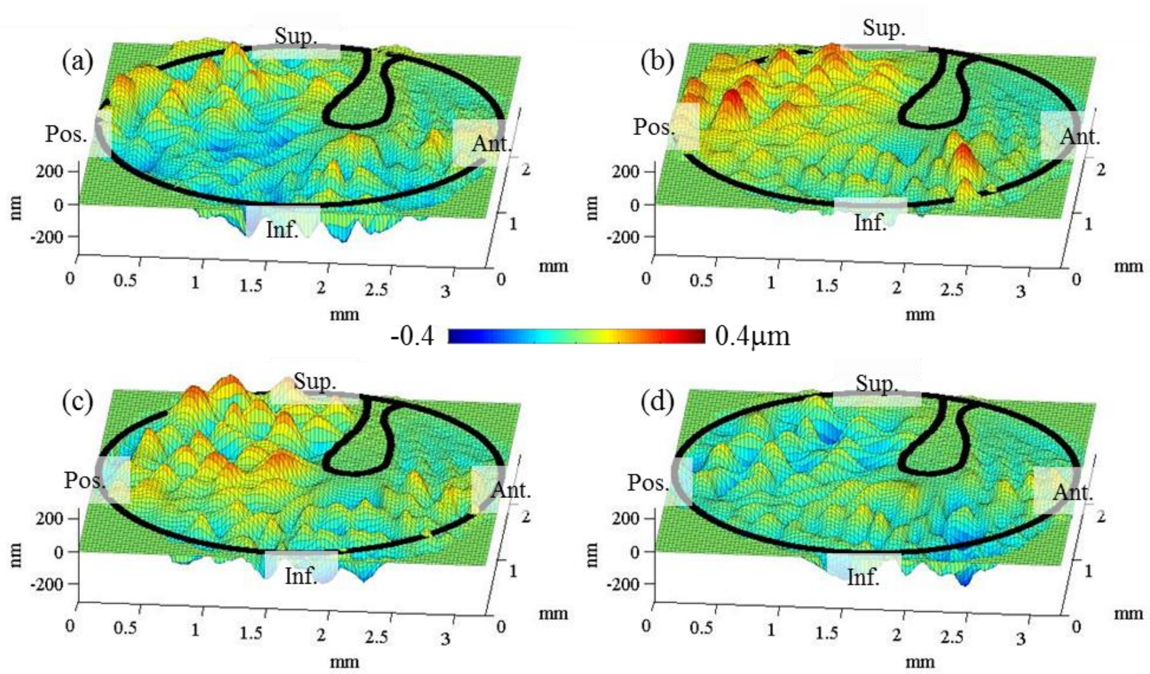

Fig. 13.5. Displacement maps of a postmortem chinchilla TM at stroboscopic phase positions with 90°increments throughout its vibration cycle. The TM was excited with single tone at 6979 Hz with 91 dB SPL producing a p-p amplitude of 389 nm. Repeatability of the displacement maps at each phase position is approximately λ/35 (<8 nm). The handle, or manubrium, of the malleus is outlined with solid line.

13.3 Behavior of the human TM under transient excitation

In this Section, representative results of the use of CHHS model of the HHS to quantifying the full-field nanometer scale displacements of human TMs under transient (wideband) excitation are described. Samples are excited by either acoustic or mechanical means. Representative results of the CHHS, in the form of spatio-temporal displacement data cubes (STDDC), are presented and used for data mining and interpretation of medically relevant motion parameters (MRMP).

13.3.1 Acoustic excitation

13.3.1.1 Experimental conditions

The experimental setup used for measurements of the acoustically induced transient behavior of the TM consist of the CHHS, LDV, and sound presentation (SP) module, as described in Section 12.2. LDV is incorporated to validate the transient measurement capabilities of the CHHS.

The TM sample used is part of a cadaveric temporal bone from a 46-year-old female donor. The sample was prepared in accordance with previously established procedures [Cheng et al., 2013]. Complimentary to each CHHS measurement, LDV measurements of the TM sample were conducted at two points on the surface of the TM. Point 1 was positioned at approximately the center of the membrane near the ‘umbo’, which is the connection between the TM and the inferior tip of the malleus, the most lateral of the ossicles. Point 2 was positioned at approximately the center of the anterior half of the surface of TM. A third LDV point, at the bony structure close to the boundary of the TM, was used to monitor the rigid body motions of the temporal bone. Retro-reflective markers were placed at each point to improve the signal quality of the LDV measurements, analogue to the procedures described in Section 12.2.

Acoustic excitation for all dynamic measurements were based on a 50 μs acoustic click produced by the signal generator in the I/O module and introduced to the sample by the speaker in the SP module. Figure 13.6 shows temporal and frequency characteristics of the acoustic excitation signal produced by the SP, indicating a settling time of 3 ms and flat frequency response

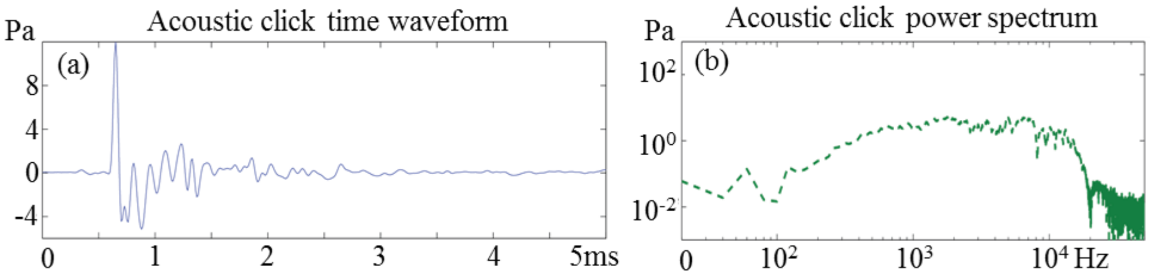

Fig. 13.6. Time waveform (a) and power spectrum (b) of an average of 20 acoustic clicks indicating 10Pa, or 115dB peak SPL, measured with a calibrated microphone that is part of the sound presentation (SP) module.

The acoustic source was positioned approximately 12cm away from the sample, resulting in a 350μs acoustical transmission delay, which was taking into consideration for both acquisition and representation of data shown in this Section.

Preliminary LDV measurements of the response of the TM at the umbo indicate a total duration of the transient event of <4ms. Frequency analysis of the response indicates significant frequency content up to 11 kHz. The delay between the acoustical excitation and the response of the sample was within the estimated transmission delay. The LDV was sampled at 84 kHz through a 16-bit analog input at the I/O module.

In order to adequately sample the full-field transient response of the human TM, the CHHS camera's sampling rate, exposure time, and recording duration were adjusted to be consistent with the acquisition design constraints, as specified in Section 6.3, while taking into consideration the preliminary LDV measurements. The CHHS was set at a sampling rate of 42 kHz (corresponding to 24μs inter-frame time) with 6.62 μs exposure time (corresponding to a shutter speed of 151 kHz). The duration of every measurement was set to 1000 frames corresponding to a period from -2.5 ms to ~20ms relative to the beginning of the acoustic excitation. While the settling time of the human TM is <5ms, as described in Table 6.3, more frames were collected after the settling of the sample, in order to allow for precise estimation of the background component (DC) of the holographic data, as described in Section 8.2.

13.3.1.2 Full-field transient measurements of a human TM

Representative full-field measurements of the spatial, temporal and frequency measurement capabilities of the CHHS, based on the acoustically induced transient response of a human TM, are shown in Fig 13.7. Displacement time-waveforms of the response of the umbo (point 1), as shown in Fig 13.7a, indicate >90% correlation between the CHHS and LDV measurements above the noise floor (<11 nm) of the CHHS. The average correlation of the time waveforms of the CHHS and LDV at points 1 and 2 on the TM's surface was determined to be better than 94%.

Based on the frequency domain of the CHHS and the calibrated microphone measurements of the displacement and acoustical pressure time-waveforms, the transfer function (TF) of each point across the surface of the TM can be calculated [Cheng et al., 2013]. Using a numerical method, described in Section 11.1, the modal frequencies corresponding to the local maxima of the TF can be automatically identified. Due to the short duration of the transient event (i.e., <5 ms), frequency components <200 Hz (i.e., > 5ms period) are excluded from the local maxima search algorithms. With the exception of the lowest modal frequency (0.98 kHz, which was not identifiable in the LDV), there was a less than 5% difference between CHHS and LDV determined modal frequencies.

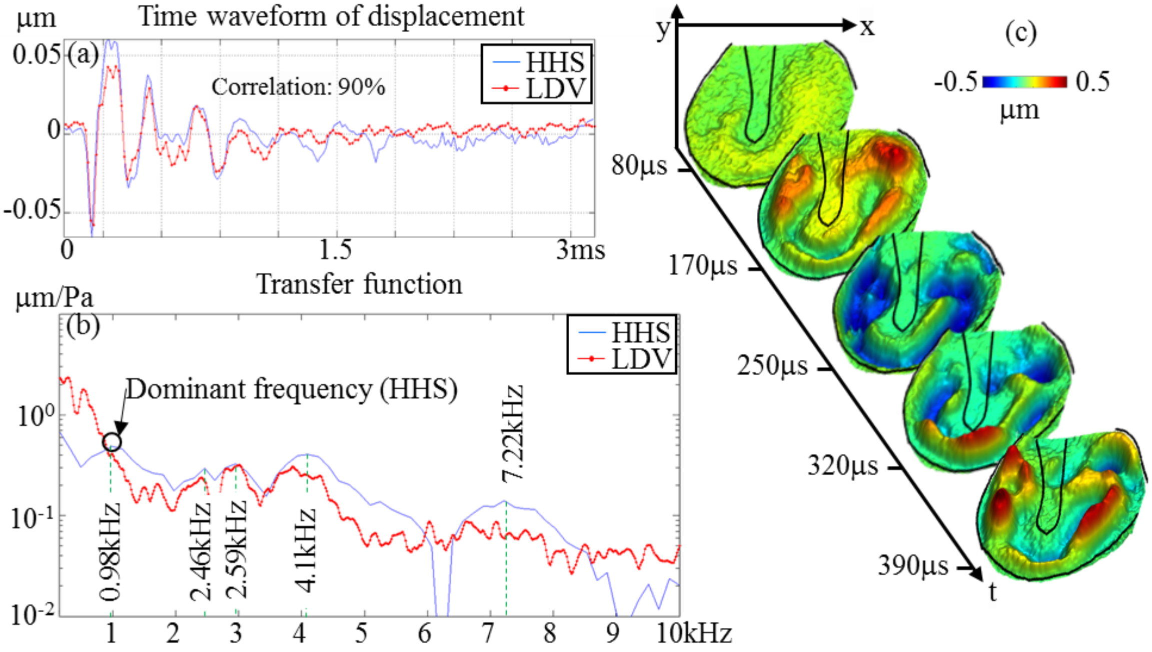

Fig. 13.7. Representative measurement of the spatial, temporal and frequency measurement capabilities of the CHHS based on the acoustically induced transient response of a human TM sample: (a) displacement versus time waveform of the umbo measured with CHHS and LDV indicating 90% correlation of the time waveforms; (b) magnitude of the displacement transfer function (TF) at the umbo measured with CHSS (solid line) and LDV (dotted line); and (c) representative spatio-temporal evolution of the TM deformations after sample excitation, as obtained by CHHS. Vertical dashed lines in (b) indicate the locations of automatically determined modal frequencies. Outlines of the outer boundary of the membrane and the manubrium in (c) are indicated with solid lines.

Based on the numerical methods discussed in Chapter 11, the displacement measurements at each deformed frame of the CHHS can be converted into a STDDC representing the transient response of the human TM. Analysis of the STDDC indicates that the spatio-temporal deformations of the TM are characterized by two distinct stages: (1) global initiation of the surface motion, and (2) propagation of local surface waves. These stages are consistent with the FEM predictions that are presented in Section 12.3. The first 30-100 µs of the initiation stage, shown in Fig. 13.8, indicate motions that are approximately in-phase across the full surface of the TM. In addition, data analysis indicate that there is less than 30μs delay between the estimated arrival of the acoustic pressure wavefront at the surface of the TM and the beginning of its transient response. This delay can be attributed to the temporal resolution of the CHSS system (approximately 24 μs inter-frame time) and the reaction time of the speaker.

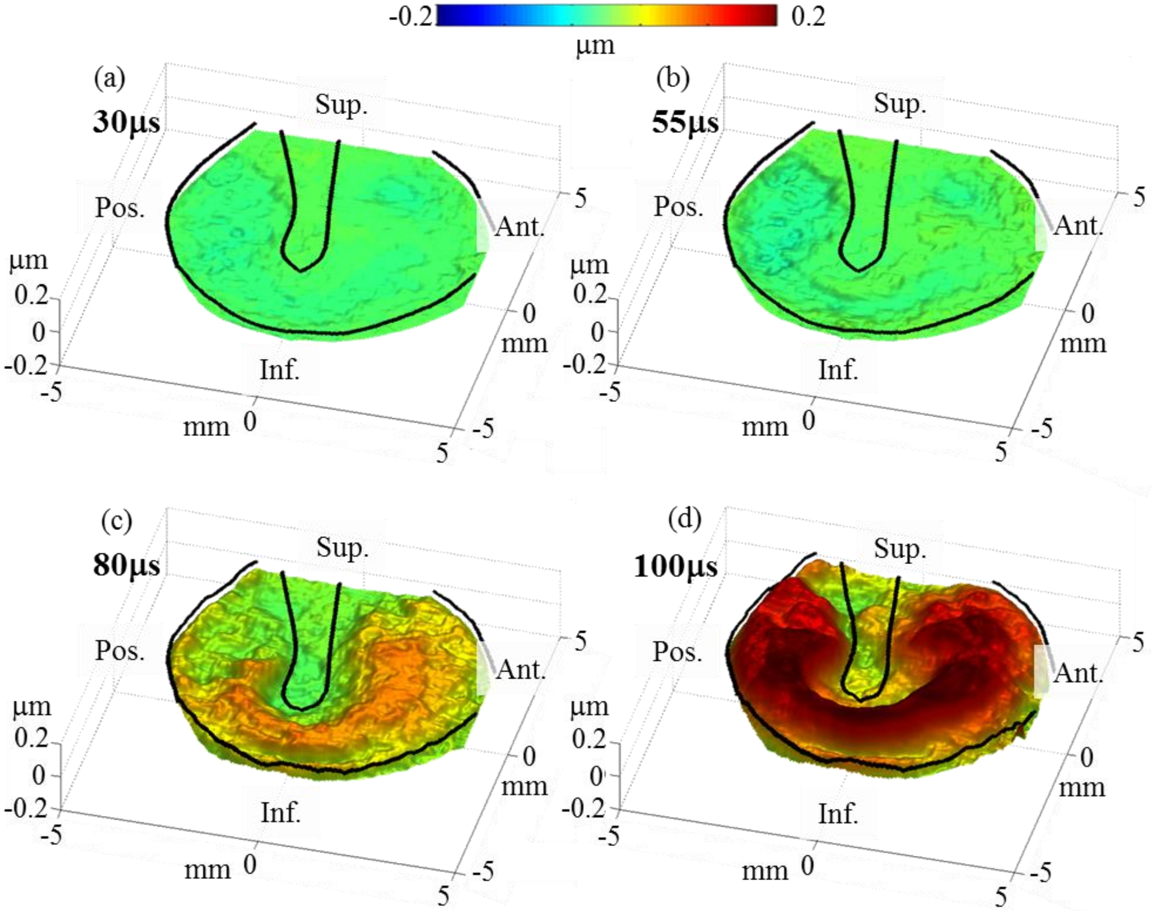

Fig. 13.8. Representative deformation maps corresponding to the first 30-100 μs of the initiation stage of the transient response of the human TM, indicating displacements that are mostly in-phase across the full surface. The acoustic excitation was a 50 μs click with a 115 dB maximum SPL. Outlines of the outer boundary of the membrane and the manubrium are indicated with solid lines.

During the surface wave propagation stage, the spatio-temporal evolution indicates circumferentially traveling surface waves propagating symmetrically relative to the manubrium and radially from the inferior to the superior parts of the TM, as shown in Fig 13.9.

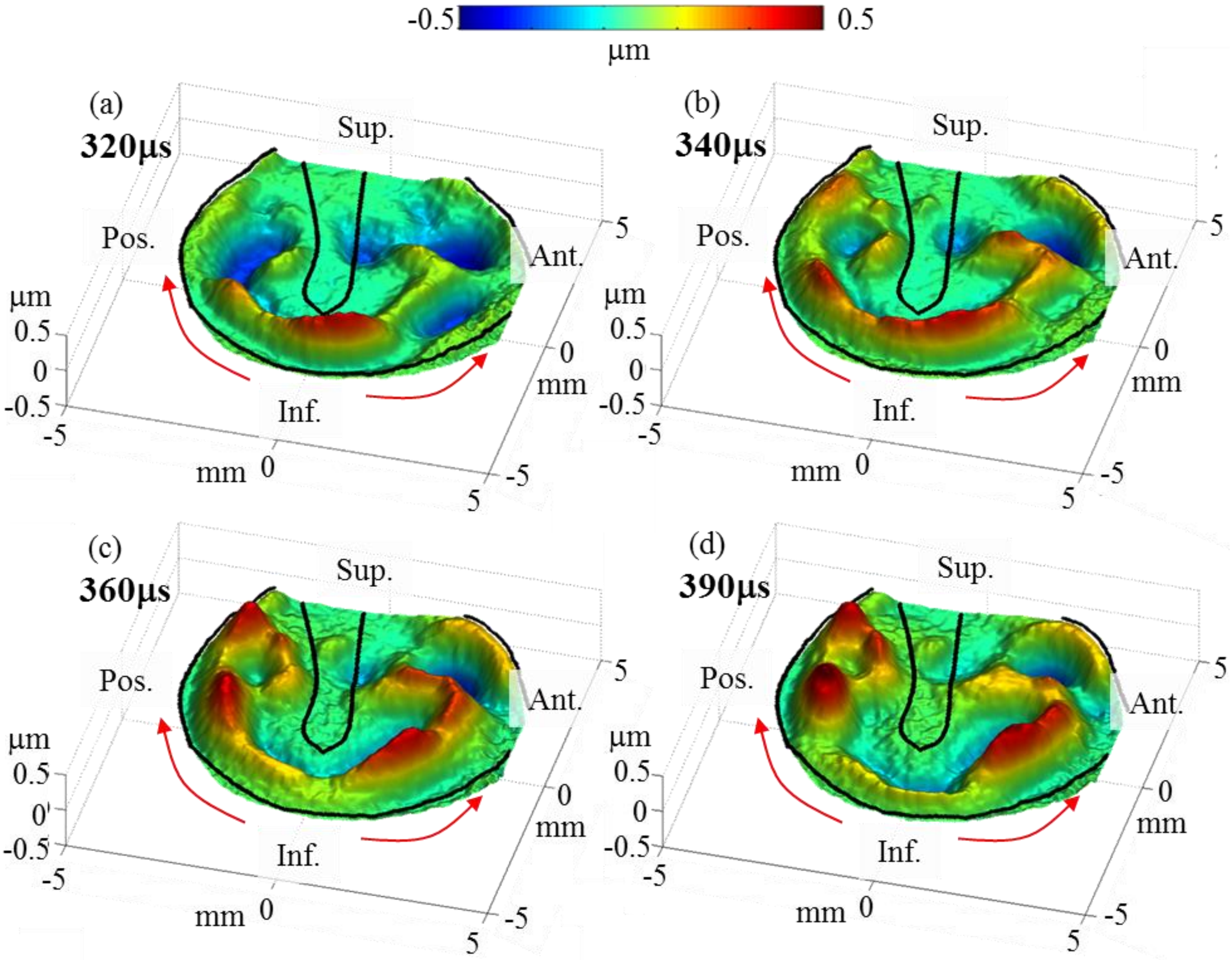

Fig. 13.9. Representative deformation maps corresponding to the 320-390 µs of the surface wave propagation stage of the transient response of the human TM indicating circumferentially traveling surface waves propagating at 24 m/s symmetrically relative to the manubrium and radially from the inferior to the superior parts of the TM as shown by solid arrows. The acoustic excitation is a 50 µs click a peak SPL of 115 dB. Outlines of the outer boundary of the membrane and the manubrium are indicated with solid lines.

The local phase velocity of the surface waves can be estimated by automatically identifying the shift of the spatial location of the local minima and maxima of the displacement maps between successive frames. Preliminary surface wave speeds of 24m/s for the human TM investigated are in agreement with previously reported estimates [Cheng et al., 2013; O'Connor and Puria, 2008].

13.3.1.3 Motion parameters

Each transient recoding of the CHHS provides a STDDC that contains the time waveforms of the transient response of all points across the surface of the human TM sample. Application of parallel data mining and interpretation (PDMI) methods, as described in Chapter 11, on the STDDC allows for estimation of the spatial dependence of medically relevant motion parameters (MRMP).

The time constant (TC) of the transient decay response at a particular point of the TM, as shown in Fig. 13.10, is related to the damping of the TM and the local material properties [Zhang and Gan, 2010; Aernouts and Dirckx, 2013]].

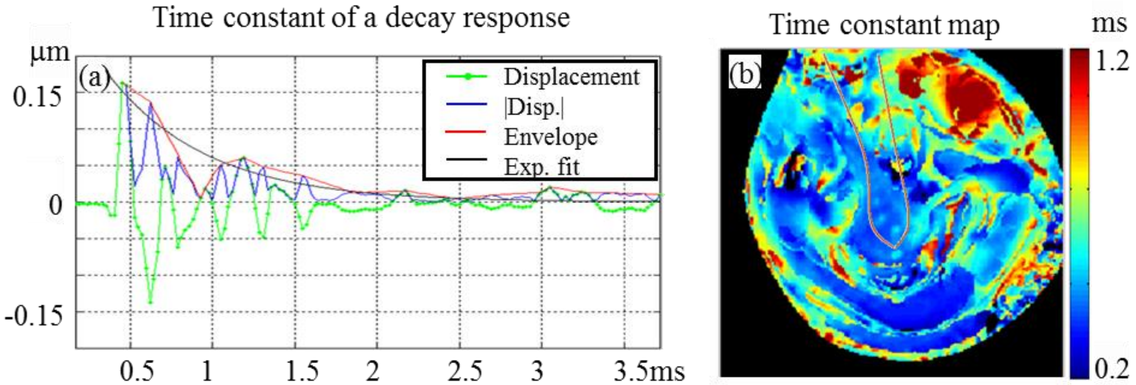

Fig. 13.10. Spatial variation of the time constant of a human TM as determined with the CHHS: (a) quantification of the time constant based on automatic decay envelope estimation and exponential fitting of the time waveform at the umbo; (b) spatial dependence of the time constant across the surface of the TM, indicating a range of 0.3-1.5 ms with a mean of 0.72 ms. The manubrium is outlined with solid lines in (b).

The TC of the decaying time waveform at a particular point is automatically estimated by fitting an exponential function to the envelope of the waveform, as shown in Fig. 13.10a. Automatically applying this analysis to all measured time waveforms across the full surface of the TM allows for quantification of the spatial dependence of the time constants, as shown in Fig 13.10b. The range of measured time constants is from 0.3 to 1.5 ms, with a mean of 0.71 ms, which are in agreement with previously reported estimates [Kemp et al., 1978; Wit and Ritsma, 1979].

The acoustical delay map, as shown in Fig. 13.11a, is calculated by automatically identifying the first local peak time (FLPT) of the TWF of every point across the surface of the TM and referencing it to the FLPT of the umbo, indicated with ⊕ in Fig. 13.11a. This quantifies the spatial distribution of the delay of the time-domain response of each point relative to the umbo. The range of the measured acoustical delays across the surface of the human TM, as shown in Fig. 13.11b, is within previously reported estimates [Rosowski et al., 2013; O’Connor and Puria, 2008].

The acoustic delay map and histogram, shown in Figs 13.11a and b, indicate that the response of the >50% the surface is within ± 50 μs of the response of the umbo, which supports the observations of predominantly in-phase motion during the initiation stage, as shown in Fig. 13.9. The acoustic delay data, shown in Fig. 13.11a, also indicates that the pars tensa of the surface of the TM moves with -25μs acoustical delay relative to the umbo. This suggests that the acousto-mechanical response of the TM reaches its first local peak (extrema) in the region between the TM boundary and the umbo, which agrees with theories of acousto-mechanical energy transfer from the TM periphery to the umbo [Puria and Allen, 1998].

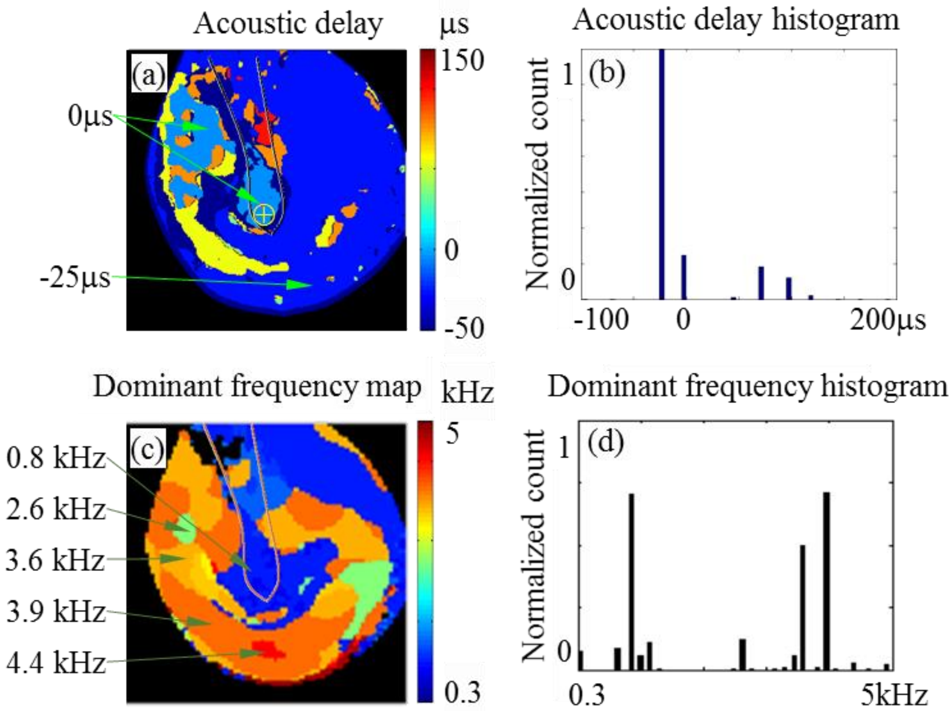

Fig. 13.11. Spatial dependence of the: (a) acoustic delay of each point on the TM relative to the peak time of the center of the umbo (marked with ⊕); histogram of (b); spatial distribution map of the dominant frequency at each point on the surface of the TM; and (d) histogram of (c). Outline of the manubrium is indicated with a solid line.

Based on automatic identification of the local maxima of the TF, shown in Fig. 13.7b, at every point across the TM, the dominant modal frequency (DMF) and its spatial distribution can be determined, as show in Fig. 13.11c. The DMF map indicates noticeable differences (3-4 fold) between the regions of the TM near the manubrium and the central region midway between the manubrium and the TM boundary. Assuming that the spatial distribution of the dominant frequency is representative of the local variations of stiffness and thickness of the TM, the DMF map can be related to previous studies indicating more than a three-fold increase in the local thickness of the TM near the manubrium relative to the central region of the TM [Van der Jeught et al., 2013].

In order to relate the data in Figs 13.11a and c, it is assumed that the initial displacements (i.e., <100 μs) of the click response of the TM, as shown in Fig. 13.8, exhibit single tone decayed response based on a dominant frequency spatially varying across the TM as shown in Fig. 13.11c. Based on this assumption and the approximately in-phase start of the motion of all points suggested by Fig.13.8, the acoustical delay (i.e., based on the FLPT) between any two points is predicted to be within a ¼ of the difference of the periods of oscillation of the points. Figure 13.11c indicates dominant frequencies of ~1 kHz (~250 μs for ¼ cycle) at the manubrium and an average of 3.5 kHz (~70 μs for ¼ cycle) across the central region midway between the manubrium and the TM boundary. This suggests approximately 180μs of maximum acoustic delay that can be associated with the difference in the natural frequency of the response between the umbo and the region midway between the umbo and the rim. Such a 'delay' is in agreement with the range of measured delay to first extrema (-25 to 75 μs) indicated in Fig. 13.11b. It should be also noted that the DMF map indicates a gradient oriented circumferentially around the umbo, coinciding with the direction of propagation of the surface waves, as indicated in Fig. 13.9.

In order to obtain modal frequencies representative of the full surface of the TM, magnitudes of the TFs at every point are averaged spatially, resulting in a single global TF, as shown in Fig. 13.12a. By automatically identifying the local maxima of the global TF, modal frequencies (MF) of the click response of the human TM can be determined and used to extract the corresponding magnitude and phase of the TF of every measurement point. This defines magnitude and phase maps of the mode shape of vibration, as shown in Fig. 13.12b, at the modal frequencies similar to previously reported data [Cheng et al., 2013].

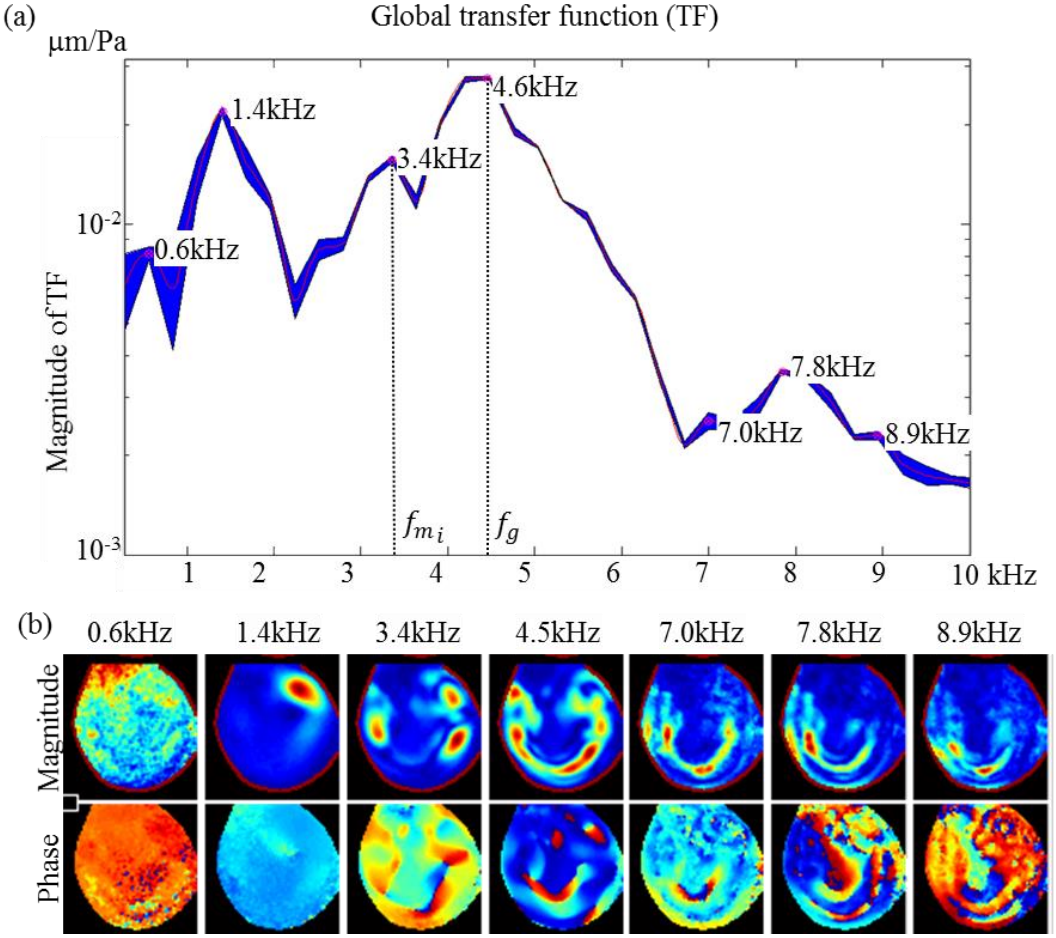

Fig. 13.12. Modal frequencies and mode shapes of vibrations of the click response of the human TM: (a) global transfer function (TF) with local maxima (marked with ⊕) representative of the modal frequencies of the click response normalized by a calibrated microphone; (b) magnitude and phase maps of the mode shape of vibration at the local maxima of (a).

Based on the acquisition parameters in Table 6.3, the frequency limit for the local maxima (peak) search was set for 10 kHz resulting in at least 4 samples per cycle at a sampling rate. Based on noise floor measurements of the HHS presented in Chapter 12, the amplitude limit for the local maxima (peak) search was set for 20dB relative to amplitude of the global maxima.

13.3.2 Mechanical excitation

A set of experiments have been designed and conducted to quantify the transient displacement of the human TM excited by a localized mechanical input. By providing a local (point or small area) rather than global (full surface) excitation, it is assumed that the initial stages of energy transfer from the mechanical input into the TM can be quantified through the displacement of the surface of the TM, without the effects of surface wave reflections and interference.

13.3.2.1 Experimental setup

The experimental setup, as shown in Fig. 13.13, consists of four major components: a high-speed holographic system (HHS) for displacement measurements along the sensitivity direction; a plunger with a force feedback that allows for a controlled displacement click (i.e., 50us) at a localized (i.e., <1mm^2) area; a mechanical positioner providing support and control over the orientation of the plunger; and a Laser-Doppler Vibrometer for control measurements of the motion of the TM at the umbo. In order to perform experiments, the human TM sample is exposed from lateral and medial sides to allow access to the plunger and to the CHHS. The plunger, as shown in Fig. 13.13c, consists of a force application tip, a piezo-transducer (PZT) based load cell and actuator, and a support beam. The load cell produces a voltage output that is directly proportional to the applied strain and force on the PZT material based on the direct piezo-electric effect. The actuator provides controlled displacement that is proportional to the voltage input based on the reverse piezo-electric effect. A support beam connects the structure of the plunger to the mechanical positioner, thus providing means of controlling the position of the application of the local force input. The actuation tip consists of a hollow tube with ~0.7 mm outside and 0.6 mm inside diameters providing ~0.4 mm^2 force application area. In the experiments, the excitation signal of the plunger was a 50 μs click with a 1.5 V maximum amplitude. In order to ensure continuous contact with the membrane during excitation, the plunger was pre-loaded >100μm into the surface of the TM (towards the camera).

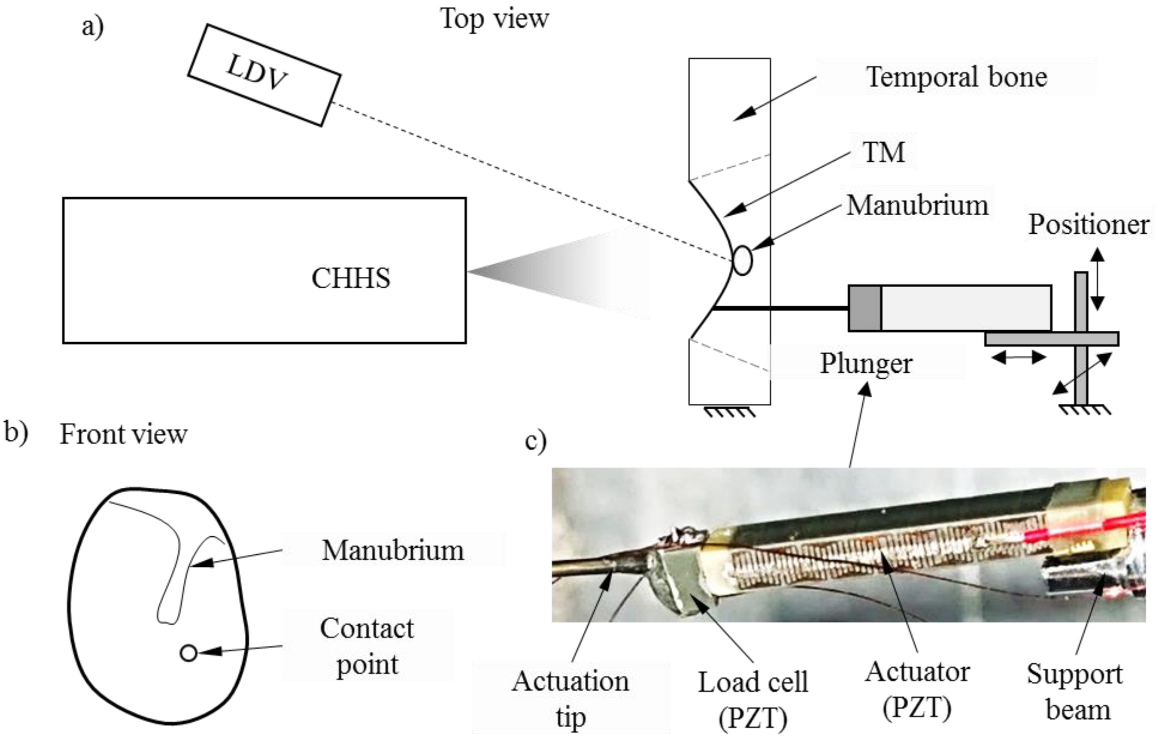

Fig. 13.13. Major components to perform localized mechanical excitation of TM samples: (a) schematic of the experimental setup that includes the CHHS, LDV, plunger, positioner and sample; (b) location of the contact point; (c) details of the plunger showing a PZT based load cell (force feedback) and actuator.

Based on FEM simulations, as described in Chapter 12, and preliminary LDV measurements, the initial stage of the transient response of the human TM is <200 μs. Based on this, the CHHS camera (Photron SA5) was set to record at a sampling rate of 87.5 kfps (with 11.4 μs inter-frame time), a spatial resolution of 256^2 pixels (>25 lines/mm at the object plane) and temporal resolution (i.e., exposure time) of 6.5 μs (1/153,000 s shutter speed). All triggering signals to synchronize the excitation and camera acquisition were executed with <1 μs temporal jitter.

13.3.2.2 Results

Figure 13.14 shows a summary of the first 80 μs of the spatio-temporal evolution of transient displacements of a human TM excited locally at the pars tensa, as indicated in Fig. 13.13b, by a 50 μs mechanical click. All timing labels are referenced with respect to the beginning of the application of the control signal to the plunger. Figure 13.14a shows the spatial distribution of the displacement of the TM corresponding to 20-80 μs after the application of a local mechanical click. The initial (23-46 μs) global minima and maxima corresponds to the spatial location of the tip of the plunger and the umbo, respectively. It can be seen that as the area of the TM above the plunger (point 1) moves up (out-of-plane towards the CHHS), the umbo moves down nearly instantaneously (within one camera frame or 11.4 μs). The motion of the anterior part of the surface of the TM gradually (within 57-80 μs) evolves into surface traveling waves that emanate from the contact point of the plunger and move circularly around the umbo. Focusing at the anterior and posterior areas close to the middle of the manubrium, it can be seen that the posterior part of the TM reacts before the surface wave on the anterior reaches the manubrium. This suggest a coupling between the anterior and posterior halves of the TM through the manubrium and the fiber structure.

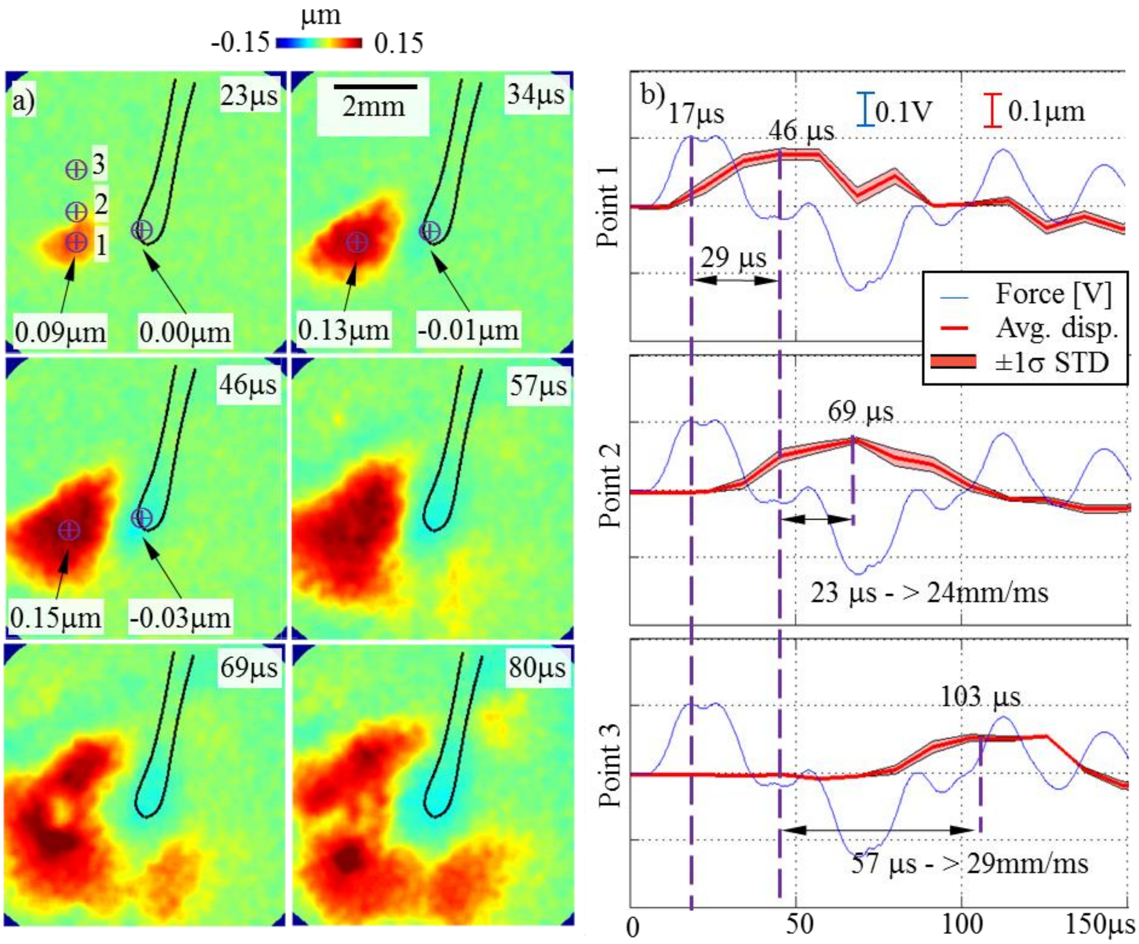

Fig. 13.14. Transient response of the human TM excited locally at the pars tensa by a 50μs mechanical click: (a) spatial distribution of displacements during the first 20-80μs after the beginning of the application of the mechanical click; (b) time waveform of the first 150 μs of the displacement at points 1-3 along with the signal from the load cell (force sensor) of the plunger. Outline of the manubrium is indicated with a solid line.

In order to quantify the speed of propagation of the surface traveling waves, the time waveforms at points 1-3, marked in Figure 13.14a, were plotted together with the measured voltage from the load cell of the plunger, shown in Figure 13.14b. The three points are located along the inferior-superior direction. Point 1 is 0.55 mm away from point 2 and 1.65mm away from point 3. Each displacement waveform shows the average of three measurements together with a confidence interval of ±1σ standard deviation for each time instance. The temporal distance between first local maxima of the load cell and the displacement of Point 1 indicates a 29 μs delay. This can be attributed to a propagation delay of the mechanical impulse across the thickness of the pars tensa. Comparing the first local maxima of the time waveforms of point 1 and 2 indicates 23 μs. By accounting for the spatial separation (~0.55 mm) between the two points, the average speed of the traveling wave is estimated at 24 m/s. Similarly, the relative delay between points 1 and 3 is estimated to be 57 μs, which corresponds to an average surface wave speed of 29 m/s.

The increase in surface wave speed at point 3 relative to point 2 could be explained by the finite duration of the mechanical click (50 μs) and the finite energy transfer rate between the plunger and the surface of the TM. This can be illustrated by summing the finite duration (50 μs) of the mechanical click, the combined effect of the delays of the plunger (17 μs) and the TM (29 μs), resulting in approximately 100 μs required for the dissipation of all the energy of the plunger into the TM. This delay matches with the total delay between the beginning of plunger's control signal and the first local maxima at point 3 (i.e., 103 μs), as opposed to point 2 (i.e., 69 μs). In other words, at the time of global first local maxima at point 2, not all mechanical energy from the plunger has been coupled into motion of the TM surface. This assumes approximately equal local (between point 1 and 3) material properties of the TM, resulting in constant surface wave speeds. This also assumes that the temporal location of the first maxima of the instantaneous displacement will be representative of the mechanical energy transferred from the plunger into the TM.

Figure 13.15 shows a comparison of the first 80 μs of the spatio-temporal evolution of the displacement of the transient response of the human TM excited locally through the malleus and the pars tensa by a 50 μs mechanical click.

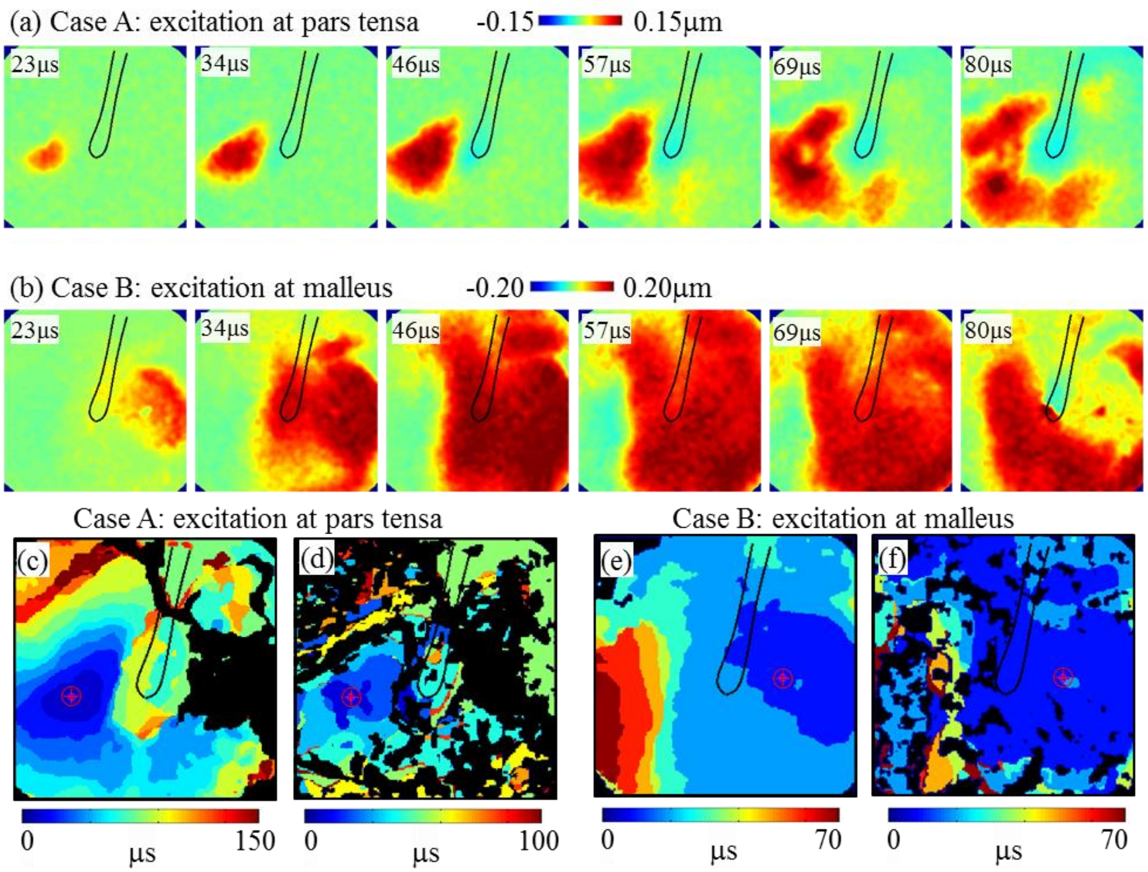

Fig. 13.15. Transient response of the human TM mechanically excited two points during the first 20-80μs after the application of the load: (a) excitation at the pars tensa (Case A); (b) excitation at the malleus (Case B); (c) and (d) spatial dependence of the reaction time (RT) and the first local peak time (FLPT) for loading case A; (e) and (f) are equivalent to (c) and (d) for loading case B. MRMPs are referenced with respect to location marked with ⊕. Outline of the manubrium is indicated with a solid line.

Comparison between Fig. 13.15a and b indicates that the response of the TM to a mechanical click at the malleus (Case B) results in approximately 2-3 fold (i.e., 50-80m/s) higher surface wave speeds relative to excitation at the pars tensa (Case A). It should also be noted that in Case B the response of the TM starts nearly simultaneous at both the umbo and at the pars tensa.

13.4 In-vivo measurements of the human TM

13.4.1 Demonstration of PHHS operation in simulated *in-vivo* conditions

In other to demonstrate the capabilities of the PHHS for operation in *in-vivo* conditions, a set of measurements were conducted to experimentally simulate *in-vivo* conditions. The OH was held by the MOP-2 and the object (a resolution target) was held by hand at 40±2 mm away from the tip of the OH and normal (±5°) to the sensitivity axis. A spatial phase sampling method was utilized to perform single frame acquisition (Chapter 7). The acquisition time was controlled from 0.2 ms to 1.4 ms. For every acquisition setting, a 3 s recording (~50 frames) was taken at the maximum frame rate of the camera (i.e., 15 Hz). A sample of five consecutive frames from recordings with different acquisition settings are shown in Fig. 13.16a. The image quality based on the image contrast was analyzed and the mean and standard deviation of the contrast of every set were quantified. The standard deviation (SD) of the contrast normalized with respect to the mean of the contrast is shown in Fig. 13.16b. The probabilities of obtaining a contrast of >70% for every acquisition setting are shown in Fig. 13.16c. The results in Fig 13.16b indicate > 3 fold increase in the variation of contrast (less stability) at 1ms versus 0.2ms acquisition time. Similar results can be seen in Fig, 13.16c, indicating ~3 fold decrease in the probability of obtaining >70% contrast at acquisition times of >1ms as opposed to

<0.2ms. Data indicate that exposure times of less than 0.5ms produce sufficiently stable images for in-vivo applications.

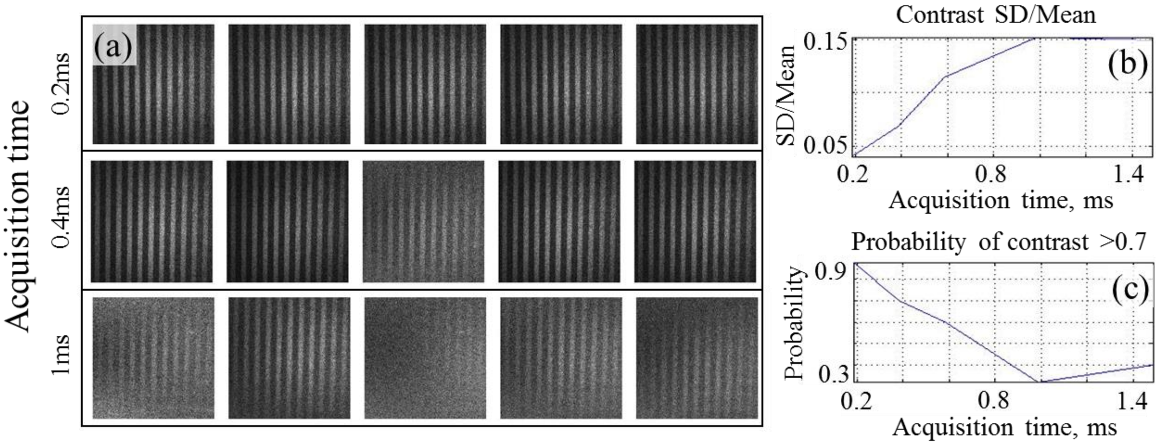

Fig. 13.16. Representative results of the image quality of a 1951 USAF resolution target held by hand and recorded at several acquisition settings of the enhanced OH: (a) set of five consecutive frames from 3 recordings with acquisition times of 0.2 ms, 0.4 ms and 1 ms, respectively; (b) normalized SD of the contrast versus acquisition time; and (c) probability versus acquisition time of recording an image with a contrast >70%

13.4.2 Holographic measurements in a patient

The PHHS performance was tested in *in-vivo* conditions by quantification of the image quality of measurements of a patient’s TM.

13.4.2.1 Patient preparation and experimental setup

The TM was prepared prior to the measurement by application of reflective coating of ZnO, which allows for improved fringe visibility, as shown in Fig. 13.17. Based on feedback from physicians and researchers at the MEEI as well as previous research [Cheng et al., 2013], zinc oxide (ZnO) was chosen as it is safe (commonly used in cosmetics), highly reflective (3-5 fold increase in reflectivity versus untreated TM) and is soluble in weak acetic acid (one of the main ingredients in vinegar) making it easy and safe for removal off the TM.

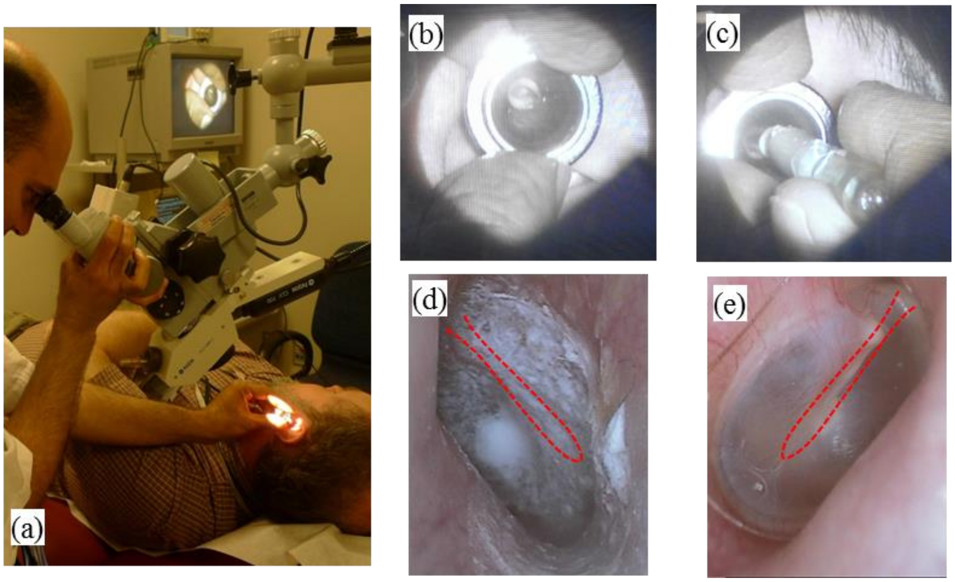

Fig. 13.17. Coating of a patient TM: (a) clinical setup for application of reflective coating of ZnO; (b) surgeon's view during localization; and (c) coating of the membrane; (e) coated left ear; and (d) uncoated right ear used as a reference.

The patient's head was supported by a customized head positioner (HP), as shown in Fig. 13.18. The speculum tip of the OH is carefully inserted into the patient's ear canal and positioned approximately 15-20 mm away from the TM.

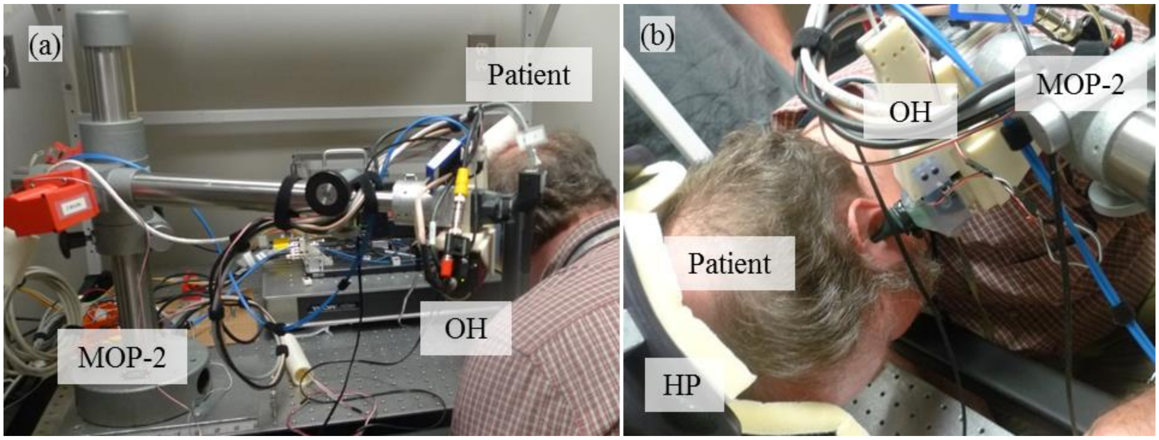

Fig. 13.18. Experimental setup for *in-vivo* holographic measurements: (a) examination setup at the clinic including the MOP-2 and OH systems; and (b) patient during examination with the PHHS. HP in (b) stands for head positioner.

The orientation of the OH is adjusted to maximize the visible surface of the TM. The live-feed subsystem in the OH is used extensively during these adjustment procedures. During the measurement procedures, the OH was autonomously supported by MOP-2. A major challenge was to measure the TM's acoustically induced vibrations with nanometer accuracy, while isolating displacements due to patient's tremor of the head, breathing and heartbeat. This was aided by capabilities of the LaserView software for synchronization of the image acquisition with the patient's heartbeat via an electrocardiographic (EKG) feedback to minimize its effect on measurements [Harrington et al., 2011]. Other challenges of the *in-vivo* measurements were the light-tissue interactions in the enclosed space of the ear canal, as well as visual obtrusion of the TM by the ear canal.

13.4.2.2 Representative results of operation in in-vivo conditions

Initial experiments were performed with a previous generation in-line digital holographic setups [Flores-Moreno et al., 2011] utilizing temporal phase sampling with an acquisition time of ~50ms. Experiments were done at 1 kHz sound excitation at 90dB SPL and representative results are shown in Fig. 13.19a. The image quality was insufficient for analysis of the deformations. The same data were reprocessed with a single frame (5ms measurement time) phase sampling methods (Chapter 7) and results are shown in Fig. 13.19b. Contrast variations between frames indicate 50% improved stability; however, noise from the overlapping holographic twin image reduces image quality compared to static conditions.

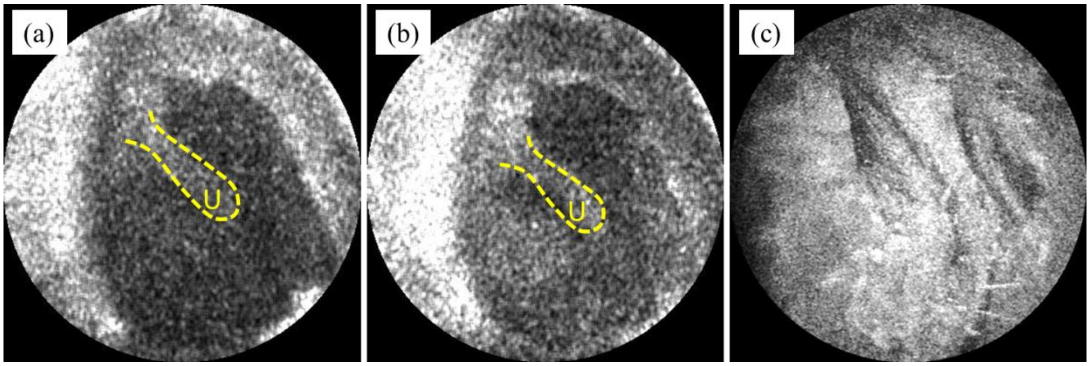

Fig. 13.19. Representative *in-vivo* measurements with the PHHS: (a) and (b) numerically reconstructed holograms with fringes induced by sound excitation of 1 kHz at 90 dB SPL; and (c) TM without sound excitation. Temporal resolution is 45 ms, 5 ms, and 0.5 ms, respectively. The handle, or manubrium, of the malleus is outlined and the umbo at the end of the handle near the center of the TM is labeled as "U."

A second set of experiments were performed with the improved PHHS including implementation of an off-axis holographic setup for spatial phase sampling acquisition (Chapter 9), single frame phase measurement (Chapter 8) and enhanced design of the OH (Chapter 9), as shown in Fig. 13.19c. The membrane was not coated and no sound excitation was applied. The aim of the two sets of experiments was to compare the image quality and stability for *in-vivo* conditions between an enhanced PHHS and previous [Flores-Moreno et al., 2011] systems. A summary of the comparison of several parameters is shown in Table 13.1.

Table 13.1. Comparison of the performance of the enhanced PHHS versus previous designs [Flores-Moreno et al., 2011].

Parameter	**Previous design**	**Current design**	**Improvement**
Spatial frequency limit at the CCD	70 lines/mm	150 lines /mm	x2.1
Spatial resolution at the reconstruction plane	7.13 lines /mm	12.7 lines /mm	x1.8
Working distance for in-vivo measurements	150 mm	100 mm	x1.5
Minimum exposure time	2 ms	0.2 ms	x10
Minimum recording time	36 ms	0.2 ms	x180
Image stability – fraction of images >65% contrast	5%	75%	x15

14 Conclusions and future work

This Dissertation proposes a new high-speed holographic system (HHS) for full-field nanometer transient (i.e., > 10 kHz) displacement measurement of the human middle-ear. The measurement capabilities of the system have been verified on both artificial and cadaveric samples at steady state and transient excitations.

Novel phase sampling and acquisition approaches have been developed and implemented to allow the use of state-of-the-art high spatial and high temporal resolution cameras through a modular and expandable custom control approach. The novel approaches utilize the advantages of each camera type by overcoming any spatial or temporal resolution constraints, which allow the use of the HHS with a wide range of current and future cameras [Dobrev et al., 2014c]. The noise floor and accuracy of my enhanced HS 2+N phase sampling method is compared against a 4-step phase sampling method, indicating <8 nm error and <11 nm noise floor SD. The noise floor and accuracy of my enhanced MPDE phase sampling method is compared against a 4-step phase sampling method, indicating <8 nm error and <6 nm noise floor SD. Comparison between HHS and LDV indicate <10 μs temporal and <15 nm displacement SD.

Additionally, this Dissertation demonstrated the realization and capabilities of a holographic otoscope head (OH) [Dobrev et al. 2012] and the mechatronic otoscope positioner (MOP) [Dobrev et al., 2013b] aimed at extending the capabilities of the HHS for medical research and *in-vivo* applications. The OH provides a compact multi-domain tool capable of steady state and transient displacement measurements, averaged acoustical estimations as well as traditional qualitative visual inspections. The MOP incorporates a novel and inherently safe control approach that is based on passively actuated system to automatically facilitate an operator in positioning and holding the OH during measurements in research or medical settings. The modular architecture of the MOP control system allows its application on a variety of existing passive medical positioners, thus expanding the possibilities for implementation of the HHS in the clinical environment.

The high temporal (i.e., >80 kHz) and spatial (i.e., >500k data points) resolutions of the HHS enables parallel measurements of all points on the surface of the TM, which allows quantification of spatially dependent motion parameters such as modal frequencies, time constants, and acoustic delays [Dobrev et al. 2015]. Such capabilities could be used to infer local material properties across the surface of the TM as well as further the understanding of the sound-receiving function of the TM in the process of acousto-mechanical energy coupling into to the ossicular chain and inner ear. The total measurement time is decreased $>10^3$ fold compared to existing stroboscopic holographic measurement methods [Rosowski et al. 2012], thus reducing the effects of the environmental disturbances and allowing *in-vivo* applications. This Dissertation presents preliminary results on *in-vivo* measurement capabilities of the HHS indicating 180 fold shorter recording time and 15 fold improvement in image quality stability compared to previous digital holographic systems [Flores-Moreno et. al, 2011]. The HHS provides opportunities for new medical tools that enable physicians to improve the quality of diagnosis and treatments of the human ear.

Future work should be focused on the extraction of medically meaningful information on TM’s health condition through analysis and interpretation of the measured transient displacement response. Further research is also needed to explain the transient dynamics of the TM and its relationship to the energy transfer into the middle-ear, as well as its connection to previous steady-state dynamics research. Improvements of the HHS should include enhancement of the optical design and temporal resolution, as well as applications *in-vivo.*

References

Adrian, J. R., “Twenty years of particle image velocimetry,” *Exp. in Fluids*, 39(2): 159-169, 2005

Aernouts, J. and Dirckx J. J., “Static versus dynamic gerbil tympanic membrane elasticity: derivation of the complex modulus,” *Biomech. & Mod. in Mechanobio.*, 11(6): 829-840, 2012

Alexander M. and Laubach L. L., “Anthropometry of the human ear: A photogrammetric study of USAF flight personnel,” Aerospace Medical Research Laboratories, Aerospace Medical Division, Air Force Systems Command, 1968

Arroyo, M. P. and Lobera J., “A comparison of temporal, spatial and parallel phase shifting algorithms for digital image plane holography,” *Meas. Sci. & Tech.*, 19(7):074006, 2008.

AVT, “Application Note: PIV – Minimum time between exposures for AVT GigE Cameras,” http://www.alliedvisiontec.com/fileadmin/content/PDF/Support/Application_Notes/AppNote_-_PIV_-_Min_Time_Between_Exposures_-_AVT_GigE.pdf. Last accessed: October 2013

AVT, “Pike F505B,” http://www.alliedvisiontec.com/us/products/cameras/firewire/pike/f-505bc.html. Last accessed: January 2014

Awatsuji, Y., Koyama, T., Tahara, T., Ito, K., Shimozato, Y., Kaneko, A., Nishio, K., Ura, S., Kubota, T., and Matoba, O., “Parallel optical-path-length-shifting digital holography,” *App. Opt.*, 48(34): H160-H167, 2009.

Awatsuji, Y., Sasada, M., and Kubota, T., “Parallel quasi-phase-shifting digital holography,” *App. Phys. Letters*,” 85(6): 1069-1071, 2004

Badulescu, C., Bornert, M., Dupré, J. C., Equis, S., Grediac, M., Molimard, J., Picart, P., Rotinat, R., and Valle, V., “Demodulation of spatial carrier images: performance analysis of several algorithms using a single image,” *Exp. Mech.*, 53(8): 1357-1370, 2013

Bapat, N. D., "Development of sound presentation system (SPS) for characterization of sound induced displacements in tympanic membranes," MS Thesis, Worcester Polytechnic Institute, Worcester, MA, USA, 2011

Burkhard, M. D. and Sachs, R. M., "Anthropometric manikin for acoustic research," *JASA*, 58(1): 214-22, 1975

Castellini, P., Martarelli, M., and Tomasini, E. P., “Laser Doppler vibrometry: Development of advanced solutions answering to technology’s needs,” *Mech. Sys. & Sig. Proc.*, 20: 1265-1285, 2006

Chang, E. W., Cheng, J. T., Röösli, C., Kobler, J. B., Rosowski, J. J., and Yun, S. H., "Simultaneous 3D imaging of sound-induced motions of the tympanic membrane and middle ear ossicles," *Hear. Res.*, 304: 49-56, 2013

Chen, T. Y. and Chen, C. H., “An instantaneous phase shifting ESPI system for dynamic deformation measurement,” *Proc. SEM, in Optical Measurements, Modeling, and Metrology*, 5: 279-283, 2011

Cheng, J. T., Aarnisalo, A. A., Harrington, E., Hernandez-Montes, M. S., Furlong, C., Merchant, S. N., and Rosowski, J. J., "Motion of the surface of the human tympanic membrane measured with stroboscopic holography," *Hear. Res.,* 263(1): 66-77, 2010

Cheng, J. T., Hamade, M, Merchant, S. N., Rosowski, J. J., Harrington, E., and Furlong, C., “Wave motion on the surface of the human tympanic membrane: holographic measurement and modeling analysis,” *JASA*, 133: 918-937, doi: 10.1121/1.4773263, 2013

Chikkerur, S., Sundaram, V., Reisslein, M., and Karam, L. J., "Objective video quality assessment methods: a classification, review, and performance comparison," *IEEE Trans. Broadcast.*, 57(2): 165-182, 2011.

Chittka, L. and Brockmann, A., “Perception Space-The Final Frontier,” *PLoS Biol.*, 3(4):e137, doi:10.1371/journal.pbio.0030137, 2005

Crochiere, R. E., Webber, S. A., and Flanagan, J. L., “Digital Coding of Speech in Sub-bands,” *Bell Sys. Tech. Jour.*, 55(8): 1069-1085, 1976

Culmer, P., Jackson, A., Levesley, M. C., Savage, J., Richardson, R., Cozens, J. A., and Bhakta, B. B., “An admittance control scheme for a robotic upper-limb stroke rehabilitation system,” *Proceedings of the 2005 IEEE Engineering in Medicine and Biology 27th Annual Conference,* 5: 5081-5084, 2005

Dancer, A. L., Franke, R. B., Smigielski, P., Albe, F., and Fagot, H., “Holographic interferometry applied to the investigation of tympanic-membrane displacements in guinea pig ears subjected to acoustic impulses,” *JASA*, 58(1): 223-228, 1975

Dandliker, R. and Thalmann, R., “Heterodyne and quasi-heterodyne holographic interferometry,” *Opt. Eng.*, 24(5): 245824-245824, 1985

De Greef, D., Aernouts, J., Aerts, J., Cheng, J. T., Horwitz, R., Rosowski, J. J., and Dirckx, J. J., “Viscoelastic properties of the human tympanic membrane studied with stroboscopic holography and finite element modeling,” *Hear. Res.*, 312: 69-80, 2014

Decraemer, W., Khanna, S. M., and Funnell, W. R. J., “Vibrations at a fine grid of points on the cat tympanic membrane measured with a heterodyne interferometer,” *in*

EOS/SPIE International Symposia on Industrial Lasers and Inspection, Conference on Biomedical Laser and Metrology and Applications, 1999

Dirckx, J. J. and Decraemer, W. F., “Optoelectronic moiré projector for real-time shape and deformation studies of the tympanic membrane,” *J. Biomed. Opt.*, 2: 176-185, 1997

Dirckx, J. J. and Decraemer, W. F., “Interferometer for eardrum shape measurement, based on projection of straight line rulings,” *Lasers Med. Sci.*, 15: 131-139, 2000

Djalilian, H. R., Ridgway, J., Tam, M., Sepehr, A., Chen, Z., and Wong, B. J., “Imaging the human tympanic membrane using optical coherence tomography in vivo,” *Otology & neurotology: official publication of the American Otological Society, American Neurotology Society [and] European Academy of Otology and Neurotology*, 29(8): 1091, 2008

Dobrev, I., Furlong, C., and Rosowski, J. J., “Design of a mechatronic positioner for a holographic otoscope system,” *Proc. SEM 2011, in Mechanics of Biological Systems and Materials*, 2: 193-198, 2011

Dobrev, I., Flores Moreno, J. M., Furlong, C., Harrington, E. J., Rosowski, J. J., and Scarpino, C., “Design of a positioning system for a holographic otoscope,” *Proc. SPIE 2010, in Optical Engineering & Applications*, 77910D-77910D, 2010

Dobrev, I., Furlong, C., Rosowski, J. J., Cheng, J. T., and Harrington, E. J., “Implementation and evaluation of single frame recording techniques for holographic measurements of the tympanic membrane in-vivo, ” *Proc. SEM 2013, in Advancement of Optical Methods in Experimental Mechanics*, 3: 85-95, 2014a

Dobrev, I., Furlong, C., Cheng, J. T., and Rosowski, J. J., “Acousto-mechanical response of the human TM characterized by high-speed digital holographic methods,” *Proc. Fringe 2013*, 657-660, 2014b

Dobrev, I., Furlong, C., Cheng, J. T., and Rosowski, J. J., “Full-field transient vibrometry of the human tympanic membrane by correlation based holographic otoscope,” submitted to *J. Biomed. Optics,* April 2014c

Dobrev, I., Furlong, C., Cheng, J. T., and Rosowski, J. J., “Optimization of a lensless digital holographic otoscope system for transient measurements of the human tympanic membrane,” submitted to *Exp. Mech.*, June 2014d

Dobrev, I., Furlong, C., Cheng, J. T., and Rosowski, J. J., “High-speed digital holographic methods to characterize the transient acousto-mechanical response of human TM,” *21st DYMAT Technical Meeting, High-speed imaging for dynamic testing of materials and structures*, Institute of Physics, London, UK, Nov. 18-20, 2013a

Dobrev, I., Furlong, C., Rosowski, J. J., Cheng, J. T., and Harrington, E. J., "High-speed digital holography for transient response of the human Tympanic Membrane," *Proc. SEM 2014, Annual Conference & Exposition on Experimental and Applied Mechanics*, in print, 2015

Dobrev, I., Harrington, E. J., Cheng, J. T., Furlong, C., and Rosowski, J. J., "Digital holographic otoscope for measurements of the human tympanic membrane in vivo," *Proc. SEM 2012*, 3: 39-45, 2013b

Dobrev, I., Harrington, E. J., Cheng, J. T., Furlong, C., and Rosowski, J. J., "Digital holographic otoscope for measurements of the human tympanic membrane in vivo," *Proc. SPIE 2012, in Interferometry XVI: Applications*, (8494), 849409, 2012

Dobrev, I., Balboa, M., Fossett, R., "MEMS for real-time imaging," Major Qualifying Project, Worcester Polytechnic Institute, Worcester, MA, USA, 2009

Ear Nose Throat (ENT) USA, "Eardrum and middle ear", http://www.entusa.com/eardrum_and_middle_ear.htm. Last accessed: March 2014

Fanuc Robotics, "LR Mate 200iC and R-30iA Mate Controller," Fanuc Robotics America, Inc., 2007, http://www.robotsdotcom.com/Fanuc/lrmate.pdf. Last accessed: March 2010

Flores-Moreno, J. M., Furlong, C., Rosowski, J. J., Harrington, E., Cheng, J. T., Scarpino, C., and Santoyo, F. M., "Holographic otoscope for nanodisplacement measurements of surfaces under dynamic excitation," *Scanning*, 33(5): 342-352, 2011

Funnell, W. R. J., "High-frequency time-domain behaviour of a finite-element model of the eardrum," *24th ARO MidWinter Meeting*, St. Petersburg Beach, FL, USA, 2001

Furlong, C., **Dobrev, I.**, Harrington, E. J., Hefti, P., and Khaleghi, M., "Miniaturization as a key factor to the development and application of advanced metrology systems", *SPECKLE 2012: V International Conference on Speckle Metrology*, 84130T-84130T, 2012

Furlong, C., **Dobrev, I.**, Rosowski, J. J., and Cheng, J. T., "Assessing eardrum deformation by digital holography," *SPIE Newsroom*, 2013

Furlong, C., Yokum, J. S., and Pryputniewicz, R. J., "Sensitivity, accuracy, and precision issues in opto-electronic holography based on fiber optics and high-spatial- and high-digital-resolution cameras," *Proc. SPIE, International Symposium on Optical Science and Technology*, 4777: 77-84, 2002

Furlong, C., Rosowski, J. J., Hulli, N., and Ravicz, M. E., "Preliminary analyses of tympanic-membrane motion from holographic measurements," *Strain*, 45(3): 301-309, 2009

Geisler, C. D., *From sound to synapse, physiology of the mammalian ear*, Oxford University Press, 1998

Georgas, P. J. and Schajer, G. S., “Modulo-2pi phase determination from individual ESPI images,” *Opt. Las. Eng.*, 50(8): 1030-1035, doi: 10.1016/j.optlaseng.2012.03.005, 2012

Goodman, J. W., *Introduction to Fourier Optics*. McGraw-Hill, New York, second edition, 1996

Harrington, E., **Dobrev, I.**, Bapat, N., Flores, J. M., Furlong, C., Rosowski, J. J., Cheng, J. T., Scarpino, C., and Ravicz, M., "Development of an optoelectronic holographic platform for otolaryngology applications", *Proc. SPIE 2010, in Engineering and Applications*, 77910J, doi:10.1117/12.862130, 2010

Harrington, E., Furlong, C., Rosowski, J. J., and Cheng, J. T., “Automatic acquisition and processing of large sets of holographic measurements in medical research,” *Proc. SEM 2011, In Optical Measurements, Modeling, and Metrology*, 5: 219-228, 2011

Hecht, E., *Optics*, 2nd ed., Addison-Wesley Publishing Company, 1989

Herráez, M. A., Burton, D. R., Lalor, M. J., and Gdeisat, M. A., "Fast two-dimensional phase-unwrapping algorithm based on sorting by reliability following a noncontinuous path," *App. Opt.*, 41(35): 7437-7444, 2002

Hernández-Montes, M., Furlong, C., J. J. Rosowski, N. Hulli, E. Harrington, J. T. Cheng, M. E. Ravicz, and F. M. Santoyo, “Optoelectronic holographic otoscope for measurement of nanodisplacements in tympanic membranes,” *J. Biomed. Opt.*, 14(3): 034023, 2009

Hömberg, V., Hefter, H., Reiners, K., and Freund, H. J., "Differential effects of changes in mechanical limb properties on physiological and pathological tremor," *J. of Neurology, Neurosurgery, and Psychiatry*, 50(5): 568-79, 1987

Huang, G., Gan, R. Z., Lu, H., and Daphalapurkar, N. P., “A method for measuring linearly viscoelastic properties of human tympanic membrane using nanoindentation,” *J. Biomech. Eng.*, 130(1): 014501, 2008

Hulli, N., “Development of an optoelectronic holographic otoscope system for characterization of sound-induced displacements in tympanic membranes,” MS Thesis, Worcester Polytechnic Institute, Worcester, MA, USA, 2009

Jones, R. and Wykes, C., *Holographic and speckle interferometry: A discussion of the theory, practice and application of the techniques*, vol. 6, Cambridge University Press, 1983

Katz, J., *Handbook of Clinical Audiology*, 4th ed., Williams & Wilkins, Baltimore, Maryland, 1994

Kemp, D. T., “Stimulated acoustic emissions from within the human auditory system,” *JASA*, 64: 1386, 1978

Khaleghi, M., Lu, W., **Dobrev, I.**, Cheng, J. T., Furlong, C., and Rosowski, J. J.., "Digital holographic measurements of shape and 3D sound-induced displacements of Tympanic Membrane," *Opt. Eng.*, 52(10): 101916, doi: 10.1117/1.oe.52.10.101916, 2013

Khaleghi, M., **Dobrev, I.**, Klausmeyer, P., Harrington, E., and Furlong, C., "Investigation of thermo-mechanical effects of lighting conditions on canvas paintings by laser shearography," *Proc. SPIE 2012, in Engineering and Applications*, 84940A: 1-8, 2012

Khaleghi, M., **Dobrev, I.**, Klausmeyer, P., Cushman, M., Harrington, E., and Furlong, C., "Long term effects of cyclic environmental conditions on painting in museum exhibition by laser shearography", *Proc. SEM 2013, Annual Conference & Exposition on Experimental and Applied Mechanics*, 3: 283-288, 2014a

Khaleghi, M., **Dobrev, I.**, Harrington, E., Furlong, C., and Rosowski, J. J., "Study of the transient response of Tympanic Membranes under acoustic excitation", *Proc. SEM 2013, Annual Conference & Exposition on Experimental and Applied Mechanics,* 4: 1-9, 2014b

Kilpatrick, J. M. and Markov, V., "Matrix laser vibrometer for transient modal imaging and rapid nondestructive testing," *Proc. SPIE 2008, in Eighth International Conference on Vibration Measurements by Laser Techniques: Advances and Applications*, 709809-709809, 2008

Klausmeyer, P., Cushman, M., **Dobrev, I.**, Furlong, C., and Meybodi, M., "Developing a shearographic monitoring system for quantifying thermo-mechanical characteristics of oil-on-canvas paintings and informing policy regarding museum climate standards," *ICOM-CC, The Non-Invasive Analysis of Painted Surfaces: Scientific Impact and Conservation Practice*, oral presentation, Feb. 20-21, 2014

Kolenovic, E., Furlong, C., and Jüptner, W., "Inspection of micro-optical components by novel digital holographic techniques," *Proc. SEM 2004*, 470–475, 2004

Koliopoulos, C. L., "Simultaneous phase-shift interferometer," *Proc. SPIE 1992, in 8th Intl Symp. on Gas Flow and Chemical Lasers*, 119-127, 1992

Kreis, T., *Holographic Interferometry. Handbook of Holographic Interferometry: Optical and Digital Methods*, Wiley-VCH Verlag GmbH & Co. KGaA, 2005

Kristan, M., Perš, J., Perše, M., and Kovačič, S., "A Bayes-spectral-entropy-based measure of camera focus using a discrete cosine transform," *Pattern Recognition Letters*, 27(13): 1431-1439, 2006

Laferriere, J., Lietaert, G., Taws, R., and Wolszczak, S., "Reference Guide to Fiber Optic Testing," JDC Uniphase Corp., 2(1): 1-41, 2011

Larkin, G. T., ”Natural demodulation of two-dimensional fringe patterns. II. Stationary phase analysis of the spiral phase quadrature transform,” *JOSA A,* 18(8): 1871-1881, 2001

LaVision, “Imager LX,” http://www.lavision.de/en/products/cameras/piv_cameras.php. Last accessed: January 2014

Liebling, M., Blu, T., Cuche, E., Marquet, P., Depeursinge, C., and Unser, M., “A novel non-diffractive reconstruction method for digital holographic microscopy,“ *Proc. IEEE International Symposium, in Biomedical Imaging,* 625-628, 2002

Mamiya Leaf, “Mamiya Credo,” http://www.mamiyaleaf.com/credo.html. Last accessed: January 2014

McCarron, D., J., *A guide to acousto-optic modulators,* Technical report, Durham University, 2007

Medscope, "Welch Allyn Reusable Ear Specula," http://www.medscope.co.uk/Reusable_Ear_Specula_5mm~pp~8802.htm. Last accessed September 2011

Mikoklai, T. K., Duffey, J., and Adlin, D., “A guide to tympanometry for hearing,” http://www.maico-diagnostics.com/eprise/main/Maico/Products/Files/MI24/Guide.Tymp.pdf. Last accessed: August 2008

Millerd, J. E., Brock, N. J., Hayes, J. B., and Wyant, J. C., “Instantaneous phase-shift point-diffraction interferometer,” *Proc. SPIE, in Optical Science and Technology,* 264-272, 2004a

Millerd, J. E., Brock, N. J., Hayes, J. B., North-Morris, M. B., Novak, M., and Wyant, J. C., “Pixelated phase-mask dynamic interferometer,” *Proc. SPIE, in Optical Science and Technology,* 304-314, 2004b

Nakajima, H. H., Pisano, D. V., Röösli, C., Hamade, M. A., Merchant, G. R., Mahfoud, L., Halpin, C. F., Rosowski, J. J., and Merchant, S. N., “Comparison of ear-canal reflectance and umbo velocity in patients with conductive hearing loss: a preliminary study,” *Ear & Hear.,* 33(1):35, 2012

Nakajima, H. H., Rosowski, J. J., Shahnaz, N., and Voss, S. E., “Assessment of ear disorders using power reflectance,” *Ear & Hear.*, 34:48s-53s, 2013

Novak, M., Millerd, J., Brock, N., North-Morris, M., Hayes, J., and Wyant, J., “Analysis of a micropolarizer array-based simultaneous phase-shifting interferometer,” *App. Op.*, 44(32):6861-6868, doi: 10.1364/AO.44.006861, 2005

O’Connor, K. N. and Puria, S., “Middle-ear circuit model parameters based on a population of human ears,” *JASA*, 123:197, doi: 10.1121/1.2817358, 2008

Owner-Petersen, M., "Decorrelation and fringe visibility: on the limiting behavior of various electronic speckle-pattern correlation interferometers," *JOSA A*, 8(7): 1082-1089, 1991

Pedrini, G., Osten, W., and Gusev, M. E., “High-speed digital holographic interferometry for vibration measurement,” *App. Opt.*, 45(15): 3456-3462, doi: 10.1364/AO.45.003456, 2006

Pedrini, G., Froening, P., Fessler, H., and Tiziani, H. J., “Transient vibration measurements using multi-pulse digital holography,” *Opt. & Laser Tech.*, 29(8): 505-511, 1998

Pedrini, G., Tiziani, H. J., and Zou, Z., “Digital double pulse-TV-holography,” *Opt. Lasers Eng.*, 26(2): 199-219, 1997

Photron, “Photron Fastcam SA-5 Manual Rev. 1.00E (US/EU),” http://http://highspeedimaging.com/media/downloads/files/docs/FASTCAM_SA5_HW_Manual_Rev100en_USEU.pdf. Last accessed: December 2013

Photron, “Photron Fastcam SA-Z,” http://www.photron.com/?cmd=product_general&product_id=41&product_name=FASTCAM+SA-Z. Last accessed: January 2014

Physik Instrumente (PI), ‘Application notes,” http://www.pi-usa.us/pdf/Piezo-Actuators_Ceramics-www.pdf. Last accessed: January 2014

Pryputniewicz, R. J., and Stetson, K. A., “Measurement of vibration patterns using electro-optic holography,” *Proc. SPIE, in 33rd Annual Technical Symposium International Society for Optics and Photonics*, 456-467, 1990

Puria, S., “Measurements of human middle ear forward and reverse acoustics: implications for otoacoustic emissions,” *JASA*, 113(5): 2773-2789, 2003

Puria, S. and Allen, J. B., “Measurements and model of the cat middle ear: evidence of tympanic membrane acoustic delay,” *JASA*, 104:3463, doi: 10.1121/1.423930, 1998

Ramesh, K., Ganesan, V. R., and Mullick, S. K., “Digital image processing of photoelastic fringes–a new approach, “ *Exp. Tech.*, 15(5): 41-46, 1991

Reu, P. L. and Miller, T. J., “The application of high-speed digital image correlation,” *JSA*, 43(8): 673-688, 2008

Rondeau, G., “Steer-by-Wire Systems with Integrated Torque Feedback Improve Steering Performance and Reduce Cost, “ Thomson Industries, Inc., http://www.thomsonlinear.com/website/common/download/document/THO_09_SteerByWire2.pdf. Last accessed: January 2010

Rosowski, J. J., Cheng, J. T., Ravicz, M. E., Hulli, N., Hernandez-Montes, M., Harrington, E., and Furlong, C., “Computer-assisted time-averaged holograms of the motion of the surface of the mammalian tympanic membrane with sound stimuli of 0.4–25kHz," *Hear. Res.*, 253(1): 83-96, doi:10.1016/j.heares.2009.03.010, 2009

Rosowski, J. J., **Dobrev, I.**, Khaleghi, M., Lu, W., Cheng, J. T., Harrington, E., and Furlong, C., "Measurements of three-dimensional shape and sound-induced motion of the chinchilla tympanic membrane," *Hear. Res.*, 301: 44-52, 2013a

Rosowski, J. J., Stenfelt, S., and Lilly, D. "An overview of wideband immittance measurements techniques and terminology: you say absorbance, I say reflectance," *Ear & Hear.*, 34: 9s-16s, doi: 10.1097/AUD.0b013e31829d5a14, 2013b

Rosowski, J. J., Nakajima, H. H., and Cheng, J. T., "Current topics in the study of sound conduction to the inner ear," *Perspectives on Auditory Research*, Springer New York, 493-511, 2014

Rosowski, J. J., Mehta, R. P., and Merchant, S. N., "Diagnostic utility of laser-doppler vibrometry in conductive hearing loss with normal tympanic membrane," *Otol. Neurotol.*, 25(3): 323–332, 2004

Rosowski, J. J., "External and middle ear function," *Oxford Handbook of Auditory Science: The Ear*, Chapter 3, doi: 10.1093/oxfordhb/9780199233397.013.0003, 2010

Rosowski, J. J., Nakajima, H. H., and Merchant, S. N., "Clinical utility of laser-doppler vibrometer measurements in live normal and pathologic human ears," *Ear & Hear.*, 29(1): 3–19, 2008

Rutledge, C., Thyden, M., Furlong, C., Rosowski, J. J., and Cheng, J. T., "Mapping the histology of the human tympanic membrane by spatial domain optical coherence tomography," *Proc. SEM 2012, in MEMS and Nanotechnology*, 6: 125-129, 2013

Saldner, H. O., Molin, N. E., and Stetson, K. A., "Fourier-transform evaluation of phase data in spatially phase-biased TV holograms," *App. Opt.*, 35(2): 332-336, 1996

Sanna, M., Sunose, H., Mancini, F., Russo, A., and Taibah, A., *Middle ear and mastoid microsurgery*, Georg Thierne Verlag, Stuttgart, Germany, 1-15, 2003

Schmitt, D. R. and Hunt, R. H., "Optimization of fringe pattern calculation with direct correlations in speckle interferometry," *App. Opt.*, 36(34): 8848-8857, doi: 10.1364/AO.36.008848, 1998

Schnars, U. and Jüptner, W. P. O., "Digital recording and numerical reconstruction of holograms," *Meas. Sci. Tech.*, 13 R85, doi: 10.1088/0957-0233/13/9/201, 2002

Schnars, U. and Jüptner, W. P. O., *Digital holography*, Springer Berlin Heidelberg, 2005

Seraji, H.,"Adaptive Admittance Control: An Approach to Explicit Force Control in Compliant Motion," *Proc. IEEE International Conference, in Robotics and Automation*, 4: 2705-2712, 1994

Smythe, R. and Moore, R., “Instantaneous phase measuring interferometry,” *Opt. Eng.*, 23(4): 234361, 1984

Sollid, J. E., "Holographic interferometry applied to measurements of small static displacements of diffusely reflecting surfaces," *App. Opt.*, 8(8): 1587-1595, 1969

Specialized Imaging, “Kirana - High Speed Video Camera,” http://specialised-imaging.com /products/kirana-high-speed-video-camera. Last accessed: January 2014

Specialized Imaging, “SIMD,” http://specialised-imaging.com/products/simd-ultra-high-speed-framing-camera. Last accessed: November 2013

Stiles, R. N. and Randall, J. E., "Mechanical factors in human tremor frequency," *J. of App. Phys.*, 23(3): 324-30, 1967

Stinson, M. R. and Lawton, B. W., "Specification of the geometry of the human ear canal for the prediction of sound-pressure level distribution," *JASA*, 85(6): 2492-503, 1989

Subhash, H. M., Nguyen-Huynh, A., Wang, R. K., Jacques, S. L., Choudhury, N., and Nuttall, A. L., “Feasibility of spectral-domain phase-sensitive optical coherence tomography for middle ear vibrometry,” *J. Biomed. Opt.*, 17(6): 0605051-0605053, 2012

Sundberg, M., “Optical methods for tympanic membrane characterization towards objective otoscopy in otitis media,” Department of Biomedical Engineering, Linköpings , Linköping, Sweden, Universitet Linköping Dissertation No. 1173, 19-21, 2008

Suzuki, Y. and Takeshima, H., “Equal-loudness-level contours for pure tones,” *JASA*, 116(2): 918-933, 2004

Takeda, M., Ina, H., and Kobayashi, S., “Fourier-transform method of fringe-pattern analysis for computer-based topography and interferometry,” *JOSA*, 72(1): 156-160, 1982

Todd, N. W., "Tympanum-Canal Angles Anteriorly, Anteroinferiorly, and Inferiorly: a Postmortem Study of 41 Adult Crania," *Ear, Nose, & Throat Journal*, 88(9): 22-27, 2009

Tonndorf, J. and Khanna, S. M., "Tympanic-membrane vibrations in human cadaver ears studied by time-averaged holography," *JASA*, 51: 1904, doi: 10.1121/1.1913050, 1972

Van der Jeught, S., Dirckx, J. J., Aerts, J. R., Bradu, A., Podoleanu, A. G., and Buytaert, J. A., “Full-field thickness distribution of human tympanic membrane obtained with optical coherence tomography,” *JARO*, 14(4): 483-494, 2013

Von Unge, M., Decraemer, W. F., Bagger-Sjöbäck, D., and Dirckx, J. J., "Displacement of the gerbil tympanic membrane under static pressure variations measured with a real-time differential moiré interferometer, " *Hear. Res.*, 70(2): 229-242, 1993

Wåhlin, A. O., Gren, P. O., and Molin, N. E., "On structure-borne sound: Experiments showing the initial transient acoustic wave field generated by an impacted plate," *JASA*, 96:2791, 1994

Wilson, P., and Johnstone, J. R., "Basilar-membrane and middle-ear vibration in guinea pig measured by capacitive probe," *JASA*, 57(3): 705-723, doi: 10.1121/1.380472, 1975

Wit, H. P., and Ritsma, R. J., "Stimulated acoustic emissions from the human ear," *JASA*, 66:911, 1979

Xu, J., "Shearogram analysis by improved spiral phase transform and its application in dynamic testing of WTB," TWI Limited, UK, 2011

Yaroslavsky, L. P., Zhang, F., and Yamaguchi, I., "Point spread functions of digital reconstruction of digitally recorded holograms," *Proc. SPIE 2004, in Photonics Asia*, 271-282, 2005

Yaroslavsky, L. P., "Lect. 3 Digital Recording and Numerical Reconstruction of Holograms," http://www.eng.tau.ac.il/~yaro/lectnotes/pdf/L3_TICSP_HologramRecording&Reconstr.pdf. Last accessed: December 2012

Zahnert, T., "The differential diagnosis of hearing loss," Deutsches Arzteblatt international, 108: 433–444, 2011

Zhang, X., and Gan, R. Z., "Dynamic properties of human tympanic membrane - experimental measurement and modeling analysis," *Int. J Exp. & Comp. Biomech.*, 1(3): 252-268, doi: 10.1504/IJECB.2010.03526, 2010

Appendix A: Reference beam distance range

This appendix provides a detailed derivation of the spatial frequency content of all points on the surface of the object to the hologram on the sensor in the optical setup of the OH, as described in Chapter 9. Figure A.1 shows a schematic of the optical setup of the OH, indicating major parameters defining the footprint of system.

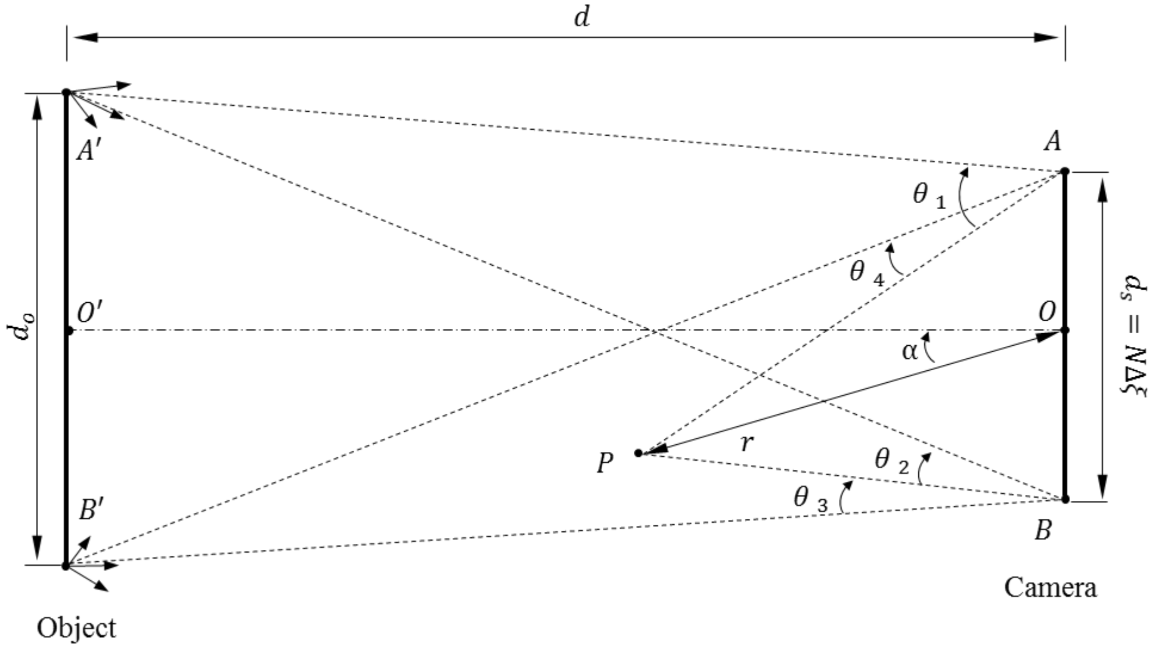

Fig. A.1. Geometrical setup of the optical system of the OH based on an enhanced lensless Fourier transform holographic setup. Indicated are geometrical major parameters defining the footprint of optical system.

Points A' and B' are the outermost points on the object, while points A and B are the outermost points on the camera sensor relative to the optical axis OO'. Point P is the origin of the spherical wavefront of the reference wave, located at a distance r and angle α from the center, O, of the camera sensor.

Figure A.2 shows the geometrical setup used for derivation of an analytical solution for angle θ_1. Based on that, $\theta_1 = \theta_1' + \theta_1''$, which can be further expressed by a trigonometric relationships in triangles ADA', ACP and POE.

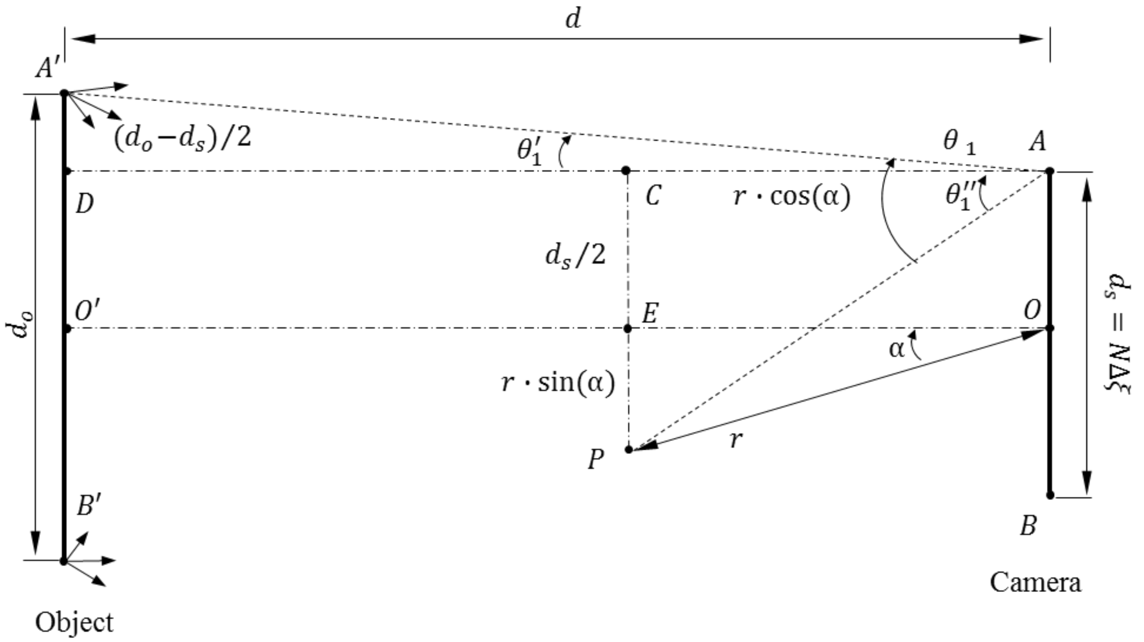

Fig. A.2. Geometrical setup for analytical derivation of angle θ_1.

From triangle ADA', θ_1' is

$$\theta_1' = tan^{-1}\left(\frac{d_o - d_s}{2d}\right) \cong \frac{d_o - d_s}{2d}. \tag{A.1}$$

Note that sensor, d_s, and object, d_o, size are much smaller than d. Thus a small angle approximate is applied in Eq. A.1. By analogy, from triangles ACP and POE, θ_1'' is

$$\theta_1'' = tan^{-1}\left[\frac{d_s/2 + r \cdot sin(\alpha)}{r \cdot cos(\alpha)}\right] \cong \frac{d_s/2}{r \cdot \cos(\alpha)} + \tan(\alpha) \cong \frac{d_s}{2r} + \alpha\,. \tag{A.2}$$

Thus, θ_1 is

$$\theta_1 = \theta_1' + \theta_1'' \cong \frac{d_o - d_s}{2d} + \frac{d_s}{2r} + \alpha\,. \tag{A.3}$$

Combining Eqs 9.1 and A.3, a design constrain for the distance, r, between the reference wave origin and the camera sensor, can be expressed as

$$\begin{gathered} \frac{d_o - d_s}{2d} + \frac{d_s}{2r} + \alpha < \theta_{max}\,, \\ \frac{d_s}{2\left(\theta_{max} - \alpha - \frac{d_o - d_s}{2d}\right)} < r\,. \end{gathered} \tag{A.4}$$

Equation A.4 is equivalent to Eq. 9.7. Figure A.3 shows the geometrical setup used for derivation of an analytical solution for angle θ_2. Based on that, $\theta_2 = \theta_2'' - \theta_2'$, which can be further expressed by a trigonometric relationships in triangles HBA' and FBP.

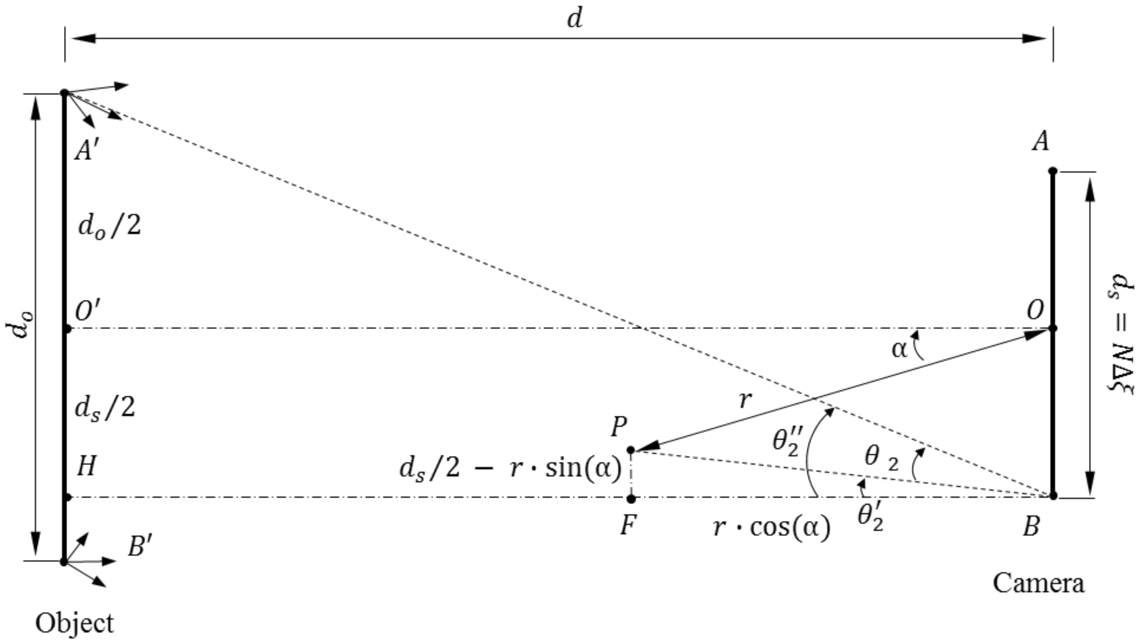

Fig. A.3. Geometrical setup for analytical derivation of angle θ_2.

From triangle HBA'

$$\theta_2'' = tan^{-1}\left(\frac{d_o + d_s}{2d}\right) \cong \frac{d_o + d_s}{2d}. \tag{A.5}$$

By analogy, from triangle FBP, θ_2' is

$$\theta_2' = tan^{-1}\left[\frac{d_s/2 - r \cdot sin(\alpha)}{r \cdot cos(\alpha)}\right] \cong \frac{d_s/2}{r \cdot \cos(\alpha)} - \tan(\alpha) \cong \frac{d_s}{2r} - \alpha\,. \tag{A.6}$$

Thus, θ_2

$$\theta_2 = \theta_2'' - \theta_2' \cong \frac{d_o + d_s}{2d} - \frac{d_s}{2r} + \alpha\,. \tag{A.7}$$

Combining Eqs 9.1 and A.7, a design constrain for the distance, r, between the reference wave origin and the camera sensor, can be expressed as

$$\begin{gathered} \frac{d_o + d_s}{2d} - \frac{d_s}{2r} + \alpha < \theta_{max}\,, \\ \frac{d_s}{2\left(\frac{d_o + d_s}{2d} + \alpha - \theta_{max}\right)} > r\,. \end{gathered} \tag{A.8}$$

Equation A.8 is equivalent to Eq. 9.8. Figure A.4 shows the geometrical setup used for derivation of an analytical solution for angle θ_3. Based on that, $\theta_3 = \theta_3' + \theta_3''$, which can be further expressed by a trigonometric relationships in triangles $B'BH$ and FBP.

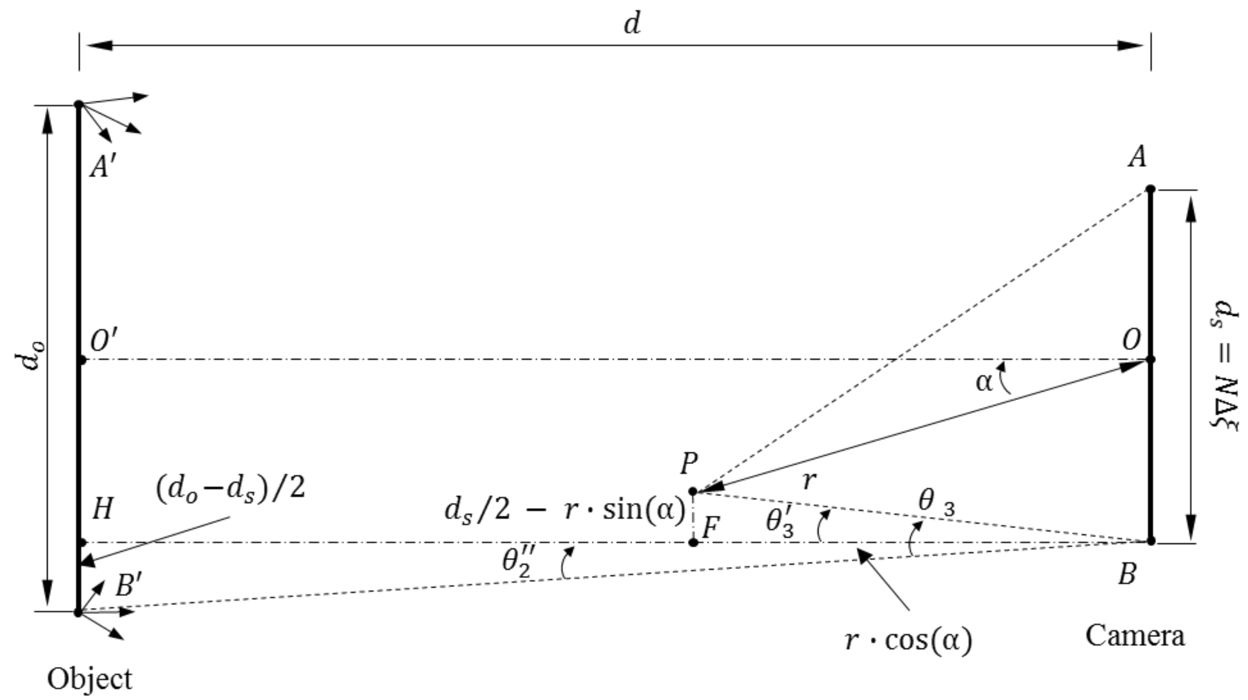

Fig. A.4. Geometrical setup for analytical derivation of angle θ_3.

It should be noted that $\theta_3' = \theta_2'$

$$\theta_3' = \theta_2' = tan^{-1}\left[\frac{d_s/2 - r \cdot sin(\alpha)}{r \cdot cos(\alpha)}\right] \cong \frac{d_s/2}{r \cdot \cos(\alpha)} - \tan(\alpha) \cong \frac{d_s}{2r} - \alpha\,. \quad \text{(A.9)}$$

Based on symmetry, relative to the optical axis OO', $\theta_3'' = \theta_1'$

$$\theta_3'' = \theta_1' = tan^{-1}\left(\frac{d_o - d_s}{2d}\right) \cong \frac{d_o - d_s}{2d}\,. \quad \text{(A.10)}$$

Thus, θ_3 is

$$\theta_3 = \theta_3' + \theta_3'' \cong \frac{d_o - d_s}{2d} + \frac{d_s}{2r} - \alpha\,, \quad \text{(A.11)}$$

Combining Eqs 9.1 and A.11, a design constrain for the distance, r, between the reference wave origin and the camera sensor, can be expressed as

$$\frac{d_o - d_s}{2d} + \frac{d_s}{2r} - \alpha \ < \theta_{max} \,,$$

$$\frac{d_s}{2\left(\theta_{max} + \alpha - \frac{d_o - d_s}{2d}\right)} < r \,. \tag{A.12}$$

Equation A.12 is equivalent to Eq. 9.9. Figure A.5 shows the geometrical setup used for derivation of an analytical solution for angle θ_4. Based on that, $\theta_4 = \theta_4' - \theta_4''$, which can be further expressed by a trigonometric relationships in triangles $B'AA'$ and PAC.

Based on symmetry, relative to the optical axis OO', $\theta_4'' = \theta_2''$

$$\theta_4'' = \theta_2'' = tan^{-1}\left(\frac{d_o + d_s}{2d}\right) \cong \frac{d_o + d_s}{2d} \,. \tag{A.13}$$

Also I should be noted that $\theta_4' = \theta_1''$

$$\theta_4' = \theta_1'' = tan^{-1}\left[\frac{d_s/2 + r \cdot sin(\alpha)}{r \cdot cos(\alpha)}\right] \cong \frac{d_s/2}{r \cdot \cos(\alpha)} + \tan(\alpha)$$
$$\cong \frac{d_s}{2r} + \alpha. \tag{A.14}$$

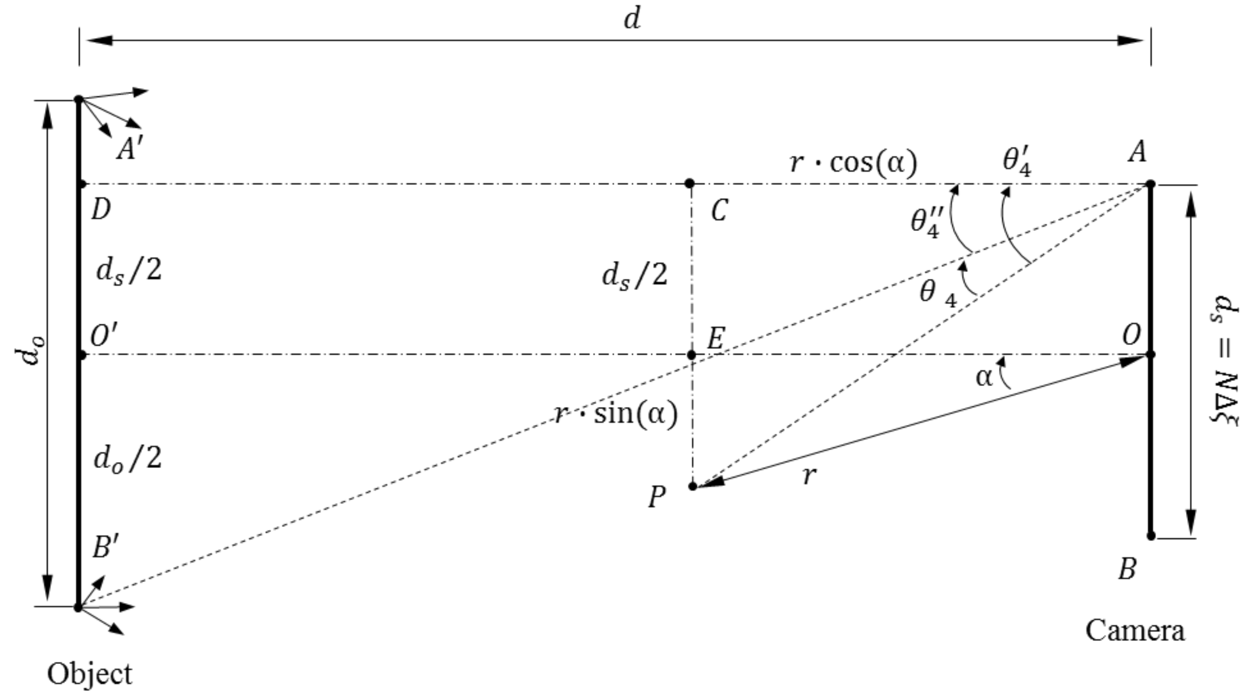

Fig. A.5. Geometrical setup for analytical derivation of angle θ_4.

Thus, θ_4 is

$$\theta_4 = \theta_4' - \theta_4'' \cong \frac{d_s}{2r} + \alpha - \frac{d_o + d_s}{2d} . \tag{A.15}$$

Combining Eqs 9.1 and B.15, a design constrain for the distance, r, between the reference wave origin and the camera sensor, can be expressed as

$$\begin{gathered} \frac{d_s}{2r} + \alpha - \frac{d_o + d_s}{2d} < \theta_{max} , \\ \frac{d_s}{2\left(\theta_{max} - \alpha + \frac{d_o + d_s}{2d}\right)} < r . \end{gathered} \tag{A.16}$$

Equation A.16 is equivalent to Eq. 9.10.

Appendix B: LaserView GUI for hardware setup and high-speed acquisition

This Appendix describes the GUI of LaserView for operation of the several live procedures, part of the holographic measurement process (HMP) described in Chapter 10. All corresponding LaserView GUI upgrades have been implemented by Ellery Harrington.

Hardware and software setup procedures

The hardware and software setup stage of the HMP is aimed at adjustment of all system modules and corresponding components for a particular measurement or a routine calibration/adjustment of the system. This section describes the software adjustments required for the operation of the reference beam alignment and the sample alignment procedures.

Reference beam alignment (RBA)

The aim of the reference beam alignment procedure (RBA) is to provide live visual feedback and software adjustment capabilities during the alignment of the reference beam (RB) to allow for the optimization of the spatial phase sampling method within the PHHS (described in Chapter 7). The RBA procedures is implemented by two upgrades of the UI of Laser View:

- 2D FFT display – live display of the power spectrum of the 2D FFT of each camera frame with options for color map and brightness.

- Reconstruction distance calibration – correction of the reconstruction distance to account for a new position of the reference beam.

The aim of the 2D FFT display functions is to provide feedback on the orientation of the RB relative to the camera plane. While the optical setup of the MPDE system includes a hardware structure defining the position of the RB, it also allows fine tuning (+/- 5deg) of the orientation of the beam relative to the normal of the camera plane. Within the scope of this work, the fine tuning of the RB is manual and is aided by the capability for a live feedback of the current orientation of the RB. Based on Eq. 9.1 the relative angle between the RB and the camera defines the carrier frequency of the spatial phase sampling and the spatial separation of the twin images and the DC component in the frequency domain of the hologram. The software allows for live display of the power spectrum of the 2D FFT of each camera frame, as shown in Fig. B.1, which aids the user in the adjustment the orientation of the RB.

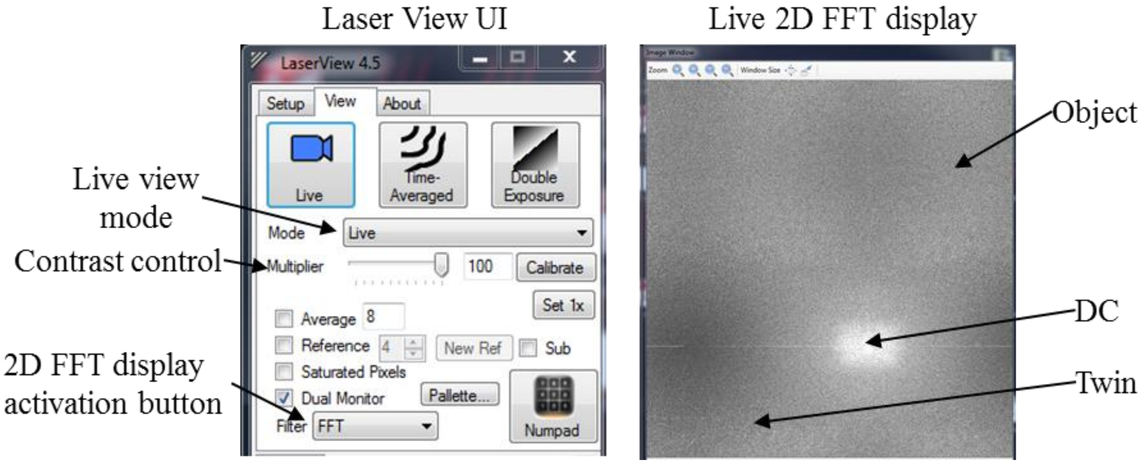

Mode Live
Multiplier 100
☐ Average 8
☐ Reference 4
☑ Dual Monitor
Filter FFT

Fig. B.1. 2D FFT display for live view of the spatial frequency content of the hologram during a reference beam alignment (RBA) procedure.

Based on Eq. 5.32, the holographic reconstruction algorithm relies on a mathematical model of the reference beam as well as the accuracy of the Fresnel approximation. Any user modification to the position of the reference beam will change its complex field from the one that is preprogramed in the software. In practice, if everything else within the optical setup and the reconstruction algorithm is kept the same, the RB readjustment results in a reconstruction distance that is different from the actual working distance to the object. Similar effect could result from application of the reconstruction algorithm in optical settings that are close to the limitations of the Fresnel approximation. To account for these effects after the hardware adjustment of the reference beam, the software allows for calibration of the reconstruction distance in order to match the actual working distance to the object. The GUI allows for a user input of up to 4th order polynomial that defines the relation between the holographic reconstruction distance and actual working distance to the object of interest, as shown in Fig. B.2.

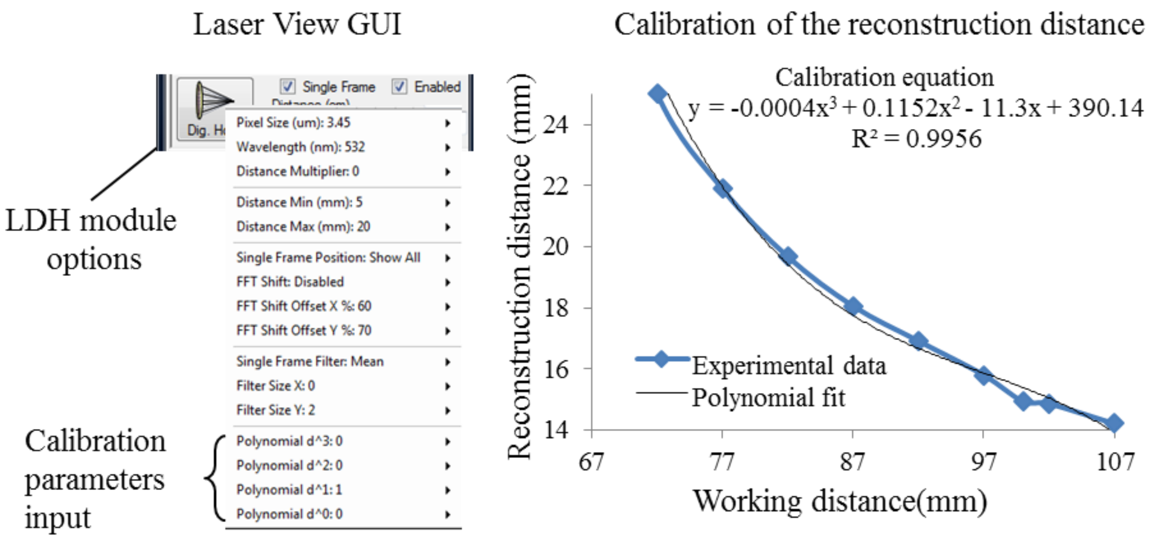
☑ Single Frame ☑ Enabled

Pixel Size (um): 3.45

Wavelength (nm): 532

Distance Multiplier: 0

Distance Min (mm): 5

Distance Max (mm): 20

Single Frame Position: Show All

FFT Shift: Disabled

FFT Shift Offset X %: 60

FFT Shift Offset Y %: 70

Single Frame Filter: Mean

Filter Size X: 0

Filter Size Y: 2

Polynomial d^3: 0

Polynomial d^2: 0

Polynomial d^1: 1

Polynomial d^0: 0

$y = -0.0004x^3 + 0.1152x^2 - 11.3x + 390.14$

$R^2 = 0.9956$

Fig. B.2. Experimental data and corresponding GUI for calibration of the reconstruction distance of the lensless digital holography module of LaserView during the reference beam alignment (RBA) procedure.

Sample alignment

A crucial procedure of the hardware and software setup stage is the alignment of the sample to the FOV and WD of the system. For the PHHS utilizing lensless digital holography, the visual feedback is provided by the LaserView's holographic reconstruction module [Harrington et al., 2011] whose frame rate is governed by the computational speed of the PC and the size of the images. It is beneficial for the user to have higher frame rate (even at the cost of lower resolutions) for faster feedback and improved dexterity during sample manipulation and alignment relative to the optical system of the interferometer module. To allow for that, a sample alignment (SA) procedure has been implemented in LaserView through GUI upgrade allowing dynamic switching between full, half or VGA camera resolutions. This dynamic resolution change is done at the camera which not only decreases the image size for faster live processing but also increases the capture rate of the camera. As an example, typical live holographic reconstruction speed for 2048x2048 pix is ~5 fps for LaserView 4.5.17 running on Windows 7 PC with Xeon E5420 CPU and 4 GB RAM. Switching to half resolution (1024x1024) speeds up the live holographic reconstruction to ~17 fps (i.e., 3.5 fold). Figure B.3 illustrates the section of the LaserView GUI for dynamically controlling the camera resolution as well as the corresponding frame rates at various AOI width (assuming a square AOI).

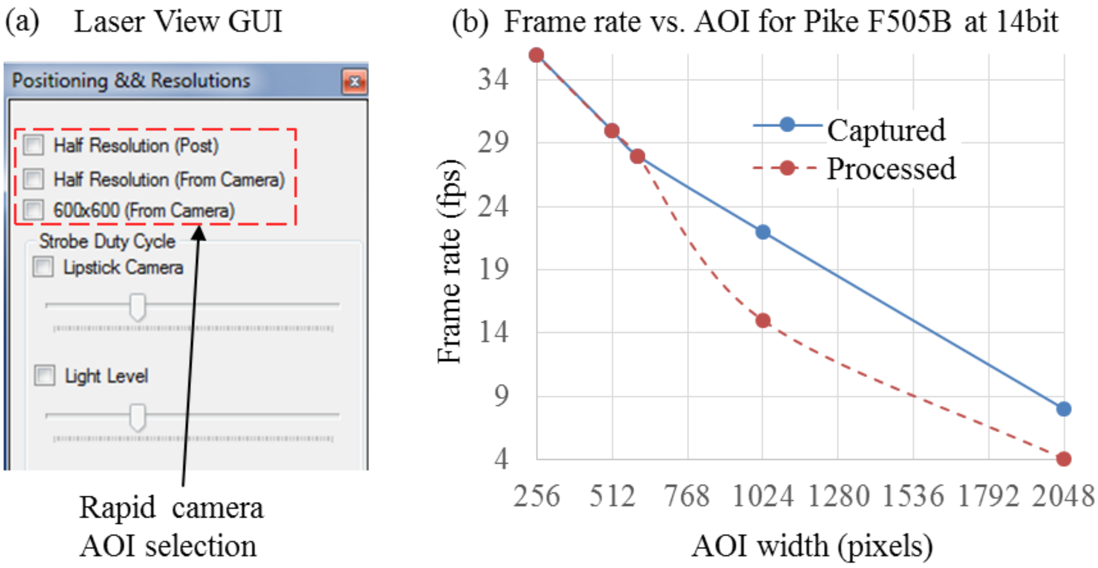

Fig. B.3. Dynamic adjustment of the captured and processed (displayed) frame rate of the reconstructed holograms in the LHD module of LaserView: (a) GUI for dynamic switching between full, half and VGA resolution during the sample alignment procedure; and (b) Frame rate versus AOI (assuming a square AOI) based on the Pike F505B and a Xeon E5420 CPU.

Data acquisition procedures

The data acquisition stage of the HMP provides several acquisition modes for the study of static, steady state and transient measurements of the response of the human ME. This section describes the software adjustments required for the operation of the multi-pulsed double exposure (MPDE) and high-speed 2+N frame (HS 2+N) acquisition modes.

Multi-pulsed double exposure (MPDE) acquisition mode

The multi-pulsed double exposure (MPDE) acquisition mode is based on the MPDE acquisition algorithm described in Chapter 8. The implementation of the algorithm within LaserView allows for the user's control over the camera acquisition, laser illumination and acoustic excitation through a custom GUI, as shown in Fig. B.4. The GUI, shown in Fig. B.4a, allows the user to control the timing of all events of the MPDE acquisition sequence by adjusting settings of the digital output component and the camera: camera exposure, camera trigger, strobe 1, strobe 2 start, stimulus start, and strobe 2 end, as shown in Fig. B.4b. To perform MPDE transient measurements of a TM sample, the user is required to specify the following parameters:

- *Camera exposure* - The camera exposure is adjusted to match or exceed the minimum inter-frame time of the camera (i.e. ~72ms for 14fps camera). This ensures that the time between exposures is reduced to minimum, as described Chapter 8.
- *Number of frames per trigger* - The camera is set to capture 2 frames at maximum frame rate upon receiving an external trigger. The GUI allows for adjustment of the number of frames (up to the camera's buffer size) for other applications.
- *Camera trigger* – The moment of camera trigger relative to the time reference of the DAQ (i.e. master clock). In typical applications of MPDE acquisition, the camera trigger time is set to 0 μs.

- *Stimulus* – Time of start of the signal that is send from the DAQ to the signal generator in order to produce an acoustic stimulus.
- *Strobe length* – The length of each illumination pulse effectively defining the exposure time and the corresponding temporal resolution the measurements. For human TM measurements, this is adjusted based on the acquisition design parameters described in Chapter 6.
- *Strobe 1* – The beginning of the first illumination pulse that is used to capture the reference state of the object before the application of the acoustic excitation. The Strobe 1 time is adjusted such that it's approximately at the end of the first frame of the camera for each reference-deformed frames pair taking into account the temporal jitter of the particular camera model (i.e., ~30 μs for Pike F505B).
- *Strobe 2 start and end and interval* – The beginning and end of the range of time instances for the start of the second illumination pulse that is used to capture the deformed state of the object during the second frame (frame N+1 in Fig. B.4b) for each reference-deformed frames pair of the MPDE acquisition. The range of *Strobe 2* defines the effective measurement time for the transient response of the object. The *Strobe 2 interval* controls the temporal separation between consecutive *Strobe 2* instances at two consecutive reference-deformed frames pairs. The *Strobe 2 interval* defines the sampling period and the corresponding sampling frequency of the MPDE acquisition.
- *Frequency of the output clock* – defines the output sample frequency of the DAQ's digital outputs within the I/O module of the control system. The output frequency defines the temporal resolution of the correlated timing signals of the 3

digital output channels that correspond to the *Camera trigger*, *Strobe*, and *Stimulus* signals in the UI of the MPDE software module in Fig. B.4a.

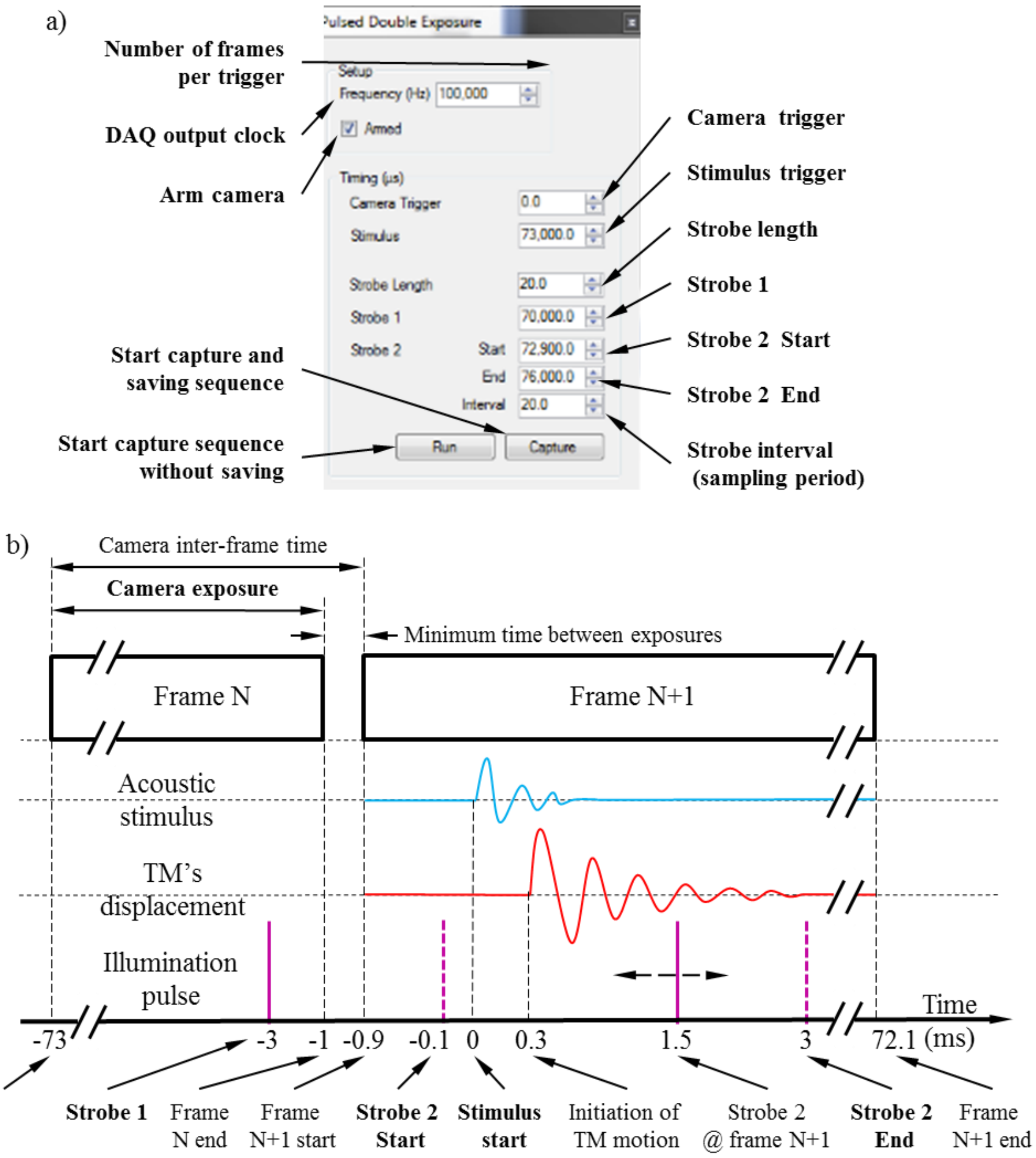
ulsed Double Exposure

Setup

Frequency (Hz) 100,000

☑ Armed

Timing (µs)

Camera Trigger 0.0

Stimulus 73,000.0

Strobe Length 20.0

Strobe 1 70,000.0

Strobe 2 Start 72,900.0

End 76,000.0

Interval 20.0

Fig. B.4. User controlled parameters of the multi-pulsed double exposure (MPDE) acquisition mode: (a) and (b) UI and corresponding timing diagram for control of the timing parameters (highlighted in bold) of the acquisition procedure.

High-speed 2+N frame (HS 2+N) acquisition mode

User control over the temporal phase shifting, camera trigger and acoustic excitation parameters of the HS 2+N acquisition mode is provided by the MPDE acquisition mode GUI in LaserView with no software modifications and only minor adjustment of the settings, as shown in Fig. B.5.

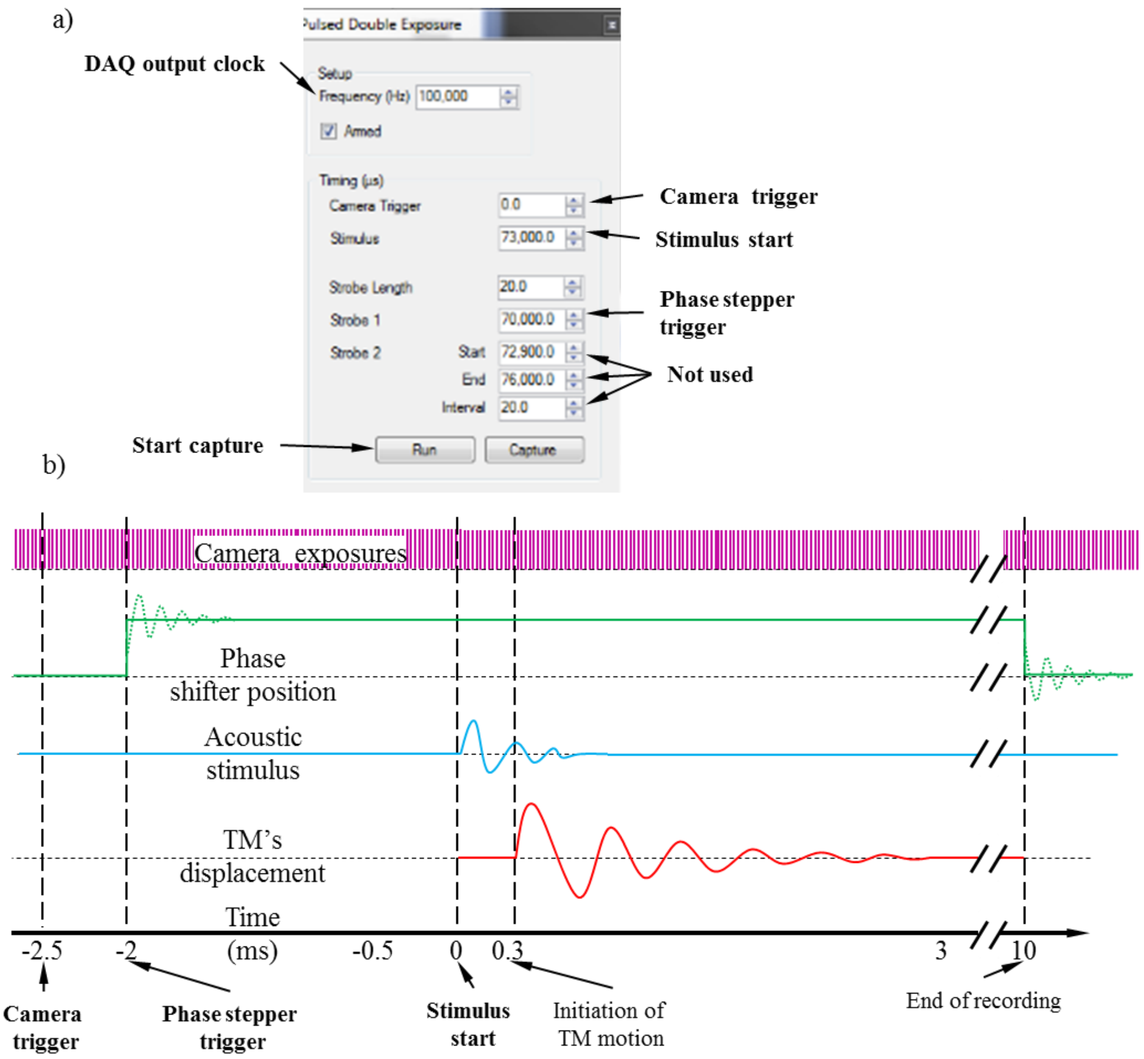

Pulsed Double Exposure

Setup

Frequency (Hz) 100,000

☑ Armed

Timing (µs)

Camera Trigger 0.0

Stimulus 73,000.0

Strobe Length 20.0

Strobe 1 70,000.0

Strobe 2 Start 72,900.0

End 76,000.0

Interval 20.0

Fig. B.5. User controlled parameters of the high-speed 2+N frames (HS 2+N) acquisition mode: (a) and (b) GUI and corresponding timing diagram for control of the timing parameters (highlighted in bold) of the acquisition procedure. The GUI is equivalent to the one used for the MPDE acquisition mode.

Based on Chapter 10, the *Camera trigger* is set for 0 μs so that the camera recording starts before or at the beginning of all other control events. While *Strobe 1* is used for control of the illumination during the MPDE acquisition mode, during the HS acquisition mode, it is used for control of the Phase stepper trigger, typically set for 500 μs after *Camera trigger*. However, only one trigger pulse is needed, thus all parameters of *Strobe 2* are disabled by setting then to produce one pulse overlapping with the pulse from *Strobe 1* (i.e., *Start* = *Strobe 1*, *End* = *Start*, *Interval* = 0). The phase shift voltage is controlled through the existing LaserView GUI [Harrington et al., 2011]. The *Stimulus* is set to start the acoustic excitation after the second set of reference frames (i.e. at 2500 μs after *Camera trigger*), in accordance with 2+N frame high-speed acquisition algorithm described in Chapter 8.

Appendix C: Overview of the "Holographic processing toolbox"

This appendix presents an overview and data workflow of the software library "Holographic processing toolbox" (HPT) that has been developed in MATLAB environment,. The HPT consists of functions and scripts for the processing, analysis, data mining, and interpretation of 3DHDSs and STDDCs.

Workflow

Due to the similarities of the PHHS and the CHHS, the scripts and functions for each measurement system follows a similar workflow, as shown in Fig C.1. The workflow consists of 3 stages that convert data from 3DHDS, Chapter 10, to STDDC and finally to MRMP (Chapter 11). All 3 stages are handled by the ***HR_LPR_v3*** and the ***Pulsed_DE_v1*** MATLAB scripts. Both scripts share similar set of functions based on the numerical methods of the holographic measurement process (HMP), Chapter 10, and the parallel data mining and interpretation (PDMI) procedures, Chapter 11.

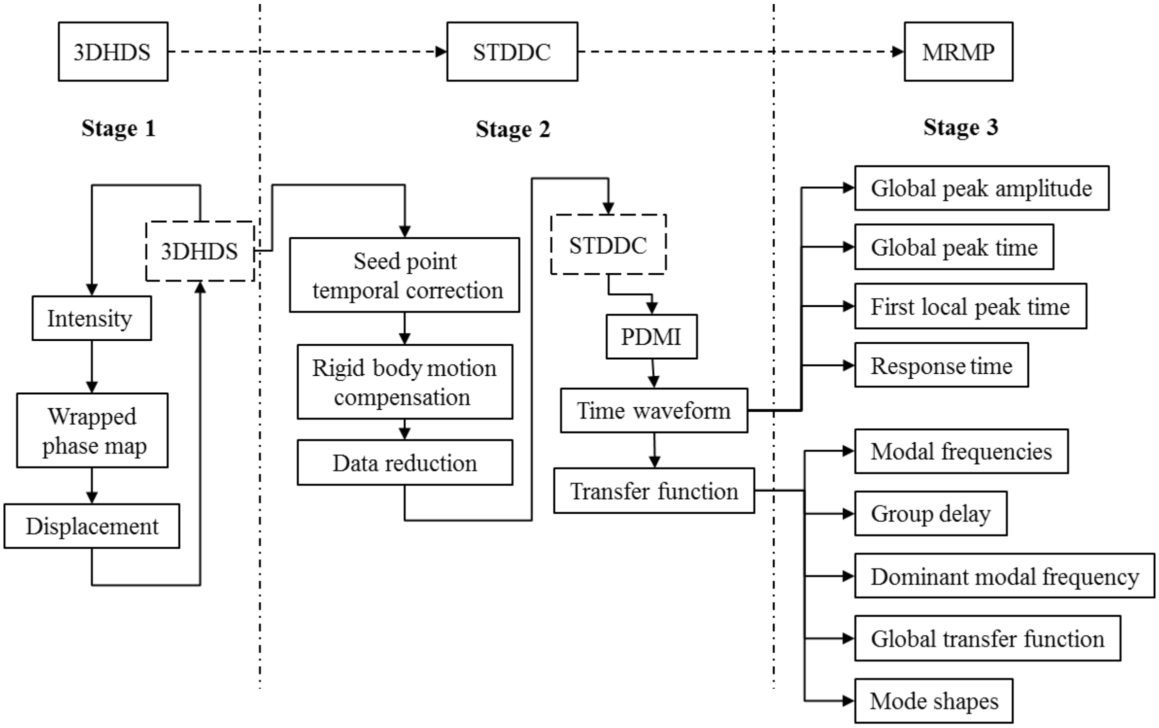

Fig. C.1. Workflow of data processing in PHHS and CHHS handled by the ***HR_LPR_v3*** and the ***Pulsed_DE_v1*** MATLAB scripts.

Figure C.2 shows an overview of a representative set of high-level functions that compose both scripts. The functions are categorized based on their main task and stage in the workflow, defined in Fig. C.1.

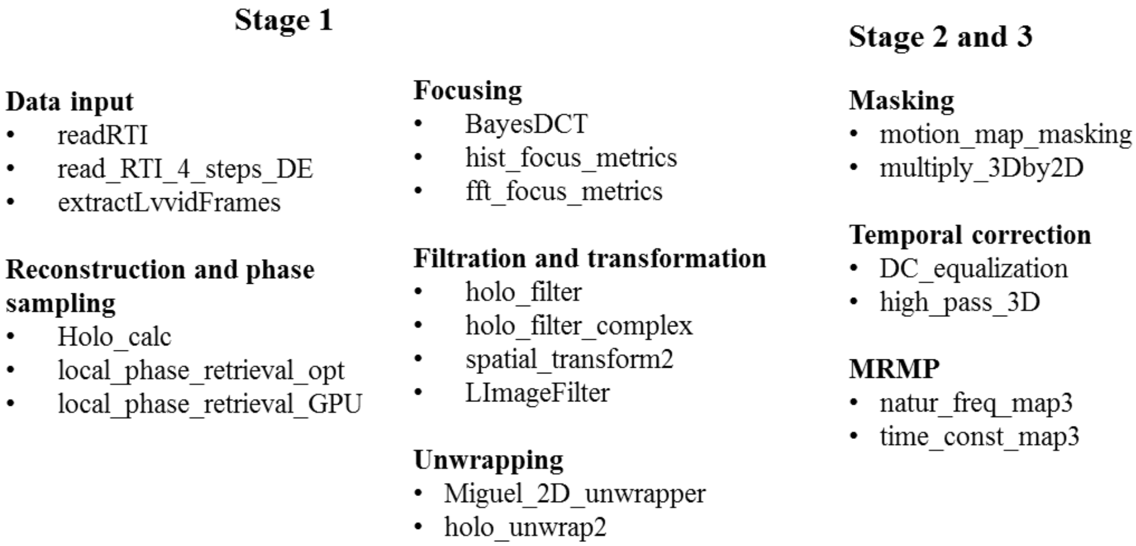

Stage 1

Data input

- readRTI
- read_RTI_4_steps_DE
- extractLvvidFrames

Reconstruction and phase sampling

- Holo_calc
- local_phase_retrieval_opt
- local_phase_retrieval_GPU

Focusing

- BayesDCT
- hist_focus_metrics
- fft_focus_metrics

Filtration and transformation

- holo_filter
- holo_filter_complex
- spatial_transform2
- LImageFilter

Unwrapping

- Miguel_2D_unwrapper
- holo_unwrap2

Stage 2 and 3

Masking

- motion_map_masking
- multiply_3Dby2D

Temporal correction

- DC_equalization
- high_pass_3D

MRMP

- natur_freq_map3
- time_const_map3

Fig. C.2. Overview of the representative set of functions of the “Holographic processing toolbox” software library.

The following sections contain a brief description of the functionality, input and output of each function presented in Fig. C.2. The full “Holographic processing toolbox” library is included with the digital supplementary materials of this Dissertation.

Stage 1

Data input

- **readRTI –** reads intensity data (hologram) and the header (metadata) of one RTI file. Implemented by Ellery Harrington.
    - Input:
        - *filename* - file location of the RTI file
    - Output:

        - *image* – a 2D matrix containing intensity values in double precision representing the recorded hologram.
        - *lvvMetadata* – an empty placeholder for LVVID meta data.
        - *rtiMetadata* – RTI metadata such as frame time stamp, size, scale, etc.

- **read_RTI_4_steps_DE**– reads an ordered set of frames (holograms) and the header (metadata) of sequence of RTI files corresponding to 4 temporally phase stepped double-exposure holograms (a total of 8 files)
    - Input:
        - *directory* - directory location of the set of RTI files.
        - *file_name_base* - file name base for of the set.
    - Output:
        - *I_all* – a 3D matrix containing intensity values in double precision for each frame of the requested set ordered as 4 reference followed by 4 deformed frames.
        - *framesN* – number of read frames.
        - *frameH* – height of each frame in pixels.
        - *lvvMetadata* – an empty placeholder for LVVID meta data..
        - *rtiMetadata* – RTI metadata.

- **extractLvvidFrame –** reads an ordered set temporally phase stepped frames (holograms) and the header (metadata) of a LVVID file.
    - Input:
        - *filePath* - file location of the LVVID file
        - *frames* - a vector of indexes corresponding to sequential frames to be read
    - Output:
        - *cur_AOI* – a 3D matrix containing intensity values in double precision for each frame of the requested set.
        - *framesN* – number of read frames.
        - *frameH* – height of each frame in pixels.
        - *frameW* – width of each frame in pixels.

Reconstruction and phase sampling

- **Holo_calc**– reads performs DC removal, reconstruction, phase sampling and complex data filtration.
    - Input:
        - *I*- a 3D matrix containing intensity values in double precision for a set of DE temporally and/or spatial phase shifted holograms. Based on the 3rd dimension of the data set, **Holo_calc** automatically switches between 1, DE 1 (2 frames), 4, and DE 4 (8 frames) frame mode of processing. DE 5+1 and 2+1 frame modes are under construction.

    - *dh_param* – a set of parameters for lensless digital holographic reconstruction
    - *espi_param* – a set of parameters for electronic speckle pattern interferometry
    - *holo_method* – defines the use holographic reconstruction and phase sampling method.
    - *filt* – defines filter size for spatial filtration of the complex data
    - *filt_type* – defines filter type for spatial filtration of the complex data
  - Output:
    - *Imod* – A 2D matrix of the modulation map of the reference state.
    - *ImodD* – A 2D matrix of the modulation map of the deformed state.
    - *ImodDE* – A 2D matrix of the modulation map of the DE state.
    - *OpPhase*– A 2D matrix of the phase map of the DE state.
    - *Icomplex*– A 2D matrix of the complex field map of the DE state.

- **local_phase_retrieval_opt –** implementation of the 2+1 LCPS method (Chapter 7) for multi-threaded CPU using the MATLAB parallel computing toolbox (*matlabpool*).
  - Input:
    - *Iin* - 3D matrix containing intensity values in double precision for a set (i.e., 2+1 or 4+1) of DE temporally phase shifted holograms.

        - *cell_size* – size for the local correlation kernel
        - *coarse_res* – coarse sampling grid size to control computation speed.
        - *DC* - 3D matrix containing intensity values in double precision corresponding to the background illumination of the reference and deformed frames *Iin.*
    - Output:
        - *Ic* – A 2D matrix of the complex filed map of the DE state.

- **local_phase_retrieval_opt** – implementation of the 2+1 LCPS method (Chapter 7) for massive parallel GPU execution using the MATLAB *gpuArray* toolbox. Input and output is equivalent to **local_phase_retrieval_opt.**

Focusing

- **BayesDCT –** implementation of the Bayes spectral entropy (BSE) of an image spectrum [Kristan et al., 2006] for focus/sharpness estimation.
    - Input:
        - *X* - 2D matrix containing a grayscale image.
        - *Y* - subwindow size, e.g. [8,8].
        - *lo* – the lowest order coefficient used by sharpness measure.
        - *hi* – the highest order coefficient used by sharpness measure.
    - Output:

        - *measure* – a value of the sharpness measure.

- **hist_focus_metrics** – implementation of the focus/sharpness estimation based on the intensity histogram (Chapter 10).
    - Input:
        - *cur_frame* - 2D matrix containing the focusing window intensity data.
    - Output:
        - *measure* – a value of the sharpness measure.

- **hist_focus_metrics** – implementation of the focus/sharpness estimation based on the intensity power spectrum (Chapter 10).
    - Input:
        - *cur_frame* - 2D matrix containing the focusing window intensity data.
    - Output:
        - *measure* – a value of the sharpness measure.

Filtration and transformation

- **holo_filter** – a set of spatio-temporal filters including mean, median, Gaussian, etc.

    - Input:
        - *I_in* - 2D or 3D matrix containing the image(s) to be filtered.
        - *filt* – defines filter size for spatial filtration of the image(s).
        - *filt_type* – defines filter type for spatial filtration of the image(s).
    - Output:
        - *I_out*– filtered image(s).

- **holo_filter_complex–** same as **holo_filter** but upgraded for work with complex field data.

- **spatial_transform2–** allows for a set of cropping, shifting (in-plane translation) and various 2D transformations based on affine and projective models.
    - Input:
        - *I_in* - 2D matrix containing the image to be spatially transformed.
        - *img_center_XY* – 1x2 input defining location of the image center for in-plane translation.
        - *T_transf* – spatial transformation object as defined by MATLAB's *imtransform.*
        - *AOI_range_norm* – value in the range of [0,1] defining the size of the cropped image.
    - Output:

        - *I_out*– 2D matrix containing final result of the spatial transformations.

- **LImageFilter –** a wrapper function for the computing core of HoloStudio [Harrington et al., 2011]. The function allows full access, within the MATLAB environment, of the functions (filters) within HoloStudio with capabilities for digital reconstruction, masking, spatial filtration, and unwrapping. Input is a string equivalent to the filter commands in HoloStudio. Developed and implemented by Ellery Harrington.

Unwrapping

- **holo_unwrap2–** a wrapper function for the *Unwrap* function in HoloStudio [Harrington et al., 2011]. The function allows for spatial unwrapping of discontinuous phase maps based on original complex field.
    - Input:
        - *I_ph* - 2D matrix containing the complex field corresponding to the wrapped phase map.
        - *I_mask* – 2D binary mask defining areas to be excluded from the unwrapping process.
        - *param* – a vector of parameters controlling the spatial unwrapping process.
    - Output:

        - *I_out*– 2D matrix containing the unwrapped phase map in units of radians.

- **Miguel_2D_unwrapper –** a wrapper function for the fast, two-dimensional phase-unwrapping algorithm, based on sorting by reliability, following a non-continuous path (2D-SRNCP) [Herráez et al., 2002]. The function allows for spatial unwrapping of discontinuous phase.
    - Input:
        - *I_ph* - 2D matrix containing the wrapped phase map as a single precision (32-bit float) data type.
    - Output:
        - *I_out*– 2D matrix containing the unwrapped phase map in units of radians.

Stage 2

Masking

- **motion_map_masking –** creates a binary mask designating the areas of significant motion based on user provided motion map. The motion map is typically obtained by 3D or 4D data sets containing the motion of the object at several instances (phase or time positions) and/or excitation frequencies/types.
    - Input:
        - *I_in* - 2D matrix representing a motion map of the object.

        - *bw_thresh* – threshold controlling the conversion from the motion map into a binary mask. Values are in the range of $[0,1]$.
        - *dilate_erode_ratio* – ratio between the kernel size of the morphological dilation and erosion operators used for spatial filtration of the edge of the binary motion mask. Values in the range of $[0;\ 1)$ will increase the mask and vice versa.
        - *border_filter_size_norm* – normalized kernel size of the filter for border of the binary motion mask. Filter size is normalized relative to the full image size and values are in the range of $[0,1]$.
        - *area_thresh_norm* - normalized minimal area size for blob area filtration of the binary motion mask. Minimal area size is normalized relative to the full image size and values are in the range of $[0,1]$.
    - Output:
        - *I_mask_auto*– binary mask output representative of the area of significant motion.

- **multiply_3Dby2D –** applies a 2D mask (binary or NaN) on a 3D data set by multiplying each frame with the mask.
    - Input:
        - *I_3D* - 3D matrix with data set to be masked.
        - *I_2D* - 2D matrix with mask to be applied.
    - Output:

    - *I_3D* – masked 3D data set. The function uses the same input and output variable in order to reduce memory consumption.

Temporal correction

- **DC_equalization –** applies temporal seed point correction (Chapter 11) to a data set of unwrapped phase maps. The function allows for 3 types of corrections based on: (1) a new seed point; (2) and automatically estimated seed level based on the data at the border of a motion mask; and (3) averaged of the full map at each temporal instance of the data set. Used in the conversion from 3DHDS (Chapter 10) to STDDC (Chapter 11).
  - Input:
    - *I* – 2D or 3D matrix containing a data set (3DHDS) to be seed-point-corrected.
    - *DC_comp_type* – Type of temporal seed point correction.
    - *Settings* – a data structure containing parameters for each type of temporal seed point correction.
  - Output:
    - *I_ac* – 2D or 3D matrix containing the corrected data set.

- **high_pass_3D –** applies a high-pass filter along the temporal direction of each spatial point of a STDDC, which allows for rigid body motion compensation (Chapter 11). All filter types are designed for parallel (multi-threaded) execution.
  - Input:

    - *I_raw* – 3D matrix containing a data set (STDDC) to be compensation for rigid body motion.
    - *type* – Type of high-pass filter: (1) temporal average; (2) spatio-temporal running average; and (3) polynomial fit.
    - *option* – a data structure containing parameters for each type of high-pass filter correction
  - Output:
    - *I_high_pass* – temporal high-pass of the STDDC.
    - *I_low_pass* – temporal low-pass of the STDDC.

Stage 3

MRMP

- **natur_freq_map3**– estimates the spatial dependence (maps) of temporal and frequency domain MRMPs including: global peak time (GPT) and amplitude, the first local peak time (FLPT), response time (RT), dominant modal frequency (DMF), and group delay (GD) (Chapter 11).
  - Input:
    - *I_full* - 3D matrix containing a data set (STDDC) to be used for estimation of MRMP. Assumes displacement units of μm and time units of μs.
    - *time_pos* – a time vector. Units are μs.

    - *time_lim* – 1 × 2 vector indicating the time range of STDDC to be used for time domain MRMP estimation. Units are the same as in *time_pos.*
    - *mic_ftt* – vector containing the FFT (double complex data type) of the microphone measurement used for calculation of the transfer function (TF).
    - *mic_fft_f*- vector containing the frequency range corresponding to *mic_ftt.* Units are Hz.
    - *coarse_res* - 1 × 2 vector containing the horizontal and vertical resolution for the coarse grid used for data reduction (Chapter 11). If only a scalar is provided, a square grid is used.
    - *cell_size* – scalar indicating the kernel size for the coarse grid used for data reduction (Chapter 11).
    - *sampling_freq* – sampling frequency of the temporal axis of the STDDC. Units are Hz.
    - *amp_lim* – minimum amplitude limit used to distinguish values with insufficient signal-to-noise ratio (SNR). Typically this value is set to 2-3 fold of the displacement noise floor of the interferometric measurement. Units are the same as in *I_full.*
    - *freq_search_lim* - 1 × 2 vector indicating the frequency range of STDDC to be used for time domain MRMP estimation. Units are the same as in *sampling_freq.*
- <u>Output:</u>

    - *dominant_modal_frequency* - dominant modal frequency (DMF) map.
    - *global_peak_amp* - global peak amplitude map.
    - *global_peak_time* - global peak time (GPT) map.
    - *response_time* - response time (RT) map.
    - *first_local_peak_time* - first local peak time (FLPT) map.
    - *group_delay* - group delay (GD) map.

- **time_const_map3**– estimates the spatial dependence (maps) of the time constant (TC) (Chapter 11).
  - Input:
    - *I_full* - 3D matrix containing a data set (STDDC) to be used for estimation of TC. Assumes displacement units of μm and time units of ms or μs.
    - *X* – time vector. Units are ms or μs.
    - *coarse_res* - 1×2 vector containing the horizontal and vertical resolution for the coarse grid used for data reduction (Chapter 11). In only a scalar is provided, a square grid is used.
    - *cell_size* – scalar indicating the kernel size for the coarse grid used for data reduction (Chapter 11).
    - *method* – selects a decay envelop estimation method based on: (1) Hilbert transform; (2) running average with a cut-off frequency based on the dominant modal frequency of the signal; (3) running

        average maximum slope; and (4) local peak detection and spline interpolation.
    - *option* – string that controls the robust fitting type for the exponential fit. For details, see MATLAB’s *fit* and fit type *exp1*. Typical values are either ‘*LAR*’ or ‘*Off*’.
    - *env_option* – a scalar that controls the sensitivity (resolution) of the decay envelope fitting methods.
    - *range* – defines the units of the time vector which in turn define the initial guess for the exponential fit: 1 for *ms* and 0 (Default) for *μs*.
    - *Y_lim* - minimum amplitude limit used to distinguish values with insufficient signal-to-nosie ratio (SNR). Typically this value is set to 2-3 fold of the displacement noise floor of the interferometric measurement. Units are the same as in *I_full*.
- Output:
    - *Tau* – time constant (TC) map.
    - *R_2* – map of the goodness of fit (R^2) of the TC map.

Additional scripts and functionalities

Additional scripts for post processing of quasi-static, steady state and transient measurements include:

- ***Compare_HS_data_v1*** – PDMI for extraction of MRMP from multiple STDDC obtained from transient measurements [Dobrev et al., 2015].

- ***Q_factor_estimation081913*** – quantifies the spatial distribution of the Q-factor based on multiple PHHS stroboscopic recordings corresponding to a range of frequencies around a central modal frequency.
- ***Pulsed_DE_test_human082113_repeatability*** – quantifies the spatial and temporal repeatability of multiple STDDC based on the PHHS in MPDE acquisition mode.
- ***Batch_processor_v2_072012*** and ***MEEI_processing_demo_071412*** – quantification of phase and magnitude of motion as well as shape of the TM based on multiple PHHS stroboscopic recordings at a range of frequencies.
- ***Museum_thermal_cycle1*** – PDMI of shearographic data obtained by steady quasi-static excitation through thermal cycling. Typically used for measurements of artwork [Khaleghi et al., 2012].
- ***Museum_thermal_cycle_repeatability*** – comparison between multiple shearographic measurements under quasi-static excitation through thermal cycling. Typically used in combination with ***Museum_thermal_cycle1***.
- ***Museum_thermal_cycle_postProc1*** – comparison of shearographic data with IR cameras and reflectance transformation imaging (RTI) under quasi-static excitation through thermal cycling [Klausmeyer et al., 2014b]. Typically used in combination with ***Museum_thermal_cycle1***.
- ***Museum_long_term_test2*** - PDMI of shearographic data obtained by quasi-static state excitation through random environmental changes over long time (i.e., >1day) periods. Typically used for measurements of artwork [Khaleghi et al., 2014b].